

**UNIVERSIDAD DE GRANADA
FACULTAD DE CIENCIAS**

**Departamento de Física Aplicada
Grupo de Física de Fluidos y Biocoloides**

*Electrostatic heteroaggregation
processes arising in
two-component colloidal
dispersions*



José Manuel López López

TESIS DOCTORAL

Editor: Editorial de la Universidad de Granada
Autor: José Manuel López López
D.L.: Gr. 1830 - 2006
ISBN: 978-84-338-4094-3

*Electrostatic heteroaggregation
processes arising in
two-component colloidal
dispersions*

por

JOSÉ MANUEL LÓPEZ LÓPEZ

Licenciado en Ciencias (Físicas)

DIRECTORES:

Dr. D. Artur Schmitt
Prof. Titular de Física Aplicada

Dr. D. Arturo Moncho Jordá
Prof. Colaborador de Física Aplicada

Dr. D. Roque Hidalgo Álvarez
Catedrático de Física Aplicada

Este trabajo de investigación se presenta
para alcanzar el grado de
DOCTOR EN CIENCIAS FÍSICAS
DOCTOR EUROPEUS

José Manuel López López
Granada, julio de 2006

Este trabajo ha sido financiado por el proyecto del plan nacional de materiales MAT2003-08356-C04-01.

A mis padres

Agradecimientos

- Deseo agradecer en primer lugar al Dr. D. Roque Hidalgo Álvarez por haberme dado la oportunidad de llevar a cabo este trabajo de investigación. Su apoyo y su confianza en mí y en este proyecto han sido constantes desde el primer momento, antes incluso de que terminase mi licenciatura.
- Al Dr. Artur Schmitt debo agradecerle tantas cosas que para enumerarlas todas requeriría una sección propia. Todos los puntos de este trabajo son un intento de reflejar su afán por el detalle y el orden, desde el protocolo de medida experimental hasta la propia edición de la tesis. Queden aquí mi respeto y admiración por un magnífico profesor y aún mejor persona.
- Agradezco al Dr. Arturo Moncho Jordá que aceptase el reto de codirigir una tesis ya iniciada. Es mérito suyo que se incluyan aquí resultados de simulación que complementen al experimento. Sin su aportación, sin duda, esta tesis hubiese quedado coja. No menos importante ha sido su contagiosa inyección de entusiasmo, justo en el momento en que más necesaria me era.
- Por supuesto, no puedo dejar de mencionar al Dr. José Callejas Fernández —mi “cuarto director”— que, en un magnífico ejemplo de honestidad personal, prefirió concentrar sus esfuerzos en aquellos campos que mejor domina. Además de su dedicación inicial, le agradezco que haya financiado este trabajo a través del proyecto de investigación del que es responsable.
- Este trabajo estaría incompleto de no ser por la inestimable y desinteresada colaboración del Dr. Antonio Puertas, de la Universidad de Almería. Mi más sincero agradecimiento por permitirme utilizar sus programas sin ninguna limitación, y por las fructíferas conversaciones que hemos mantenido y de las que tanto he aprendido.
- Doy las gracias al Prof. Jean Pierre Hansen por haberme permitido realizar una estancia de verano en el *Cambridge University Centre for Computational Chemistry* (CUC³), y al Dr. Ard Louis por todo el tiempo y esfuerzo que me dedicó durante la misma. Quiero hacer extensivo mi agradecimiento a todo el personal del CUC³, que me acogió desde el primer momento

como a un miembro más, especialmente al Dr. Johan Padding, al Dr. Mark Miller y a la Dra. Catherine Pitt.

- Agradezco a Teresa y Pedro, con quienes me une una amistad que viene desde los años de la carrera, todo lo que hemos compartido dentro y fuera del laboratorio; y a Juanjo, Roberto, Fernando, Cati, Juan Carlos, Julia, Joaquín, Manolo y todos los demás compañeros becarios/precarios, el haber contribuido a crear un ambiente sano de trabajo... ¡y esparcimiento!
- Mi agradecimiento a todos los compañeros del Grupo de Física de Fluidos y Biocoloides que participasteis de alguna forma en este trabajo y que no he podido mencionar expresamente en un espacio tan reducido. También a todo el personal del Departamento de Física Aplicada por haberme permitido la realización de esta Tesis.
- Tampoco hubiese sido posible este trabajo sin la participación de las instituciones que me han financiado durante estos últimos cinco años, principalmente el Plan Nacional de Formación de Profesorado Universitario del Ministerio de Educación y Ciencia; pero también el Programa de Formación de Personal Docente e Investigador de la Junta de Andalucía; y el mismo Grupo de Fluidos y Biocoloides, que me financió durante unos meses mediante una beca con cargo a sus propios fondos.
- Finalmente, agradezco la paciencia y el apoyo de aquellos que más me han animado y más han sufrido conmigo. Me refiero, claro está, a mis padres, a mis amigos —gracias Javi por insistirme tanto en “cuatro páginas al día”— y, especialmente, a Encarni.

Contents

1. INTRODUCTION	1
1.1. Some fundamental definitions	1
1.2. Motivations	2
1.3. A short overview	5
2. THEORETICAL BACKGROUND	9
2.1. Heteroaggregation kinetics	9
2.1.1. General aggregation kinetics	9
2.1.2. Homoaggregation kinetics	14
2.1.3. Classical solutions of the Smoluchowski's equation	16
2.1.4. Other important aggregation <i>kernels</i>	21
2.1.5. Binary heteroaggregation kinetics	22
2.1.6. HHF approximation	23
2.2. Microscopic description	25
2.2.1. Brownian motion and diffusion	26
2.2.2. Diffusion-limited cluster-cluster aggregation	28
2.2.3. Reaction-limited cluster-cluster aggregation	29
2.2.4. Attraction-driven cluster-cluster aggregation	32
2.3. Particle-particle interactions	32
2.3.1. DLVO theory	32
2.3.2. London-van der Waals interactions	33
2.3.3. Double layer potential energy	33
2.3.4. Kinetic stability	37
2.3.5. HHF theory	37
2.3.6. Non-DLVO forces	38

3. MATERIALS AND METHODS	39
3.1. Single-Cluster light-scattering	39
3.1.1. Principle of function and description	40
3.1.2. Data acquisition and treatment	46
3.1.3. Measuring protocol	50
3.2. Other experimental techniques	57
3.2.1. Nephelometry	58
3.2.2. Electrophoretic mobility	61
3.3. Experimental systems	63
3.3.1. General characteristics	64
3.3.2. Particle size and shape	66
3.3.3. Stability versus KBr concentration	69
3.3.4. Aggregation regimes	70
3.3.5. Electrophoretic mobility	75
3.4. Computer simulations	77
3.4.1. Brownian dynamics simulations without interactions	77
3.4.2. Brownian dynamics simulations with interactions	80
3.4.3. Solving the Smoluchowski's equations	82
4. AGGREGATION RATE	85
4.1. Experimental aggregation rate constants	85
4.1.1. High electrolyte concentrations	87
4.1.2. Intermediate electrolyte concentrations	91
4.1.3. Low electrolyte concentrations	95
4.2. Comparison with BDS and theoretical predictions	99
4.2.1. Brownian dynamics simulations	99
4.2.2. HHF theory	103
4.3. Concluding remarks	105
5. CLUSTER-SIZE DISTRIBUTIONS	107
5.1. Experimental cluster-size distributions	108
5.1.1. High electrolyte concentrations	109
5.1.2. Intermediate electrolyte concentrations	111
5.1.3. Low and very low electrolyte concentrations	114
5.2. Brownian dynamics simulations	116

5.2.1.	BDS without interactions	117
5.2.2.	BDS with interactions	121
5.3.	Cluster discrimination	125
5.3.1.	Experimental evidences of cluster discrimination	125
5.3.2.	Comparison with Brownian dynamics simulations	128
5.3.3.	Conclusions	131
5.4.	Electrostatic heteroaggregation regimes	132
5.4.1.	Heteroaggregation <i>kernels</i>	132
5.4.2.	Concluding remarks	140
6.	ASYMMETRIC HETEROAGGREGATION	143
6.1.	Ideal BDLCA processes	144
6.1.1.	Short time kinetics	147
6.1.2.	Long time behaviour	152
6.1.3.	Stable aggregates	158
6.1.4.	Aggregation model for $x < x_c$	161
6.2.	Experimental evidences of stable aggregates	164
6.2.1.	CSD in asymmetric two-component systems	164
6.2.2.	Stable aggregates in experiments	169
6.2.3.	Influence of the electrolyte concentration	172
6.3.	Concluding remarks	174
7.	SUMMARY AND CONCLUSIONS	179
A.	RESUMEN Y CONCLUSIONES	185

List of Figures

1.1. Microphotograph of a colloidal heteroaggregate	3
2.1. CSD calculated for several classical <i>kernels</i>	18
2.2. Product <i>kernel</i> with the Flory model	21
2.3. Microphotograph of a typical fractal aggregate	27
2.4. Brownian <i>kernel</i> solution	29
3.1. Scheme of our SCLS instrument	43
3.2. Hydrodynamic focusing cell	44
3.3. Typical phototube output	47
3.4. Frequency histograms of a SCLS measurement	48
3.5. Scheme of the mixing setup	54
3.6. Monomer correction due to coincidences	56
3.7. Typical nephelometre output	60
3.8. Fundamentals of a electrophoretic mobility set-up	62
3.9. TEM microphotograph of the experimental systems	67
3.10. Particle size distribution of the experimental systems	68
3.11. Stability factor of the experimental systems	70
3.12. CSD in homoaggregation experiments	72
3.13. Effects of some salts on the homoaggregation behaviour	74
3.14. Electrophoretic mobility versus pH	75
3.15. Snapshots of a simulated BDLCA process	80
4.1. k_S in homo- and heteroaggregation experiments at high [KBr]	89
4.2. k_S in homoaggregation experiments at intermediate [KBr]	92
4.3. k_S in heteroaggregation experiments at intermediate [KBr]	93
4.4. k_S in heteroaggregation experiments at low [KBr]	95

List of Figures

4.5.	k_S in heteroaggregation experiments with no added salt	96
4.6.	Determination of k_S in simulations with interactions	100
4.7.	k_S : comparison between experiments and simulations	102
4.8.	k_S : comparison between experiments and HHF predictions	104
5.1.	CSD in heteroaggregation experiments at high [KBr]	110
5.2.	CSD in heteroaggregation experiments at intermediate [KBr]	112
5.3.	Average cluster-size for experiments at high and medium [KBr]	113
5.4.	CSD in heteroaggregation experiments at low [KBr]	115
5.5.	Average cluster-size for experiments at low and very low [KBr]	116
5.6.	Simulated CSD for DLCA and BDLCA processes	118
5.7.	Comparison experiments / simulations: DLCA and BDLCA	119
5.8.	CSDs in heteroaggregation simulations at different κa values	122
5.9.	Comparison experiments / simulations: attraction-driven	124
5.10.	An ALCA experiment, from Yoshioka <i>et al.</i> (2005)	126
5.11.	Experimental cluster-concentration profiles	128
5.12.	Dimer-trimer concentration ratio	130
5.13.	Comparison experiments / simulations / theory: DLCA	133
5.14.	Comparison experiments / simulations / theory: BDLCA	136
5.15.	CSDs for parity-dependent <i>kernels</i>	139
6.1.	Snapshots of simulated BDLCA processes	145
6.2.	k_S versus x in BDLCA simulations	147
6.3.	Determination of k_S in BDLCA simulations	149
6.4.	CSDs of simulated BDLCA processes	153
6.5.	Octamer-composition distribution	156
6.6.	Time evolution of monomers	157
6.7.	CSD profile for simulated BDLCA	159
6.8.	Typical stable clusters	159
6.9.	Total number of aggregates of l th-order	161
6.10.	Time evolution of monomers and clusters	162
6.11.	CSDs for asymmetric systems: no added salt	166
6.12.	CSDs for highly asymmetric systems: no added salt	169
6.13.	Pulse histogram evolution for an asymmetric system	171
6.14.	CSDs in asymmetric heteroaggregation with interactions	174

List of Tables

3.1. Main properties of both experimental systems	66
3.2. Particle size of AS1 and IDC latexes	69
3.3. Low ionic strength buffers	76
4.1. Experimental values of k_{AB} obtained by different authors	86
4.2. k_S, k_{AA}, k_{BB} and k_{AB} at high electrolyte concentrations	94
4.3. k_S and k_{AB} at low electrolyte concentrations	98
4.4. k_S values in simulations with different κa	101
6.1. Main characteristics of some two-component simulations	146

1. INTRODUCTION

1.1. Some fundamental definitions

This is a thesis dissertation about *electrostatic heteroaggregation processes arising in two-component colloidal dispersions*. In what follows, we try to provide an adequate definition for a such long topic name. A *colloidal dispersion* is a complex fluid consisting of two distinguishable phases: i) a dispersed phase composed of solid particles and ii) a dispersion phase, usually a liquid. The adjective *colloidal* implies that the typical size of the particles¹ is compressed between 10 nm and 1 μ .

The most distinctive property of colloidal dispersions —which is even responsible of the own word “colloid”²— is their tendency to *aggregate*. In fact, most colloidal particles are lyophobic, *i.e.*, they tend to reduce their interphase area. For solid, hard particles, this only can be achieved by forming clusters of particles. The process of rearranging the colloidal dispersion into clusters is called aggregation, coagulation, flocculation or association. The term coagulation is generally used to describe processes that lead to permanent contact between particles and hence are irreversible. Flocculation and association are referring to reversible or temporary association between particles. Aggregation is a more general term, and can be applied instead of any other. This process may eventually leads to a phase separation. Even although a typical colloidal dispersion is thermodynamically unstable, it is usually kinetically stable, *i.e.*, the time scale of the coagulation process is generally longer than the time scale we are interested

¹The particle diameter, since only colloidal suspensions of microspheres are considered here.

²The term “colloid” was introduced by the Scottish scientist Thomas Graham in 1861. It derives from the Greek word “Kollas”, which means “glue”.

1. INTRODUCTION

in. This can be due, for instance, to the presence of repulsive particle-particle interactions.

The prefix *hetero* implies that the nature of all the particles is not the same. Hence, by a *heteroaggregation* process we refer to an aggregation process in which several species of particles are involved. Analogously, we speak about *homoaggregation* when the nature of all the particles involved in the aggregation process is the same. In this work, we focus on heteroaggregation processes arising in two-component systems.

Particles may differ on any of their properties: chemical composition, electrical charge, size or shape of particles, etc. Here, we focus on particles with the same shape, size and chemical composition, but with opposite electrical charges. Two terms are found in the literature which refers to heteroaggregation of oppositely charged particles: “Charge heteroaggregation” (Puertas *et al.*, 2001a; Fernández-Barbero and Vincent, 2001) and “electrostatic heteroaggregation” (Kim *et al.*, 2003). The latter term emphasises the nature of the particle-particle interactions and, hence, it is preferred here.

In summary, we study the aggregation processes arising in two-component colloidal dispersions, where both types of particles only differ in the sign of their electrical charges.

1.2. Motivations

Binary colloidal dispersions have received significant interest in the recent scientific literature due to their potential use in many technological processes and natural phenomena (López-López *et al.*, 2006). Aggregation of binary colloids with varying composition, charge or size has been shown to be important in industrial applications such as mineral flotation (di Feo *et al.*, 2001; Bandini *et al.*, 2001; di Feo and Finch, 2002), waste water treatment (Findlay *et al.*, 1996; Buffle *et al.*, 1998; Rubio *et al.*, 2002), stability of emulsions (Sunkel and Berg, 1996; Abend *et al.*, 1998; Lagaly *et al.*, 2001) and rapid separation of

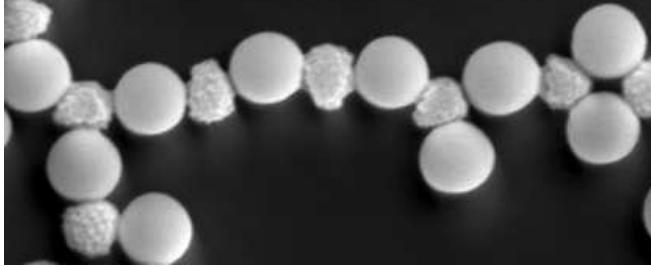


Figure 1.1.: TEM microphotograph of a heteroaggregate, reproduced from (Snoswell *et al.*, 2005) for academic purposes.

phases (Ito *et al.*, 2002). It is also fundamental for the manufacture of new materials, such as molecular materials (Lipskier and Tran-Thi, 1993; Ion *et al.*, 1999) and, especially, the so-called composite materials.

Many of the composite materials present a core-shell internal structure (Miao and Marquis, 1992; Harley *et al.*, 1992; Ottewill *et al.*, 1997; Morris *et al.*, 1999; Yang *et al.*, 2001; Tangboriboonrat and Buranabunya, 2001; Costa *et al.*, 2002; Luna-Xavier *et al.*, 2002; Furusawa *et al.*, 2003; Galindo-González *et al.*, 2005), although other topologies are found in the literature (Deng and Lu, 1998; Taylor *et al.*, 2003; Snoswell *et al.*, 2005; Ying *et al.*, 2005; Plunkett *et al.*, 2005; Sunagawa *et al.*, 2006). The variety of synthesis mechanisms and final properties of these composite materials is quite large. For instance, Snoswell *et al.* (2005) make use of the heteroaggregation of hard and soft colloids to synthesise composite materials of high porosity (see Fig. 1.1); Costa *et al.* (2002) prepared core-shell microparticles by coating a phosphor particle with pigment ones; and Sunagawa *et al.* (2006) demonstrated that the performance of a solid oxide fuel cell improves when the anode is synthesised by means of a heterocoagulation process. The technology of synthesising core-shell particles is quite sophisticated, despite the fact that it is usually based on empiric recipes. Furusawa *et al.* (2003), for instance, were able even of synthesise a complex particle composed by a hematite core, a inner layer of silica nanoparticles and an outer layer of phosphatidyl-choline liposomes.

Understanding heteroaggregation is also a key issue for developing novel biotech-

1. INTRODUCTION

nologies, such as bacteria recovery (Hayashi *et al.*, 2001) and industrial extraction of enzymes from *in culture* fungi (Mukherjee *et al.*, 2002). Colloidal heteroaggregation have been also applied to medical areas, from enhanced immunoassays (Cölfen *et al.*, 2002), to new approaches to fight human tumours (Jadhav *et al.*, 2001; McCarty *et al.*, 2002). Ouali *et al.* (1994) even used a technique similar to ours (a Coulter counter) to study the heteroaggregation kinetics of sensitised latexes, in order to improve the accuracy of pregnancy tests.

Apart from its numerous applications, heteroaggregation phenomenon itself is important from the fundamental science point of view. In fact, scientific literature about heteroaggregation have remarkably increased during the last ten years (López-López *et al.*, 2006). Particularly, electrostatic heteroaggregation processes at low and very low electrolyte concentrations have been revealed full of scientific surprises. Very recently, for example, Puertas *et al.* (2000) and Fernández-Barbero and Vincent (2001) made the exciting discovery that oppositely charged polymer spheres at low ionic strength can lead to fractal dimensions significantly lower than DLCA (rapid homoaggregation). These authors found a continuous increase in the fractal dimension from 1.3 to 1.7 as the background electrolyte concentration was increased. Brownian dynamics simulations followed a similar trend (Puertas *et al.*, 2001*b*), although the obtained fractal dimensions were not as low as in experiments. Kim *et al.* (2003) also studied heteroaggregates prepared by aggregation of oppositely charged polystyrene spheres. When no electrolyte was added, they measured fractal dimensions as low as 1.21 ± 0.15 , which is the lowest mass fractal dimension ever measured for aggregating colloids.

Other interesting phenomena are predicted to occur in electrostatic heteroaggregation processes at low and very low electrolyte concentrations. Computer simulations performed by Puertas *et al.* (2002) predicted that a odd-even cluster discrimination takes place at very low electrolyte concentrations. At long aggregation times, clusters with an even number of particles disappear faster than those composed by an odd number of particles. The first experimental support to this hypothesis has been found during this researching work (López-López *et al.*, 2004*b*).

In summary, two aspects of the electrostatic heteroaggregation processes are par-

ticularly interesting and still not well understood. On the one hand, the distinct behaviour of heteroaggregates that are formed at very low electrolyte concentrations. On the other hand, the formation and properties of clusters with a core-shell structure. In this work we deal with these two aspects by two complementary approaches: single-cluster light scattering experiments and Brownian dynamics simulations. Moreover, our study does not restrict only to processes arising at very low electrolyte concentrations, but it covers a wide range. This will allow us to identify the different aggregation regimes that take place in electrostatic heteroaggregation processes.

1.3. A short overview

This PhD thesis is structured in the following chapters:

Chapter I: Introduction

The research topic and my motivations are briefly introduced here.

Chapter II: Theoretical background

The theoretical background needed for describing electrostatic heteroaggregation processes arising in colloidal dispersions is provided here. It comprises a general kinetic description, a detailed microscopic description of the process and an overview on particle-particle interactions.

Chapter III: Materials and methods

Experimental techniques, simulation methods and colloidal dispersions used in this work are described here. Especial attention is paid to the *single-cluster light-scattering* (SCLS) technique, used for acquiring most experimental data.

**Chapter IV: Symmetric heteroaggregation:
aggregation rate constants**

The short time kinetics of symmetric two-component systems is discussed here. Effective and absolute dimer formation rate constants are determined by means of SCLS over a wide range of electrolyte concentrations. The absolute aggregation rate constant is found to

increase from diffusion-limited values at high electrolyte concentrations to quite larger values at very low electrolyte concentrations. Brownian dynamics simulations and theoretical approaches are used in order to interpret the experimental results.

Chapter V: Symmetric heteroaggregation: cluster-size distributions

This chapter is devoted to the study of the long time kinetics behaviour of symmetric heteroaggregation processes. The cluster-size distribution is monitored by means of SCLS over a wide range of electrolyte concentrations. The first evidences of cluster discrimination are found (López-López *et al.*, 2004b). Additionally, Brownian dynamics simulations complement experimental data, and allow us to distinguish several aggregation regimes: from diffusion-limited at high electrolyte concentration to attraction-driven at very low electrolyte concentrations. A novel binary diffusion-limited colloid aggregation (BDLCA) regime is proposed for the intermediate region. Furthermore, some theoretical *kernels* for the coagulation equation are discussed.

Chapter VI: Asymmetric heteroaggregation: stable aggregates

Here, a study on asymmetric heteroaggregation processes arising in two-component colloidal dispersions is reported. It is specially focused on the formation and structure of stable aggregates, which are found in BDLCA processes arising in highly asymmetric systems (López-López *et al.*, 2005). These stable aggregates present a core-shell structure and, hence, may help to improve our knowledge about nanocomposite materials. Other interesting phenomena that take place in these processes, such as bimodal cluster concentration curves (“two hump effect”, López-López *et al.*, 2005) are also discussed. Most data corresponds to computer simulations, although some experimental evidences of stable clusters are reported for the first time to the best of our knowledge.

Chapter VII: Conclusions

It is a brief summary of the conclusions of this research work, with some emphasis on our original results.

2. THEORETICAL BACKGROUND

In this chapter, we briefly describe the theoretical background needed to study electrostatic heteroaggregation processes. Only those results relevant to our purposes are discussed. Complete derivations are avoided in general. Instead, references where they can be found are provided.

The aggregation kinetics is described in Sec. 2.1, with some emphasis put on one-component homoaggregation and two-component heteroaggregation processes in dilute systems. A microscopic description of the aggregation processes is developed in Sec. 2.2. Finally, Sec. 2.3 deals with the particle-particle interactions considered by the Derjaguin-Landau-Verwey-Overbeek (DLVO) and Hogg-Healy-Fuerstenau (HHF) theories.

2.1. Heteroaggregation kinetics

In this section, aggregation processes are described from the kinetics point of view. We start from the most general case of colloidal aggregating systems (Sec. 2.1.1), and finish with the particular case of two-component systems (Sec. 2.1.5).

2.1.1. General aggregation kinetics

Consider an ideal colloidal dispersion, *i.e.*, an aqueous suspension of identical microspheres. These particles encounter each other randomly, due to their intrinsic Brownian motion (Overbeek, 1977; Broide and Cohen, 1990; Stoll and

2. THEORETICAL BACKGROUND

Pefferkorn, 1992a) or due to external forces, such as shear (Wang, 1992), concentration gradients (Adler, 1981; Chung and Hogg, 1985) or gravity (Chung and Hogg, 1985; Wang, 1992; Allain *et al.*, 1995). After a collision, two particles may be linked and become a *dimer*. The dimer, on its part, may collide with another particle and form a trimer. And so on, any two *aggregates* or *clusters* may encounter and form a larger aggregate.¹ This aggregation process continues until macroscopic flocs are formed, or until a stationary cluster-size distribution is reached.

Two alternative —and equivalent— descriptions of the aggregation process exists: deterministic and stochastic. The deterministic description was born by the pioneering works of von Smoluchowski (1917), and it is basically a mean-field approximation, valid for infinitely diluted and large systems. The stochastic description, on the contrary, takes into account the limited size of the system and the consequent random fluctuations in the population of the different species (Gillespie, 1977). This leads to a more complex, although also more rigorous, description of the aggregation phenomenon.

Deterministic description

Consider a non-limited colloidal system undergoing an irreversible aggregation process. Particles are grouped in clusters with different properties: mass, composition, inner structure, etc. In order to describe the aggregation state of the system at a time t , we need to know the *cluster population*, $c^\gamma(t)$, *i.e.*, the concentration of clusters of the γ type. Here, γ and other Greek letters represent generic indexes that go through all the different cluster species. The basic reaction is the union of two aggregates, α and β , to form a larger cluster γ . We indicate this reaction with the “direct sum” notation: $\alpha \oplus \beta = \gamma$. After this reaction, the concentration of γ -aggregates increases and the concentrations of α - and β -aggregates decreases. Since this is just a general binary reaction, we can

¹In this work, the words “aggregate” and “cluster” are used indistinctly to refer to any group of particles that move together as a whole. A n -mer refers to a cluster composed by n particles. For the sake of simplicity, individual colloids will be considered as “clusters of size one” or *monomers*.

assume that the reaction rate is proportional to the concentration of the reactants. Let $k^{\alpha,\beta}$ be the corresponding proportionality constant. Then, we can say that:

$$\left. \frac{dc^\gamma}{dt} \right|_{\alpha \oplus \beta} = - \left. \frac{dc^\alpha}{dt} \right|_{\alpha \oplus \beta} = - \left. \frac{dc^\beta}{dt} \right|_{\alpha \oplus \beta} = k^{\alpha,\beta} c^\alpha(t) c^\beta(t) \quad (2.1)$$

When the γ -cluster is created by the reaction of two identical α -clusters, we have to take into account that the α -concentration decreases twice as fast as the γ -concentration increases. Formally,

$$\left. \frac{dc^\gamma}{dt} \right|_{\alpha \oplus \alpha} = - \frac{1}{2} \left. \frac{dc^\alpha}{dt} \right|_{\alpha \oplus \alpha} = \frac{1}{2} k^{\alpha,\alpha} (c^\alpha(t))^2 \quad (2.2)$$

On the other hand, the γ -aggregate concentration decreases when the reaction $\gamma \oplus \delta$ takes place, being δ an aggregate of any type. Hence, if we put together all the reactions that affect the concentration of γ -aggregates, we obtain the following non-linear differential equation:

$$\frac{dc^\gamma(t)}{dt} = \frac{1}{2} \sum_{\alpha \oplus \beta = \gamma} k^{\alpha,\beta} c^\alpha(t) c^\beta(t) - c^\gamma(t) \sum_{\delta} k^{\delta,\gamma} c^\delta(t) \quad (2.3)$$

The first term in the r.h.s. of (2.3) deals with all the reactions that create aggregates of the γ type, and consequently is called *birth term* (see, e.g., Ramkrishna, 2000). Analogously, the second term deals with the reactions that decrease the γ -concentration and is called *death term*. Finally, the set of aggregation constants $k^{\alpha,\beta}$ is called the *kernel* of the system. Note that the $\frac{1}{2}$ coefficient in the birth term means different things when $\alpha = \beta$ and when $\alpha \neq \beta$. In the former case is due to (2.2), and in the latter is introduced just to avoid double counting since “ $\alpha \oplus \beta$ ” and “ $\beta \oplus \alpha$ ” are actually the same reaction. Once the *kernel* is known, the equation (2.3) could, in principle, give us the time evolution of the cluster population.

It should be noted that two assumptions have been taken for the above derivation:

2. THEORETICAL BACKGROUND

Dilute system hypothesis

Only binary collision have been taken into account. Consequently, (2.3) only holds when the system is dilute enough to neglect the probability of a three-body reaction. For real systems, it is usually considered that a system is dilute enough when the particle volume fraction is less than 1% (Broide, 1988). Even when this limit may be questionable, in this work the experiment were carried out at a quite low volume fraction, less than 0.001%. Also in the simulations the system may be considered diluted enough, since the particle volume fraction ranges between 0.01% and 0.1%.

Mean-field hypothesis

When we state that the cluster concentrations $c^\gamma(t)$ are continuous functions, we implicitly are assuming that the system is infinite. Otherwise, any time a γ -cluster is created or destroyed its concentration should vary in a finite quantity, namely $1/V$, where V is the volume of the system. The stochastic description of the aggregation process deals with this limitation (Gillespie, 1977).

Stochastic description

The stochastic description of the aggregation process takes into account the finite size of the system. The cluster population is described by using the number of cluster, $N^\gamma(t)$, instead of the cluster concentrations. The set $\{N^\gamma(t)\}$ for all possible γ is usually notated as a vector $\vec{N}(t)$ and called *state vector*. The stochastic description introduces another fundamental idea: if we only know the state vector at a given time t_0 and the set of aggregation rate constants, $\{k^{\alpha,\beta}\}$, we cannot determine the exact state vector at a different time t , but only the state probability density $P(\vec{N}, t)$. This function gives the probability of finding the system in the state \vec{N} at time t . The probability density obeys the following master equation (Gillespie, 1977; Thorn and Seesselberg, 1994; Odriozola *et al.*, 2004):

$$\frac{dP(\vec{N}, t)}{dt} = \frac{1}{2V} \sum_{\alpha,\beta} k^{\alpha,\beta} \left[(N^\alpha + 1)(N^\beta + 1 + \delta_\alpha^\beta)P(\vec{N}', t) - N^\alpha(N^\beta - \delta_\alpha^\beta)P(\vec{N}, t) \right] \quad (2.4)$$

where δ_α^β is the Kronecker symbol and \vec{N}' is the vector state prior to the $\alpha \oplus \beta$ reaction:

$$\vec{N}' = \begin{cases} (\dots, N^\alpha + 1, \dots, N^\beta + 1, \dots, N^{\alpha \oplus \beta} - 1, \dots) & , \alpha \neq \beta \\ (\dots, N^\alpha + 2, \dots, N^{\alpha \oplus \alpha} - 1, \dots) & , \alpha = \beta \end{cases} \quad (2.5)$$

Fortunately, for larger systems both deterministic and stochastic descriptions are equivalent. The deterministic description is more convenient for obtaining mathematical properties of the solution, such as their long time behaviour (van Dongen and Ernst, 1985a) and scaling properties (van Dongen and Ernst, 1985b). On the other hand, the master equation (2.4) is easier to solve numerically (Thorn and Seesselberg, 1994).

Reversible aggregation

We have considered so far only irreversible aggregation, where bonds between particles never break. Nevertheless, some systems aggregate in a reversible manner (examples of reversible aggregation processes will be presented later on, see Fig. 3.13). Then, after some time, the population achieves a stationary state, in a sort of dynamic equilibrium (see, *e.g.*, Vanni, 2000). Reversible aggregation may be included in the aggregation theory, in both the deterministic (Vanni, 2000) and the stochastic (Odriozola *et al.*, 2003) descriptions, by including a *fragmentation kernel* in addition to the aggregation *kernel*.

The meaning of the aggregation rate constants

As stated above, $k^{\alpha,\beta}$ is related with the rate at which aggregates of species α and β react. This quantity has dimensions of volume per unit of time² and, hence, it expresses somehow a *flux*. Consider the reaction between an α -cluster and a β -cluster. Consider the origin of coordinates to be solidary to a concrete α -cluster. Then, if a β -cluster reacts with our α -cluster, it disappears reducing

²All k values of this work are expressed in cm^3s^{-1} , as usually. In this units, it takes values of the order of 10^{-12} .

2. THEORETICAL BACKGROUND

the β -concentration. Hence, the α -cluster acts as a β -cluster sink. Accordingly, we can state that $k^{\alpha,\beta}$ is the flux of β -clusters forward each α -cluster. This scenario is used in Sec. 2.2.1 for calculating the aggregation rate constants from the microscopic properties of the colloidal dispersion.

2.1.2. Homoaggregation kinetics

A particular case of special importance is found when all the particles are identical. Then, the main difference among aggregates is their mass or, equivalently, their number of constituent particles. Accordingly, it is usual to group together the clusters with the same number of component particles, and consider that the state of the system is described by knowing the concentration of clusters of each size (*cluster-size distribution*, $c_n(t)$ or CSD³). Obviously, the CSD does not describe completely the aggregation state of the system, because it does not take into account the internal structure of the clusters. $c_3(t)$, for instance, comprises the overall concentration of trimers, independently of the angle that form the three component particles. Nevertheless, the CSD is a widely used tool for studying aggregating systems.

Smoluchowski's equation

If we are only interested in determine the cluster-size distribution, (2.3) takes an easier form:

$$\frac{dc_n(t)}{dt} = \frac{1}{2} \sum_{i=1}^{n-1} k_{i,n-i} c_i(t) c_{n-i}(t) - c_n(t) \sum_{i=1}^{\infty} k_{ni} c_i(t) \quad (2.6)$$

which is known as Smoluchowski's equation of the coagulation (von Smoluchowski, 1917). Please note that in the cluster-size distribution —CSD in what follows— we do not distinguish the spatial configuration of the clusters, only their mass. It is quite reasonable to state that the cluster reactivity may depend not only on its size but also on its inner structure (the spatial configuration of the

³In this work, we use Greek letters ($\alpha, \beta, \gamma, \dots$) to refer to general indexes, and lower-case Latin letters (n, i, j, \dots) to refer to integer indexes.

constituent particles of the cluster). Hence, the aggregation rate constant k_{ij} have to be considered as an average of the aggregation rate constants corresponding to the different reactions between aggregates of masses i and j . This average is somehow weighted according to the abundance of the different spatial configurations. Hence, (2.6) does not hold when the population of clusters with the same size but different reactivity changes during the aggregation process. Fortunately, computer simulations demonstrate that this is quite unlikely to happen in homoaggregation processes (Odriozola *et al.*, 2001b), even when reversible aggregation is included (Odriozola *et al.*, 2002).

Stochastic description

Analogously, also the stochastic master equation may be restricted to study the cluster-size distribution of a homoaggregation process. Then, it reads:

$$\frac{dP(\vec{N}, t)}{dt} = \frac{1}{2V} \sum_{i,j} k_{ij} \left[(N_i + 1)(N_j + 1 + \delta_i^j) P(\vec{N}_{ij}^+, t) - N_i(N_j - \delta_i^j) P(\vec{N}, t) \right] \quad (2.7)$$

where $N_i(t)$ is the number of i -mers and \vec{N}_{ij}^+ is the vector state prior to the i -mer- j -mer reaction, which is given by:

$$\vec{N}_{ij}^+ = \begin{cases} (\dots, N_i + 1, \dots, N_j + 1, \dots, N_{i+j} - 1, \dots) & , i \neq j \\ (\dots, N_i + 2, \dots, N_{2i} - 1, \dots) & , i = j \end{cases} \quad (2.8)$$

Dimensionless aggregation equation

In theoretical studies of homoaggregation processes, it is usual to rewrite (2.6) in the following dimensionless way:

$$\frac{dX_n}{dT} = \frac{1}{2} \sum_{i=1}^{n-1} K_{i,n-i} X_i X_{n-i} - X_n \sum_{i=1}^{\infty} K_{ni} X_i \quad (2.9)$$

where $X_n = c_n/c_0$ is the dimensionless cluster-size distribution, $K_{ij} = 2k_{ij}/k_{11}$ is the dimensionless aggregation *kernel*, and T is a dimensionless time obtained by dividing the time by the so-called *aggregation time*, given by:

$$t_{\text{aggr}} = \frac{2}{c_0 k_{11}} \quad (2.10)$$

2.1.3. Classical solutions of the Smoluchowski's equation

The Smoluchowski's coagulation equation is a set of coupled nonlinear ordinary differential equations, which have a unique solution if positive initial conditions $X_j(0)$ are given, such that the moments:

$$M_n \equiv \sum_{j=1}^{\infty} j^n X_j \quad (2.11)$$

are initially finite for all integers n (Leyvraz and Tschudi, 1981). Nevertheless, exact solutions of (2.9) are only known for a few specially simple *kernels* (Leyvraz, 2003). They, although scarce, are of great importance since provide an easy way of checking the accuracy of numerical methods. In this section, we briefly comment on the solutions of (2.9) corresponding to the classical *kernels*, namely the “constant”, “sum” and “product” *kernels*. We only present explicit solution for aggregation processes starting from monomeric initial conditions, *i.e.*, $X_n(0) = \delta_n^1$.

Constant kernel

The simplest functional form of the *kernel* of (2.9) is the mass-independent *kernel*, or constant *kernel*:

$$K_{ij} = 2, \quad \forall i, j \in \mathbb{N} \quad (2.12)$$

Despite its simple form, the constant *kernel* provides a first point of reference to every aggregation process, and it is even a fair approximation to some real aggregation processes, such as those limited by diffusion. The solution from monomeric initial conditions was firstly derived by von Smoluchowski (1916), and have been often rederived (Leyvraz, 2003):

$$X_n(T) = \frac{T^{n-1}}{(1+T)^{n+1}} \quad (2.13)$$

The CSD for n -mers with $n \leq 7$ is plotted in Fig. 2.1.3a. The overall concentration of clusters, M_0 , given by

$$M_0 \equiv \sum_{n=1}^{\infty} X_n = \frac{1}{1+T} \quad (2.14)$$

is also plotted in the figure. Please note that the overall concentration of clusters is halved in one aggregation time, *i.e.*, $M_0(T = 1) = 1/2$. This fact has led to an alternative definition for the aggregation time, t'_{aggr} , which does not involve the dimer formation rate constant:

$$t'_{\text{aggr}} \quad / \quad M_0(t = t'_{\text{aggr}}) = \frac{1}{2} \quad (2.15)$$

A numerical solution of the constant *kernel* —obtained by the stochastic method that will be described in Sec. 3.4.3— is plotted in Fig. 2.1d. As can be seen, the agreement between exact and approximated solutions, is excellent.

Some of the features of the CSD plotted in Fig. 2.1a are shared by all the irreversible aggregation processes that start from monomeric initial conditions. Firstly, monomers cannot be created and, consequently, $X_1(T)$ is always a decreasing function. Clusters, on the other hand, are both created and destroyed during the aggregation processes. In the early stages of the aggregation process ($T \ll 1$) they are created at a larger rate than they are destroyed and, hence, their concentration increase. When their concentration is large enough, this tendency reverses. Consequently, all $X_n(T)$ curves with $n > 1$, are bell-shaped. Other features of the CSD corresponding to the solution of (2.9) with the constant *kernel*, are particular of this functional form. For instance, at long times, all X_n curves decay as T^{-2} .

The constant *kernel* have been intensively studied in the literature and its solution is actually known for arbitrary initial conditions (Leyvraz, 2003).

2. THEORETICAL BACKGROUND

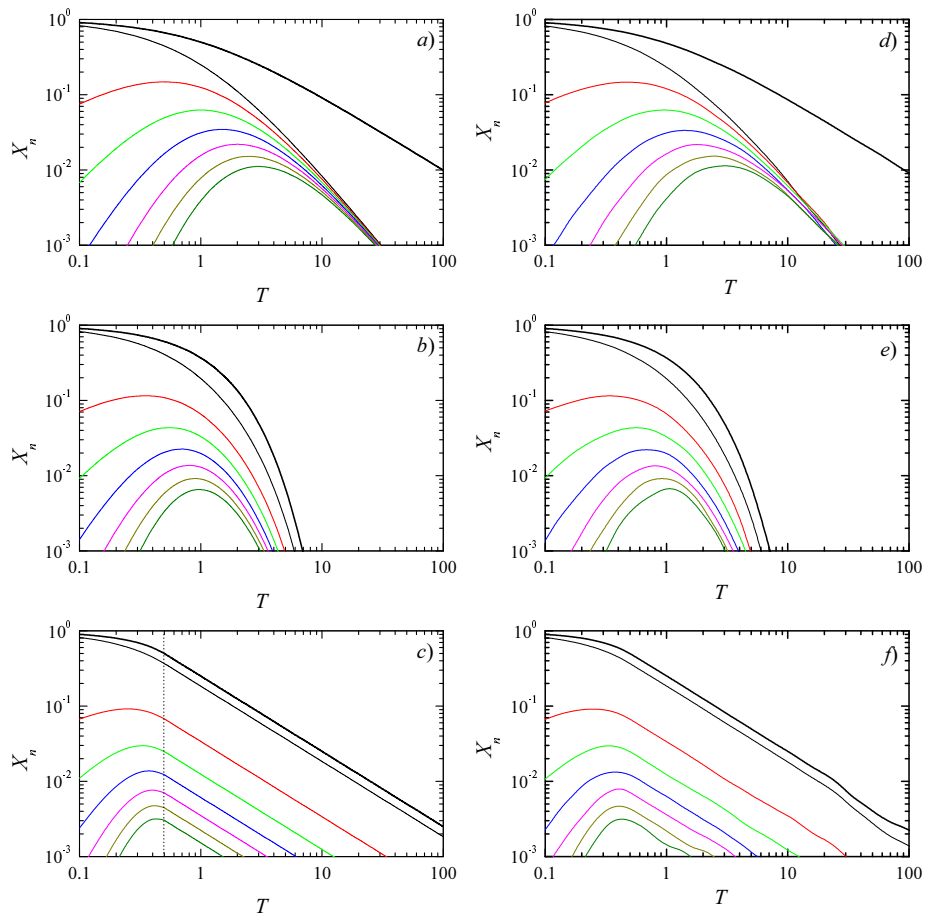


Figure 2.1.: Cluster-size distribution calculated for several classical *kernels*: constant (top row); sum (medium row) and product (bottom row). The plots on the left side are the analytical solutions discussed in this section, and those of the right side are approximated solutions obtained by numerically solving the stochastic master equation. In each plot, the concentration of n -mers for $n \leq 7$ (thin lines) and the overall concentration of clusters (thick line) are shown.

Sum kernel

In the sum *kernel*, the reactivity of two clusters is proportional to the mass of the resulting aggregate:

$$K_{ij} = i + j, \forall i, j \in \mathbb{N} \quad (2.16)$$

The solution, starting from monomeric initial conditions, was derived by Melzak (1953):

$$X_n(T) = \frac{(nb)^{n-1} e^{-nb-T}}{n!} \quad (2.17)$$

$$M_0 = e^{-T} \quad (2.18)$$

where $b = (1 - e^{-T})$. It is plotted in Fig. 2.1b. When we compare it with the CSD of the constant *kernel*, the most clear difference is that the concentration of clusters of different sizes do not tend to have the same value for long times. An important increase in the overall aggregation rate is also evident.

In fig. 2.1e the sum *kernel* is solved by the algorithm that will be described in Sec. 3.4.3. The approximate solution is quite accurate, as can be seen.

Product kernel

In the product *kernel*, the reactivity of two clusters is proportional to their masses:

$$K_{ij} = 2ij, \forall i, j \in \mathbb{N} \quad (2.19)$$

The reactivity of the aggregates increases so steeply that an infinite aggregate is formed in a finite time. This is interpreted in terms of a phase transition sol-gel. The infinite aggregate is called a *gel phase* and it is reached at the gelation time $T = T_{\text{gel}} = 0.5$. The solution from monomeric initial conditions, for times before the phase separation, was firstly derived by McLeod (1962):

$$X_n(T) = \frac{(2nT)^{n-1} e^{-2nT}}{n n!}, T \leq \frac{1}{2} \quad (2.20)$$

$$M_0 = 1 - T, T \leq \frac{1}{2} \quad (2.21)$$

2. THEORETICAL BACKGROUND

McLeod (1962) originally believed that no solutions could be found beyond that time, although it was eventually realised (Ziff and Stell, 1980) that such solutions existed and were physically meaningful. The decrease in total mass was interpreted as the flow of mass to an infinite cluster. For times larger than the gelation time, we have two cluster populations: on the one hand, we have the clusters that are small with respect to system size, the concentrations of which tend to a well defined limit as system size is made to go to infinity. These are known as the *sol* particles. On the other hand, the large clusters of the finite system have sizes that go to infinity with the system size, and contain a finite portion of the mass, and are called *gel* particles. The solution for times after the gelation point depends on the model of interaction between the sol particles and the gel particles. If (2.20) is assumed to be valid at all times, we have the so-called Flory solution, which is indeed valid for finite systems. If we neglect the sol-gel interaction, but still consider the system to be infinite, we obtain the so-called Stockmayer solution (Leyvraz, 2003):

$$X_n(T) = \frac{X_n(\frac{1}{2})}{2T}, \quad T > \frac{1}{2} \quad (2.22)$$

$$M_0 = \frac{1}{4T}, \quad T > \frac{1}{2} \quad (2.23)$$

In Fig. 2.1c the CSD for the product *kernel* is plotted. In this case, the Stockmayer solution was chosen for times beyond the gelation point (a dotted vertical line indicates the gelation time in the plot). As have done above for the constant and sum *kernels*, we have obtained the numerical solution by using the stochastic algorithm described in Sec. 3.4.3. The corresponding CSD is plotted in Fig. 2.1f. Apparently, the agreement is quite good both before and after the gelation point. Nevertheless, this is actually due to the particular election of parameters used to solve the stochastic equation. In order to save memory during the calculations, a trick is used: those clusters whose size is larger than certain maximum cluster size are completely ignored. This have very little effect in the solution of the constant and sum kernels, but a quite drastic importance when gelation is taken place. If we consider that every cluster size is significant, we obtain a different solution, plotted in Fig. 2.2b.⁴ Not surprisingly, the obtained solution is actually

⁴Fig. 2.1f was obtained by using 100 000 particles and a cut-off cluster size of 10 000. In contrast, Fig. 2.2b was obtained by averaging five performances with only 10 000 particles, but without

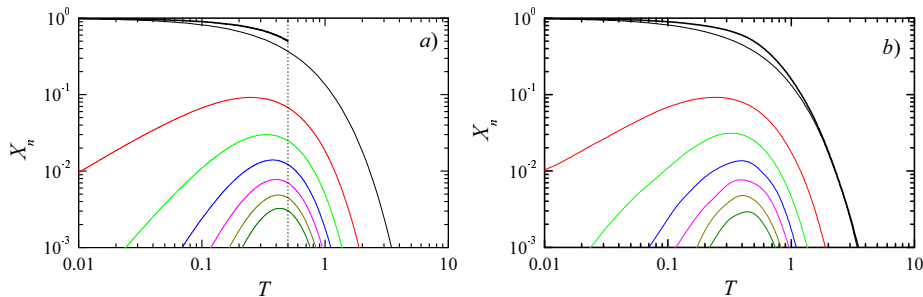


Figure 2.2.: Cluster-size distribution obtained for the product *kernel* with the Flory model. On the left side the exact solution and on the right side a numerical approximation by solving the stochastic master equation.

the Flory solution (see Fig. 2.2a).

2.1.4. Other important aggregation kernels

The *kernels* described in Sec. 2.1.3 have received much attention since are, somehow, “classical”. Nevertheless, other aggregation *kernels* are known to have analytical solution (Leyvraz, 2003). In particular, the linear combination of the three classical *kernels*, the so-called “bilinear *kernel*” (Drake, 1972):

$$K_{ij} = A + B(i + j) + Cij \quad (2.24)$$

where A , B and C are arbitrary constants (restricted to guarantee the positivity of K_{ij} for all positive integer values of i and j , and the normalisation condition $A + 2B + C = 2$). Exact solutions for the bilinear *kernel* with arbitrary constants A , B and C are known (see, *e.g.*, the excellent review by Leyvraz, 2003).

More recently, exact solutions of other *kernels* have been found. Leyvraz and Redner (1986a), for example, studied the following parity-dependent *kernel*:

$$K_{dd} = 2 \quad ; \quad K_{pp} = L \quad ; \quad K_{dp} = M \quad (2.25)$$

cut-off cluster size.

2. THEORETICAL BACKGROUND

where L and M are positive constants and the arguments d respectively p run over the odd (*dispari*), and respectively even (*pari*) integers. Exact solutions for arbitrary L and M have been derived by Calogero and Leyvraz (2000).

Hendriks and Ernst (1984) studied a *kernel*, which they called “addition-aggregation *kernel*”, in which the monomer behaviour is quite different from the behaviour of larger clusters:

$$K_{11} = 2 \quad ; \quad K_{1,j>1} = L \quad ; \quad K_{i>1,j>1} = M \quad (2.26)$$

where L and M are arbitrary positive constants. These authors found that the dynamics crucially depends on M . Exact solutions for (2.26) with arbitrary parameters L and M have been very recently derived by Mabilia *et al.* (2003).

Another example of an exactly solvable *kernel*, is the q -sum *kernel* recently introduced by Calogero and Leyvraz (1999):

$$K_{ij} = 4 - q^i - q^j \quad (2.27)$$

where $0 < q < 1$.

2.1.5. Binary heteroaggregation kinetics

In two-component systems, it seems quite likely that the reactivity of two clusters depend not only on their sizes, but also in their compositions. A first approach could be to consider that the reactivity of a cluster not only depends on its mass, but also in the number of particles of each species. Accordingly, we define the composition-detailed cluster-size distribution (CDCSD), $c_i^l(t)$, as the concentration of clusters composed by i particles, being l of them of type A and $(i - l)$ of type B . The CDCSD is straightforwardly related with the non-detailed CSD, since $\sum_{l=0}^i c_i^l = c_i$. Analogously, we define k_{ij}^{lm} as the aggregation rate constant controlling the aggregation of an i -size cluster containing l particles of type A , and a j -size cluster containing m particles of type A . The corresponding aggregation equation reads (López-López *et al.*, 2005):

$$\frac{dc_i^l}{dt} = \frac{1}{2} \sum_{j=1}^{i-j} \sum_{m=0}^j k_{j,i-j}^{m,l-m} c_j^m c_{i-j}^{l-m} - c_i^l \sum_{j=1}^{\infty} \sum_{m=0}^j k_{ij}^{lm} c_j^m \quad (2.28)$$

It should be noted that $c_i^l(t)$ does not contain information on the internal structure. Hence, the rate constants k_{ij}^{lm} have to be understood as averages over all possible spatial configurations.

Monomeric initial conditions are the most usual: $c_i^m(0) = \delta_1^i [x\delta_0^m + (1-x)\delta_1^m]$, where x is the relative concentration of both particles:⁵

$$x \equiv \frac{c_1^0}{c_1^0 + c_1^1} = \frac{c_A}{c_A + c_B} \quad (2.29)$$

The analytical treatment of (2.28) is quite complex, and numerical methods are needed.

It should be taken into account that, in real heteroaggregation processes, many of the k_{ij}^{lm} constants that appear in (2.28) are zero. In selective heteroaggregation, for instance, $k_{ij}^{00} = k_{ij}^{jj} = 0$, $\forall i, j$.

2.1.6. HHF approximation

Hogg, Healy and Fuerstenau (1966) derived an approximate expression for the short time evolution of the monomer concentration in two-component system that undergo heteroaggregation from monomeric initial conditions. According to (2.28), the monomer evolution is given by:

$$\frac{dc_1^l}{dt} = -c_1^l \sum_{j=1}^{\infty} \sum_{m=0}^j k_{ij}^{lm} c_j^m \quad (2.30)$$

In the zero time limit, the concentration of clusters, apart from monomers, is negligible and, so, (2.30) reduces to:

$$\begin{aligned} \frac{dc_A}{dt} &\simeq -k_{AA} c_A^2 - k_{AB} c_A c_B \\ \frac{dc_B}{dt} &\simeq -k_{BB} c_B^2 - k_{AB} c_A c_B \end{aligned} \quad (2.31)$$

⁵An alternative name for quantity is “number ratio”, θ .

2. THEORETICAL BACKGROUND

Then, the total monomer concentration, $c_1(t) = c_A(t) + c_B(t)$, is given by:

$$\frac{dc_1}{dt} = \frac{dc_A}{dt} + \frac{dc_B}{dt} \simeq -k_{AA} c_A^2 - 2k_{AB} c_A c_B - k_{BB} c_B^2 \quad (2.32)$$

At zero time, the concentration of monomer of each type is related with the total concentration of monomers by (2.29). Nevertheless, as time goes on, this quantity may change. In particular, every reaction between two unlike monomers produces a rarefaction of the minority particles. Hogg *et al.* (1966), however, considered that the relative concentration of both species remain constant during the short time interval which is under study. Hence, (2.32) can be approximated to:

$$\frac{dc_1}{dt} \simeq -k_{11}^{\text{HHF}} c_1^2 \quad (2.33)$$

where k_{11}^{HHF} is an apparent monomer-monomer reaction constant given by:

$$k_{11}^{\text{HHF}} = x^2 k_{AA} + (1-x)^2 k_{BB} + 2x(1-x)k_{AB} \quad (2.34)$$

Equation (2.33) was originally derived by Hogg, Healy and Fuerstenau (1966) and, so it is called HHF approximation. Note that two different approximations have been performed to derive (2.33): i) only monomer-monomer reactions take place, and ii) the relative concentration of monomers of both species remains constant. It is possible to improve the accuracy by considering reactions between monomers and larger aggregates. Puertas *et al.* (2001a), for instance, derived a more complex kinetic equation for the monomer evolution, by considering monomer-dimer reactions in addition to the monomer-monomer reactions.

Finally, it should be mentioned that (2.34) is a more robust approximation than (2.33). In fact, the former becomes exact at *all the times* when x takes the actual ratio of monomers of each species.⁶

⁶A quantity that, in general, depends on time.

2.2. Microscopic description

The interpretation of the aggregation rate constants $k^{\alpha\beta}$ as a flux of β -particles forward an α -particle has been widely used in order to calculate these constant from a microscopic description of the aggregation processes. The simplest possible case is found when there is no interaction between particles, apart from an infinite attractive interaction at the contact. The particle-particle collisions are due only to the Brownian motion of particles and clusters. This aggregation scheme is called *diffusion-limited cluster-cluster aggregation* (DLCA⁷). This aggregation regime is described in Sec. 2.2.2. Other classical aggregation regime is found when the particles hardly react among themselves because there is a strongly repulsive energy barrier when they encounter each other. In the limit of infinitely low sticking probability, the aggregation is said to be reaction-limited, and the corresponding aggregation regime is called *reaction-limited cluster-cluster aggregation* (RLCA⁸). This limit regime, and the transition between RLCA and DLCA are commented in Sec. 2.2.3. Finally, another extreme case is found when long-ranged attractive interactions are present between the particles. Then, the diffusion can be completely overwhelmed and the particle trajectories are no longer similar to random paths, but perfectly directed. Then, the aggregation regime is called *attraction-limited cluster-cluster aggregation* (ALCA). Although long-range attractive interactions are present between oppositely charged colloids, the corresponding aggregation regime cannot be described as “attraction-limited” since the diffusion step is still important. Hence, a different denomination has been proposed: *attraction-driven colloid aggregation* (ADCA⁹). The ADCA regime is briefly described in Sec. 2.2.4.

⁷Two different interpretations of the letter ‘C’ are found, in the literature. Some times it means “cluster-cluster”, like here, but others means “colloid”. Generally, the first denomination is used when we refer to an ideal diffusion-limited aggregation process, such as those found in simulation or theoretical studies. The second denomination is preferred to refer to real aggregating colloids which, strictly speaking, never can be completely free of particle-particle interactions. In this work, the short form “DLCA” is generally used to refer to both ideal and real diffusion-limited aggregation processes. When the long form is used, we have tried to distinguish both denominations.

⁸As in the DLCA case, some ambiguity remains in the meaning of the ‘C’ letter of RLCA.

⁹In this case, the “colloid” meaning of the ‘C’ letter is preferred because this applies to real colloidal systems.

2.2.1. Brownian motion and diffusion

Any mesoscopic particle immersed in a liquid undergoes a random force due to the collisions with the fluid molecules. As a consequence, the particle is continuously moving and describes a random path motion. Robert Brown (1827), an English botanic, was the first in describing this phenomenon, which he found looking at pollen grains immersed in water with a microscope. The Brownian motion—as this random movement was called—was the focus of scientific interest at the beginning of the 20th century, until three great scientists, Einstein (1905), von Smoluchowski (1906) and Langevin (1908), established its fundamentals. As is now well known, we witness in Brownian movement the phenomenon of molecular agitation on a reduced scale by particles very large on the molecular scale. The perpetual motions of the Brownian particles are maintained by fluctuations in the collisions with the molecules of the surrounding fluid. Under normal conditions, in a liquid, a Brownian particle will suffer about 10^{21} collisions per second (Chandrasekhar, 1943).

The quantity that describes the extension of the Brownian motion of a particle is its self-diffusion coefficient D_0 . For a hard sphere of radius a , it is given by the Einstein-Stokes relation (Einstein, 1905):

$$D_0 = \frac{k_B T}{6\pi\eta a} \quad (2.35)$$

where $k_B T$ is thermal energy and η is the solvent viscosity. The coefficient of diffusion is related with the mean square displacement by (Langevin, 1908):

$$\langle |\vec{r}(t) - \vec{r}(t + \Delta t)|^2 \rangle = 6D_0 \Delta t \quad (2.36)$$

Cluster of particles, of course, also undergo Brownian motion. Equation (2.35) is still valid when the hydrodynamic radius R_h is used. It is generally accepted that, for rigid clusters, the hydrodynamic radius is equal to the radius of gyration of the cluster, $R_h \approx R_g$, which is given by:

$$R_g \equiv \sqrt{a^2 + \frac{1}{n} \sum_j^n |\vec{r}_j - \vec{r}_{\text{cm}}|^2} \quad (2.37)$$

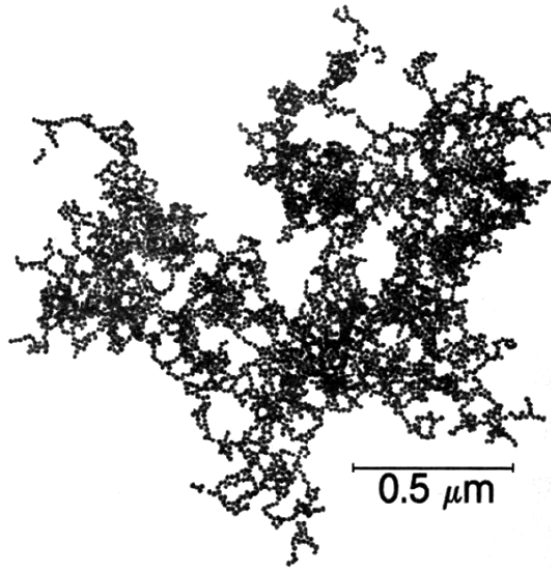


Figure 2.3.: Microphotograph of a typical fractal aggregate, composed by 4739 gold nanoparticles. Reproduced from Weitz and Oliveria (1984) for academic purposes.

where a is the radius of the constituent particles, \vec{r}_j the position of the j -th particle and \vec{r}_{cm} the position of the n -mer centre-of-mass. Nevertheless, rigorous calculations and light-scattering experiments demonstrate that R_h is generally larger than R_g for fractal aggregates (Lattuada *et al.*, 2003). Finally, computer simulations (Meakin, 1983; Kolb, 1984) and experiments (Weitz and Oliveria, 1984; Aubert and Cannell, 1986), indicate that the radius of gyration of fractal clusters is given by:

$$R_n \simeq an^{1/d_f} \quad (2.38)$$

where d_f is the fractal dimension of the n -mer and a is the radius of the monomer. A microphotograph of a typical fractal aggregate with a $d_f \simeq 1.75$, obtained by Weitz and Oliveria (1984), is reproduced in Fig. 2.3 for academic purposes.

2.2.2. Diffusion-limited cluster-cluster aggregation

The first to address the problem of calculating the collision rate of two spheres, of radii a_1 and a_2 , describing Brownian motion was von Smoluchowski (1914). He followed a suggestion of Zsigmondy: to solve the Fick's diffusion equation for one particle, considering the other one as a sink of radius $a_1 + a_2$. The solution is (for rigorous, modern derivations of this and next results, please see Ramkrishna, 2000):

$$k_{a_1, a_2}^{\text{Brw}} = 4\pi D_{12}(a_1 + a_2) \left(1 + \frac{a_1 + a_2}{\sqrt{\pi D_{12} t}} \right) \quad (2.39)$$

where D_{12} is the mutual diffusion coefficient of both particles. As a first approximation,

$$D_{12} \simeq D_{12}^\infty \equiv D_1 + D_2 \quad (2.40)$$

where D_j is the self-diffusion coefficient of particles of radius a_j . The time dependence of (2.39) is usually neglected in dilute systems, since a stationary value is achieved in a time scale much shorter than the aggregation time scale. Neglecting the time dependence, and assuming (2.40), (2.39) simplifies to:

$$k_{a_1, a_2}^{\text{Brw}} = 4\pi(D_1 + D_2)(a_1 + a_2) \quad (2.41)$$

Finally, D_j can be obtained from the Einstein-Stokes equation (2.35), giving:

$$k_{a_1, a_2}^{\text{Brw}} = \frac{2k_B T}{3\eta} \frac{(a_1 + a_2)^2}{a_1 a_2} \quad (2.42)$$

For equally sized spheres, (2.42) does not depend on R :

$$k^{\text{Brw}} = \frac{8k_B T}{3\eta} \quad (2.43)$$

which is the famous von Smoluchowski's coalescence rate (von Smoluchowski, 1917). For water at $T = 293$ K, one obtains $k_{11}^{\text{Br}} = 10.79 \times 10^{-18} \text{ m}^3 \text{ s}^{-1}$.

Expression (2.41) can be used to obtain the reaction rate constant between any two clusters:

$$k_{ij}^{\text{Brw}} = 4\pi(D_i + D_j)(R_i + R_j) \quad (2.44)$$

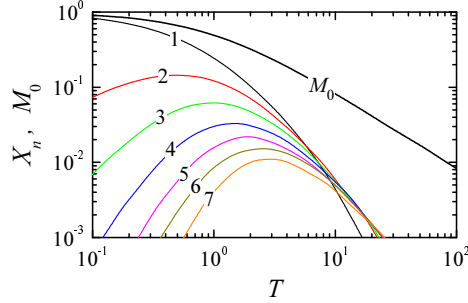


Figure 2.4.: Cluster-size distribution up to heptamers obtained for the Brownian *kernel*.

where D_i and R_i are the diffusion coefficient and the radius of the i -mer. Assuming that $R_i = R_g$, $R_h = R_g$ and the relation (2.38), it yields to:

$$k_{ij}^{\text{Brw}} = k^{\text{Brw}}(i^{1/d_f} + j^{1/d_f})(i^{-1/d_f} + j^{-1/d_f}) \quad (2.45)$$

which is called Brownian *kernel*.

The solution of the coagulation equation (2.6) with the Brownian *kernel* (2.45) is plotted in Fig. 2.4. The coagulation equation was solved by using the stochastic algorithm that will be described in Sec. 3.4.3. The fractal dimension was fixed to 1.75, a value generally accepted for clusters formed under DLCA conditions (Kolb, 1984; Lin *et al.*, 1990a).

2.2.3. Reaction-limited cluster-cluster aggregation

Equation (2.41) was derived by assuming that no forces of any kind were present. Hence, it is not valid when particle-particle interactions are not negligible. Fuchs (1934) derived an expression for the particle-particle reaction rate that explicitly consider particle-particle interactions:

$$k_{a_1, a_2} = 4\pi(D_1 + D_2) \left(\int_{a_1+a_2}^{\infty} \frac{1}{r'^2} e^{\beta V_{12}(r')} dr' \right)^{-1} \quad (2.46)$$

2. THEORETICAL BACKGROUND

where $V_{12}(r)$ is the particle-particle potential energy, and $\beta = 1/k_B T$ as usual.

Equation (2.46) is still not completely general because it is assumed that the movements of both particles are completely uncorrelated (2.40). Basic hydrodynamics, however, states that this is not the case: the motion of one particle induces long-range hydrodynamics interactions on the other particle. This hydrodynamic effect can be treated by considering that the diffusion coefficient depends on the particle-particle separation $D_{12}(r)$ (Spielman, 1970). Honig *et al.* (1971) derived the following expression for $D_{12}(r)$, which is valid assuming that the radii of the two spheres do not differ much:

$$D_{12}(r) = D_{12}^{\infty} \frac{6H^2 + 4RH}{6H^2 + 13aH + 2a^2} \quad (2.47)$$

where $H \equiv r - (a_1 + a_2)$ is the distance of closest approach between two spheres and $a \equiv (a_1 + a_2)/2$ is their mean radius.

With this hydrodynamic correction, (2.46) now reads:

$$k_{a_1, a_2} = \frac{4k_B T}{3\eta a} \left(\int_{a_1 + a_2}^{\infty} \frac{1}{r'^2} \frac{D_{12}^{\infty}}{D_{12}(r')} e^{\beta V_{12}(r')} dr' \right)^{-1} \quad (2.48)$$

It is worth noting that (2.48) leads to $k_{11} = 0$ for non interacting particles ($V_{12}(r) = 0$). Hence, some attractive interaction must exist if aggregation is taking place. Consider that $V_A(r)$ is such an attractive particle-particle interaction. Then, the aggregation occurs at a relative fast rate, and the process is said to be diffusion-limited (DLCA). On the other hand, when a repulsive particle-particle interaction $V_R(r)$ exists in addition to $V_A(r)$, aggregation occurs more slowly and is said to be reaction-limited (RLCA).

In experimental works, it is quite convenient to define a stability factor in the following way:

$$W = \frac{k_{11}^{\text{fast}}}{k_{11}^{\text{slow}}} \quad (2.49)$$

This quantity can be calculated from the Fuchs approach (2.48) by assuming that “fast” aggregation is taken place when only the attractive particle-particle

potential is significant, while “slow” aggregation occurs when both attractive and repulsive interactions are considered:

$$W = \frac{\int_{a_1+a_2}^{\infty} \frac{1}{r'^2} \frac{D_{12}^{\infty}}{D_{12}(r')} e^{\beta[V_A(r') + V_R(r')]} \mathbf{d}r'}{\int_{a_1+a_2}^{\infty} \frac{1}{r'^2} \frac{D_{12}^{\infty}}{D_{12}(r')} e^{\beta V_A(r')} \mathbf{d}r'} \quad (2.50)$$

Equation (2.48) may be used, in principle, for calculating any rate between particles or clusters. Unfortunately, its practical application is usually reduced to the monomer-monomer reaction, since detailed models of interaction potentials between clusters are not found in the literature. Hence, it is not possible to obtain a full set of constant k_{ij} from the Fuchs approach. In fact, all reaction *kernels* for RLCA processes are, in more or less extend, semiempirical. The following *kernel*, a generalisation of the product *kernel* proposed by Family *et al.* (1985) results a good approximation for simulated and experimental RLCA processes (Lattuada *et al.*, 2003):

$$k_{ij} = \frac{k_{ij}^{\text{Brw}}}{W} (ij)^{\lambda} \quad (2.51)$$

where k_{ij}^{Brw} is the Brownian *kernel* given by (2.45), W the stability ration given by (2.49) or (2.50)¹⁰ and λ is a homogeneity parameter, generally used as a free parameter. Please note that (2.51) necessarily has to fail for very large aggregates, since it predicts that $k_{ij} > k_{ij}^{\text{Brw}}$ when $i, j \rightarrow \infty$.

More recently, Odriozola *et al.* (2001b) derive a *kernel* that correctly describes the full transition between DLCA and RLCA regimes, based on physically sound arguments:

$$k_{ij} = \frac{k_{ij}^{\text{Brw}}}{W} \frac{(ij)^{\lambda}}{1 - W^{-1}[(ij)^{\lambda} - 1]} \quad (2.52)$$

¹⁰Obviously, (2.49) should be used if we only have experimental data, while (2.50) would be our election if we are interested in inferring the *kernel* from a theoretical particle-particle interaction potential.

2. THEORETICAL BACKGROUND

This *kernel* yields to the Brownian *kernel* for $W = 1$ and to the generalised product *kernel* for $W \rightarrow \infty$. Moreover, the *kernel* by Odriozola *et al.* (2001b) also avoid the contradiction for large aggregates of (2.51).

2.2.4. Attraction-driven cluster-cluster aggregation

The Fuchs approaching (2.48) is still valid when the particle-particle interactions become attractive and long-ranged. This is the case for mixtures of oppositely charged particles at low electrolyte concentrations. Then, the interaction between unlike particles are so important that the aggregation rate surpasses the DLCA limit. The absolute dimer formation rate constants k_{AA} , k_{BB} and k_{AB} can be calculated by using the appropriate particle-particle potential on (2.48). Then, for times short enough to consider that (2.34) holds, the effective dimer formation rate constant can be calculated. To the best of our knowledge, the challenge of obtain a full *kernel* for (2.28) that describes the attraction-driven colloid aggregation regime is still an open problem.

2.3. Particle-particle interactions

In Sec. 2.2, the fundamentals to obtain kinetics constants from the microscopic description of the aggregation process have been summarised. Nevertheless, the Fuchs approaching (2.48) is useless if a model of the particle-particle interactions is not provided. Hence, in this section we briefly describe the most widely used expression for these interactions.

2.3.1. DLVO theory

The first quantitative treatment of the particle-particle interactions in colloidal systems is the so-called DLVO theory (Derjaguin and Landau, 1941; Verwey and Overbeek, 1948). It suggest that the colloid stability depends on the balance of two kinds of interactions: London-van der Waals forces and forces due to the overlapping of the electric double layers of the particles. Generally speaking, the

former are always attractive and short-ranged, while the latter are repulsive and their range depends on the medium properties (ionic strength, pH ...).

2.3.2. London-van der Waals interactions

Van der Waals forces are attractive, short-range forces that originate from molecular dipole-dipole interactions. Particularly, London-van der Waals interactions are due to random fluctuations of the electronic molecular layer, which induce instant dipoles in adjacent molecules. Hamaker (1937) derived an expression for the van der Waals interactions between macroscopic bodies, by assuming pairwise additivity. The London-van der Waals-Hamaker interaction between two spheres of radii a_1 and a_2 is (see, *e.g.*, Hunter, 1987):

$$V_{\text{vdW}}(r) = -\frac{A_{1,3,2}}{6} \left\{ \frac{2a_1a_2}{r^2 - (a_1 + a_2)^2} + \frac{a_1a_2}{r^2 - (a_1 - a_2)^2} + \ln \left(\frac{r^2 - (a_1 + a_2)^2}{r^2 - (a_1 - a_2)^2} \right) \right\} \quad (2.53)$$

where $A_{1,3,2}$ is the so-called Hamaker constant which depends on the chemical composition of both particles and the dispersion medium. For equally sized spheres of the same composition, it yields:

$$V_{\text{vdW}}(r) = -\frac{A_{1,3,1}}{6} \left\{ \frac{2a^2}{r^2 - 4a^2} + \frac{2a^2}{r^2} + \ln \left(1 - 4\frac{a^2}{r^2} \right) \right\} \quad (2.54)$$

2.3.3. Double layer potential energy

The double layer potential energy arises from the overlap of diffuse clouds of ions (double layers) that accumulate near charged surfaces to balance the surface charge. If the interacting surfaces are like-charged, the double layer potential energy will be repulsive.¹¹ If the surfaces are oppositely charged, the double layer potential energy will be attractive. All formulations of the double layer potential

¹¹Nevertheless, under some circumstances, attractive interactions between surfaces with the same sign of charge are predicted (McCormack *et al.*, 1995).

2. THEORETICAL BACKGROUND

energy are sensitive to variations in: i) the surface potentials of the colloids, ii) the ionic strength of the solution, and iii) colloid size. While the dependence of the double layer potential energy on surface potentials and ionic strength has been demonstrated in coagulation and deposition studies, the dependence on colloid size has not been verified (Ryan and Elimelech, 1996).

Expressions for this interaction are numerous. An usual approach consists in assuming that ions surround the particle in two different layers:

- A thin layer of ions strongly bonded to the particle surface (Stern layer). These may arise from regular electrostatic forces or from specific ion adsorption. In the latter case, they can even invert the sign of the effective charge of the colloid.
- A diffuse layer that extends out into the bulk solution (Gouy-Chapman layer). This region is characterised by an excess of counterions and a defect of coions, with respect to their bulk concentrations.

A detailed discussion about the double layer potential energy, however, falls outside the scope of this work. Hence, only an outline of the derivation is provided. First, a model of the colloid-solution interface is needed, which has to provide the effective electric potential on the Stern layer ψ^* and its thickness Δ . Secondly, the Poisson-Boltzmann equation,

$$\nabla^2 \psi(\vec{r}) = -\frac{e_0}{\epsilon_0 \epsilon_r} \sum_i^N z_i n_i e^{\beta e_0 z_i \psi(\vec{r})} \quad (2.55)$$

which gives the ion concentration profiles, has to be solved as a function of the particle-particle separation. In (2.55), N ionic species are present, whose bulk concentrations and electric charges are n_i and $z_i e_0$, respectively. Solving the non-linear Poisson-Boltzmann equation requires numerical methods. Several approaches are found in the literature, such as the network simulation method of Lopez-García *et al.* (2002). A specially controversial point here is whether the surface potential or the surface charge keeps constant during the particle-particle approaching. Moreover, in the general case, both quantities vary during this process (McCormack *et al.*, 1995). Finally, for each ion configuration, the electrostatic and osmotic forces acting on the particles are calculated. Several

expression can be found in the literature, with different mathematical complexity and accuracy (see, *e.g.*, Hidalgo-Álvarez *et al.* (1996) and references therein).

The Debye-Hückel parameter

The ionic concentration of the solution controls the extent to which double layers extend from the surface into the bulk solution. At high electrolyte concentration, the surface charge can be balanced by a thin double layer because the ion concentration near the surface is high; conversely, low electrolyte concentration will produce thick double layers. The so-called Debye-Hückel parameter κ , defined as:

$$\kappa = \sqrt{\frac{e_0^2}{\epsilon_r \epsilon_0 k_B T} \sum_i^N z_i^2 n_i} \quad (2.56)$$

is usually employed as a measure of the double layer thickness, since the ionic excess decays approximately as $e^{-\kappa r}$. Here, r is the distance to the particle surface. For 1:1 electrolytes, as those used in the experimental part of this work, (2.56) yields to:

$$\kappa = \sqrt{\frac{2n_0 e_0^2}{\epsilon_r \epsilon_0 k_B T}} \quad (2.57)$$

Double layer potential expressions

Consider two microspheres, with radii a_1 and a_2 and surface potentials ψ_1 and ψ_2 , separated by a distance H . Then, the following expressions applies (see, *e.g.*, Lyklema, 1991):

If both surface potentials are relatively low ($\psi_j \lesssim k_B T / e_0 \simeq 25$ mV), then the Poisson-boltzmann equation (2.55) can be linearised and exactly solved. The double layer potential depends on the imposed boundary conditions. If we assume that surface potentials do not change when the particles approach, then:

$$V_{\text{DL}}^{(\psi)}(H) = 2\pi\epsilon_0\epsilon_r \frac{a_1 a_2}{a_1 + a_2} \left[(\psi_1^2 + \psi_2^2) \ln(1 - e^{-2\kappa H}) + 2\psi_1 \psi_2 \ln\left(\frac{1 + e^{-\kappa H}}{1 - e^{-\kappa H}}\right) \right] \quad (2.58)$$

2. THEORETICAL BACKGROUND

For identical spheres ($a_1 = a_2 = a$, $\psi_1 = \psi_2 = \psi_0$), (2.58) yields to:

$$V_{\text{DL}}^{(\psi)}(H) = 2\pi\epsilon_0\epsilon_r a\psi_0^2 \ln\left(1 + e^{-\kappa H}\right) \quad (2.59)$$

On the other hand, if they change in such a way that the electrical charges keep constant when the particles approach, then:

$$V_{\text{DL}}^{(\sigma)}(H) = 2\pi\epsilon_0\epsilon_r \frac{a_1 a_2}{a_1 + a_2} \left[2\psi_1 \psi_2 \ln\left(\frac{1 + e^{-\kappa H}}{1 - e^{-\kappa H}}\right) - (\psi_1^2 + \psi_2^2) \ln\left(1 - e^{-2\kappa H}\right) \right] \quad (2.60)$$

For identical spheres, (2.60) yields to:

$$V_{\text{DL}}^{(\sigma)}(H) = 2\pi\epsilon_0\epsilon_r a\psi_0^2 \ln\left(1 - e^{-\kappa H}\right) \quad (2.61)$$

When surface potentials are not low enough to allow the linear approximation for the Poisson-Boltzmann equation, it is usual to assume the linear superposition approximation (LSA). It consists in assuming that the ion concentration in the middle region between two spheres is the sum of the ion concentrations corresponding to these spheres considered as isolated. Fortunately, an analytical expression for the latter can be obtained directly solving the non-linear Poisson-Boltzmann. The resulting expression reads:

$$V_{\text{DL}}^{(\text{LSA})}(H) = 4\pi\epsilon_0\epsilon_r \frac{a_1 a_2}{a_1 + a_2} \psi_1 \psi_2 e^{-\kappa H} \quad (2.62)$$

Although (2.62) was derived for the limit of $\kappa H \gg 1$ (highly separated particles, or highly compressed electrical double layers), rigorous calculations by Reiner and Radke (1993) demonstrated that the LSA approximation accuracy is fair good over a wide range of parameters (κH , κa , a_1/a_2 ratio...).

Finally, when more accuracy is required, the full non-linear treatment of Overbeek (1990) should be used.

Stern layer correction

The above expression were derived neglecting the role of the Stern layer. The first, somehow trivial, step to consider is substituting the surface potentials ψ_j

by the effective surface potential at the Stern layer ψ_j^* . Vincent *et al.* (1970) refined this picture by shifting the reference plane for the repulsive energy outwardly over a distance corresponding with the thickness Δ of the Stern layer. Considering these corrections, the LSA expression for the electrical double layer interaction (2.62), for example, is now given by:

$$V_{\text{DL}}^{(\text{LSA})}(H) = 4\pi\epsilon_0\epsilon_r \left(\frac{a_1 a_2}{a_1 + a_2} + \Delta \right) \psi_1^* \psi_2^* e^{-\kappa(H-2\Delta)} \quad (2.63)$$

2.3.4. Kinetic stability

Consider a colloidal system perfectly described by the DLVO theory. Then, the particle-particle interactions have two components: the attractive and short-ranged van der Waals forces and the repulsive interactions due to the EDL overlap. The range of the latter interactions depends, of course, on the EDL thickness. That is to say, it depends on the Debye-Hückel parameter, independently of how accurate were the explicit expression of these interactions. At low electrolyte concentrations the repulsive interaction is long-ranged and the total particle-particle interaction present an energy barrier that prevents the particles to become in touch. On the contrary, at high electrolyte concentrations the EDL is compressed on the particle surface and the van der Waals forces prevail. Roughly speaking, this implies the colloidal dispersion to be kinetically stable at low electrolyte concentrations, but to aggregate at high electrolyte concentrations.

2.3.5. HHF theory

The original DLVO theory was developed to deal with one-component colloidal dispersions. It seems that the first attempt to adapt the DLVO expressions for particle-particle interactions to unlike particles were carried out by Hogg, Healy and Fuerstenau (1966). In fact, these author derived expression (2.58). HHF theory or DLVO-HHF theory are frequent names to refer to the DLVO theory applied to unlike particles. Nevertheless, it should be pointed out that the interactions considered by this theory are, essentially, the same as those considered by the original DLVO theory.

2.3.6. Non-DLVO forces

The particle-particle interactions considered by the DLVO theory does not comprise all relevant interactions among colloidal particles. Probably, the most evident limitation of this theory is found in the $H \rightarrow 0$ limit. Since the dependence on H at short distances is stronger for the van der Waals interaction than for the double layer potential, $V_{12}^{\text{DLVO}}(H)$ diverges in that limit. Obviously, some strong repulsive interaction must exist at the contact to prevent the particles to interpenetrate. The effect of this short range repulsion has been included in DLVO profiles in two ways (Ryan and Elimelech, 1996): i) designation of a minimum distance corresponding to the layers of hydration water between surfaces; and ii) calculation of the Born potential energy. The application of either of these potentials implies that the energy minimum at short distances has a finite depth. It opens the possibility of reversible aggregation to take place. Anyhow, the accurate estimation of the depth of this minimum is highly speculative.

Other extensions to the DLVO theory has been proposed to deal with other situations, such as the discreteness of the surface charge (Kihira *et al.*, 1992), the presence of a hairy layer of adsorbed polymer on the particle surface (Vincent *et al.*, 1986), the presence of hydrophilic surface groups (Škvarla, 1993).

3. MATERIALS AND METHODS

In this chapter, we describe the materials and methods used during this research work. The first section deals with the single-cluster light-scattering technique, which has provided most of the experimental data. Besides a general description of the SCLS instrument, we also comment on the improvements introduced in the data acquisition and analysis. Auxiliary experimental techniques, namely a low-angle light-scattering instrument and a electrophoretic mobility set-up, are briefly described in Sec. 3.2. A complete characterisation of the colloidal dispersions is provided in Sec. 3.3, including comments on their homoaggregation behaviour. Finally, Sec. 3.4 deals with the numerical procedures used to complement and interpret the experimental data. They comprise Brownian dynamics simulations —with and without particle-particle interactions— and a stochastic numerical algorithm, which is used to solve the coagulation equation.

3.1. Single-Cluster light-scattering

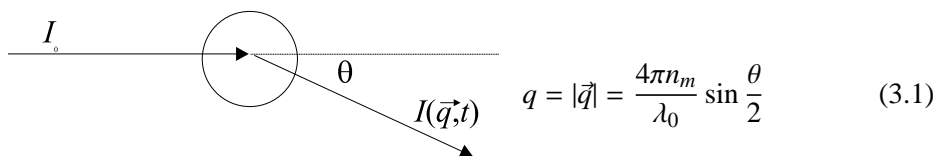
Most experimental data used in this work was obtained by using the single-cluster light-scattering (SCLS) device located in the laboratories of the “Departamento de Física Aplicada” of the University of Granada. It was built by Dr. Miguel Cabrerizo-Vílchez as a part of the PhD thesis of Antonio Fernández-Barbero (1994), based on a prototype by Pelssers *et al.* (1990a), of the Wageningen Agricultural University (The Netherlands). Some technical improvements were subsequently made by Dr. Artur Schmitt (2000) and by Dr. Gerardo Odriozola (2001). Our SCLS instrument allows us to obtain the cluster-size distribution for small aggregates, without any assumptions about the cluster structure. It have been used to obtain the cluster-size distribution (CSD) of

3. MATERIALS AND METHODS

aggregating one-component systems (Fernández-Barbero *et al.*, 1996; Schmitt *et al.*, 2000b; Odriozola *et al.*, 2004) and, as part of this thesis, of two-component systems (López-López *et al.*, 2004a; López-López *et al.*, 2004b).

3.1.1. Principle of function and description

The SCLS technique belongs to the general group of light-scattering (LS) techniques, in which the properties of the colloidal dispersion are inferred from the intensity of the light scattered by a sample of the system, $I(\vec{q}, t)$. The following figure shows a scheme of a typical LS experiment, and the definition of the *scattering vector* \vec{q} :



Here, λ_0 is the wave length of the light and n_m the medium refraction index.

Depending on the time scale used to record the light-scattering intensity, we can distinguish between two classes of LS techniques:

SLS Static light-scattering: the time response of the instrument is larger than the Brownian diffusion time. The detected light intensity is somehow an average light intensity $\langle I(\vec{q}, t) \rangle$, related with the concentration and size of the suspended particles.

DLS Dynamic light-scattering: the time response of the instrument is so short that it is possible to record the rapid fluctuations of the light intensity due to the Brownian motion of the particles. Although it is mathematically more complex than SLS, DLS allows to obtain more accurate information about size and structure of colloidal aggregates.

Single-cluster light-scattering is a SLS technique with one important particularity: the scattering centre consists in a single particle or cluster.

Rayleigh scattering law

At the ending of the 19th century, Strutt (Lord Rayleigh) (1899) derived the following expression for the intensity of scattered light in the $q \rightarrow 0$ limit:

$$I \propto V_{\text{sc}}^2 \quad (3.2)$$

where V_{sc} is the scattering centre volume. Rigorous calculations demonstrates that this relationship holds when the adimensional quantity qR_{sc} is reasonably small, being R_{sc} the radius of the scattering centre (see, *e.g.*, Kerker, 1969).

In a SCLS experiment, the scattering centre consists in a single cluster composed of n colloidal particles of radius a . Hence, if $qR_{\text{cluster}} \ll 1$ then the Rayleigh scattering law applies and so:

$$I \propto n^2 \quad (3.3)$$

In this case, it would be possible to clearly distinguish the number of constituent particles from the light intensity.

A simple calculation shows that for colloids with $a = 0.25 \mu\text{m}$ and our experimental setup, $qa \approx 0.18$ and so, the Rayleigh scattering law is a valid assumption. For larger aggregates, however, qR_{cluster} is no longer smaller than unity. For pentamers, for instance, this quantity may vary from 0.3 to 0.9 depending on its spatial configuration. Since we are somehow working near the Rayleigh limit, Eq. (3.3) is not expected to be fulfilled exactly. In fact, Fernández-Barbero *et al.* (1996) experimentally found that the actual dependence of the light intensity on n , for $n \leq 6$, is:

$$I \propto n^\gamma \quad ; \quad \gamma = 1.83 \pm 0.03 \quad (3.4)$$

Although this is not the exact Rayleigh's law, the dependence on n is still steep enough to clearly discriminate the different cluster sizes.

Instrument overview

Hence, the device designers had to manage the following challenges (Fernández-Barbero, 1994):

3. MATERIALS AND METHODS

- physical separation of the clusters without breaking them up;
- creation of a light-scattering volume as small as possible;
- detection of the scattering light at low angles;
- determination and compartmentalisation of the light pulses;
- data storage, instrument control and measuring automatisation.

Our SCLS device separate the particles by hydrodynamic focusing, *i.e.*, by slowly injecting the sample into a fast laminar water stream.

The flow velocities of the sample and water streams are equalled in the surface that separates them. Hence, the sample flow velocity is importantly increased. As a consequence, the sample stream is narrowed and the mean cluster-cluster distance enlarges. Then, the sample stream crosses the focus of a laser beam and the scattered light pulses are detected by a phototube located at a low scattering angle. The light pulses are processed by a personal computer provided with an A/D converter and then, classified on-line using an integration algorithm. The sample handling is entirely computer-controlled so that the measurements can continue without any human supervision. This makes it possible to obtain time-resolved CSD measurements for time intervals of several days (Schmitt, 2000). Fig. 3.1 shows an scheme of our SCLS device (López-López *et al.*, 2004c). In the following paragraphs, there is a brief explanation on each one of the instrument components, except the data acquisition software, which is described in a different section (Sec. 3.1.2) because it was completely updated during this research work.

Laser and entrance optics

According to Fernández-Barbero (1994), the entrance optics is composed of a 10 mW He-Ne laser, a spatial filter, two cylindrical lenses and a microscope objective; all of them lying on a passive isolation anti-vibration table. The laser supplies a collimated and linearly polarised light beam with a wavelength of 632.8 nm, a output diameter of 0.68 mm and an angular divergence of just 1.2 mrad. Although it theoretically works on the TEM₀₀ mode, unavoidable imperfections in its resonance cavity make that its transversal profile slightly differs

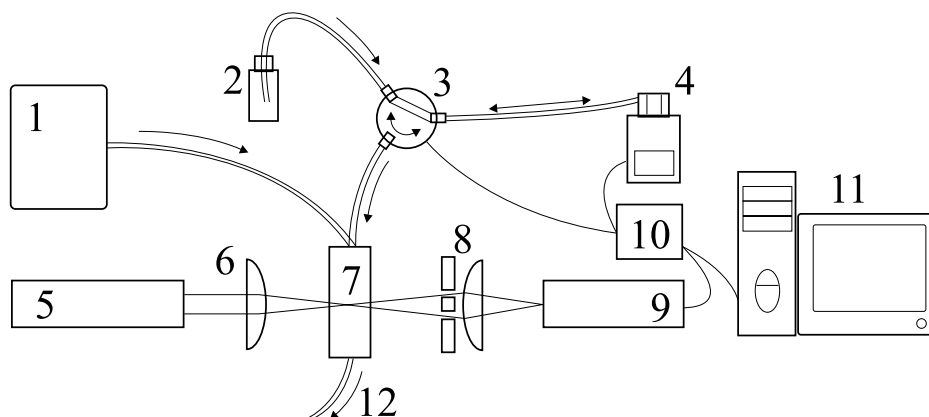


Figure 3.1.: Scheme of our SCLS instrument showing its main parts: distilled and filtered water supply (1), reaction vessel (2), magnetic valve (3), peristaltic pump (4), He-Ne laser (5), entrance optics (6), hydrodynamic focusing cell (7), detection optics (8), phototube (9), AD/DA converter (10), computer (11) and waste water (12).

from the gaussian one. The spatial filter is intended to correct these deviations and to obtain a smooth light spot. It is composed of two spherical lenses, a pinhole and a diaphragm. Firstly, the laser beam is focused on a $20\ \mu\text{m}$ pinhole by means of a 10 mm lens. A second lens, with a focal length of 100 mm, collimates the beam. Finally, the corresponding diffraction pattern is cut off by a 4.0 mm diaphragm, in such a way that only the first diffraction maximum is allowed to pass.

The laser beam, now with a smooth profile, crosses a optical system with two 40 mm cylindrical lenses, separated by a distance slightly longer than twice the focal length. The beam profile is no longer circular, but elliptical: now it is somewhat convergent in one of the normal directions and collimated in the other one. Finally, the laser beam is focused on a point inside the measuring cell by a 30.8 mm microscope objective. The aim of this is to obtain a small illuminated region where the light intensity is almost constant. Hence, small fluctuations of the sample location does not change significantly the incoming radiation

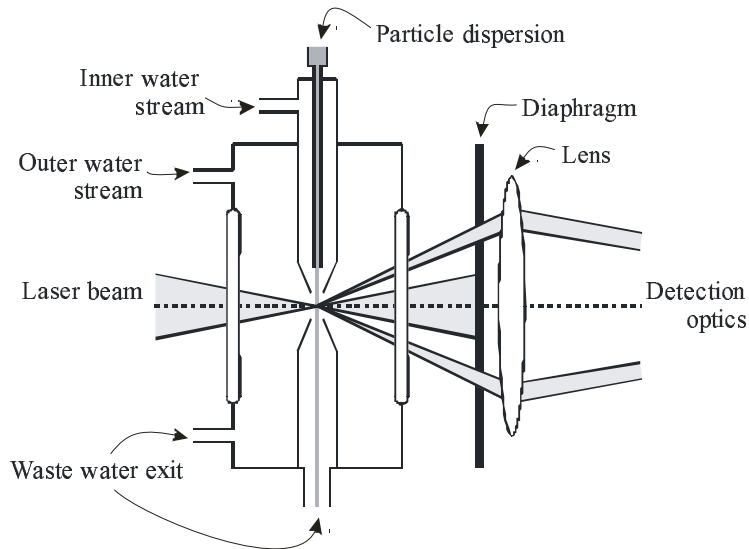


Figure 3.2.: Scheme of the hydrodynamic focusing cell, adapted from Fernández-Barbero (1994).

intensity.

Hydrodynamic focusing cell

The hydrodynamic focusing cell is the most sensible, complex and important part of the device, as it is the place where the sample stream crosses the laser focus. As can be seen in Fig. 3.2, the colloidal sample is injected through the top of the cell into a faster water stream. Then the hydrodynamic focusing phenomenon enlarges the cluster-cluster separation and the single cluster detection is feasible. The particle concentration, however, must be low enough to avoid *coincidences*, *i.e.*, the fact of two clusters being inside the illuminated volume at the same time. In the regular operation mode, this is achieved by keeping the colloid concentration below approximately 10^8 cm^{-3} (Schmitt, 2000). The inner water stream is also surrounded by another, slower, water stream that prevents the former from suffering a significant shear disruption. The whole cell may be

precisely moved in the three spatial directions by acting on micrometric screws. Finally, a regular optical microscope allow us to watch the illuminate region and help us to align the device properly.

Phototube and detection optics

According to Fernández-Barbero (1994), the detection optics is composed of an annular diaphragm, a microscope objective, a regular diaphragm and a phototube. The annular diaphragm is located just in the outside of the hydrodynamic focusing cell, as it is shown in Fig. 3.2. It prevents transmitted light and allows the light to be scattered only at angles between 2.7 and 3.2 degrees. A 22.5 mm microscope objective focuses the selected light on a regular diaphragm with aperture 0.8 mm. It is located there to block parasite light from uncontrolled reflections on the cell windows and other optical surfaces. Finally, a phototube linearly translates from light intensity to voltage. The sensitivity peak of the phototube is centred at 650 nm, close to the He-Ne laser wavelength.

Water supply

Any dust particle suspended in the water streams that crosses the measuring cell may scatter some light which eventually provokes a false peak. Although the detection optics is designed to discriminate between these spurious signals and the actual signal, it is always convenient to use water as clear as possible. Therefore, our device uses only deionised water, obtained by inverse osmosis, ionic interchanging and activated carbon filtering (Odriozola, 2001). A 10 litre Mariotte siphon acts as a water reservoir and feeds an ordinary distiller intended mainly to remove air bubbles. Distilled water is filtered by a 220 nm microfilter (Millipore Millipak 20) and then split between the inner and the outer streams. The system may continuously supply clear water during up to 14 hours, without any human supervision (Schmitt, 2000).

Sample injection

Although the first prototype of our SLCS device made use of a syringe injector (Fernández-Barbero, 1994), it was afterward substituted by a computer-

3. MATERIALS AND METHODS

controlled peristaltic pump¹ in order to extend the duration of a series of measurements (Schmitt, 2000). The pump also improves significantly the overall reproducibility of the measuring process (Schmitt, 2000). An electro-valve —also computer-actuated— selects whether the pump acts on the reaction vessel or on the hydrodynamic focusing cell. In the regular operation mode, a small amount of sample is firstly extracted from the reaction vessel and then is slowly injected into the hydrodynamic focusing cell. Usually, the extraction is much faster — 3.00 rpm— than the subsequent injection —0.0117 rpm— (Odriozola, 2001). Since the sample is kept some time inside the tubes, it is required the use of inert materials. Hence, all tubing² and valves are teflon coated. The main handicap of using a peristaltic pump is that the flow velocity is not constant, since rollers perturb the flow when they constrict the tubes. This undesirable effect may, however, be overcome by fixing the measurement duration τ equal to an integer number of pump cycles (Schmitt, 2000).

3.1.2. Data acquisition and treatment

During the present research work, the AD/DA converter was substituted by a newer model and all the programs had to be rewritten. The new software features some improvements that are described in some detail in this section.

New pulse classifier algorithm

The phototube signal is digitalised by an AD/DA card³ at a sample rate of 225 kHz. An example of the digitalised phototube output is shown in Fig. 3.3. As can be seen in the figure, the phototube signal consists basically in several peaks which stand out from the background noise. Each one of these peaks corresponds to the pass of one aggregate thorough the illuminated volume. In particular, two of such peaks are visible in Fig. 3.3, which corresponds to the pass of two monomers. Our software detects and classifies the light pulses by using an integral algorithm (Fernández-Barbero, 1994; Schmitt, 2000). The correlative

¹Minipuls 312, Gilson S.A.S., France.

²Gilson S.A.S., Ref. 817741A. Inner diameter: 0.5 mm.

³DT302, Data Translation Inc., Marlboro, MS (USA).

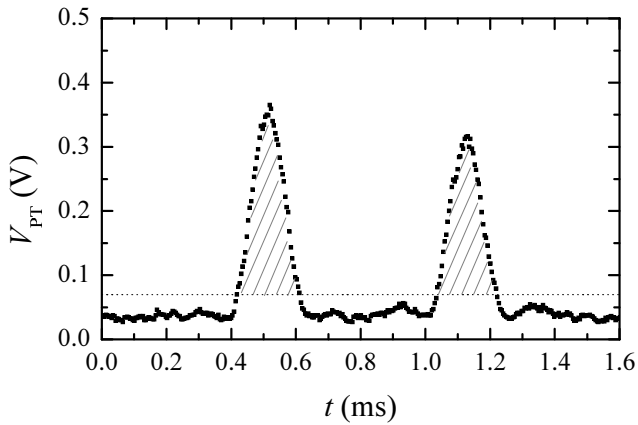


Figure 3.3.: A short segment of a typical phototube output after the digitalising process. Two monomer peaks are clearly distinguishable. The detection threshold is represented by a horizontal dotted line, and the areas used for classifying the pulses are shadowed.

data points that surpasses certain threshold are considered to form a pulse. These pulses are then classified according to their area. The duration of the pulses is also recorded in order to correct the death time of the algorithm. Additionally, a duration checking allows us to identify and eliminate spurious pulses that correspond to fluctuations of the base line.

The former data acquisition software of our SCLS device classified the pulses according to their area (Schmitt, 2000), while the current version classified then according to the square root of their area (López-López *et al.*, 2004c). Since the intensity of scattered light is approximately proportional to the squared number of constituent particles of the cluster (3.3), this non-linear manner of classify light pulses is quite convenient. As an example, in Fig. 3.4 are plotted the count histograms obtained with both classifying methods, for the same data set. As can be seen, the non-linear classifier improves the statistics, the resolution and the interval of cluster-sizes able to be discriminated. It should be mentioned that all pulses are counted, even those whose size is larger than the histogram range. These large aggregates are summed up all together in the last position

3. MATERIALS AND METHODS

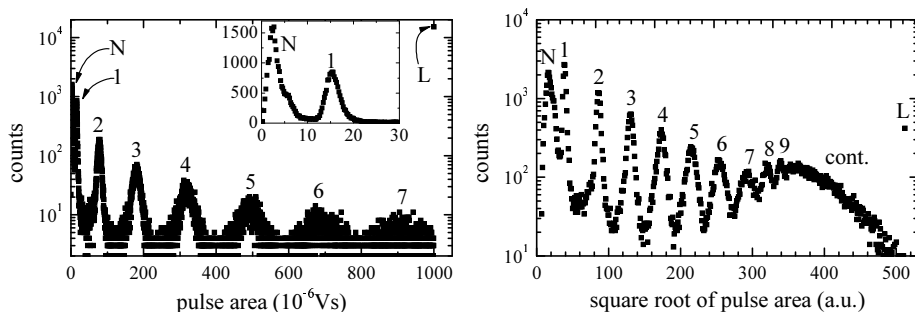


Figure 3.4.: Frequency histograms of a typical SCLS measurement obtained with a linear (left) and non-linear (right) classifying algorithm. Numbers indicate the number of constituent particles of the cluster, ‘N’ refers to noise, ‘L’ to large aggregates and “cont.” to the continuous region. Both plots correspond to the same data set.

of the histogram array (they are marked with the letter ‘L’ in Fig. 3.4). Please note that the number of large aggregates is smaller when the non-linear classifier is used. In the histograms is also appreciable the count peak corresponding to noise (marked with the letter ‘N’ in the figure), which is removed during the data analysis (see Sec. 3.1.3).

Real time determination of the count histograms

The new version of the software runs on Microsoft Windows⁴ and, hence, takes advantage of the multi-task capabilities of this operative system. Thus, while the data acquisition program is running on the background, most of the CPU⁵ can be used for running other programs. This was used to plot the count histogram, in real time⁶, using a commercial software⁷. This feature shorten the calibration

⁴The software was developed by using *Microsoft Studio 6.0* and the function libraries of the *DataAcquisition Software Development Kit*. Two programming languages were used: *Visual Basic* for the user interface and *Visual C++* for the program core.

⁵About 98%, in a regular personal computer.

⁶Actually, the histogram plot updates every 5 seconds.

⁷Origin Pro 7.0, OriginLab Corp., USA.

process.

Cluster break-up detection

One of the main criticisms that had received the single-cluster light-scattering technique, is the possibility of introducing some undesired cluster break-up in the hydrodynamic cell, due to shear forces (see, *e.g.*, the discussion about this in Odriozola *et al.*, 2003). Accordingly, some effort have been made in prevent cluster break-up, or at least, in detecting it.⁸ One manner of detecting cluster break-up in the hydrodynamic cell consists in measuring a stable sample at different shear rates. This was done by Schmitt (2000) for a flocculated sample of polystyrene colloidal particles, partially coated with BSA (bovine serum albumin). No appreciable alterations in the cluster-size distribution were found for pulse durations between 50 μ s and 200 μ s.⁹

A different approach has been implemented in this work. If a cluster would break up during the injection process, the fragments will cross the laser beam one-after-another. This would create a strong correlation between the fragments, that could be detected. Consider a measurement where aggregates can be detected up to those composed by M particles, *i.e.*, we know the set $\{n_i\}_{i=1}^M$. Let $N = \sum_{i=1}^M n_i$ be the total number of detected aggregates. Now, we define the quantities $\{n_{ij}\}_{i,j=1}^M$ as the number of i -mers that are followed by a j -mer. If some breakage is carried out in the measuring cell, then some n_{ij} will take values different from those corresponding to a random process. If the order of the aggregates is completely at random, then the expected values of n_{ij} are:¹⁰

$$n_{ij}^{\text{rand}} = \frac{n_i n_j}{N} \quad (3.5)$$

⁸Of course, *natural* cluster break-up arising in reversible aggregation should not be prevented.

In this section, when we speak about cluster break-up, we refer only to the *induced* cluster break-up as a consequence of the measuring process.

⁹The typical pulse duration for the measurements carried out during this research work is 120 μ s.

¹⁰The derivation of (3.5) and (3.6) is based on the properties of the multinomial distribution, when it is assumed that all the $\{n_i\}$ are large enough.

3. MATERIALS AND METHODS

and their standard deviation are:

$$\sigma_{ij}^{\text{rand}} = \sqrt{n_{ij}^{\text{rand}} \left(1 - \frac{n_{ij}^{\text{rand}}}{N}\right)} \quad (3.6)$$

If the experimental n_{ij} values are normally distributed, then, the probability of finding a n_{ij} which differs from its expected value in more than $2\sigma_{ij}^{\text{rand}}$, is less than 2%. Accordingly, if we would find that $|n_{ij} - n_{ij}^{\text{rand}}| > 2\sigma_{ij}^{\text{rand}}$, we could conclude that the correlation between i -mers and j -mers cannot be attributed to randomness, but probably to break-up in the measuring cell.

This test have been carried out with a slowly flocculated cationic latex (specifically, the IDC latex described in Sec. 3.3), and the measured n_{ij} were comprised inside the $n_{ij}^{\text{rand}} \pm 2\sigma_{ij}^{\text{rand}}$ intervals almost in every case. The only discrepancies were found in cases where the statistics were quite bad, less than 25 counts. Moreover, when the test was repeated for a different measurement of the same sample, the supposed-to-be correlated n_{ij} were different. In conclusion, the correlation in the sequence of detected clusters cannot be distinguished of the correlation due to pure randomness. It should be mentioned that the sample used in these tests was weakly flocculated, and it was re-dispersed by a sonication of two minutes.

3.1.3. Measuring protocol

The general procedure for obtaining all experimental data used in this work is the following:

1. Sample preparation
2. Instrument calibration
3. Zero time measurements
4. Measure of the aggregating system
5. Data analysis and CSD obtention
6. Kinetic rate constant obtention

In what follows, we visit all these points, particularising to a typical heteroaggregation process: cationic latex (IDC) and anionic latex (AS1), in equal proportion, in the presence of a high electrolyte concentration (1 M KBr).

Sample preparation

Colloidal dispersions are stored in a refrigerator at a high particle concentration, about 10^{11} cm^{-3} . Diluted dispersions are prepared by adding ultra-purified water obtained using Millipore equipment,¹¹ which provides water with a conductivity below $0.055 \mu\text{S cm}^{-1}$. The particle concentration of the dilute dispersions, usually $2 \times 10^8 \text{ cm}^{-3}$, is twice the final desired particle concentration.¹² Reactants are kept several hours at room temperature, $(20 \pm 1)^\circ\text{C}$, and then sonicated for 10 minutes¹³ in order to approach monomeric initial conditions. To prevent undesired effects due to presence of silicic ions (Hidalgo-Álvarez *et al.*, 1989; Routh and Vincent, 2004), glassware was not used neither in sample preparation nor in sample handling.

Instrument calibration

The crossing between the sample stream and the laser focus is highly sensible and must be checked—and usually corrected acting on the corresponding screws—before *every* SCLS measurement. It is convenient to use relatively small colloids, whose diameter is close to the resolution limit of the instrument. Fortunately, AS1 is indeed able to be used to this purpose. Once the hydrodynamic focusing cell is working properly, the microscope objective (see the above description of the detection optics) has to be checked in order to ensure that it is focusing the illuminated region. Other components, as the pinhole and the entrance diaphragms, also have to be checked regularly, although not so frequently. In particular, diaphragms controls the absolute light intensity and the ratio between real signal (light scattered by clusters) and background noise (S/N

¹¹Milli-Q Academic System, Millipore Corporation, Massachusetts.

¹²It should be pointed out that this particle concentration corresponds to a particle volume fraction of less than 0.001%. Such a low volume fraction not only ensures single particle detection, but also allow us to safely state that we are studying aggregation processes arising in the dilute regime.

¹³150 W ultrasonic bath Ultrasons, Selecta S.A., Spain.

3. MATERIALS AND METHODS

ratio). It is necessary to make a compromise between them, because allowing more light intensity increases the S/N ratio but, at the same time, reduces the size-discrimination interval of the instrument.

Other maintenance tasks include bubbles removing from cell and tubes, especially when the instruments have been several days stopped. Finally, it is convenient to fix occasionally the pump *flow factor* f_{flow} , *i.e.*, the amount of injected volume per unit of time and pump revolution velocity. Although f_{flow} slightly fluctuates among measurements, a typical value is:

$$f_{\text{flow}} = (0.478 \pm 0.012) \mu\text{L s}^{-1} \text{ rpm}^{-1}$$

This factor allows us to calculate the sample volume injected in each measurement. Immediately from its definition, the injected volume is:

$$V_{\text{inj}} = f_{\text{flow}} \nu \tau \quad (3.7)$$

where τ is the injection time and ν is the pump revolution frequency. A typical V_{inj} value, corresponding to a measurement duration of 512 s, and where the pump works at 0.0117 rpm, is:

$$V_{\text{inj}} = (2.86 \pm 0.07) \mu\text{L}$$

Zero time measurements

The stable colloidal dispersions are measured before the aggregation process begins. These zero time measurements are used to experimentally determine the initial particle concentration of both colloidal dispersions and their relative concentration x . In the experimental part of this work, it is assumed that $x = x_{\text{IDC}}$, *i.e.*, the ratio between the cationic particle concentration and the total particle concentration:

$$x = x_{\text{IDC}} = \frac{c_0^{\text{IDC}}}{c_0^{\text{IDC}} + c_0^{\text{AS1}}} \quad (3.8)$$

Zero time measurements also allow us to check if we have monomeric initial conditions. Since colloidal dispersions slowly flocculate when they rest for a long time, even if no salt is added, perfect initial conditions never could be reached. In this work, we consider that a colloidal dispersion approaches monomeric initial conditions when the overall concentration of clusters —dimers, the most of them— is less than 5% of the monomer concentration. Otherwise, dispersions are sonicated once again, or even new samples are prepared. Despite of this somehow relaxed initial condition, in the most of the experiments, dimer concentration was less than 2% of the monomer concentration for the anionic latex AS1 and less than 3% for the cationic latex IDC. Initial concentration of clusters larger than dimers was negligible in almost all experiments. Additionally, zero time measurements complete the calibration process, as they act as a test for the algorithm parameters: threshold voltage and typical pulse duration. In order to achieve good statistics, zero time measurements are repeated at least three times.

Another previous measurement is required: the background noise measure. It is a SCLS analysis of the suspension medium, without any colloidal particle. Even with no colloidal particles, the phototube signal often surpasses the threshold value due to unavoidable effects like fluctuations in the light intensity or flow velocity, spurious reflections on the cell windows, light-scattering due to dust particles, etc., which leads to false pulse detections. Most of them are in-line rejected because their duration is clearly shorter than the typical pulse duration. But some of them may match genuine pulses in duration and, less frequently, also in intensity (please see the noise peaks marked with letter ‘N’ in Fig. 3.4). Hence, pulse histograms have to be corrected by subtracting the pulses detected in these noise measurements. Additionally, noise measurements are a test of the cell cleaning state.

Measure of the aggregation process

The heteroaggregation process starts when all reactants, colloidal dispersions and salt solution, are poured thorough the mixing device schematically showed in Fig. 3.5. The Y-shape devices assure a homogeneous mixing. It should be noticed that the mixing, although is performed as rapidly as possible, takes some

3. MATERIALS AND METHODS

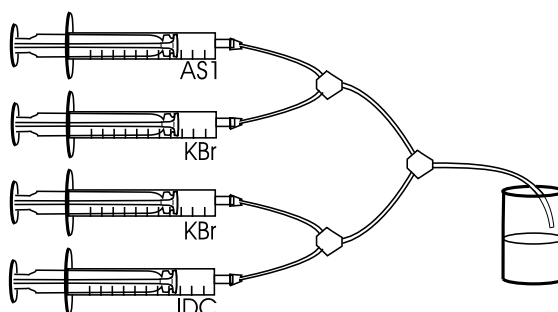


Figure 3.5.: Scheme of the mixing setup, used to initiate heteroaggregation processes.

time, typically about 30 seconds.

Immediately after the mixing process, the first measurement starts by extracting a small amount of sample and injecting it into the cell. Typically, injection is performed at the slowest velocity and takes 512 s. Then, another amount of sample is extracted and a new measurement begins. Although the injected volume is less than $3\ \mu\text{L}$, it is necessary to extract a larger amount of sample in each measurement because the contents of the tubes have to be refilled. Hence, about $175\ \mu\text{L}$ of sample are wasted in each single measurement. Even so, a typical experiment starts with 40 mL of sample, so more than 200 measurements may be performed. It corresponds to about 50 hours of continuous measuring. In addition, it is possible to set a delay between every two consecutive measurements.

Data analysis and CSD obtention

The data acquisition software analyses the phototube signal and classifies the pulses according to their size, as described in Sec. 3.1.2. The numbers of pulses of each area and duration are stored in files for posterior analysis. This analysis consists of the following steps:

1. Noise correction: The background noise is subtracted from all the experimental data (including the zero time measurements of the reactants).

2. Dead time correction: If one cluster enters the detection region before another one leaves it, only the first cluster is recorded. This introduces a dead time in the measuring time which have to be corrected. If the number of detected pulses of a given size is n_i^{det} , then the corrected number of pulses of this size n_i^{cor} is:

$$n_i^{\text{cor}} = n_i^{\text{det}} \frac{\tau}{\tau - \tau_{\text{pulses}}} \quad (3.9)$$

where τ is the measuring time and τ_{pulses} is the duration of all the detected pulses. This correction is always small, since the relative dead time never exceeds 1%.

3. Determination of the size intervals corresponding to each cluster size: Commercial software¹⁴ is used to plot several pulse frequency histograms and determine the intervals corresponding to each cluster size. The histograms must be distributed along the whole measuring time, since fluctuations may move the sample stream and, consequently, alter the intensity of the scattered light. The cluster-size distribution (CSD) N_i is obtained, obviously, by summing up the pulse counts of each interval.
4. Monomer coincidence correction: As stated before, when two aggregates cross the detection region at the same time, only one pulse is recorded. The area of the detected pulse is, obviously, the sum of the areas of the two actual pulses. Effectively, when the monomer concentration is large, a small peak located between the monomer and dimer peaks can be found in the frequency histograms. Then, the monomer count has to be updated by adding twice the monomer coincidence count. This correction may be quite important, especially in the early stages of the aggregation process, when it may be as large as 10% (Fig. 3.6a). If we consider that the probability of finding a monomer in the the illuminated volume obeys a Poisson distribution, then the probability of monomer coincidence is proportional to the squared concentration of monomers (see, *e.g.*, Fernández-Barbero, 1994). A log-log plot of the number of coincidences n_c versus the number of monomers n_1 detected during a measurement is shown in Fig.

¹⁴Origin Pro 7.0, OriginLab Corp., USA.

3. MATERIALS AND METHODS

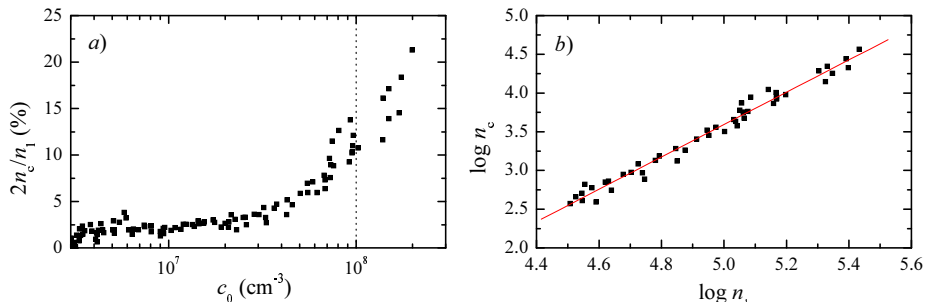


Figure 3.6.: Monomer correction due to coincidences: *a*) percentage of the monomer count due to the coincidence correction, versus the initial monomer concentration; and *b*) allometric fitting of the number of coincidences versus the number of monomers. The dotted vertical line in plot *a*) indicates the maximum monomer concentration used in experiments.

3.6*b*. The best fit is obtained for $n_c \propto n_1^\alpha$ with $\alpha = 2.09 \pm 0.05$, in good agreement with the theoretical prediction ($\alpha = 2$). At the particle concentrations used in this work, the cluster coincidence is a relatively rare event, only relevant for monomers.

5. Translation from counts to actual concentration: The CSD obtained so far is expressed in number of counts per measurement. It is convenient to translate this quantity to physically significant units. It is easily done by dividing N_i by the injected volume V_{inj} , which was calculated in (3.7).

Kinetic rate constant obtention

The effective initial dimer formation rate, k_S , can be obtained from the monomer time evolution at short aggregation times, following the method reported by Drake (1972). It consists of a linear fitting of the $g(t)$ function, defined as

$$g(t) \equiv \frac{2}{c_0} \left(\sqrt{\frac{c_0}{c_1(t)}} - 1 \right) \quad (3.10)$$

At sufficiently short times, when the linear fit holds, k_S can be identify with the slope of the fitting straight line:

$$g(t) \approx k_S t \quad (3.11)$$

c_0 , the initial concentration of monomers, is known from the zero time measurements. Additionally, it is possible to determine both k_S and c_0 from the same fitting. In that case, it is more convenient to rewrite (3.10) and (3.11) as follows:

$$\frac{1}{\sqrt{c_1(t)}} = \frac{1}{\sqrt{c_0}} + \frac{k_S \sqrt{c_0}}{2} t \quad (3.12)$$

Then, c_0 is obtained from the ordinate at the origin and k_S from the slope of the fitting straight line. Both possibilities have been used in this work, although it is preferred to use the measured c_0 values for obtaining k_S . The c_0 value obtained from the fitting is used just as a checking procedure.

Although (3.10) was derived for homoaggregation processes, $g(t)$ is always expected to behave linearly at short aggregation times. In these cases, it should at least be possible to fit a straight line to the onset of $g(t)$. This procedure has been shown to be a suitable method for obtaining quite accurate k_S values from experiments (Barany *et al.*, 1996; Holthoff *et al.*, 1997; Schmitt *et al.*, 2000a) and simulations (Moncho-Jordá *et al.*, 2003; López-López *et al.*, 2005), even when the aggregation kernel differed quite strongly from the constant kernel.

3.2. Other experimental techniques

Most experimental data of this work was obtained by using the single-cluster light-scattering instrument described above. Nevertheless, other experimental techniques have been used for properly characterise the experimental systems. In this section, we briefly comment on the two most relevant: nephelometry and electrophoretic mobility measurement.

3.2.1. Nephelometry

Nephelometry is a SLS technique in which the light scattered by an aggregating sample is collected at very low scattering angle. It differs from SCLS because the scattering centre is a macroscopic portion of the colloidal sample that contains a large number of clusters. Consequently, nephelometry gives us only average information about the system. In particular, the CSD is not accessible with this technique. On the other hand, a nephelometry measurement of an aggregating colloidal system takes only a few minutes. In fact, the measuring time is so short that nephelometry is generally used to determine the region where certain aggregation regime prevails. In this work, for instance, nephelometry has been used to study the homoaggregation behaviour of both colloidal dispersions versus Potassium Bromide concentration and, particularly, to find their critical coagulation concentrations (CCC).

Instrument overview

The instrument records the average light intensity as a function of time at a fixed scattering angle, $\langle I(\theta_0, t) \rangle$ or, with a simpler notation, $I(t)$. It is used to study the early stages of the aggregation process, starting from monomeric initial conditions. Here, it is applicable the model proposed by Lips, Smart and Willis (1971) (LSW model). According to this model, $I(t)$ increases linearly with time, and the effective dimer formation rate is proportional to the slope of the fitting straight line:

$$\frac{dI(t)}{dt} \propto k_s c_0 \quad (3.13)$$

Therefore, if we perform a series of measurements changing the medium properties but keeping constant the particle concentration, it is possible to compare the corresponding aggregation rates. Particularly, if we take the fast homoaggregation rate as a reference point, we obtain directly the stability factor W defined in (2.49):

$$W = \frac{\left(\frac{dI(t)}{dt}\right)_{\text{fast}}}{\left(\frac{dI(t)}{dt}\right)_{\text{slow}}} \quad (3.14)$$

Instrument description

The nephelometre used in this work is a prototype donated by Biokit¹⁵ and calibrated by Dr. Artur Schmitt. The instrument is located on a light-protected optical bank and is composed by the following elements:

- A 10 mW He-Ne laser source which provides a collimated 632.8 nm laser beam.
- Entrance optics, composed by a spatial filter to smooth the laser profile and several lenses to focalise the laser beam into the measuring cell.
- A rectangular quartz cell with two orifices, for the entrance and the exit of sample.
- A special diaphragm with three openings located in the vertical direction. It blocks transmitted light and only permits the light at three scattering angles, namely: $(4.5 \pm 1.0)^\circ$, $(10.0 \pm 2.0)^\circ$ and $(20 \pm 3)^\circ$.
- Detection optics, composed by a lens set to separate the three scattering light beams and an optical prism to lead them towards the detectors.
- A set of three photodiodes, one for each permitted scattering angle.
- A electronic system formed by three I/V converters, a multiplexor and an amplifier.
- A personal computer with an A/D card.

Aggregation is induced by rapidly mixing the reactants using a Y-shape device (see Fig. 3.5, where three of such devices are shown). The mixing process is very fast, less than one second, because the 1 mL syringes are actuated by a high compressed air plunger.

CCC determination

The critical coagulation concentration (CCC) of a one-component colloidal system can be accurately determined by using nephelometry. Basically, the proce-

¹⁵Biokit S.A., Spain.

3. MATERIALS AND METHODS

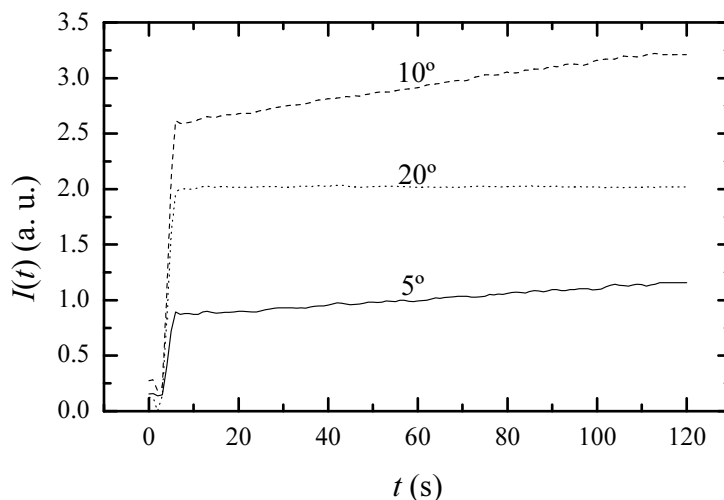


Figure 3.7.: Typical nephelometre output for a homoaggregation experiment.

ture lies in measuring $I(t)$ for a series of homoaggregation processes with different electrolyte concentrations. The appropriate particle concentration, which is kept constant in the series of experiments, depends inversely on the particle size (Molina Bolívar, 1999). For each experiment, three $I(t)$ curves are obtained (see Fig. 3.7), corresponding to the three scattering angles.

The steep increasing of $I(t)$ at the first moments is due to the substitution of the water inside the cell by the colloidal sample. Immediately after this, the onset of $I(t)$ is linearly fitted, being dI/dt the slope of the fitting line. As can be appreciated in the figure, only the onset of the $I(t)$ curves behave linearly. Later on, when the concentration of trimers and larger clusters is no longer negligible, the $I(t)$ curves apart from the linear behaviour. The linear range is longer as lower is the scattering angle. Nevertheless, at very low angles the noise increases so much that the fitting loses accuracy. Hence, the data set used in the fitting process is usually the corresponding to a scattering angle of 10° , where the best compromise between linear behaviour and signal/noise ratio is achieved (Molina Bolívar, 1999).

According to the DLVO theory (see Sec. 2.3.1), the aggregation rate increases when the electrolyte concentration increases, until the CCC is reached. Then, the system aggregates in the rapid aggregation regime and k_s —and, consequently, dI/dt — takes its maximum value. The W stability factor is then obtained by means of (3.14).

3.2.2. Electrophoretic mobility

Since colloidal particles bear electrical charge and are able to move, some interesting electrokinetic phenomena arise. Electrophoresis is one of this phenomena, in which colloids move in a coherent way due to the presence of a external electrical field (see, *e.g.*, Hidalgo-Álvarez *et al.*, 1996).

Principle of function

Let \vec{E} be the electrical field intensity. Then every charged colloid or *macroion* will acquire a coherent motion, parallel to this field, that combines with its random Brownian motion. If the external field is not too strong, the electrophoretic drift velocity \vec{v}_e is found to be proportional to the field intensity:

$$\vec{v}_e = \mu_e \vec{E} \quad (3.15)$$

where μ_e is the *electrophoretic mobility* of the colloidal particle. It is evident that μ_e has to be related with the electrical properties of the colloidal particle, although the exact relationship is not a solved question at all (Hidalgo-Álvarez *et al.*, 1996). Furthermore, it is assumed that the particle drifts some surrounding water in its movement. Hence, electrophoresis theories usually does not refer directly to the particle surface properties but to the electrical properties at the shear surface dividing the solidary water and the bulk medium. This surface is known as the ζ -plane and so the electrical potential in this surface is referred as the ζ -potential. The theory concerning the relationship between the electrophoretic mobility and the ζ -potential —and, ultimately, with the surface properties— is currently a matter of some debate (Hidalgo-Álvarez *et al.*, 1996).

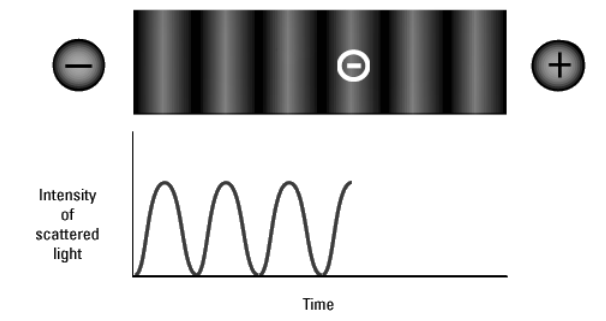


Figure 3.8.: Principle of function of a electrophoretic mobility set-up: electrophoretic motion of a macroion crossing a interference pattern (top); phototube signal (bottom).

Instrument overview

Measuring the electrophoretic mobility is a straightforward task in current research labs and even in large scale industry. A typical electrophoretic mobility set-up applies a known electrical field of magnitude $E = |\vec{E}|$ and measures the drift velocity of the colloidal particles $v_e = |\vec{v}_e|$. Then, μ_e is obtained by applying (3.15). The electrophoretic mobility measurements of this work were performed by using a commercial electrophoretic mobility set-up of Malvern Instruments¹⁶. This instrument is composed of a optic unit, a correlator and a computer.

The optic units consists of the following elements:

- A capillary cell, sizing 4 mm of diameter and 40 mm of length, in whose extremes are located the electrodes. When an external electric field is applied, the fluid inside the cell flows due to the ion migration. As the fluid is almost incompressible and cannot escape from the cell, a counter-flow is created close to the cell walls. Somewhere in an intermediate distance between the cell axis and the cell wall, a cylindric stationary region without

¹⁶Zeta-Sizer IV, Malvern Instruments, United Kingdom.

any flow should exist. According to the manufacturer, this region is located at a distance of 71.8% of the cell radius, if the disperser medium is water.

- A He-Ne laser source which provides a 5 mW collimated laser beam with $\lambda_0 = 632.8 \text{ nm}$. The laser beam is split into two perpendicular beams, which are forced to cross each other just in the stationary region of the cell. Consequently, an interference pattern composed of alternating dark and light bands is obtained.
- A phototube detects the light scattered by the sample. The electrophoresis motion of the particles is perpendicular to the bands, so particles change periodically from dark to light zones as they move. Consequently, the intensity of the scattered light also varies periodically. The frequency of this variation is proportional to the drift velocity of the particles. Fig. 3.8 shows the principle of function of the instrument: the particle crosses the interference bands (top) and scatters light whose intensity varies periodically.

The electronic correlator is used to calculate the autocorrelation function of the signal. A computer controls the whole operation of the instrument and calculates the electrophoretic mobility from the autocorrelation function.

3.3. Experimental systems

The election of a suitable experimental system is a critical point of this researching work. Obviously, we need two colloidal dispersions whose particles bear electrical charge of opposite signs. Then, electrostatic heteroaggregation starts when both species of particles are mixed together. The properties of both colloidal dispersions have to be accurately determined in order to face the comparatively more complex understanding of the mixed system. Hence, it is desirable the use of *model colloids*. Here, we say that a colloidal dispersion is composed by model colloids when (Bastos-González, 1992):

- It is composed by spherical, equally sized particles.

3. MATERIALS AND METHODS

- The surface properties do not vary significantly among the particles.
- The colloidal dispersion is kinetically stable during long periods of time, unless the properties of the dispersion medium are intentionally changed.

Aqueous suspensions of micro-spheres composed of a polymer lattice, usually known as *latexes*, are widely used as model colloidal dispersions. The kinetic stability of a latex may be achieved at least by three different mechanisms (see, *e.g.*, Hunter, 1987):

- Steric stabilisation due to adsorbed macromolecules, usually polymers, on the particle surface. These macromolecules extend into the surrounding medium creating a “hairy layer”. When the hairy layers of two particles interpenetrate, repulsive osmotic forces prevent coagulation.
- Electrostatic stabilisation due to the presence of electric charges on the particle surface. As stated in Sec. 2.3.3, charged surfaces develop an electric double layer (EDL) which extends out into the bulk solution. When two EDLs overlap, repulsive osmotic forces prevent coagulation. Electric charges may originate from the dissociation of the main lattice or, more commonly among polymer colloids, from charged groups on the particle surface.
- Spontaneous stabilisation is possible when the colloid surface is highly hydrophilic. Although polymer latices usually present hydrophobic surfaces, they may be covered by an appropriate hydrophilic layer.

Electrostatic stabilisation is preferred here because the particle-particle interactions can be tuned precisely by changing the medium characteristics. Generally speaking, the electrolyte concentration controls the EDL thickness and the medium *pH* changes the overall interaction strength.

3.3.1. General characteristics

James *et al.* (1977) suggested that the best way to experimentally study heteroaggregation is by using two latexes with the same composition, one with

a pH -independent charge and the other one being amphoteric. This is the approach followed in this work. Two polystyrene latexes were used, one with sulphate groups and the other one with amidine groups. The amphoteric amidine latex was supplied by Interfacial Dynamics Corp.¹⁷ It bears positive charge at acid pH , and negative charge at basic pH . The anionic sulfate latex was synthesised in our laboratories —according to the recipe described by Goodwin *et al.* (1974)— by Schmitt (2000). It bears a negative charge almost independent of the medium pH . For the sake of simplicity, in what follows we will refer to them as ‘IDC’ and ‘AS1’ respectively. Analogously, we will refer to the IDC + AS1 mixtures with the letter ‘X’ plus the percentage of the cationic particles (IDC). For instance, ‘X70’ means a binary dispersion composed by a 70% of cationic particles and a 30% of anionic particles.

Already for homoaggregation experiments, highly monodisperse microspheres are required in order to distinguish clusters of different size with SCLS. The size monodispersity is even more important for heteroaggregation experiments with SCLS. If A and B particles are used and, for instance, the radius of the former is greater than the radius of the latter, then an A – A dimer scatters more light intensity than a B – B dimer. Although it could allow us to distinguish between the different dimer compositions, it also implies an important loss of resolution. Hence, much care was taken that both systems used for the heteroaggregation experiments were as similar in size as possible.

The ratio of the surface charges of both latexes can be varied by changing the medium pH , as stated before. Nevertheless, what is understood when we speak about surface charge is somehow a complex thing. There are, at least, three different “surface charges” involved in colloidal science, namely:

- Titrated surface charge. It is obtained by titration and it is the maximum electric charge that can bare the particle.
- Stability effective surface charge. It is responsible of the formation of the EDL and, eventually, of the kinetic stability of the colloid. It is related to the critical coagulation concentration (CCC), although it is necessary

¹⁷Amidine latex 3-600, batch 1138, Interfacial Dynamics Corporation, Portland, Oregon, USA.

3. MATERIALS AND METHODS

Table 3.1.: Main properties of the experimental systems used in this work: latex name, type of charged surface groups, particle diameter ($2a$), polydispersity index (PDI), KBr critical coagulation concentration (CCC), and electrophoretic mobility (μ_e) at free pH.

Name	Groups	$2a$ (nm)	PDI	CCC (mM)	μ_e ($10^{-8} \text{ m}^2 \text{ V}^{-1} \text{ s}^{-1}$)
AS1	Sulfate	524 ± 19	1.005	320 ± 20	$-(4.82 \pm 0.14)$
IDC	Amidine	525 ± 14	1.002	180 ± 20	$+(4.72 \pm 0.05)$

a model of the particle-particle interaction in order to obtain a quantitative value. Anyhow, a larger CCC value corresponds to a larger effective surface charge.

- Electrokinetic effective surface charge. It is similar to the preceding one, although it is responsible of the electrokinetic phenomena instead of the stability. It may be obtained, for example, from electrophoretic mobility measurements. Again here, a larger $|\mu_e|$ value corresponds to a larger effective surface charge, although a quantitative value can only be obtained once a detailed ζ -potential model is used.

In this work, we make use of both stability and electrokinetic effective surface charges, although the discussion about which one is more appropriate or even if they are really equivalent, is out of our scope.

In summary, we measured size, monodispersity, stability versus electrolyte concentration and electrophoretic motion of our experimental systems. These properties are summarised in Tab. 3.1 and are studied in some detail in the following sections.

3.3.2. Particle size and shape

Shape, size and polydispersity of the colloidal particles used in this work were determined by transmission electron microscopy (TEM)¹⁸, at the “Centro de Ins-

¹⁸Model EM 10C, Carl-Zeiß, Germany.

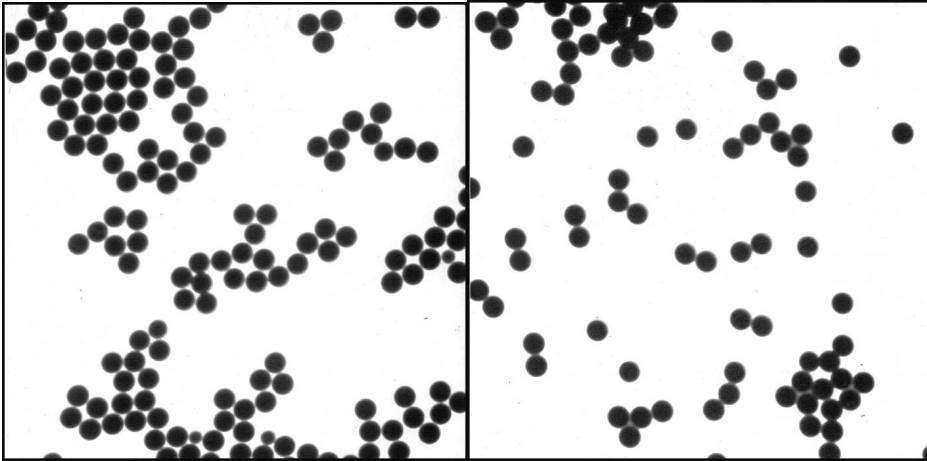


Figure 3.9.: Microphotograph of both colloidal dispersions, AS1 (left) and IDC (right), obtained by transmission electron microscopy.

trumentación Científica” of the “Universidad de Granada”. Several microphotographs of each sample were taken with a $6825\times$ magnification factor. Two of the photographs are reproduced in Fig. 3.9. As can be seen, the particles are quite monodispersed spheres. Additional microphotographs at a higher magnification ($12600\times$) were taken to check that the particle surface is highly smooth.

Photograph negatives were digitalised at high resolution and analysed by using `bool2k`¹⁹, software developed by Dr. Galisteo and Dr. Holgado. `bool2k` automatically detects the particle contour and obtains the corresponding particle size distribution (PSD). The particle sizes are coarse grained into several intervals, so we actually get a frequency histogram f_i , *i.e.*, the frequency of the particles whose diameters are comprised in the interval centred at d_i . The size histogram of both systems are shown in Fig. 3.10 on the left side, with a interval width of 1 nm. On the right side of this figure, it is shown the continuous distribution obtained from the former by a Savitzky-Golay smoothing process²⁰.

¹⁹`bool2k` 1.0, BooLERO Software, Spain.

²⁰Origin Pro 7.0, OriginLab Corp., USA.

3. MATERIALS AND METHODS

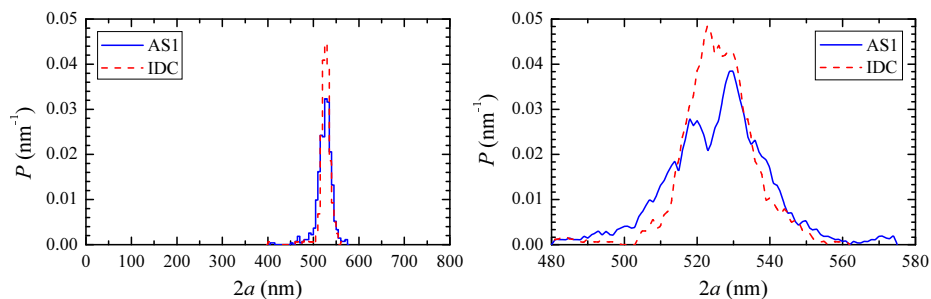


Figure 3.10.: Particle size distribution of both experimental systems: size histogram (left side) and smoothed, continuous size distribution (right side).

The Bool2k software also gives us some average diameters, defined as follows:

Number-averaged diameter:

$$\langle d \rangle_n = \sum f_i d_i \quad (3.16)$$

Weight-averaged diameter:

$$\langle d \rangle_w = \frac{\sum f_i d_i^4}{\sum f_i d_i^3} \quad (3.17)$$

Volume-averaged diameter:

$$\langle d \rangle_v = \left(\sum f_i d_i^3 \right)^{1/3} \quad (3.18)$$

The polydispersity of the particulate system may be quantified by its *polydispersity index* (PDI), defined as the ratio between the weight and number average diameters:

$$\text{PDI} = \frac{\langle d \rangle_w}{\langle d \rangle_n} \quad (3.19)$$

Table 3.2.: Size analysis of the two latexes used in this work: N number of particles used in the analysis; $\langle d \rangle_{n,w,v}$ particle diameters (nm) averaged as described in the main text; SD standard deviation (nm); PDI polydispersity index.

	N	$\langle d \rangle_n$	$\langle d \rangle_w$	$\langle d \rangle_v$	SD	PDI
AS1	527	524.2	524.6	524.9	19.7	1.004
IDC	326	525.3	525.4	525.6	13.8	1.002

All the statistical parameters described above are listed in the table 3.2. Since all the TEM measurements were performed the same day and with the same experimental conditions, we can safely state that AS1 and IDC particles are equally sized. Furthermore, it is generally accepted that a particulate system is monodispersed when its PDI is less than 1.05. Hence, our experimental systems are highly monodispersed.

3.3.3. Stability versus KBr concentration

The stability factor W of both systems versus the KBr concentration was measured by using the nephelometre described in Sec. 3.2.1. We choose KBr because it is a indifferent 1:1 electrolyte, where no specific adsorption is expected. Since relatively large particles are used, samples could be quite diluted, about 10^9 cm^{-3} . This is quite convenient, because the linear region of $I(t)$ is consequently longer. In fact, the whole $I(q)$ curves could be fitted to a straight line, and not only their onset. Furthermore, the signal/noise ratio was so good that we could safely use the smallest available scattering angle (5°). The measured W factors of both systems are plotted in Fig. 3.11. In this figure, it is evident that the stability behaviour of both systems agrees qualitatively with the DLVO predictions: when the electrolyte concentration surpasses certain value (the CCC value) then the system aggregates in the fast aggregation regime.

As can be seen in the figure, the anionic latex is more stable than the cationic one. In other words, with the same electrolyte concentration the anionic latex

3. MATERIALS AND METHODS

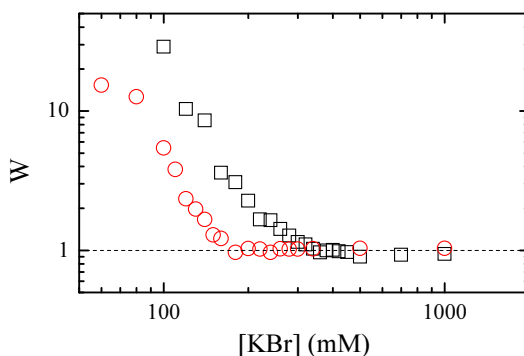


Figure 3.11.: Fuchs stability factor W vs KBr concentration of the latexes AS1 (\square) and IDC (\circ).

aggregates more slowly than the cationic one.²¹ At 180 mM KBr, for instance, aggregation undergoes three times more slowly in the AS1 latex than in the IDC one. Also the CCC values are consistent with the prior statement about the larger stability of the AS1 latex. Although its exact value may depend somehow on the experimenter subjective appreciations, it is clear that the AS1's CCC is larger than the IDC's CCC. Representative values for these CCC could be about 180 mM KBr for IDC and about 320 mM KBr for AS1.

3.3.4. Aggregation regimes

DLVO theory predicts that both systems aggregate in the diffusion-limited colloid aggregation regime above their CCCs and in somehow reaction-limited colloid aggregation regime below their CCCs. Strictly speaking, however, the term RLCA should be restricted to the limit case where the diffusion step is negligible compared with the reaction step. This ideal situation would be reached at very low electrolyte concentrations, and the flocculation process would be quite slow. Hence, at electrolyte concentrations below the CCC but not so low, the

²¹Except, of course, if the electrolyte concentration is above the CCCs of both latexes.

aggregation regime is somehow intermediate between DLCA and RLCA. For a description of this intermediate regime, see (Odriozola *et al.*, 2001a).

This can be appreciate in Fig. 3.12, where several experimental CSDs for the IDC and AS1 latexes are plotted. On the left side there are there homoaggregation experiments corresponding to the IDC latex and on the right side those corresponding to the AS1 latex. On the top the electrolyte concentration was set at 1.0 M, clearly above their KBr CCCs, estimated around 180 mM for IDC and 320 mM for AS1 (see Sec. 3.3.3). These CSD exhibit all the characteristic of a CSD corresponding to a DLCA process. The overall shape of the cluster-concentration curves is quite similar to those corresponding to the constant *kernel* (see Sec. 2.1.3 and Fig. 2.1a), although there are small differences at long times, where some crosses are appreciable. It should be noted that the Brownian *kernel* (See Sec. 2.2.2 and Fig. 2.4), usually used to describe ideal DLCA processes, reproduces all these small deviations with respect to the constant *kernel* (Schmitt *et al.*, 2000b).

In the middle row are plotted the CSDs corresponding to experiments at lower electrolyte concentrations, although still above the CCCs of the systems (200 mM and 500 mM for IDC and AS1, respectively). Here again the CSDs are typical of a DLCA process, although the finest details are not so clearly visible. It could be due to the presence of small —but not negligible— interactions between particles. Schmitt *et al.* (2000b) found the same discrepancies between experimental rapid aggregation and the solution of the Brownian *kernel*. They call this experimental aggregation regime “difussionlike” aggregation.

The CSDs shown on the bottom row correspond to experiments carried out at KBr concentrations below the CCCs of the systems (100 mM for IDC and 200 mM for AS1). As expected, the aggregation kinetics here does not correspond to a diffusion-limited aggregation process. The aggregation rate is clearly slower²² and the concentration curves are more alike to those of the sum *kernel* than to those of the constant *kernel* (see Sec. 2.1.3). For a discussion about the different *kernels* that may describe the CSD in this region, see (Odriozola *et al.*, 2004).

²²See also Sec. 4.1.2 and Tab. 4.2 for a more quantitative probe of this statement.

3. MATERIALS AND METHODS

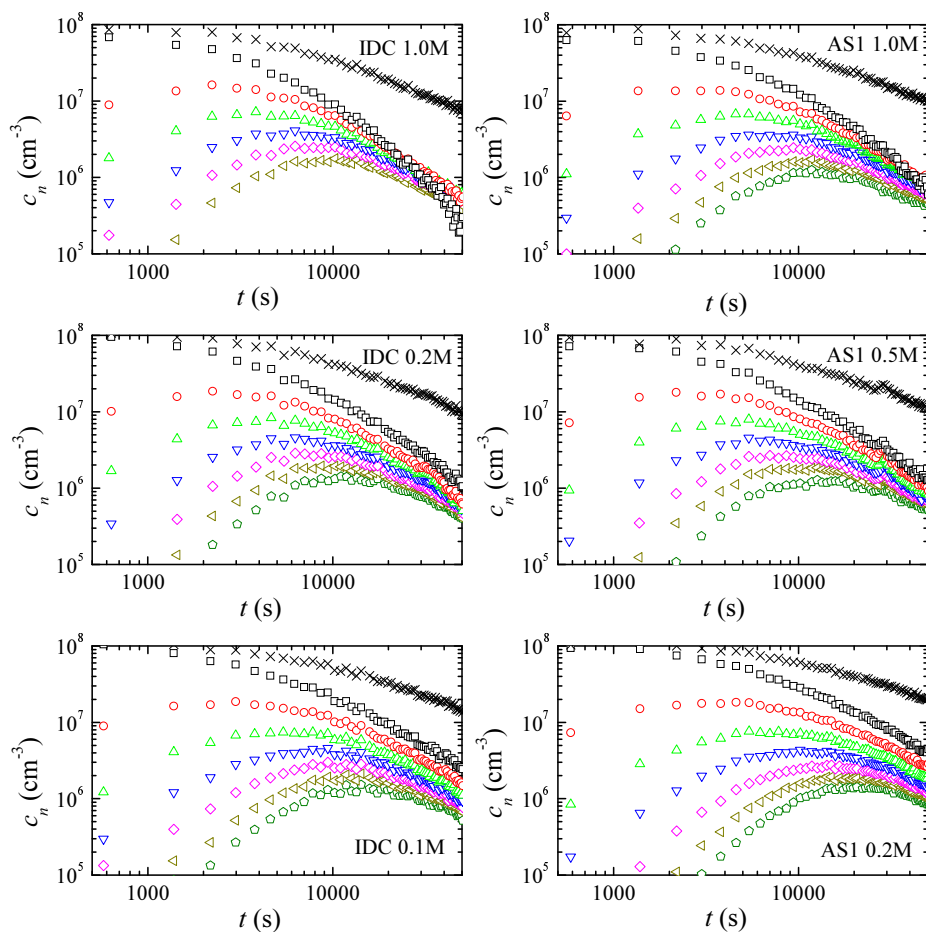


Figure 3.12.: Cluster-size distributions for IDC (left side) and AS1 (right side) homoaggregation experiments, at three KBr concentrations: clearly above their CCCs (top row), not so high but still above their CCCs (middle row), and below their CCCs (bottom row). In each plot, the concentration of monomers (\square), dimers (\circ), trimers (\triangle), tetramers (∇), pentamers (\diamond), hexamers (\triangleleft) and heptamers (\trianglerightarrow) are shown; as well as the total concentration of aggregates (\times).

Finally, at lower KBr concentrations, both systems are kinetically stable. At 10 mM, for instance, samples did not show evidences of irreversible aggregation for time intervals of several days²³. In summary, both samples seem to behave as model colloidal dispersions, aggregating in the diffusion-limited colloid aggregation regime above their CCCs and in a slower, somehow reaction-limited aggregation regime below those critical concentrations.

It should be noted that the well-behaviour of both colloidal dispersion versus the electrolyte concentration is possible because both K^+ and Br^- are indifferent ions. Hence, if other salts are used instead of KBr, it could be possible to observe aggregation regimes different from the well-known DLCA and RLCA ones. This is indeed the case for both the IDC and the AS1 latexes (Lopez-León *et al.*, 2006). In Fig. 3.13 the CSDs of homoaggregation experiments carried out with the IDC latex are plotted. In all four cases the *pH* was fixed to 6.0, the salt concentration was 600 mM and the coion was Na^+ , but the counterion changes from one experiment to another. As can be seen, the aggregation behaviour depends quite strongly on the added counterion.

For Cl^- (Fig. 3.13a) and SO_3^- (Fig. 3.13b) a typical DLCA behaviour is observed.²⁴ The aggregation behaviour at 600 mM $NaNO_3$ (Fig. 3.13c), however, is clearly different from the DLCA one. It is slower than a diffusion-limited process, with a k_S value that is half the rapid value (Lopez-León *et al.*, 2006). Moreover, the concentration curves do not intersect at long times. Actually, it presents more similarities with a RLCA process than with a DLCA one. But, without any doubt, the most impressive result was found when thiocyanate was used as counterion (Fig. 3.13d): the aggregation process slowed down and eventually stopped. This is revealing that the subjacent aggregation mechanism is of a reversible nature, probably because the particles are bond in a not very deep energy well.

The specific ionic effects —also known as *Hofmeister effects*— are present not only in colloidal systems; they also participate in a plethora of phenomena,

²³Actually, some flocculation was observed, but it completely disappeared after two minutes of sonication.

²⁴Nevertheless, when $NaSO_3$ was used, it is appreciable some excess of monomers at the later stages of the aggregation process.

3. MATERIALS AND METHODS

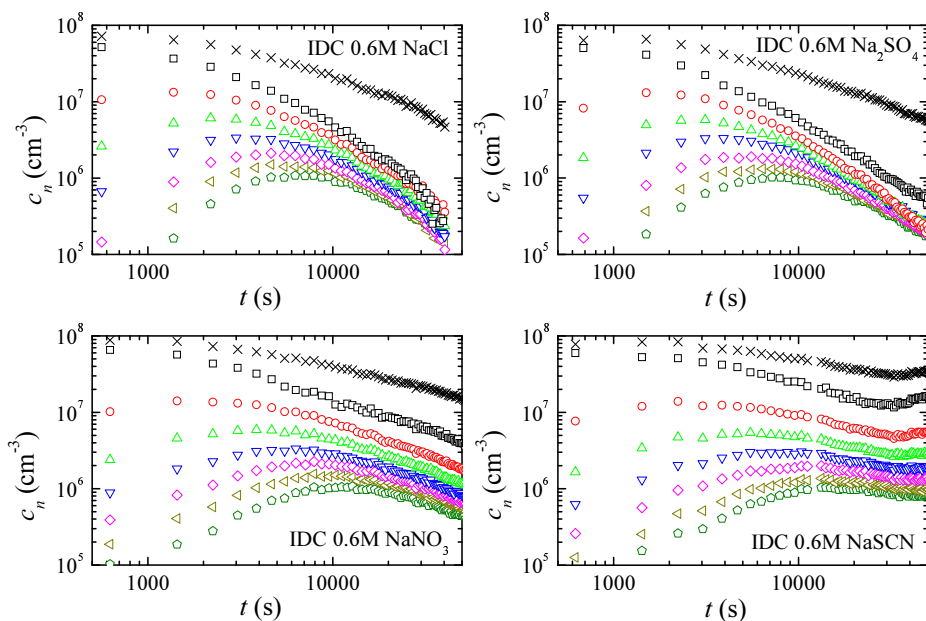


Figure 3.13.: Cluster-size distributions obtained in homoaggregation experiments of the IDC latex with different counterions: NaCl (top left), Na_2SO_4 (top right), NaNO_3 (bottom left) and NaSCN (bottom right). Please note that the salt concentration in 600 mM in all cases. Symbols mean the same as in Fig. 3.12.

such as stability and solubility of proteins, water activity coefficients, surface tension at the air-water interface, lipid solubility, chromatographic selectivity, polymer cloud points, polymer swelling, heats of hydrations, etc (Collins and Washabough, 1985; Cacace *et al.*, 1997). The origin of the Hofmeister effects is still a matter of discussion and, apparently, it is related with the structure of water around the ions and with the ion polarisabilities (Ninham and Yamin-sky, 1997).

In conclusion, the homoaggregation behaviour of the selected colloidal dispersions can be described in terms of the classic colloid stability theory (DLVO) when a convenient, non specific, electrolyte —like KBr— is chosen.

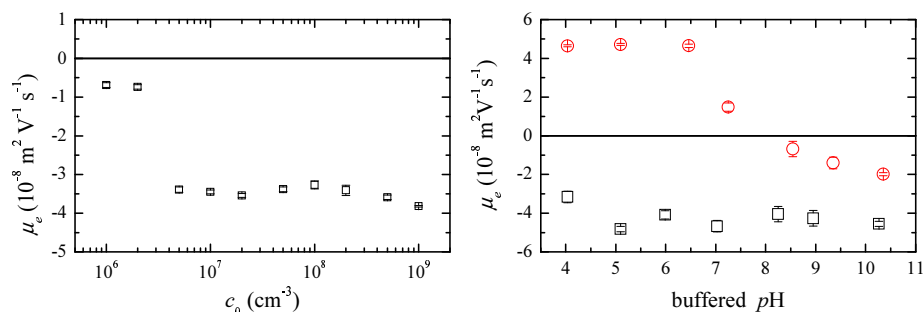


Figure 3.14.: Left side: electrophoretic mobility of AS1 latex as a function of the particle concentration, in a 5 mM KBr solution. Right side: electrophoretic mobility of both latexes, AS1 (\square) and IDC (\circ), as function of the medium pH .

3.3.5. Electrophoretic mobility

The electrophoretic mobility was measured using the electrophoretic mobility set-up described in Sec. 3.2.2. The first step was to search for the optimal particle concentration. It has to be large enough to achieve a reliable signal/noise ratio; although low enough to avoid multiple light-scattering. For this purpose, the apparent electrophoretic mobility of AS1 latex was measured versus the particle concentration. The dispersion medium was a 5 mM KBr solution with free pH . Results are plotted in Fig 3.14, left). As can be seen, the electrophoretic mobility reaches an almost constant value when the particle concentration surpasses $5 \times 10^6 \text{ cm}^{-3}$. Multiple light-scattering was not present at the particle concentrations used in this study. Regardless, it is convenient to perform measurements at a relatively low particle concentration, so we consider that the best particle concentration for electrophoretic mobility measurements is $5 \times 10^7 \text{ cm}^{-3}$.

Since amidine groups are amphoteric, the charge of the IDC particles depends on the medium pH . The charge of sulphate particle, on the contrary, is expected to be almost independent of the medium pH . In order to check this, μ_e was measured as a function of the medium pH . Only low ionic strength buffers were used, which provide a pH -controlled medium with a electrolyte concentration below

3. MATERIALS AND METHODS

Table 3.3.: Main characteristics of the buffers used in electrophoretic mobility measurements: name, type of buffer, quantity used per litre of final solution and measured pH .

<u>Anionic buffers</u>				<u>Cationic buffers</u>			
name	type	quantity	pH	name	type	quantity	pH
A4	acetate	772 μL	4.034				
A5	acetate	247 μL	5.098				
A6	phosphate	247 mg	5.991	C6	BIS-TRIS	275 mg	6.460
A7	phosphate	156 mg	7.029	C7	BIS-TRIS	871 mg	7.249
A8	borate	927 mg	8.246	C8	TRIS	217 mg	8.544
A9	borate	318 mg	8.952	C9	TRIS	1083 mg	9.348
A10	borate	136 mg	10.265	C10	AMP	376 mg	10.350

2 mM. When it was possible, anionic buffers (A_x) were used for the anionic latex and cationic buffers (C_x) for the cationic latex. Unfortunately, it was not possible to achieve cationic acid buffers with a pH below 6. Composition and other features of all the buffers are listed in Tab. 3.3. Occasionally, a small amount of ClH or NaOH was added for a fine tuning of the pH . The electrophoretic mobility of both systems as a function of the pH is plotted in Fig 3.14, right). Effectively, μ_e is almost constant for the AS1 latex, while it changes dramatically for the IDC latex. In the heteroaggregation experiments of this work, especially those related with the presence of long range interactions, it was necessary to achieve quite low electrolyte concentrations. Hence, most heteroaggregation experiments were performed without pH -buffering, at the free pH region (around 5.5). Consequently, the pH of the particle suspensions could vary slightly when mixing both particle dispersions. Fortunately, the IDC μ_e is relatively robust against small pH variations around the free pH region.

3.4. Computer simulations

Although this is primarily an experimental work, computer simulations were run in order to get further insight into the heteroaggregation phenomena. Hence, we make use of Brownian dynamics simulations (BDS) of heteroaggregation arising in oppositely charged colloids, both considering particle-particle interactions and without considering them. The latter case was found to be quite convenient for studying situations where the particle-particle interaction range was so short that these forces could be substituted by aggregation rules at the contact. When the particle-particle interaction range was not so short, then Brownian dynamics simulations including a model of these interactions were used. Additionally, in this work it was necessary to solve the stochastic master equation (2.7) for a given *kernel*. It was possible by using a stochastic algorithm. None of these programs was newly written for this work: the source code of the BDS without interactions was written by Dr. A. Moncho-Jordá, from the “Universidad de Granada”; the code of the BDS with interactions, by Dr. A. Puertas, from the “Universidad de Almería”; and the code of the stochastic algorithm, by Dr. G. Odriozola, from the “Instituto Mexicano del Petróleo”. My personal contribution restricts to some minor changes in the Input/Output functions and some performance optimisations.

3.4.1. Brownian dynamics simulations without interactions

Roughly speaking, a Brownian dynamics simulation (BDS) consists in virtually reproduce the behaviour of colloidal particles suspended in a fluid phase. BDS are focused only in the particle behaviour, the motion of the surrounding fluid is not reproduced. Consequently, the performance of BDS is quite high and it is possible to simulate systems composed by several thousands of particles, during very large simulation times, with a reasonably small computer effort. On the other hand, as the the fluid motion is not properly simulated, the introduction of the hydrodynamic interactions (HI) is a very hard task and they are usually completely neglected (for a correct treatment of the HI in computer simulations of interacting colloids, see Padding and Louis, 2006).

Simulation overview

As early as 1983, Paul Meakin introduced a very convenient way of simulating two-dimensional irreversible diffusion-limited cluster-cluster aggregation (Meakin, 1983). These were on-lattice simulations, *i.e.*, the particle coordinates were restricted to the points of a simple square lattice. At each simulation step, clusters (including single particles) were picked at random and moved to a neighbouring lattice site with a probability proportional to their “mobility”. Meakin considered two cases: i) cluster mobility independent of the cluster size and ii) cluster mobility inversely proportional to the cluster mass. Periodic boundary conditions were used to mimic an infinite system. Posteriorly, the own Meakin and co-workers demonstrated that this scheme correctly reproduced the translational Brownian motion of particles and clusters, when the cluster “mobility” is inversely proportional to the cluster radius of gyration (Meakin *et al.*, 1985a; Meakin *et al.*, 1985b).

Short range particle-particle interactions can be added to this aggregation scheme by introducing a sticking probability, P_s . Then, when two particles encounter each other, they are irreversibly linked with a probability P_s . González (1993) showed that this approach could reproduce the behaviour of both the diffusion-limited and the reaction-limited colloid aggregation: DLCA is achieved by setting $P_s = 1$, and RLCA by setting $P_s \ll 1$. Other situations of interest can be reproduced introducing different “contact rules”. For instance, Moncho-Jordá *et al.* (2003) simulated the aggregation of colloidal particles whose surfaces are inhomogeneous because they present a circular patch with different properties. When two particles encounter each other, there are three possible contacts: bare-bare, bare-coated and coated-coated; each one with a different sticking probability. This model may imitate the aggregation of colloids partially covered by macromolecules.

Heteroaggregation processes have been also simulated with this scheme by Meakin and Djordjević (1986), and by Stoll and Pefferkorn (1993). In these works, two “contact rules” were imposed: i) collisions between unlike particles always lead to bond formation and ii) no bonds are allowed to form between like particles. The corresponding aggregation regime was called binary diffusion-limited

cluster-cluster aggregation (BDLCA) by AlSunaidi *et al.* (2000). The BDS without interactions used in this PhD thesis obey the same contact rules, as they were intended precisely to study BDLCA processes, although particles were not restricted to a lattice.

Simulation details

The BDLCA simulations are three-dimensional off-lattice Brownian dynamics simulations with periodic boundary conditions. Initially, $N_0 = 25\,000$ spherical particles of radius $a = 1$ are randomly scattered in a cubic box of side L , avoiding particle overlap. The box side is fixed to $L = 1\,015$ in order to obtain a volume fraction of $\phi = 0.0001$. To the best of our knowledge, these are the most diluted simulations of BDLCA performed so far (see Table 6.1). In view of that, the system can safely be considered as representative of the ideal dilute regime. All particles are labelled with a property that we named *charge*. This property is allowed to have two possible values, $+1$ and -1 , that correspond to the two different species of particles in a BDLCA process. The relative concentration of minority particles, x (2.29), is an input value for the simulations.

All the particles and clusters are randomly moved with a size-dependent diffusion coefficient, D , that is related to the cluster radius of gyration R_g (2.37) through the Einstein-Stokes law (2.35), *i.e.*, $D \propto R_g^{-1}$. D plays the same role than the “mobility” introduced by Meakin and Djordjević, although it has physically meaningful units. The BDLCA contact rules, described above, are imposed at the particle-particle contact. In order to save computer time, a cell model has been used. As stated before, the simulations do not account for possible rotation of the clusters. Several snapshots of a simulated BDLCA process with $x = 0.5$ are plotted in Fig. 3.15. The particle volume fraction in the simulations performed in this work is the same as in the figure, although in this demonstrative case only 200 particles were used. For snapshots of BDLCA simulations with 25 000 particles, see Fig. 6.1.

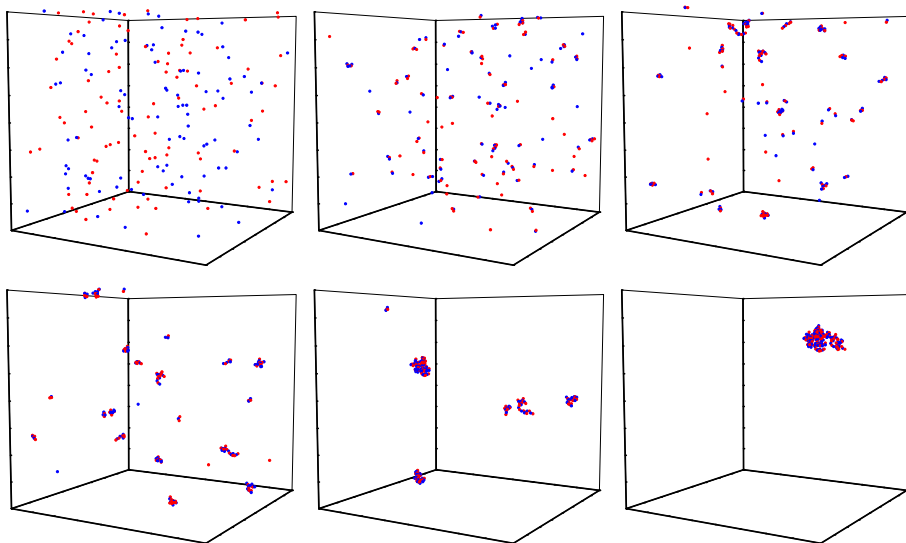


Figure 3.15.: Snapshots of a simulated BDLCA process at different times. Blue and red dots represent majority and minority particles, respectively.

3.4.2. Brownian dynamics simulations with interactions

When the particle-particle interaction range is not negligible, the “contact rules” *Ansatz* is not defensible any more and full particle-particle interaction must be taken into account in the BDS. Here, we make use of the approaching developed by Puertas *et al.* (1999a).

Simulation overview

The Brownian dynamics simulation (BDS) is based on a mesoscopic description of the particle motion, where the surrounding fluid is treated as a continuous medium. The motion of a Brownian particle is described by the so-called Langevin equation.

$$m\ddot{\vec{r}} = -\gamma\dot{\vec{r}} + \vec{f} + \vec{F}(\vec{r}, t) \quad (3.20)$$

This equation indicates that the displacement $\vec{r}(t)$ of a colloidal particle of mass m is governed by three forces: the friction force due to the viscosity γ of the fluid; a force \vec{f} that fluctuates randomly in time but with zero mean, $\langle \vec{f}(t) \rangle = 0$; and the resulting force due to external potentials like the gravity, $\vec{F}(\vec{r}, t)$. The friction coefficient for a sphere is given by $\gamma = 6\pi\eta a$, where η is the medium viscosity and a the particle radius. The fluctuating force is a Gaussian distributed white noise that can be related to the viscosity of the fluid by the fluctuation-dissipation theorem:

$$\langle \vec{f}(t) \cdot \vec{f}(t') \rangle = 6k_B T \gamma \delta(t - t') \quad (3.21)$$

Due to the presence of the fluctuating force, the particle motion is described by a Probability Density Function (PDF) rather than a deterministic trajectory. Given the initial conditions \vec{r}_0 and $\vec{p}_0 = m\vec{v}_0$ at $t = t_0$, the PDF is (for a derivation of this result, see Sec. 2.2 of the classical paper of Chandrasekhar, 1943):

$$\vec{P}(\vec{r}, t) = \frac{1}{(4\pi D_0 \Delta t)^{3/2}} \exp\left(-\frac{|\vec{r} - \vec{r}_0 - \vec{p}_0/\gamma - \vec{F}/\gamma \Delta t|^2}{4D_0 \Delta t}\right) \quad (3.22)$$

where $D_0 = k_B T/\gamma$ is the self-diffusion coefficient of the particle (2.36). If the time difference, $\delta t = t - t_0$, is much larger than the damping time $m/\gamma \approx 10^{-9}$ s, the inertial term \vec{p}_0/γ can be neglected, and the resulting PDF is said to be in the diffusive time scale (Puertas *et al.*, 2001b).

Every simulation time step, each aggregate is moved according to its PDF calculated by (3.22) in the diffusive time scale. The particle-particle interactions are introduced in the “external force term”, $\vec{F}(\vec{r}, t)$. Aggregates are moved as a whole, so possible rotations are not taken into account.

Simulation details

The simulations are three-dimensional off-lattice Brownian dynamics simulations with periodic boundary conditions. Initially, $N_0 = 21\,952$ spherical particles of radius $a = 100$ nm are randomly scattered in a cubic box. The particle

3. MATERIALS AND METHODS

volume fraction is fixed to $\phi = 0.01$, diluted enough to avoid three body interactions (Puertas *et al.*, 1999a). Time step is 10^{-4} s, clearly larger than the dumping time. Medium properties are equalled to those of pure water. Two species of particles are present, differing on the sign of their surface charge. Two contributions to the particle-particle interaction are considered: London-van der Waals dispersion (2.54) and double layer potential, with the linear superposition approximation (2.62). For more details about these interactions, please see Sec. 2.3.1). Physically reasonable values are used for the different parameters: $A = 10^{-21}$ J, $\psi_1^* = -\psi_2^* = 50$ mV. The inverse Debye length, κ , and the relative concentration of both species, x , are input parameters for the simulations.

3.4.3. Solving the Smoluchowski's equations

To obtain the theoretically predicted cluster-size distributions, the master equation has to be solved using the corresponding aggregation *kernel*. For this purpose, the equivalent “stochastic simulation” approach is employed (Odriozola *et al.*, 2003). This procedure involves the calculation of the reaction probability density function, which for pure aggregation processes may be denoted by $P_R(\tau, i, j)$. Here, $P_R(\tau, i, j)d\tau$ is the probability that, given the state \vec{N} at time t , the next reaction to take place in the volume V will be the aggregation of an i -mer with a j -mer and that this reaction will occur during the infinitesimal time interval $[t + \tau, t + \tau + d\tau]$. Hence, it is convenient to define $a_{ij}dt$ as the probability that, given the system in the state \vec{N} at time t , an i -mer- j -mer aggregation reaction will occur inside V during $[t, t + dt]$. According to Gillespie (1977), a_{ij} becomes

$$a_{ij} = k_{ij} \frac{N_i(N_j - \delta_i^j)}{V(1 + \delta_i^j)} \quad (3.23)$$

and the reaction probability density function:

$$P_R(\tau, i, j) = a_{ij}e^{-a_0\tau} \quad (3.24)$$

where

$$a_0 = \frac{1}{2} \sum_{i,j}^{N_0} a_{ij}(1 + \delta_i^j) \quad (3.25)$$

Odriozola *et al.* (2003) implemented an algorithm based on the above expressions for calculating the cluster-size distribution. It may be summarized as follows:

1. Input k_{ij} and initial conditions $\vec{N}(t = 0)$; set $t = 0$.
2. Calculate all a_{ij} and a_0 .
3. Generate the random numbers ξ_1 and ξ_2 uniformly distributed in $[0, 1]$.
4. Increment t the amount $\tau = a_0^{-1} \ln \xi_1^{-1}$.
5. Take the smallest pair (i, j) that verifies $\frac{1}{2} \sum_{m,l}^{i,j} a_{ml}(1 + \delta_m^l) > \xi_2 a_0$. Hence, the pairs of i and j cluster-sizes that have a larger a_{ij} have a higher probability to be chosen.
6. Increment N_{i+j} one unit and decrement N_i and N_j one unit, too. Go back to point 2 for recalculating a_{ij} and a_0 . Continue with the procedure.

The procedure is finished when the system is composed by only one cluster, *i.e.*, $a_0 = 0$. It should be noted that it is enough to recalculate a_{ij} only for those cluster-sizes that have changed their population. Further details about the algorithm can be found in the work by Gillespie (1977). This algorithm have been extended to deal also with reversible aggregation (Odriozola *et al.*, 2003), although this feature have not been used in this work.

In Fig. 2.1, the stochastic master equation is solved for the classical *kernels*—constant, sum and product— by using the algorithm described above, with $N_0 = 100\,000$. The computing time was about one minute in a regular personal computer. In the same figure are plotted the exact solutions of these *kernels*. As can be appreciated, the agreement is excellent.

4. SYMMETRIC HETEROAGGREGATION: AGGREGATION RATE

Both this and the next chapter deal with electrostatic heteroaggregation processes arising in symmetric two-component systems, *i.e.*, those with the same concentration of cationic and anionic particles. Here, we focus on the short time kinetics, especially on the dependence of the aggregation rate constants on the electrolyte concentration of the dispersion medium. Chapter 5, on the other hand, deals with phenomena found at longer times.

In Sec. 4.1, an experimental study on the dependence of heteroaggregation rate constants on the electrolyte concentration is presented. It covers an electrolyte concentration ranging from 1 M to just a few μM . The experimental results are compared with Brownian dynamics simulations and with the theoretical predictions that will be described in Sec. 4.2. The conclusions are summarised in Sec. 4.3.

4.1. Experimental aggregation rate constants

The heteroaggregation processes arising in aqueous suspensions of colloidal particles with opposite charge have been monitored experimentally by means of static and dynamic light-scattering (Ryde and Matijević, 1994; Maroto and de las Nieves, 1998; Yu and Borkovec, 2002; Puertas *et al.*, 2003; Galleto *et al.*, 2005a), multiple-angle light-scattering (Yu *et al.*, 2002; Galleto *et al.*, 2005a; Galleto *et al.*, 2005b) and —as a part of this PhD thesis— by single-cluster

4. AGGREGATION RATE

Table 4.1.: Experimental values of the absolute heteroaggregation rate constant obtained by different authors, using different techniques: turbidity, static light-scattering (SLS), dynamic light-scattering (DLS), multiangle static light-scattering (MSLS), multiangle dynamic light-scattering (MDLS), simultaneous static and dynamic light-scattering (SSDLS) and single-cluster light-scattering (SCLS). When an interval is given, it refers to k_{AB} measured at high and low electrolyte concentrations.

work	k_{AB} ($10^{-18} \text{ m}^3\text{s}^{-1}$)	technique(s)
Ryde and Matijević (1994)	3.2 – 4.9	DLS
Maroto and de las Nieves (1998)	5.3 ± 0.3	turbidity
Yu and Borkovec (2002)	5.42	SLS and DLS
Yu <i>et al.</i> (2002)	5.28 – 6.71	MSLS and MDLS
Puertas <i>et al.</i> (2003)	3.5 – 12	DLS
López-López <i>et al.</i> (2004a)	4.3 – 16	SCLS
Galleto <i>et al.</i> (2005a)	6.1 – 6.9	SLS, DLS and SSDLS
Galleto <i>et al.</i> (2005b)	5.3 – 6.0	SSDLS
Lin <i>et al.</i> (2006)	3.3 – 8.7	SSDLS

light-scattering (López-López *et al.*, 2004a). While all these techniques can be used to obtain aggregation rate constants, only SCLS provides additional information about the detailed cluster-size distribution. Tab. 4.1 shows the values measured by different authors for the absolute dimer formation rate constant, k_{AB} , in heteroaggregation processes with a similar concentration of oppositely charged particles at low ionic strength. Since k_{AB} is a very sensitive function of the ionic strength of the liquid medium, the relatively large dispersion of the values shown in Tab. 4.1 should be considered as normal. Puertas *et al.* (2003), for instance, measured a k_{AB} value that increases monotonously from $3.5 \times 10^{-12} \text{ cm}^3\text{s}^{-1}$ to $12 \times 10^{-12} \text{ cm}^3\text{s}^{-1}$ when the NaCl concentration decreases from 300 mM to 2 mM.

As was discussed previously in Sec. 2.1.5, we have to distinguish between effective and absolute aggregation rate constants. Absolute dimer formation rate

constants are genuine constants that correspond to concrete reactions. Thus, k_{AB} is the aggregation rate constant corresponding to the reaction between two unlike monomers, while k_{AA} and k_{BB} are the aggregation rate constants corresponding to the reactions between two like monomers. On the other hand, the effective aggregation rate constant, k_S , is somehow an average of the different reaction rate constants, where the monomer-monomer reaction prevail. At short times, k_S can be identified with the effective monomer-monomer reaction rate constant predicted by the HHF theory to be (2.34):

$$k_{11}^{\text{HHF}} = x^2 k_{AA} + (1-x)^2 k_{BB} + 2x(1-x)k_{AB} \quad (4.1)$$

Generally speaking, at high electrolyte concentrations both homo- and heteroaggregation take place simultaneously, while at low electrolyte concentration only heteroaggregation occurs (“selective heteroaggregation”). In the former case, the three different absolute dimer formation rate constants have to be considered. Then, two approaches are possible: i) homoaggregation rate constants k_{AA} and k_{BB} are measured in separate homoaggregation experiments at the same electrolyte concentration (Puertas *et al.*, 2003) and ii) the three absolute dimer formation rate constants are measured simultaneously (Yu and Borkovec, 2002; Galletto *et al.*, 2005a). Nevertheless, the latter method is only suitable for using multiple light-scattering and particles that differ in size by more than 10% (Yu and Borkovec, 2002). Hence, when selective heteroaggregation is not guaranteed, homo- and heteroaggregation rate constants have to be determined by separate experiments. We have divided the discussion about our experimental results according to electrolyte concentration intervals.

4.1.1. High electrolyte concentrations

In this section, we focus on electrostatic heteroaggregation arising at very high electrolyte concentrations, well above the critical coagulation concentrations of the reactants. In this case, the electric double layers (ELD) are highly compressed around the particles and so, the interaction due to EDL overlapping is energetically negligible with respect to the van der Waals interaction. In

4. AGGREGATION RATE

other words, not only repulsive interactions between like particles, but also attractive interactions between unlike particles are completely shielded. Hence, both homo- and hetero-aggregation processes are expected to be limited only by the diffusivity of the particles. Therefore, the corresponding aggregation regime should be DLCA.

Puertas, Maroto, Fernández-Barbero and de las Nieves used spectrophotometry (1999*b*) and light-scattering (1999*c*) to measure the effective aggregation rate constant k_S for heteroaggregation processes as a function of the electrolyte concentration. When the electrolyte concentration was higher than the CCCs of the reactants, these authors found that k_S takes similar values for homo- and heteroaggregation experiments. Moreover, if the stability of both species is significantly different, then k_S in heteroaggregation experiments takes diffusion-like values at electrolyte concentrations above the CCC of the less charged component (Puertas *et al.*, 2003).

The same authors have used BDS (Brownian dynamics simulations, please see Sec. 3.4.2 for details) to check that HHF-like interactions lead to diffusive aggregation at high electrolyte concentrations (Puertas *et al.*, 1999*b*; Puertas *et al.*, 1999*c*). More recently, Puertas *et al.* (2002) showed that not only the aggregation rate constants, but also the whole aggregation behaviour, are very similar in simulated heteroaggregation processes at high electrolyte concentration and in diffusion-limited homoaggregation.

Yu and Borkovec (2002) used a novel multiangle static and dynamic light-scattering technique to measure the homoaggregation rate constants (k_{AA} , k_{BB}) and the absolute heteroaggregation rate constant (k_{AB}) in heteroaggregation experiments. They found that the three involved rate constants were similar at high electrolyte concentrations. The small deviations they found may be due to the different particle sizes (67 nm for their cationic latex and 84 nm for their anionic latex).

In this work, we measured the effective aggregation rate constant k_S for heteroaggregation processes at high electrolyte concentration and compare it with the k_S obtained for homoaggregation processes at the same electrolyte concentration. In all the experiments of this section, k_S was determined from the monomer concentration fitting a straight line to onset of the $g(t)$ function (3.12). This procedure can be used to obtain both k_S and c_0 . Nevertheless, we preferred to fix

4.1. Experimental aggregation rate constants

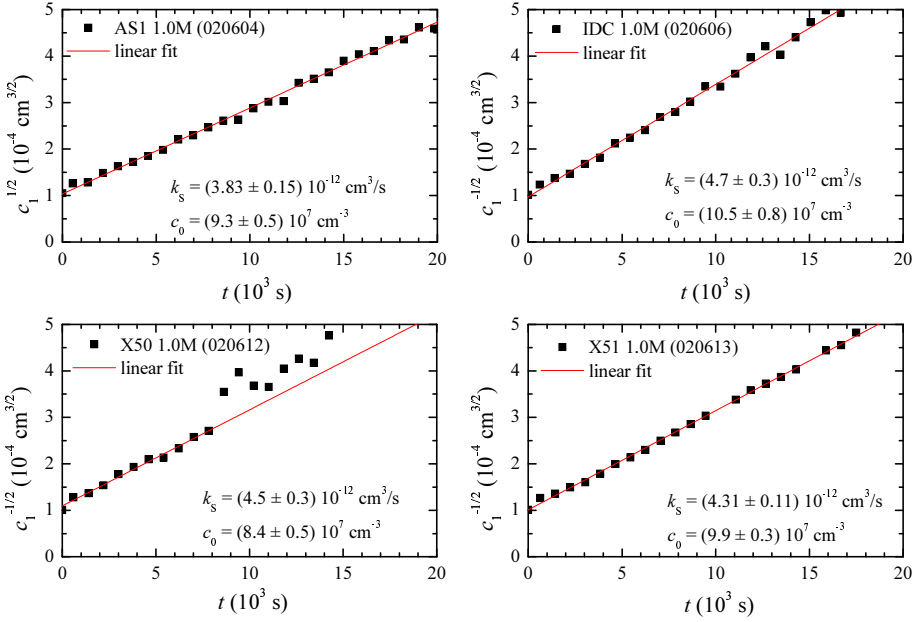


Figure 4.1.: The effective aggregation rate constants for homo- and hetero-aggregation experiments at 1.0 M KBr: anionic latex (top left), cationic latex (top right) and two 50/50 mixtures of both of them (bottom). In all cases, the inverse of the square root of the measured monomer concentration (squares) and the corresponding linear fits (solid lines) are shown.

c_0 to the value obtained in a previous SCLS measurement of the stable systems (please see Sec. 3.1.3), and to fit only k_S . In this manner, the accuracy is improved, since the relative uncertainty of a linear fitting is generally smaller for the slope than for the intercept at the origin.

The experimental data and the corresponding linear fits are plotted in Fig. 4.1 for four different experiments at high electrolyte concentration ($[\text{KBr}] = 1.0 \text{ M}$): AS1 homoaggregation, IDC homoaggregation and two heteroaggregation processes of mixtures thereof at $x \approx 1/2$. In all cases, k_S takes values that are

4. AGGREGATION RATE

well comprised within the interval of $(6\pm 3) 10^{-12} \text{ cm}^3 \text{ s}^{-1}$ given by Sonntag and Strenge (1987) as average value for a large number of experimental DLCA measurements. The values are also similar to those obtained by Puertas *et al.* (1999c) and by Yu and Borkovec (2002).

Several remarks should be made about the method used to obtain k_S :

1. The error intervals correspond only to the standard 95% confidence intervals of the linear fits. Nevertheless, the actual errors could be larger since all concentrations are affected by the uncertainty of the flow factor f_{flow} . Hence, we consider that it is convenient to enlarge these error intervals to, at least, a safe 10%. This correction is made in subsequent occurrences of k_S values, as for example those listed in Tab. 4.2. Strictly speaking, also the data points are affected by the f_{flow} uncertainty, although the error bars are not plotted for the sake of the clarity.
2. As stated in Sec. 3.1.3, only the onset of the $g(t)$ function is used for the fits. More precisely, in Fig. 4.1 —and in most of the linear fittings of this work— only the first 10 data points were used. Please notice that in three of the four plots shown in Fig. 4.1, the straight line fits at least twice the number of data points than those used in the fitting procedure. In fact, this demonstrates that the approximation (3.11) is quite convenient in these cases. The remaining case (Fig. 4.1, bottom left) was badly affected by noise during the latter stages of aggregation, although it fortunately does not affect the data interval used by the fitting procedure.

In homoaggregation experiments, k_S can be safely identified with the absolute homoaggregation dimer formation rate constant (k_{AA} and k_{BB} for cationic and anionic latexes, respectively). For heteroaggregation experiments, k_S may be identified with the apparent dimer formation rate constant defined by the HHF approximation (4.1). Hence, the absolute heteroaggregation dimer formation rate constant, k_{AB} , can be inferred from the heteroaggregation experiments:

$$k_{AB} = \frac{k_S - x^2 k_{AA} - (1-x)^2 k_{BB}}{2x(1-x)} \quad (4.2)$$

All these aggregation rate constants — k_S , k_{AA} , k_{BB} , k_S^{HET} and k_{AB} — are listed in Tab. 4.2, for experiments performed at 1 M, as well as at other electrolyte

concentrations where homo- and heteroaggregation take place simultaneously. Note that there is a small difference in the values of the rapid homoaggregation rate constants, $(3.8 \pm 0.4) \times 10^{-12} \text{ cm}^3 \text{ s}^{-1}$ for the anionic particles and $(4.8 \pm 0.5) \times 10^{-12} \text{ cm}^3 \text{ s}^{-1}$ for the cationic particles. The absolute heteroaggregation constant takes an intermediate value: $k_{AB} = (4.3 \pm 1.3) \times 10^{-12} \text{ cm}^3 \text{ s}^{-1}$. Differences of the same magnitude were also found by Yu and Borkovec (2002) and by Puertas *et al.* (2003). The former attributed it to the size difference between the oppositely charged particles they used while the later suggested it to be due to small residual particle-particle interactions. Since, cationic and anionic particles are equally sized, probably our results are also due to some residual interactions among the anionic particles even above the CCC. Nevertheless, this interaction, if it existed, must be quite weak, since the difference between k_{AA} and k_{BB} is practically within the error intervals of these quantities.

4.1.2. Intermediate electrolyte concentrations

In this section, we focus on symmetric heteroaggregation arising at intermediate but still relatively high electrolyte concentrations (below the CCC of the reactants, but high enough to allow for simultaneous homoaggregation). The DLVO theory (Sec. 2.3.1) predicts the existence of a repulsive energy barrier at short particle-particle separations between like particles. Consequently, homoaggregation is possible, but not every encounter leads to a bond formation. On the other hand, the HHF theory (see Sec. 2.3.5) predicts that the interaction between unlike particles is attractive, but so short-ranged that it is not expected to increase the particle-particle encounter rate beyond the one due to Brownian diffusion.

The critical coagulation concentration separates fast and slow homoaggregation. This can be clearly appreciated in a nephelometry study (see Sec. 3.3.3 and Fig. 3.11) but also by means of SCLS. In Fig. 4.2, the effective dimer formation rate constant k_S is determined for both latexes at electrolyte concentrations around their CCCs. It shows that for AS1 latex at 500 mM—a KBr concentration above its CCC—the aggregation rate constant takes a value similar to the value it has at 1 M; but at 200 mM—below AS1's CCC—it takes a lower value. Analogously, the IDC latex aggregates in the fast regime at 200 mM—slightly above

4. AGGREGATION RATE

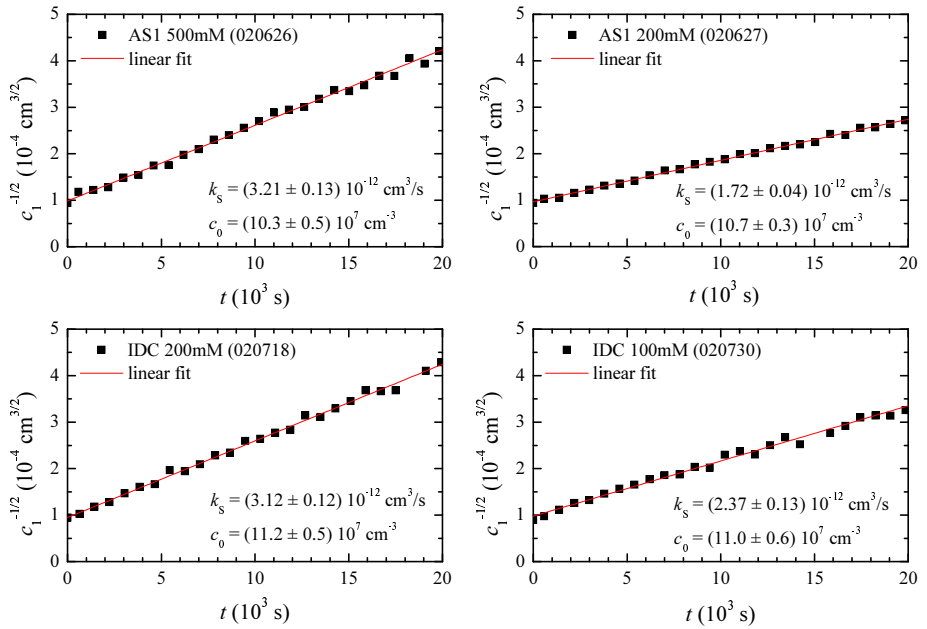


Figure 4.2.: Effective dimer formation rate constant for homoaggregation experiments at electrolyte concentrations around the CCC: above the CCC on the left side and below the CCC on the right side. The symbols have the same meaning as in Fig. 4.1.

4.1. Experimental aggregation rate constants

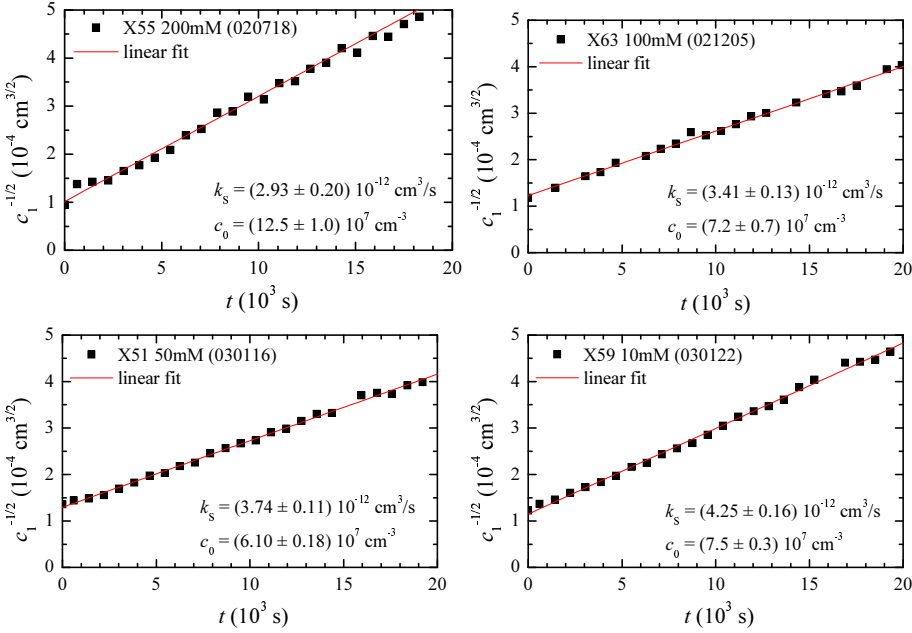


Figure 4.3.: Effective dimer formation rate constant for heteroaggregation experiments at intermediate electrolyte concentrations, ranging from 200 mM (top left) to 10 mM (bottom right). The symbols have the same meaning as in Fig. 4.1.

its CCC—, but aggregates slowly at 100 mM. The SCLS data, therefore, are fully compatible with the previous nephelometry study. Moreover, SCLS gives quantitative values for the (absolute) homoaggregation dimer formation rate constants k_{AA} and k_{BB} . On the other hand, the measuring process takes so much time that SCLS is not the best choice to obtain the CCCs of the systems.

Fig. 4.3 shows the aggregation rate constants at intermediate electrolyte concentrations, ranging from 200 mM to 10 mM, for heteroaggregation experiments at a relative concentration around $x = 0.5$. At 200 mM, the effective dimer formation rate constant has a value below the DLCA value. Then, it increases as the electrolyte concentration decreases, until it approaches again the diffusion limit

4. AGGREGATION RATE

Table 4.2.: Dimer formation rate constants obtained in homo- and hetero-aggregation experiments at several KBr concentrations: IDC and AS1 homoaggregation rate constants (k_{AA} and k_{BB} , respectively), and effective and absolute heteroaggregation rate constants (k_S and k_{AB} , respectively). The cases marked with the † symbol are those where SCLS data were not available and so, had to be estimated using nephelometry data. The aggregation rate constants are expressed in units of $10^{-12} \text{ cm}^3 \text{ s}^{-1}$.

[KBr] (mM)	Homoaggregation		Heteroaggregation		
	k_{AA}	k_{BB}	x_A	k_S	k_{AB}
1000	4.7 ± 0.5	3.8 ± 0.4	0.51	4.3 ± 0.4	4.3 ± 1.3
500	4.7 ± 0.5 †	3.2 ± 0.3	0.54	5.1 ± 0.5	6.1 ± 1.8
200	3.1 ± 0.3	1.72 ± 0.17	0.55	2.9 ± 0.3	3.3 ± 0.4
100	2.37 ± 0.24	0.17 ± 0.02 †	0.63	3.4 ± 0.3	5.2 ± 0.9
50	0.29 ± 0.05 †	negligible	0.51	3.7 ± 0.4	7.3 ± 0.8
10	negligible	negligible	0.59	4.3 ± 0.4	8.8 ± 0.8

value. We showed in Fig. 4.2 that at these electrolyte concentrations homoaggregation is partially impeded. In fact, homoaggregation at 50 mM (not shown in the figures) is so slow that SCLS is not adequate for monitoring it, neither for AS1 nor for IDC. Hence, at this electrolyte concentration, the dimer formation is mostly due to heteroaggregation. If we accept that the effective dimer formation rate constant k_S is the apparent dimer formation rate constant k_{11}^{HHF} of the HHF theory (2.34), then the absolute heteroaggregation rate constant k_{AB} is actually taking values above the diffusion limit already at 50 mM. This is shown in Tab. 4.2, where equation (4.2) was used to calculate k_{AB} .

It is worth noting that we measured a k_{AB} value slightly above the diffusion limit at 500 mM. Puertas *et al.* (2003) also reported a k_{AB} value above the diffusion limit when the electrolyte concentration was close to the CCC of the anionic system. They suggested that this anomaly was just a random fluctuation in the experiment. This may be also the reason for this discrepancy in our case, especially when we consider the large error interval. Nevertheless, since the same

4.1. Experimental aggregation rate constants

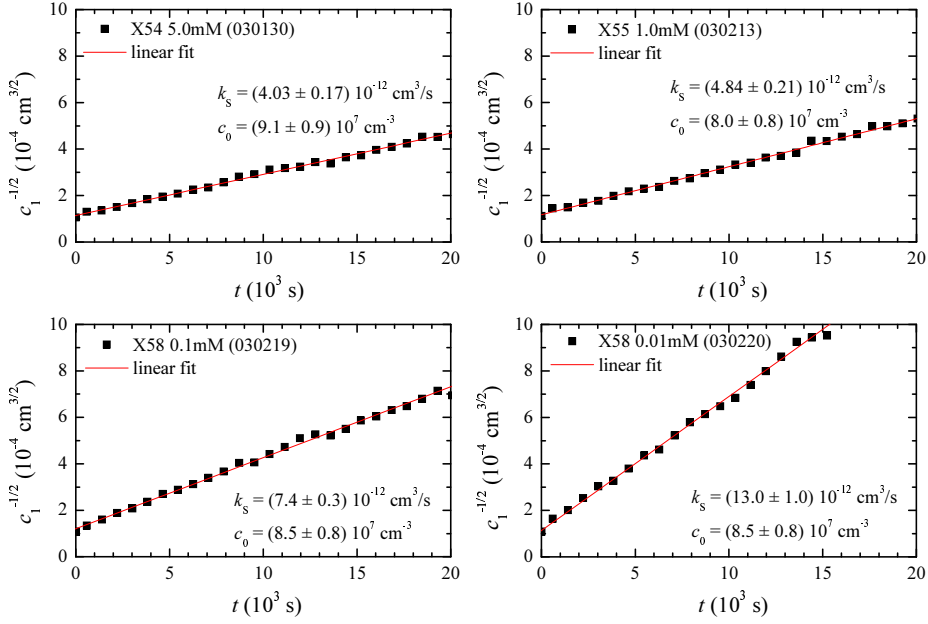


Figure 4.4.: Effective dimer formation rate constant for heteroaggregation experiments at low electrolyte concentrations, ranging from 5 mM (top left) to 0.01 mM (bottom right). The symbols have the same meaning as in Fig. 4.1.

features have been found in two very different studies —with different colloids and different techniques—, it cannot be completely disregarded that this increment in the aggregation rate is a real phenomenon.

4.1.3. Low electrolyte concentrations

In this section, we focus on selective electrostatic heteroaggregation processes, *i.e.*, heteroaggregation arising at electrolyte concentrations low enough to avoid any homoaggregation. The HHF theory predicts an attractive interaction between unlike particles whose range is increased as the electrolyte concentration

4. AGGREGATION RATE

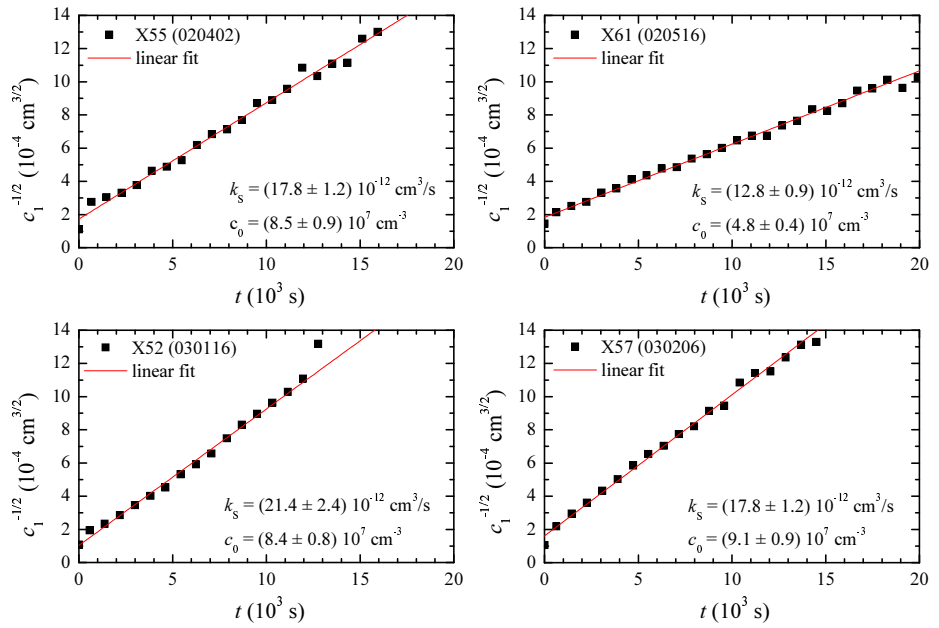


Figure 4.5.: Effective dimer formation rate constant for four heteroaggregation experiments with no added electrolyte. The symbols have the same meaning as in Fig. 4.1.

is decreased. This could lead to a particle-particle encounter rate larger than the one due only to Brownian diffusion. This is clear from the k_S values obtained in heteroaggregation experiments at low electrolyte concentrations (Fig. 4.4, please note that vertical scales are not the same as in previous figures). Moreover, the absolute heteroaggregation dimer formation rate constant, k_{AB} , takes values impressively large. These values were calculated assuming $k_S = k_{11}^{\text{HHF}}$, and are listed in Tab. 4.3. At 0.1 mM, k_{AB} is even larger than the theoretical encounter rate of a purely diffusive process without any hydrodynamic interactions (2.43). This reveals, without any reasonable doubt, the presence of long range attractive interactions between unlike particles.

Evidently, the smallest possible ionic concentration is achieved when no electrolyte is added. In this case, the ionic concentration is mainly due to the medium pH and to the counterions needed to balance the electric charge of the particles. If only these two contributions are taken into account, the overall ion concentration can be estimated to be smaller than 3 μM . Measurements with no added electrolyte, however, are highly sensible to small variations in pH and to the presence of impurities. For this reason, these measurements were repeated four times, all plotted in Fig. 4.5.¹ There, it is evident that the system is aggregating at a very high rate. Moreover, the absolute heteroaggregation rate constant k_{AB} reaches values above $30 \times 10^{-12} \text{ cm}^3 \text{ s}^{-1}$. We take the mean value of the four measurements as a representative value for k_{AB} at 3 μM :

$$\langle k_{AB} \rangle = (35 \pm 7) \times 10^{-12} \text{ cm}^3 \text{ s}^{-1}$$

To the best of our knowledge, this value is the largest rate constant ever measured for electrostatic heteroaggregation.

¹Please, note that in one case, the initial particle concentration c_0 was smaller than in the other cases.

4. AGGREGATION RATE

Table 4.3.: Effective and absolute dimer formation rate constants obtained in heteroaggregation experiments at low KBr concentrations where homoaggregation is absent. Here, “—” means that no KBr was added. KBr concentration and aggregation rate constants are given in units of mM and $10^{-12} \text{ cm}^3 \text{ s}^{-1}$, respectively.

[KBr]	x_A	k_S	k_{AB}
5.0	0.54	4.0 ± 0.4	8.1 ± 0.8
2.0	0.55	4.9 ± 0.5	9.9 ± 1.0
1.0	0.55	4.8 ± 0.5	9.8 ± 1.0
0.10	0.58	7.4 ± 0.7	15.2 ± 1.4
0.010	0.58	13.0 ± 1.3	27 ± 3
—	0.55	17.8 ± 1.2	36 ± 4
—	0.61	12.8 ± 1.2	27 ± 3
—	0.52	21.4 ± 2.2	43 ± 5
—	0.57	17.8 ± 1.2	36 ± 4

4.2. Comparison with Brownian dynamics simulations and theoretical predictions

In this section, we try to analyse and interpret the experimental results described in Sec. 4.1. Two approaches are followed: on the one hand, electrostatic heteroaggregation processes are simulated by means of Brownian dynamics simulations; on the other hand, the experimental aggregation rate constants are compared with those predicted by the HHF theory.

4.2.1. Brownian dynamics simulations

Brownian dynamics simulations (BDS) of electrostatic heteroaggregation processes were carried out in order to check whether the experimental features described in the previous section may derive solely from the particle-particle forces given by the HHF theory. A series of simulations was performed with different values for the adimensional Debye screening parameter κa (please see Sec. 2.3.5, especially Eqs. 2.57 and 2.62). The relative concentration of both components was always $x = 0.5$. The parameter κa is, basically, a measure of the particle-particle interaction range and reflects the electrical double layer thickness. Hence, varying κa is equivalent to changing the electrolyte concentration. In our simulations, κa ranges from 100 to 0.5, which is equivalent to an electrolyte concentration of 91 mM and just 2.2 μM , respectively.² Further details about these simulations can be found in Sec. 3.4.2, and in the work of Puertas *et al.* (1999a), who programmed the simulation source code.

The effective dimer formation rate constant, k_S , was calculated from the monomer concentration by following the procedure described in Sec. 3.1.3. Briefly, it consists in a linear fit of the onset of the $g(t)$ function (3.10). Then, k_S is obtained from the slope of the fitted straight line. The $g(t)$ functions and the corresponding linear fits are plotted in Fig. 4.6. The obtained k_S values are listed in Tab. 4.4. Only the first fifty data points were used in the fitting procedure (corresponding

²These values correspond to concentrations of a 1:1 electrolyte for a particle radius of $a = 100$ nm. Please note that the particle radius in the SCLS experiments was quite larger.

4. AGGREGATION RATE

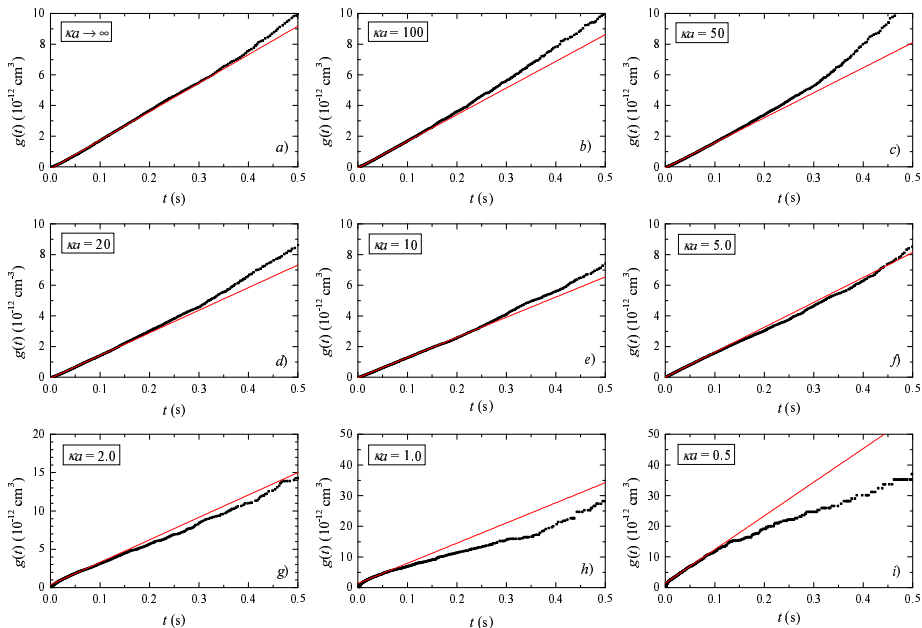


Figure 4.6.: Determination of k_S from simulated electrostatic heteroaggregation processes at different κa values. Here, “ $\kappa a \rightarrow \infty$ ” means that no particle-particle interactions were included (pure diffusion-limited homoaggregation). Please note the change of the vertical scale among the plots.

to approximately the first 0.1 s). Note that this value is smaller than 1/7 of the DLCA aggregation time $t_{\text{aggr}}^{\text{DLCA}}$ (2.10).

In general, the linear fits of the $g(t)$ function are quite good and only relatively small deviations are observed at long times (see Fig. 4.6a–g). Nevertheless, for very small κa values, where long-range particle-particle interactions are present, the deviations become larger (see Fig. 4.6h and, especially, Fig. 4.6i). This is mainly due to the important increase in the aggregation rate. According to equation (2.10), this leads to a shorter aggregation time t_{aggr} . Consequently, the data interval used for the fitting procedure includes points corresponding to later ag-

Table 4.4.: k_S values obtained in symmetric electrostatic heteroaggregation simulations at different κa . The aggregation rate constants are expressed in units of $10^{-12} \text{ cm}^3 \text{ s}^{-1}$.

κa	k_S
∞	18.62 ± 0.08
100	17.01 ± 0.07
50	16.32 ± 0.06
20	14.75 ± 0.05
10	13.15 ± 0.02
5.0	16.25 ± 0.03
2.0	29.28 ± 0.24
1.0	65.7 ± 0.5
0.5	109.8 ± 0.5

gregation stages, where the differences between the actual aggregation *kernel* and the constant aggregation *kernel* become more relevant. More quantitatively, the data interval used for the fit at $\kappa a = 0.5$ could be as large as $0.6 t_{\text{aggr}}$, while it is less than $0.14 t_{\text{aggr}}$ at $\kappa a = 100$.

The k_S values obtained are listed in Tab. 4.4 and plotted in Fig. 4.7. According to the table, the effective dimer formation rate constant at high κa (short particle-particle interaction distance) has the same values as for an ideal homoaggregation DLCA process. This is exactly what was found in the experiments. It can be understood as a consequence of the high degree of electrostatic screening, *i.e.*, the attractive (between unlike particles) and repulsive (between like particles) interactions are so short-ranged that the system behaves as a one-component system undergoing diffusion-limited aggregation. The absolute value of k_S , however, are quite larger than the experimental ones. This may be due to several factors, especially hydrodynamic interactions that have not been taken into account and to the fact that the system is not diluted enough to completely avoid three-body interactions.

As expected, k_S takes values close to the diffusion limit until homoaggregation

4. AGGREGATION RATE

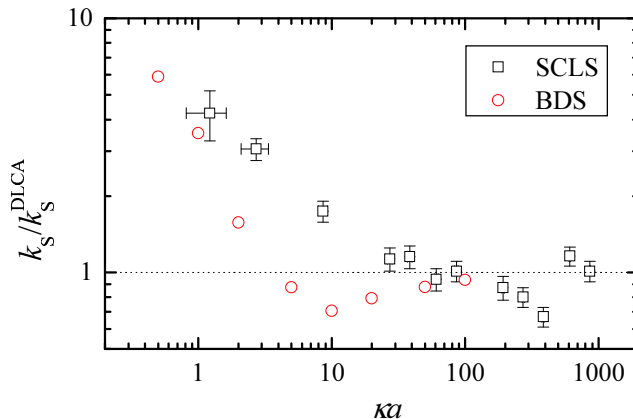


Figure 4.7.: The effective dimer formation rate constant, normalised by its rapid homoaggregation value, as a function of the κa parameter. The values obtained from single-cluster light-scattering experiments (\square) and Brownian dynamics simulations (\circ) are shown.

becomes completely forbidden. Then, k_S shows values smaller than the diffusion limit. In the BDS, this happens for $\kappa a \lesssim 20$. Hence, BDS support that the smaller k_S values obtained for electrolyte concentrations just below the CCC of the two components is a direct consequence of the decreasing homoaggregation rates. In the simulations, however, this effect is found at smaller κa values than in experiments, *i.e.*, at $5 \lesssim \kappa a \lesssim 20$ for simulations, and $100 \lesssim \kappa a \lesssim 400$ for the experiments. Puertas *et al.* (1999b) found the same discrepancy between simulations and experiments and attributed it to the fact that the interaction parameters (particle radius, surface potentials,...) in their simulations were fixed at arbitrary values. This seems to be the explanation also here, especially if one takes into account that the Brownian simulations performed here and in the work of Puertas *et al.* (1999b) are, in fact, the same.

At lower κa values, the aggregation rate increases substantially and k_S surpasses by far the diffusion limit. Hence, Brownian dynamic simulations explain the large k_S values found in experiments at low electrolyte concentrations. In Fig. 4.7, the k_S values determined from our experimental data and obtained by sim-

ulations, are plotted together. There, we can appreciate that the strong increase in the aggregation rate at low κa values is qualitatively similar in both cases. A quantitative agreement, however, is not achieved because there seems to be a shift in the κa range where this effect occurs.

It should be mentioned that the experimental k_S values show a short plateau at κa values close to 50. Here, selective heteroaggregation is taking place but the effective dimer formation rate takes diffusive values. This plateau is, however, not reproduced by the simulations. We only can guess about the reason of this discrepancy. It could be due, for instance, to a particle size effect. The κa parameter was introduced in order to normalise the particle-particle interactions due to the electric double layer overlapping. The van der Waals interactions, on contrast, have not been normalised. It could be possible that the interplay between van der Waals interactions and EDL overlapping interactions is not completely described when only one of these interactions —*i.e.*, the EDL overlapping— is normalised. Also the hydrodynamic effects, that are not included in BDS, could be responsible in some extent for this discrepancy. Anyhow, further work is necessary in order to clarify this point.

4.2.2. HHF theory

Hogg, Healy and Fuerstenau (1966) developed an extension to the DLVO theory which describes the aggregation processes of binary colloidal dispersions. It was discussed in Sec. 2.3.5. Only two kinds of particle-particle interactions are considered: van der Waals forces and electrostatic forces. The former are short-ranged and always attractive. The latter are repulsive between like particles and attractive between unlike particles and their interaction range depends on the electrolyte concentration of the suspension medium. In the same paper, Hogg *et al.* also derived an approximation for the time evolution of the monomer concentration at the early stages of the aggregation process (2.34). Basically, it consists in defining an effective dimer formation rate constant k^{HHF} that takes into account the contributions of the three possible monomer-monomer reactions: A - A , B - B and A - B . The absolute homoaggregation dimer formation rate constants, k_{AA} and k_{BB} , can be calculated using the Fuchs approach (2.50) and

4. AGGREGATION RATE

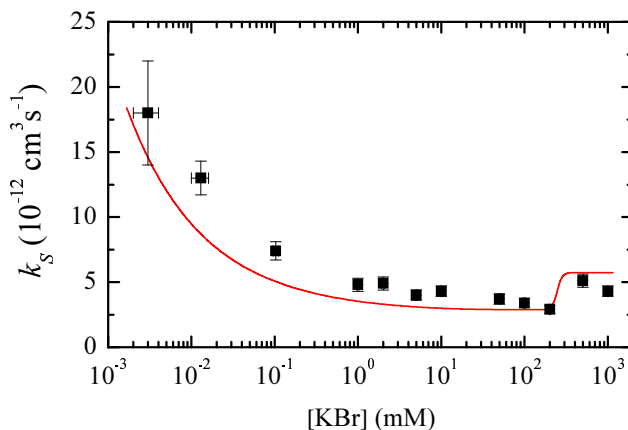


Figure 4.8.: Effective dimer formation rate constant for electrostatic heteroaggregation processes at different KBr concentrations: comparison between single-cluster light experiments (\square) and the predictions given by the HHF theory (solid line).

the classical DLVO expression for the particle-particle interactions. The absolute heteroaggregation dimer formation rate constant, k_{AB} , can also be calculated following the Fuchs approach (2.50), but now with the particle-particle interactions proposed by Hogg *et al.* (1966).

This calculation has been performed by using commercial software³ and reasonable values for the parameters: $A = 4.1 \times 10^{-21} \text{ J}$, $\psi_1^* = -\psi_2^* = 20 \text{ mV}$, $a = 260 \text{ nm}$, $T = 293 \text{ K}$ and, as dispersion medium, pure water at 20°C . In order to obtain realistic k values, the diffusion coefficients have been corrected according to (2.47), taking into account hydrodynamic effects (Spielman, 1970; Honig *et al.*, 1971). The calculated effective dimer formation rate constant k^{HHF} is plotted in Fig. 4.8. The measured k_S values are also plotted in the same figure. The qualitative agreement is evident. Starting from high electrolyte concentrations, diffusion limit values are obtained at high electrolyte concentrations (above the CCCs of the systems); then, a plateau where k_S takes smaller values than the

³*Mathematica 5.0*, by Wolfram Research, Inc.

Brownian aggregation rate; and finally, an important increase in the aggregation rate is observed. Here, k_S reaches values far above the diffusion limit. It is worth noting that in the latter region, small variations in the electrolyte concentration lead to large changes in k_S . This fact could explain the large dispersion of the k_S values listed in Tab 4.3 when no salt was added. The quantitative agreement is also quite satisfying, despite the fact that no fitting process has been carried out.⁴ The relatively small quantitative differences, however, can be summarised as follows: theoretical k_S values overestimate experimental ones in the high electrolyte concentration region, and underestimate them in the intermediate and low electrolyte concentration regions.

4.3. Concluding remarks

The effective dimer formation rate constant k_S has been measured for symmetric electrostatic heteroaggregation processes arising at different electrolyte concentrations. The study covers a wide electrolyte concentration range, from 1 M to only a few μM . k_S is assumed to be equal to the absolute dimer formation rate constant in homoaggregation experiments. In heteroaggregation experiments, k_S is assumed to be the apparent dimer formation rate constant defined by the HHF approximation. Therefore, absolute heteroaggregation rate constants have been determined, once homoaggregation rate constants k_{AA} and k_{BB} were measured in separate experiments. Depending on the electrolyte concentration, several regions can be distinguished:

- At high electrolyte concentrations ($\geq 500\text{mM}$), above the CCCs of the reactants, k_S is found to take diffusive values. Moreover, the three absolute dimer formation rate constants take similar values, close to $4 \times 10^{-12} \text{ cm}^3 \text{ s}^{-1}$.
- At intermediate electrolyte concentrations (50–200 mM), below the CCCs of the reactants, but still high enough to prevent long-range particle-particle

⁴The value of the Hamaker constant was taken from the literature for polystyrene-water-polystyrene systems (Kihira *et al.*, 1992). The effective surface potentials were chosen symmetrically, so that they give rise to CCC of about 300 mM, *i.e.*, the CCC of the anionic latex.

4. AGGREGATION RATE

interactions, k_S takes values that are smaller than the Brownian aggregation rate. This is due to the decreasing homoaggregation rate, while the absolute heteroaggregation rate constant keeps a diffusive value.

- At low electrolyte concentrations (1–10 mM), a plateau is found, where k_S takes again diffusive values. At these electrolyte concentrations selective heteroaggregation is taking place, *i.e.*, $k_{AA} + k_{BB} \lll k_S$. It implies that the absolute heteroaggregation rate constant k_{AB} is actually taking a value of about twice the diffusive one.
- At even lower electrolyte concentrations ($\lesssim 1$ mM), the attractive interactions between unlike particles become long-ranged and, consequently, k_S increases extraordinarily, to such an extent that $k_{AB} = (35 \pm 7) \times 10^{-12} \text{ cm}^3 \text{ s}^{-1}$ is obtained when no electrolyte is added. This is, to the best of our knowledge, the largest value ever measured.

Brownian dynamics simulations partially support our findings, in a sense that k_S is found to take: i) diffusive values at high electrolyte concentrations, ii) smaller values in an intermediate region and iii) values clearly above the diffusive one at low electrolyte concentrations. Nevertheless, two significant differences between experiments and simulations are found. On the one hand, there seems to be a shift in the κa values. It is reasonable to assume this fact to be due to the parameters that control the particle-particle interactions. They take arbitrary values, which are not expected to match with the experimental conditions. On the other hand, the plateau region at low electrolyte concentrations is not found in simulations. This could be a size effect. Nevertheless, more work is needed in order to clarify this point.

An excellent and even quantitative agreement, is found between the experimental k_S values and those obtained by the Fuchs approach, when the particle-particle interactions are calculated according to the DLVO and HHF theories. It is worth noting that no attempt of parameter fitting had to be carried out.

5. SYMMETRIC HETEROAGGREGATION: CLUSTER-SIZE DISTRIBUTIONS

This chapter represents a complement of the previous one. Here, symmetric electrostatic heteroaggregation is revisited, but now we focus on the long-time behaviour. More precisely, the cluster-size distributions of aggregating two-component colloidal dispersions are discussed.

In the literature about heteroaggregation, several experimental works are devoted to the study of aggregation rate constants (Ryde and Matijević, 1994; Maroto and de las Nieves, 1998; Yu and Borkovec, 2002; Yu *et al.*, 2002; Puertas *et al.*, 2003; Galleto *et al.*, 2005a; Galleto *et al.*, 2005b) or fractal dimensions (Rim *et al.*, 1992; Kim and Berg, 2000; Fernández-Barbero and Vincent, 2001; Puertas *et al.*, 2001b; Kim *et al.*, 2003). Nevertheless, no experimental studies about the cluster-size distributions (CSD) can be found in the literature, apart from those related with this PhD thesis (López-López *et al.*, 2004b; López-López *et al.*, 2006). The CSDs are discussed in Sec. 5.1. We show that the kinetic behaviour of a two-component colloidal dispersion is strongly affected by the electrolyte concentration of the dispersion medium.

In Sec. 5.2, experimental CSDs are compared with those obtained by means of Brownian dynamics simulations (BDS). Three different simulation schemes are used: i) BDS of ideal diffusion-limited cluster-cluster aggregation processes (DLCA), ii) BDS of ideal binary diffusion-limited cluster-cluster aggregation processes (BDLCA), and iii) BDS with particle-particle interactions. We show that each one is suitable to describe experimental results belonging to different electrolyte concentration regions.

Sec. 5.3 deals with a novel phenomenon found in electrostatic heteroaggregation at low and very low electrolyte concentrations: *cluster discrimination*. It was recently predicted by BDS (Puertas *et al.*, 2002), but the first experimental evidences have been found during this PhD research work (López-López *et al.*, 2004b).

In Sec. 5.4, the coagulation equations are solved for several theoretical *kernels* and solutions are compared with experimental CSDs. The section concludes with a summary of the different heteroaggregation regimes found in experiments and simulations.

5.1. Experimental cluster-size distributions

Single-cluster light-scattering (SCLS) has been successfully used by several authors to obtain cluster-size distributions in homoaggregation experiments (Pelsers *et al.*, 1990b; Broide and Cohen, 1990; Fernández-Barbero *et al.*, 1996; Schmitt *et al.*, 2000b; Odriozola *et al.*, 2004). Nevertheless, this is the first time that SCLS has been used to monitor the CSDs in heteroaggregation. This became possible because much care was taken in choosing two highly monodisperse systems with the same particle size (Sec. 3.3.2). A series of symmetric heteroaggregation experiments was carried out with KBr concentration ranging from 1 M to 10 μM . Additionally, several experiments without any added salt were also performed. In the latter cases, the overall electrolyte concentration is mainly due to the H^+ ions corresponding to a free $p\text{H}$ and, to less extent, to the intrinsic counterions of the colloidal particles. The overall electrolyte concentration with no added KBr is estimated to be less than 3 μM . Hence, in this study we have visited almost six orders of magnitude in the electrolyte concentration. The experimental CSDs are plotted in Figs. 5.1, 5.2 and 5.4. It should be recalled that i -mer curves in these plots comprise all possible types of clusters formed by i particles. For example, the trimer concentration curve $c_3(t)$ includes all possible types of trimers such as positive-negative-positive and negative-positive-negative trimers. This is due to the fact that equally sized monomeric particles have been used and so, all clusters formed by the same number of constituent particles scatter the same amount of light.

All studied aggregation processes shown in Figs. 5.1, 5.2 and 5.4 exhibit some common features:

1. Evidently, they start from monomeric initial conditions.
2. The monomer concentration decreases monotonically since monomers can not be created under the given experimental conditions.
3. Larger aggregates have to be formed before they can react with other clusters and so, the corresponding curves exhibit a maximum, *i.e.*, they are bell-shaped.
4. At long aggregation times, all curves show a decreasing tendency which means that no dynamic equilibrium is reached.¹ Consequently, the underlying aggregation mechanisms is of irreversible nature or at least the time scale of fragmentation is extremely large if compared with the experiment duration.
5. Since no precipitation was observed during the experiments, the always decreasing behaviour of the total cluster concentration curves implies that the average cluster-size keeps growing. This means that larger aggregates must be present although their size could not be resolved by the employed detection technique. From the overall concentration of clusters we can extract this average cluster-size.

Apart from this quite general common features, the CSDs present some important differences which are described in some detail in the following sections.

5.1.1. High electrolyte concentrations

Experimental CSDs for symmetric electrostatic heteroaggregation at high electrolyte concentrations, ranging from 1 M to 100 mM, are plotted in Fig. 5.1. The CSD for 1 M clearly exhibits the characteristics of a diffusion-limited process.

¹A nice example of a reversible homoaggregation experiment was found when IDC latex was aggregated by adding 0.6 M NaSCN (Fig. 3.13*d*).

5. CLUSTER-SIZE DISTRIBUTIONS

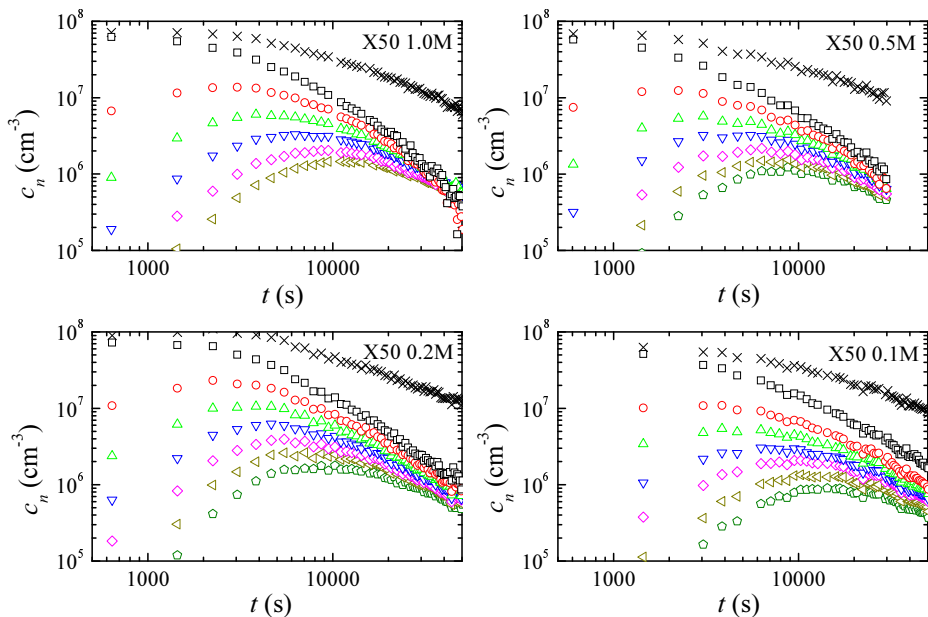


Figure 5.1.: Cluster-size distribution ($c_i(t)$, $i \leq 7$) for heteroaggregation experiments at high KBr concentrations: 1.0 M (top left), 500 mM (top right), 200 mM (bottom left) and 100 mM (bottom right). In each plot, the concentration of monomers (\square), dimers (\circ), trimers (\triangle), tetramers (∇), pentamers (\diamond), hexamers (\triangleleft) and heptamers (\triangleright) are shown as well as the total concentration of aggregates (\times).

This can be appreciated comparing this figure with homoaggregation experiments at high electrolyte concentration (Fig. 3.12) and with the solution of the Brownian *kernel* (Fig. 2.4 and what follows in Sec. 5.4.1).

The CSDs for 500 mM and 200 mM are also quite similar to those corresponding to diffusion-limited colloid aggregation processes.² It is important to put

²Unfortunately, the long-time data corresponding to the experiment at 500 mM was lost. Even so, it seems quite reasonable to assume that the aggregation behaviour here is somehow a mixture between those for 1 M and for 200 mM.

onto relief that the aggregation seems to be diffusion-limited at 200 mM, where the KBr concentration falls in the intermediate region between the CCC of both systems. This result is in good agreement with the work of Puertas *et al.* (2003). These authors found that the heteroaggregation rate constant have diffusive values when the electrolyte concentration is above the CCC of the less charged system. Hence, we can add now that, not only the aggregation rate constant have diffusive values, but the whole aggregation kinetics evolves in the same manner than a diffusion-limited process.

Below the CCCs of both latexes —at 100 mM, for instance— a different behaviour is observed. Now, the concentration curves are clearly different from those of a diffusion-limited process. They do not intersect at long times, and remain clearly separated. The CSD evolves here as in a homoaggregation process at an electrolyte concentration below the CCC. The reason for this is probably that homo- and heteroaggregation are taking place simultaneously but with different abilities. Evidently, every encounter between unlike particles leads still to bond formation, due to the opposite sign of the particle charge. When two like particles encounter each other, however, they have to overcome a repulsive energy barrier and hence, only a fraction of these encounters lead to bond formation. The aggregation rate data of Sec. 4.2 also support this explanation.

5.1.2. Intermediate electrolyte concentrations

According to the DLVO theory for one-component colloidal dispersions, the colloidal stability increases quite steeply once the salt concentration falls below the CCC. This was also experimentally found for the IDC and AS1 latexes in the nephelometry study (Fig. 3.11 and Tab. 4.2). At 50 mM KBr, for instance, the aggregation rate constant for the cationic latex is less than one tenth of its diffusive value, and for the anionic particles it is already negligible. At 10 mM, we can safely state that both systems are kinetically stable, in the time scale of the experiments. Hence, the CSDs plotted in Fig. 5.2 correspond to selective heteroaggregation processes where simultaneous homoaggregation is negligible.³

³With the exception, perhaps, of the experiment at 50 mM, where some homoaggregation of cationic particles could occur.

5. CLUSTER-SIZE DISTRIBUTIONS

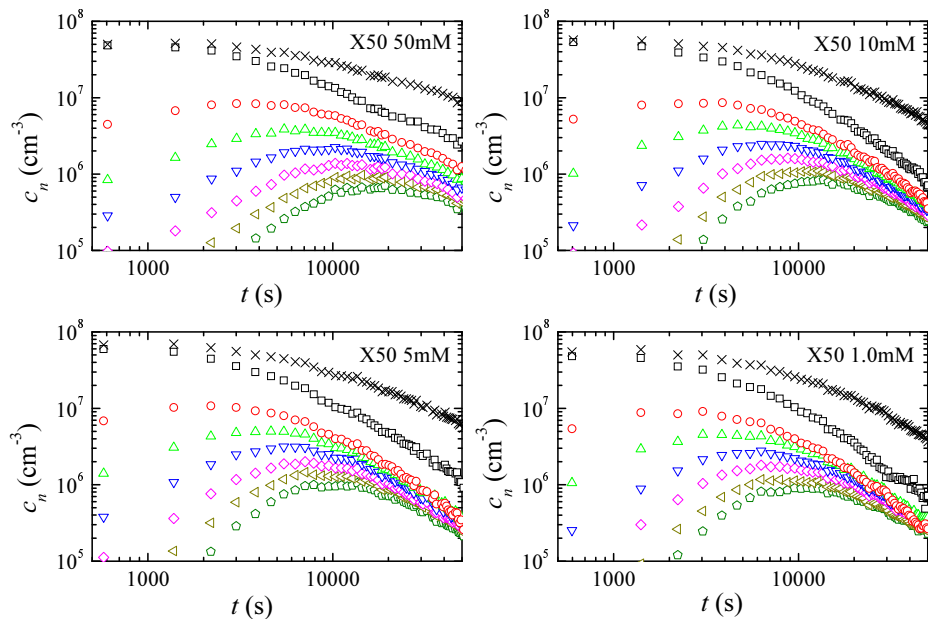


Figure 5.2.: Cluster-size distributions for heteroaggregation experiments at intermediate KBr concentrations: 50 mM (top left), 10 mM (top right), 5.0 mM (bottom left) and 1.0 mM (bottom right). The symbols have the same meaning as in Fig. 5.1.

The CSD for electrostatic heteroaggregation at 50 mM (Fig. 5.2a) is similar to the CSD at 100 mM (Fig. 5.1d). The others CSDs of Fig. 5.2, however, present some new features:

- Firstly, the overall aggregation rate increases again. This can be appreciated in the short and the long time behaviour. At short times, we measured the effective aggregation rate constant (Sec. 4.1) and checked that k_S indeed takes values similar to those of a rapid homoaggregation process (please compare Tabs. 4.2 and 4.3). At long times, the increase in the aggregation rate can be inferred from the time evolution of the average cluster-size $\langle n \rangle_n = c_0 / \sum_{i=1}^{\infty} c_i(t)$, shown in Fig. 5.3a. Since the initial par-

5.1. Experimental cluster-size distributions

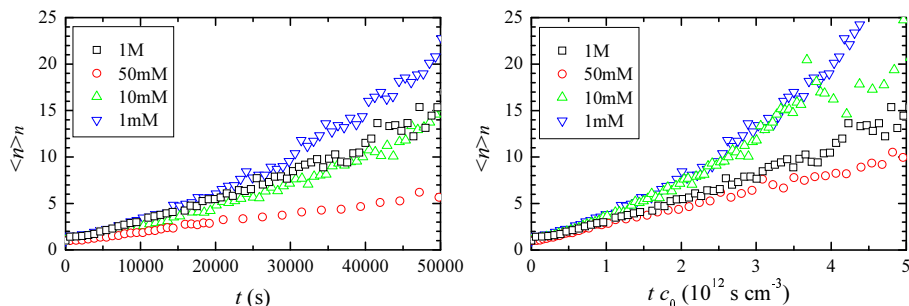


Figure 5.3.: Number-average cluster-size for electrostatic heteroaggregation experiments at different KBr concentrations: 1 M (\square), 50 mM (\circ), 10 mM (Δ) and 1 mM (∇). In the graph on the right side the time is normalised by multiplying it by the initial particle concentration, c_0 .

ticle concentration was not exactly the same in all the experiments, it is quite convenient to make use of a normalised time scale which takes into account the different c_0 values. In the dilute regime, the actual reaction rate is directly proportional to the concentration of particles. Therefore, the most natural time normalisation is, probably, $c_0 t$. In Fig. 5.3b, the average cluster-size is plotted versus this quantity. It is clear that the overall aggregation rate for 10 mM and 1 mM is faster than for 1 M whilst the aggregation rate for 50 mM is the slowest one.

- Secondly, the monomer concentration curves remain always above and quite separated from the other i -mer concentration curves. This means that the monomer behaviour differs quite strongly from the one of all the other aggregates. In this sense, some kind of “monomer discrimination” is detected here. We postpone the discussion of this interesting effect to Sec. 5.3.

5.1.3. Low and very low electrolyte concentrations

The electrostatic heteroaggregation processes at low and very low electrolyte concentrations show probably the most interesting features, since in this case, the particle-particle interactions become long-ranged. The CSD at 0.1 mM is still similar to the ones described before: increase in the overall aggregation rate and an excess of monomers are observed at long times. At even lower electrolyte concentrations, new effects can be observed. Since the strength of the attractive electrostatic interactions increases with decreasing electrolyte concentration, it is not surprising that the concentrations of all clusters decrease the faster the lower the electrolyte concentration becomes. This tendency, however, is most pronounced for dimers up to a point at which the dimer concentration curves at very low electrolyte concentration separate completely from all the other i -mer concentration curves (please see the CSDs plotted in Fig. 5.4). Hence, also “dimer discrimination” is now observed. Here again we postpone the discussion about cluster discrimination to Sec. 5.3. Nevertheless, we want to point out that this feature is quite reproducible even when no electrolyte was added. In fact, four different experiments⁴ are plotted in Fig. 5.4 and the rapid decrease in the dimer concentration is observed in all of them.

The aggregation rate is quite high in this regime at both short and long times. At short times, this can be deduced not only from the quite large k_S values measured (Tab. 4.3), but also from the i -mer concentration curves themselves. Probably the most clear prove for this hypothesis is found in the dimer concentration curve for experiments with no added salt. In all four cases aggregation was so fast that the dimer concentration maximum was reached at an aggregation time shorter than the first experimental point.

At long aggregation times, the increase in the aggregation rate at very low electrolyte concentration is better appreciated in the average cluster-size $\langle n \rangle_n$. This quantity is plotted in Fig. 5.5 for several low and very low electrolyte concentrations. The $\langle n \rangle_n$ curve for 1 M is also plotted in the figure for comparison

⁴And these four are indeed all the electrostatic heteroaggregation experiments without any added salt and $x \approx 0.5$ performed in this research work.

5.1. Experimental cluster-size distributions

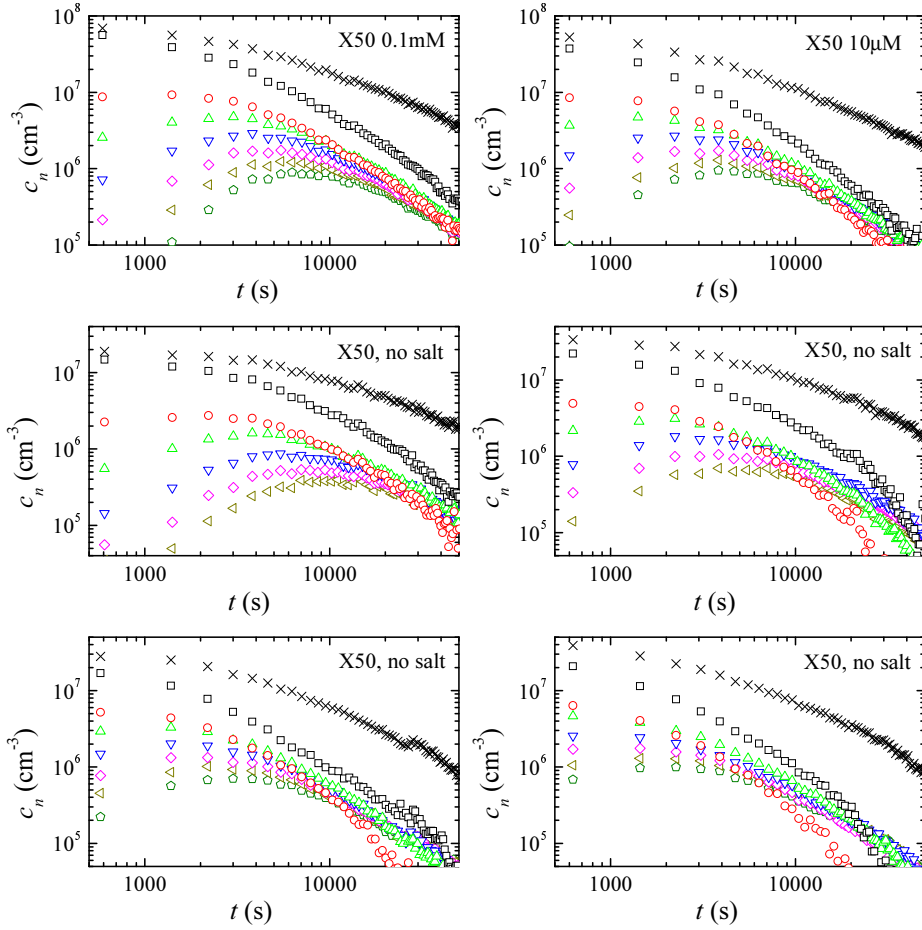


Figure 5.4.: Cluster-size distributions for heteroaggregation experiments at low KBr concentrations: 0.1 mM (top left), 0.01 mM (top right) and with no added KBr (middle and bottom rows). The symbols have the same meaning as in Fig. 5.1.

5. CLUSTER-SIZE DISTRIBUTIONS

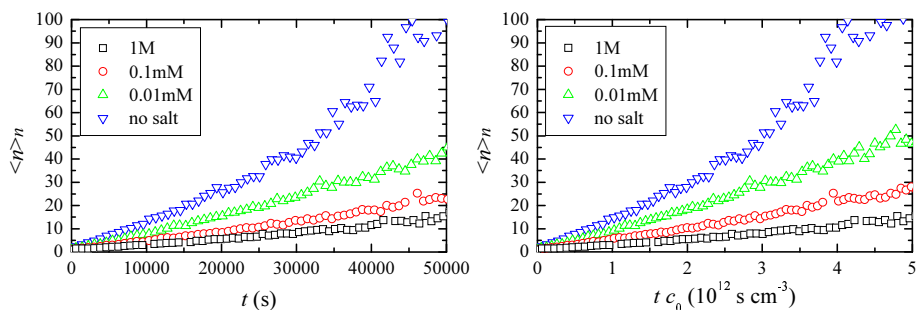


Figure 5.5.: Number-average cluster-size for electrostatic heteroaggregation experiments at different KBr concentrations: 1 M (\square), 0.1 mM (\circ), 0.01 mM (\triangle) and with no added KBr (∇). In the graph on the right side the time is normalised by multiplying it by the initial particle concentration, c_0 .

purposes. The average cluster-size grows faster for decreasing electrolyte concentrations and surpasses clearly the Brownian aggregation rate.

5.2. Brownian dynamics simulations

Brownian dynamics simulations (BDS) of heteroaggregation processes arising in symmetric mixtures of oppositely charged particles have been performed in order to explain the experimental results. Two different approaches have been used:

1. BDS with particle-particle interactions only at surface to surface contact. Hence, the particles and clusters diffuse in absence of interactions and, when they encounter each other, a bond is formed according to a given sticking probability. These BDSs are appropriate for reproducing aggregation processes when the range of the particle-particle interactions is very short compared with the particle size. The source code of these programmes was written by Dr. Arturo Moncho-Jordá (Universidad de Granada).

2. BDS with particle-particle interactions. Here, the particles and clusters are randomly moved according to the Langevin equation. Particle-particle interactions are directly included as the “external forces” term of this equation. These BDSs are suitable to simulate aggregation processes where the range of the particle-particle interactions is not negligible. The source code was written by Dr. Antonio Puertas (Universidad de Almería).

5.2.1. Brownian dynamics simulations without interactions

As stated before, in this BDS the effects of short-ranged particle-particle interactions are approximated by “sticking rules” at surface to surface contact (further details were given in Sec. 3.4.1). Two aggregation schemes have been considered. In the first scheme, all particles are identical and the only sticking rule is: an irreversible bond between two particles is formed after touching each other. This aggregation scheme correctly reproduces an ideal diffusion-limited cluster-cluster aggregation regime (DLCA) (Schmitt *et al.*, 2000b). In the second aggregation scheme, two species of particles are considered and two “sticking rules” control the bond formation: i) the contact between like particles never gives rise to bond formation and ii) the contact between unlike particles always form a bond. This scheme is known as binary diffusion-limited cluster-cluster aggregation (BDLCA) (AlSunaidi *et al.*, 2000).

The cluster-size distributions obtained for both aggregation schemes are plotted in Fig. 5.6. In order to be able to compare them with experimental CSDs, they have to be normalised. Hence, n -mer concentration curves are divided by the initial particle concentration $c_0 = N/V$, and time is divided by the aggregation time t_{aggr} (Eq. 2.10). For the latter normalisation, the dimer formation rate constant k_{11} was assumed to be equal to the effective aggregation rate constant k_S , which was calculated by fitting the onset of the $g(t)$ function as explained in Sec. 3.1.3.

DLCA

Fig. 5.6a shows the CSD simulated for an ideal DLCA process. It is quite similar to the experimental CSDs obtained at high electrolyte concentrations, for

5. CLUSTER-SIZE DISTRIBUTIONS

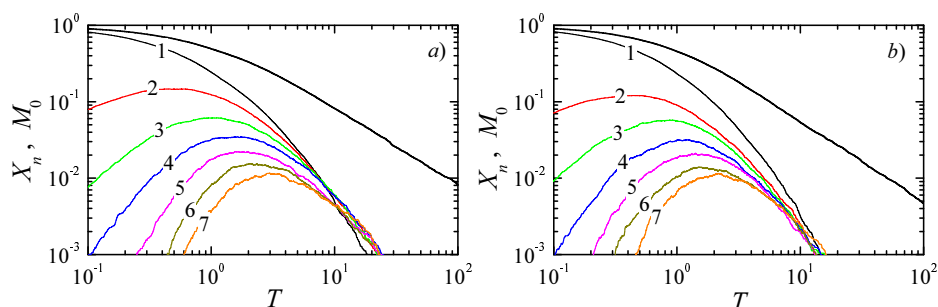


Figure 5.6.: Simulated cluster-size distributions up to heptamers (thin solid lines, the numbers indicate the number of constituent particles) and total number of aggregates (thick solid lines) for two ideal aggregation processes: a) DLCA and b) BDLCA with $x = 0.5$.

both homoaggregation (Fig. 3.12a–b) and electrostatic heteroaggregation (Fig. 5.1a). In order to make quantitative comparisons, dimensionless CSDs have to be used. Hence, the experimental data have been normalised by dividing $c_n(t)$ by the initial concentration of particles c_0 . The latter was obtained from the “zero time measurements” performed before the mixing procedure (Sec. 3.1.3). Time normalisation has been carried out, by dividing the real time by the aggregation. Therefore, the monomer-monomer reaction rate constant k_{11} was considered to be equal to the effective aggregation rate constant k_5 that has been measured in Sec. 4.1. In Fig 5.7a, the simulated CSD for an ideal DLCA process and the experimental CSD obtained in electrostatic heteroaggregation at 1 M are plotted together.⁵ As can be seen, the agreement is excellent.

It is well known that homoaggregation at high electrolyte concentrations follows a diffusion-limited aggregation scheme (see, *e.g.*, Hunter, 1987). It was, however, just a hypothesis that also electrostatic heteroaggregation at high electrolyte concentration can be described by a DLCA scheme. Both, theory (Ryde and Matijević, 1994) and simulations (Puertas *et al.*, 2002) support this hypothesis, but this is the first time —to the best of our knowledge— that it has been demonstrated by experiments.

⁵Hence, in this figure are plotted together the data of Figs. 5.1a and 5.6a.

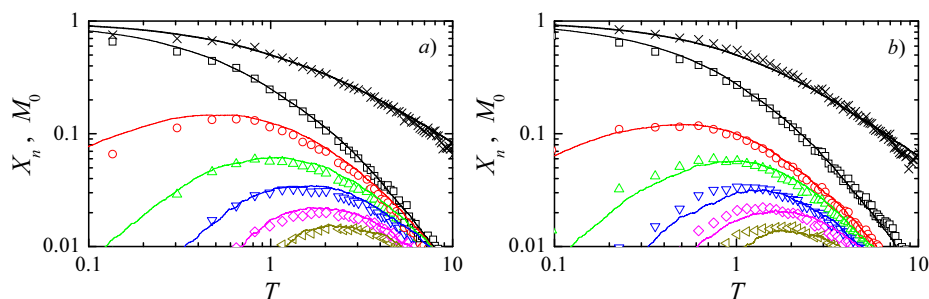


Figure 5.7.: Comparison between electrostatic heteroaggregation experiments (symbols) and Brownian dynamics simulations (solid lines): (a) experiment at 1 M versus DLCA simulations; (b) experiment at 10 mM versus BDLCA simulations. The graphs show the normalised concentration of n -mers up to hexamers and the first moment of the CSD.

BDLCA ($x = 1/2$)

The CSD corresponding to a simulation of an ideal BDLCA process is plotted in Fig. 5.6b.⁶ The most outstanding difference between the CSDs corresponding to DLCA and BDLCA processes is the relative excess of monomers in the latter case. This effect is the same “monomer discrimination” phenomenon that was found in selective heteroaggregation experiments at intermediate and low electrolyte concentrations (see Sec. 5.1.2). Hence, it is quite natural to compare the CSD of Fig. 5.6b with an experimental CSD where monomer discrimination takes place. In Fig. 5.7b, this comparison is shown for the heteroaggregation experiment at 10 mM KBr. Once again, an excellent agreement is found. This particular experiment has been selected because the similarities were evident even before the normalisation (please compare Figs. 5.2b and 5.6b and see also López-López *et al.* (2005)). Moreover, it seems to be the best candidate to fulfill the requirements for a BDLCA process because i) homoaggregation is forbidden

⁶Please recall that this chapter is devoted to symmetric heteroaggregation. Hence, Fig. 5.6b refers to a BDLCA simulation with $x = 1/2$. CSDs corresponding to asymmetric BDLCA simulations are discussed later on, in Sec. 6.1.2.

5. CLUSTER-SIZE DISTRIBUTIONS

and ii) long range particle-particle interactions are not expected.

The following considerations should be pointed out regarding the above mentioned comparison between Brownian dynamics simulations and single-cluster light-scattering experiments:

- Only k_S was obtained by a fitting procedure and only the onset of the monomer concentration was used. Hence, by fitting about ten data points with only one free parameter,⁷ we obtain an excellent agreement for the whole data set of about 300 points. This a formidable achievement.
- Moreover, this fitting procedure involves only a normalisation of the data that does not affect the curve shape at all in a log-log plot, it only introduces a horizontal shift of the data set as a whole. Hence, even if no fit procedure were performed, we still could conclude that experimental and simulated $c_n(t)$ curves are functionally identical.
- Simulation data has also been normalised by calculating the corresponding aggregation time t_{aggr} . Hence, both the BDS and the SCLS data have been normalised by applying *independent* time shifts. Please note that, although these normalisation involve fitting procedures, both data set have been fitted to a theoretical function and not among themselves. That is to say, neither the experimental data have been fitted to simulated curves nor viceversa.
- To the best of our knowledge, this is the first time that the existence of a “binary diffusion-limited colloidal aggregation” regime is found in heteroaggregation experiments. It is also the first time that the CSDs arising in electrostatic heteroaggregation at electrolyte concentrations above the CCCs of the reactants, the CSD really follow a DLCA aggregation scheme.

⁷Please recall that c_0 was directly measured before starting the aggregation process.

5.2.2. Brownian dynamics simulations with interactions

In Sec. 4.2.1, Brownian dynamics simulations with particle-particle interactions were performed in order to interpret the experimentally obtained aggregation rate constants. Nevertheless, BDSs provide much more information than aggregation rate constants. Hence, we left the same BDSs discussed in Sec. 4.2.1 to evolve for longer times and thus obtained the corresponding cluster-size distributions. The results are plotted in Fig. 5.8.⁸ As expected, the CSDs at high κa values exhibit the features of a diffusion-limited cluster-cluster aggregation process (Fig. 5.8a). At relatively low κa values, where homoaggregation is partially or totally absent (Fig. 5.8b–c), the most outstanding feature is the relative excess of monomers (monomer discrimination). At even lower κa values the simulated CSDs exhibit an important decrease of the dimer concentration (Fig. 5.8d–e) in spite of the strong increase of the aggregation rate. This “dimer discrimination” effect was also found in experiments at low electrolyte concentration (Sec. 5.1.3 and López-López *et al.* (2004b)). At extremely low κa values, that are not accessible in our experiments, the cluster discrimination phenomenon includes also larger oligomers, not only monomer and dimers. At long aggregation times and $\kappa a = 0.5$ (Fig. 5.8f) the concentration of monomers, trimers and pentamers is larger than the concentration of dimers, tetramers and hexamers. This even-odd cluster discrimination was discovered by Puertas *et al.* (2002) using the same Brownian dynamics simulations that we have used here. All aspects concerning the cluster discrimination phenomenon are further discussed in Sec. 5.3.

The monomer concentration curves corresponding to simulations with long-range interactions exhibit a peculiar inflexion point at very short times (see Fig. 5.8e–f at $t \approx 4 \times 10^{-3}$ s). Puertas *et al.* (2002) also found this anomalous behaviour for the monomers when the range of the interactions was large. They attributed this effect to the ballistic aggregation that takes place when the initial distance between particles is shorter than the particle-particle interaction range. Puertas *et al.* (2002) found this ballistic aggregation at κa values lower than 0.2, because

⁸The CSDs for the simulations at $\kappa a = 50$ and $\kappa a = 20$, as well as the one corresponding to diffusion-limited homoaggregation (“ $\kappa a = \infty$ ”) are not plotted in Fig. 5.8 because they all are virtually identical to the one at $\kappa a = 100$ (Fig. 5.8a).

5. CLUSTER-SIZE DISTRIBUTIONS

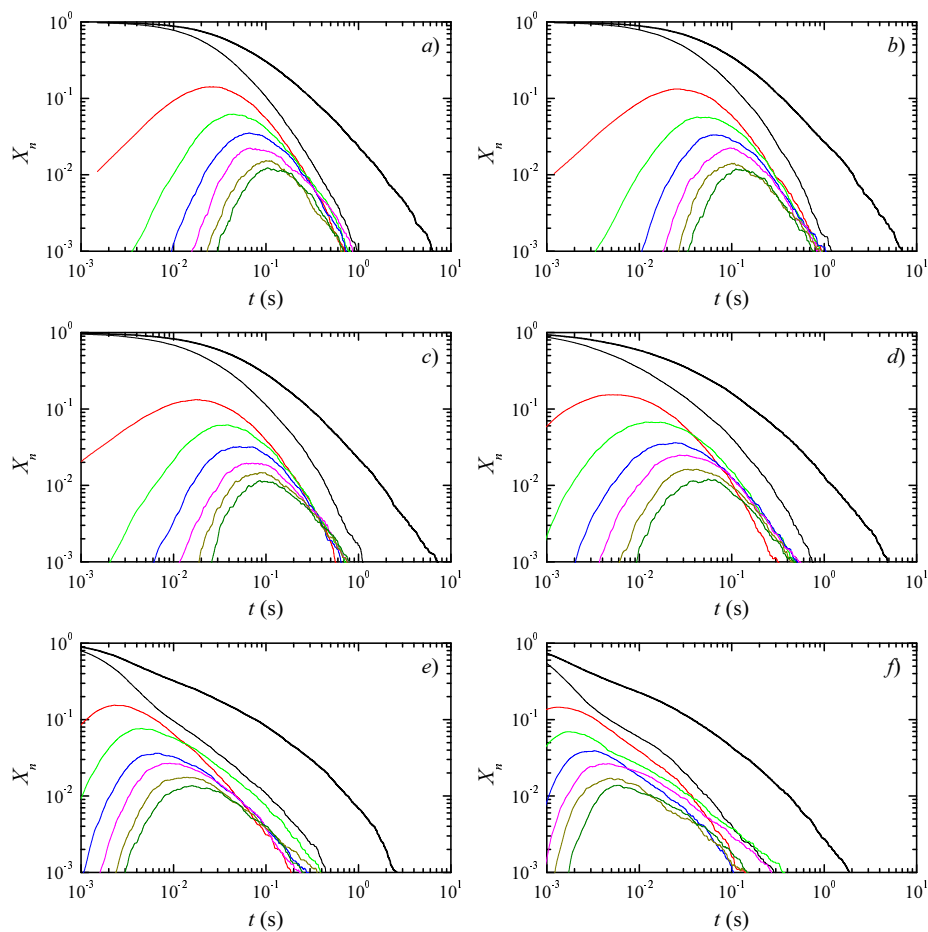


Figure 5.8.: Cluster-size distributions for heteroaggregation simulations at different κa values: a) $\kappa a = 100$, b) $\kappa a = 10$, c) $\kappa a = 5.0$, d) $\kappa a = 2.0$, e) $\kappa a = 1.0$ and f) $\kappa a = 0.5$. In each plot, the concentration of cluster up to heptamers, and the overall concentration of clusters are plotted.

the systems they studied were more diluted.⁹ In any case, the aim of performing BDS in this work is to establish a comparison with the experiments and so, the study of aggregation regimes at κa values smaller than those experimentally accessible is out of our scope.

In the previous section, it has been demonstrated that the experimental data follow a DLCA regime at high electrolyte concentrations and a BDLCa regime at intermediate electrolyte concentration. Here, we try to determine what regime corresponds to heteroaggregation experiments at low electrolyte concentrations. As discussed in Sec. 4.2.1, comparisons between experiments and BDS should be done for the same particle-particle interaction range, *i.e.*, the same κa parameter value. Hence, we have compared an experiment where no electrolyte was added with a BDS with a relatively low κa value. The best comparison was achieved for the most dilute experiment¹⁰ and the simulation for $\kappa a = 2.0$. This case is shown in Fig. 5.9. The agreement is quite good, despite the fact that the parameters used in the simulations had not to be fitted at all. Nevertheless, some points should be discussed:

- The overall electrolyte concentration in the experiments where no salt was added is estimated to be about $(3 \pm 1) \mu\text{M}$. This corresponds to $\kappa a = (1.2 \pm 0.4)$. Nevertheless, the experimental CSD has more similarities with the CSD of BDS for $\kappa a = 2.0$ than for $\kappa a = 1.0$. This could be due to differences between the real particle-particle interactions and those used in the simulations. In particular, the surface potentials in the simulations were fixed at relatively large values ($\psi_1^* = -\psi_2^* = 50 \text{ mV}$) that probably overestimate the electrostatic interaction strength.
- The time normalisation has been carried out in a different manner than in

⁹In fact, the particle volume fraction used by Puertas *et al.* (2002) was $\phi = 0.001$, while in this work $\phi = 0.01$. Consequently, ballistic aggregation in our work takes place at κa values ten times larger than the ones reported by Puertas *et al.* (2002).

¹⁰As stated before, electrostatic heteroaggregation experiments with no added salt are highly sensible to impurities and, hence, were repeated four times. In three of the cases plotted in Fig. 5.4 the particle concentration was about $9 \times 10^7 \text{ cm}^{-3}$, *i.e.*, the same value used in most of the SCLS experiments of this work. Nevertheless, since the aggregation process was so fast, c_0 was chosen to be half this value for the fourth experiment (this case is plotted in Fig. 5.4c), in order to obtain more data points at short times.

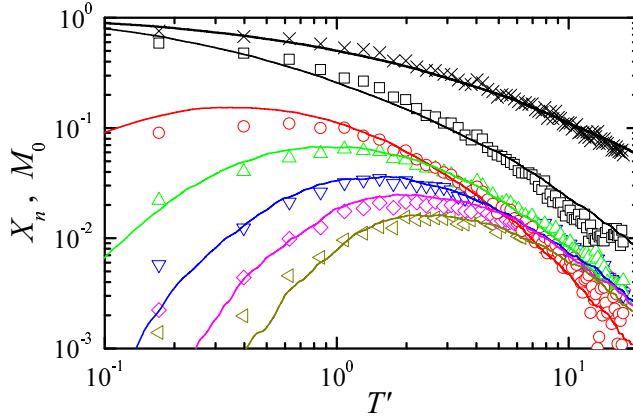


Figure 5.9.: Comparison between an electrostatic heteroaggregation experiment with no added salt (symbols) and Brownian dynamics simulations for $\kappa a = 2.0$ (solid lines). The graph shows the normalised concentration of n -mers up to hexamers and the first moment of the CSD.

Sec. 5.2.1. In order to improve the statistics, the total number of clusters has been used instead of the monomer concentration. Thus, time has been normalised by dividing by t'_{aggr} , *i.e.*, the time at which the total number of clusters has dropped to half its initial value (Eq. 2.15). Please recall that this time does not have to be equal to t_{aggr} . Additionally, t'_{aggr} is a more robust quantity since it does not need to assume $k_{11} = k_S$.

- Independently of choosing t_{aggr} or t'_{aggr} , only one curve is used for the fits. Moreover, the normalisation gives only rise to a time shift. Hence, also here simulations predict the functional form of experimental $c_n(t)$ curves correctly.
- The agreement is quite good for all the measured $c_n(t)$ curves. Especially, the dimer discrimination is correctly described by the simulations.

5.3. Cluster discrimination

The term “cluster discrimination” was introduced by Puertas *et al.* (2002), and refers to the fact that, under certain circumstances, the long-time behaviour of the $c_n(t)$ functions depends on the parity of n . Concretely, these author found a strong bias of clusters formed by an odd number of particles, when the range of the particle-particle interactions was long. Moreover, as this interaction range increases (smaller κa values), the odd-even discrimination includes a wider interval of cluster sizes. In simulations with $\kappa a = 3.2$, only monomers were discriminated, in the sense that they appear to be more stable than expected.¹¹ When $\kappa a = 0.8$, they found a defect of dimers in addition to the excess of monomers.¹² Finally, for $\kappa a = 0.2$, the odd-even discrimination includes clusters up to octamers.¹³ Puertas *et al.* (2002) suggested that in the zero κa limit, odd-even cluster discrimination would be achieved for all cluster sizes.

Yoshioka *et al.* (2005) have proposed a quite simple explanation for the even-odd cluster discrimination phenomenon. They consider a system where only reactions between unlike particles are allowed and where smaller clusters have chainlike structures. Hence, they can join other clusters only at chain ends. Odd-sized clusters, however, can form aggregates only with clusters that have oppositely charged particles, at least, at one of their ends because they have equally charged particles at both ends. In contrast, even-sized clusters have differently charged particles at both ends. Therefore, the reactivities of even-sized clusters are higher than those of odd-sized clusters.

5.3.1. Experimental evidences of cluster discrimination

The work of Puertas *et al.* (2002) was devoted only to Brownian dynamics simulations. Hence, they did not give any experimental indication that cluster dis-

¹¹Please see Fig. 1e of (Puertas *et al.*, 2002). The same effect can be observed also in Fig. 5.8c of this PhD thesis, although in this latter case, $\kappa a = 5.0$ and the particle volume fraction is larger.

¹²Fig. 1d of (Puertas *et al.*, 2002), and Fig. 5.8d ($\kappa a = 2.0$) of this PhD thesis.

¹³Fig. 1b of (Puertas *et al.*, 2002), and Fig. 5.8f ($\kappa a = 0.5$) of this PhD thesis. Nevertheless, in the latter case, the relative high particle concentration induces ballistic aggregation at short times.

5. CLUSTER-SIZE DISTRIBUTIONS

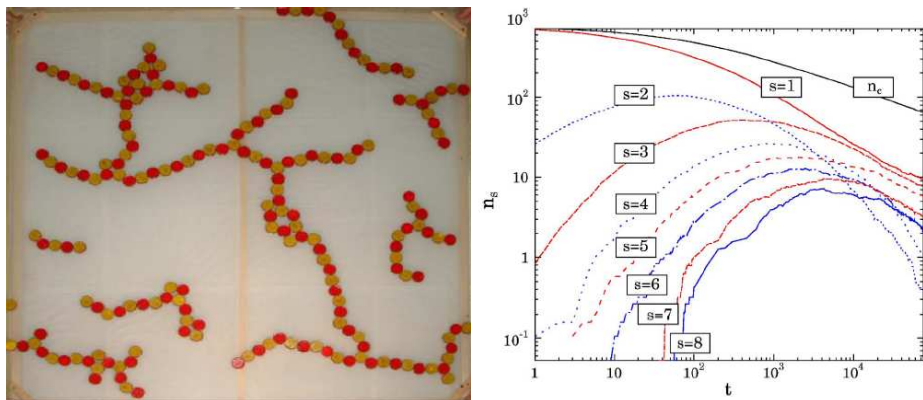


Figure 5.10.: A two-dimensional ALCA experiment with dipolar Ising particles: (a) photographic snapshot of a typical configuration and (b) time evolution of cluster-size distribution up to octamers. Both figures reproduced from (Yoshioka *et al.*, 2005) for academic purposes.

crimination is a real phenomenon occurring in electrostatic heteroaggregation processes. As far as we know, the first evidences of cluster discrimination in experiments were found during this PhD thesis (López-López *et al.*, 2004b). Monomer discrimination was found in electrostatic heteroaggregation at intermediate electrolyte concentrations (see Fig. 5.2b–d) and dimer discrimination was found at low and very low electrolyte concentrations (Fig. 5.4a–f). The odd-even cluster-discrimination could not be confirmed experimentally for colloidal heteroaggregation since it was not possible to achieve κa values below 1 with our experimental set-up. Nevertheless, Yoshioka *et al.* (2005) experimentally observed odd-even discrimination for clusters up to octamers in a macroscopic system composed by dipolar Ising particles (Fig. 5.10). These particles show strong long-range magnetic interactions, repulsive between like particles and attractive between unlike particles. Since they are not affected by Brownian motion—the particle diameter is about 0.5 cm—, they undergo actual attraction-limited cluster-cluster aggregation (ALCA).

The special behaviour of monomer and dimers in selective heteroaggregation experiments is appreciable directly in the cluster-size distributions (Figs. 5.2 and

5.4). Nevertheless, dimer discrimination is even better appreciated in Fig. 5.11, where the cluster concentration profiles at a fixed, relatively large time, t_0 , are shown for different electrolyte concentrations. As expected, the cluster concentration profile, $c_n(n)$, decays exponentially in the DLCA limit. This exponentially decaying behaviour is maintained for clusters larger than dimers although the cluster concentrations and the slope of the curves diminish for decreasing electrolyte concentration. Only the monomers and dimers abandon this exponential behaviour. The monomer concentration is always higher and the dimer concentration is always lower than the value that could be extrapolated from the exponential decay curve defined by the larger clusters. It should also be mentioned that dimer discrimination starts to become relevant at lower electrolyte concentrations than monomer discrimination. According to this tendency, trimer discrimination would be expected at an even lower ionic concentration. Under the given experimental conditions, however, this effect could not be observed since it was not possible to obtain samples with ionic concentrations below the limit given by the pH of the aqueous medium.

It is important to throw into relief that cluster discrimination is not just a consequence of the absence of homoaggregation. As mentioned before, the probability for the reaction between two like particles is already negligible at 10 mM KBr, *i.e.*, aggregation is due only to heteroaggregation at this electrolyte concentration. However, only monomer discrimination is observed. According to Fig. 5.11, the electrolyte concentration has to drop below approximately 1 mM before dimer discrimination starts to become relevant. The origin of cluster discrimination seems instead to be related to the ratio between the cluster size and the range of the attractive electrostatic interactions. As the ionic concentration decreases, the thickness of the electric double layer and, consequently, the range of the corresponding electrostatic interaction increase. The relative increase of the range of the electrostatic interactions with respect to the cluster size is, however, more pronounced for smaller aggregates than for larger ones. Hence, all phenomena related to the range of the attractive electrostatic interactions are expected to be observable first for smaller aggregates and then for larger ones. This is exactly what we observed for cluster discrimination.

5. CLUSTER-SIZE DISTRIBUTIONS

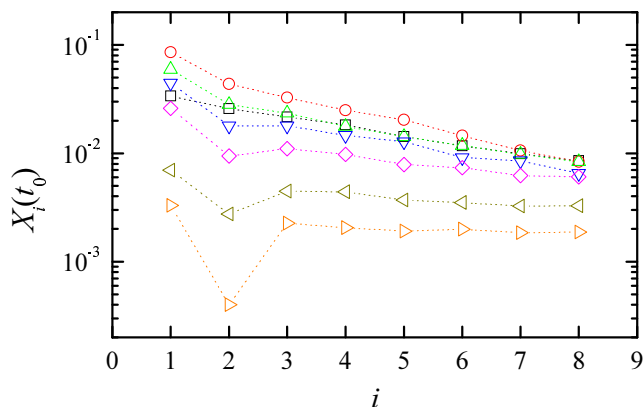


Figure 5.11.: Cluster-concentration profiles at fixed time ($t_0 \approx 2 \times 10^4$ s) for electrostatic heteroaggregation experiments at different KBr concentrations: 1.0 M (\square), 100 mM (\circ), 10 mM (\triangle), 1.0 mM (∇), 0.1 mM (\diamond), 0.01 mM (\triangleleft) and no added KBr (\triangleright). Dotted lines are drawn just as a guide for the eye.

5.3.2. Comparison with Brownian dynamics simulations

In the second part of this section, we now compare the experimental results with the predictions made by Puertas *et al.* (2002) by means of Brownian dynamics simulations (BDS). Their simulations were performed for 1:1 mixtures of perfect microspheres of identical size and opposite surface charge. As particle-particle interactions, London-van der Waals forces and double layer overlapping in the linear superposition approximation were taken into account (more details to be found in Sec. 3.4.2). Nevertheless, other important effects such as internal cluster rearrangement, aggregate rotation, hydrodynamic interactions, or aggregate sedimentation were not considered. Although typical values for the particle characteristics such as the Hamaker constant and electric surface potentials were chosen for the simulations, an exact equivalency with our experimental system is not expected.

In order to make a direct comparison between experiment and simulation, the

particle size, the cluster concentrations, the time scale and the range of the interactions have to be normalised. For this purpose, the inverse of the Debye screening length, κ , is used (Eq. (2.57)). The adimensional parameter κa provides a suitable normalisation for the particle size and the range of the electrostatic interactions. The cluster concentrations c_n are easily normalised by dividing them by the initial particle concentration c_0 . Although the particle concentration used for the simulations is about 2390 times the experimental one, it can still be considered a dilute system since only binary reactions occur.¹⁴ Time scale normalisation, however, has to be done in such a way that equivalent aggregation stages of the experimental and simulated processes are compared. Here, we used the normalised total number of clusters as an intrinsic time scale. This quantity is not only unequivocally related to the time but also has the best statistics of all the experimentally available data.

Before we compare the experimental and simulated data, we would like to make some general remarks. Just like in our experimental CSD data, monomer discrimination appears in the BDS already for κa values above 10 while dimer discrimination becomes observable for κa values below approximately 5. Discrimination of larger clusters was not found experimentally. In the simulations, cluster discrimination was detected even for aggregates as large as octamers. This octamer discrimination, however, is only observed for the smallest κa value used in the simulations ($\kappa a = 0.1$). Puertas *et al.* (2002) suggested that in the zero κa limit an odd-even cluster discrimination would be achieved with a strong bias of clusters formed by an even number of constituent particles. This hypothesis could not be confirmed experimentally since it was not possible to achieve κa values below 1 with our SCLS instrument because a minimal particle radius of 250 nm is required to ensure correct monomer detection (Fernández-Barbero *et al.*, 1996). Nevertheless, the experimentally observed monomer and dimer discrimination are compatible with the predicted odd-even behaviour, *i.e.*, the monomers become dominant and the dimers are biased in the CSDs.

For a more quantitative comparison between experiment and simulation, we calculated the dimer-trimer concentration ratio, c_2/c_3 , at a fixed, relatively advanced

¹⁴Only at extremely long interaction ranges, $\kappa a < 0.2$, ballistic aggregation is appreciable in the work of Puertas *et al.* (2002).

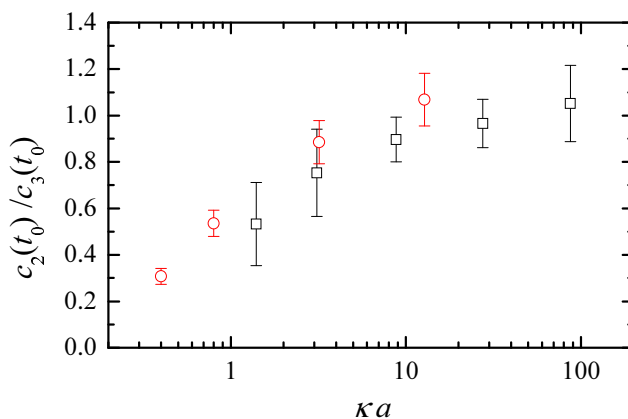


Figure 5.12.: Dimer-trimer concentration ratio, c_2/c_3 , at an advanced aggregation stage as a function of κa . The plot shows the experimental SCLS data (\square) and the BDS data (\circ) simulated by Puertas *et al.* (2002).

aggregation stage where the total number of clusters had dropped to one tenth of its initial value. The obtained results are plotted in Fig. 5.12 as a function of κa . As can be seen in the figure, the experimental and simulated data are in good agreement in their common κa interval and seem to follow a single curve over the entire κa range. For κa values larger than 10, the dimer-trimer concentration ratio does not vary very much and its value remains close to unity. This means that dimers and trimers behave in similar way in the region where dimer discrimination was not observed experimentally. At lower κa values, however, this is not the case anymore. There, the dimer-trimer concentration ratio decreases and drops to lower values the lower the electrolyte concentration becomes. In other words, the dimers reach a more advanced state than the trimers. In this sense, dimer discrimination becomes stronger for decreasing κa .

Finally, it should be mentioned that a similar good agreement between experiment and simulation was achieved also for other concentration ratios. Taking into account the objections made at the beginning of this section, it is quite surprising to see such a quantitative agreement.

5.3.3. Conclusions

Cluster discrimination was found experimentally in heteroaggregation processes arising in 1:1 mixtures of positively and negatively charged particles at low and very low ionic concentrations. Monomer discrimination could be detected already at 10 mM KBr while dimer discrimination started to appear only for electrolyte concentrations smaller than 1.0 mM. This shows that cluster discrimination is not an intrinsic property of selective heteroaggregation processes since it has not fully developed as soon as homoaggregation processes are completely absent. Furthermore, dimer discrimination was observed to become more pronounced for decreasing ionic concentrations. This finding implies that cluster discrimination is most likely related to the range of the attractive electrostatic interactions between the oppositely charged particles.

The experimental results were also compared with the Brownian dynamics simulation performed by Puertas *et al.* (2002). Not only qualitative but also quantitative agreement was obtained when the adequate normalisation were performed. Especially, the onset and the increasing strength of dimer discrimination were predicted quite satisfactorily by the BDS. In their simulations, Puertas *et al.* (2002) found that cluster discrimination gives rise to an odd-even behaviour in the cluster concentration profiles, *i.e.*, odd size clusters become dominant while even size clusters are biased in the CSDs. The experimental data confirm this prediction for monomers and dimers. It should be pointed out that the simulations were performed as a function of κa , *i.e.*, changing only the relative range of the electrostatic interactions. Hence, the good agreement between experiment and simulations supports the above mentioned hypothesis that the cluster discrimination phenomenon originates mainly from long range electrostatic interactions.

The cluster discrimination phenomenon in electrostatic heteroaggregation processes can be explained following the suggestions of Yoshioka *et al.* (2005), since light scattering experiments (Puertas *et al.*, 2001*b*) and direct microscopy studies (Kim *et al.*, 2003) have demonstrated that heteroaggregates composed by oppositely charged particles at low electrolyte concentrations are almost linear.

5.4. Electrostatic heteroaggregation regimes

Homoaggregation regimes of lyophobic latexes are well established in colloid science: DLCA at high electrolyte concentrations (Lin *et al.*, 1990a), RLCA at very low electrolyte concentrations (Lin *et al.*, 1990b), and a continuous transition between these two extreme regimes (Odriozola *et al.*, 2001a; Odriozola *et al.*, 2001b; Moncho-Jordá *et al.*, 2001). In contrast, much less is known about heteroaggregation regimes. In this section, we summarise all the experimental and simulated data collected in Chaps. 4 and 5 in order to identify the electrostatic heteroaggregation regimes. Moreover, experimental and simulated cluster-size distributions are compared with the solutions of the coagulation equation for several *kernels*. Although a complete agreement is not achieved, we hope to have brought some light on this topic.

5.4.1. Heteroaggregation kernels

In this section we compare the CSDs obtained in experiments and simulations with those obtained by solving several aggregation *kernels*. The coagulation equations were solved using the stochastic algorithm programmed by Dr. Gerardo Odriozola (details about this algorithm were given in Sec. 3.4.3).

Diffusion-limited aggregation

Both, the aggregation rate constants (Sec. 4.1.1) and the cluster-size distributions (Sec. 5.1.1), indicate that heteroaggregation arises as a diffusion-limited homoaggregation process at high electrolyte concentrations. Moreover, it was shown in Sec. 5.2.1 that computer simulated diffusion-limited cluster-cluster aggregation (DLCA) fits the data quite well. Hence, we claim that mixtures of oppositely charged particles at high electrolyte concentrations undergo diffusion-limited colloid aggregation (DLCA).¹⁵ It is widely known that the Brownian

¹⁵Please recall that the letter ‘C’ of terms such as “DLCA”, “RLCA” or “ALCA” may mean “cluster-cluster” when it is used in theory and simulation contexts; but it also may mean “colloid” when it refers to real aggregation regimes found in colloidal dispersions.

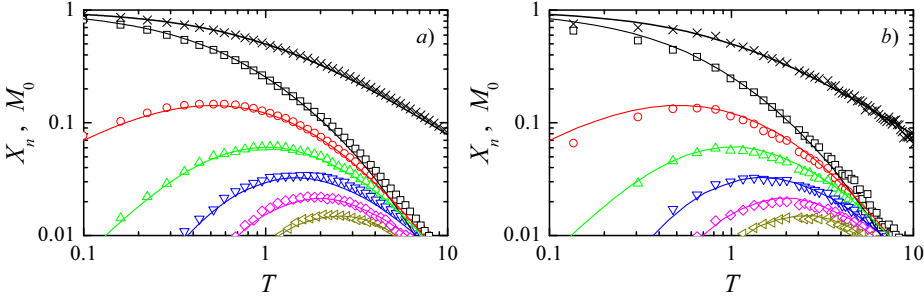


Figure 5.13.: Comparison between the Brownian *kernel* solution (solid lines) and: (a) Brownian dynamics simulations of diffusion-limited cluster-cluster aggregation; and (b) SCLS experiments of heteroaggregation at 1 M KBr. In each graph, the normalised concentration of n -mers up to hexamers and the first moment of the CSD are plotted.

kernel (see Eq. (2.45) and Sec. 2.2.2) perfectly describes the coagulation behaviour of simulated DLCA processes (Schmitt *et al.*, 2000*b*). We have tested it by solving the Smoluchowski's coagulation equation (2.6) with the Brownian *kernel* (2.45), and comparing the solution with DLCA data obtained by Brownian dynamics simulations (see Sec. 5.2.1). The agreement is excellent, as can be appreciated in Fig. 5.13*a*. Time has been normalised in simulations by calculating the aggregation time, as explained before. The fractal dimension d_f of the clusters, which appears in the functional form of the Brownian *kernel*, was chosen to be 1.75, a typical value for DLCA processes (Kolb, 1984; Lin *et al.*, 1990*a*). Nevertheless, the dependence of k_{ij}^{Brown} on d_f is not very important.

In Fig. 5.13*b*, the Brownian *kernel* solutions have been compared with the CSD of a electrostatic heteroaggregation experiment at high electrolyte concentration ($[\text{KBr}] = 1.0\text{M}$). As can be appreciated, the agreement is excellent again. It should be noted that the Brownian *kernel* is known to fit homoaggregation experiments at high electrolyte concentrations (see, *e.g.*, Odriozola *et al.*, 1999),¹⁶

¹⁶Although it is usual to find that some residual particle-particle interactions remain even above the CCC (Schmitt *et al.*, 2000*b*).

5. CLUSTER-SIZE DISTRIBUTIONS

although this is the first time that it has been shown that it also correctly reproduces an experimental CSD of a two-component colloidal dispersion.

Binary diffusion-limited aggregation

In Sec. 5.2.1, it was shown that the CSD of a selective heteroaggregation experiment at an intermediate electrolyte concentration ($[KBr] = 10 \text{ mM}$), and the CSD of an ideal binary diffusion-limited cluster-cluster aggregation (BDLCA) simulation, were quite similar. For this reason, we suggested that this experiment corresponds to an example of a novel aggregation regime: the binary diffusion-limited colloid aggregation regime (BDLCA). Only a few studies about BDLCA are found in the literature (Meakin and Djordjević, 1986; Stoll and Pefferkorn, 1993; AlSunaidi *et al.*, 2000; López-López *et al.*, 2005), and they refer only to simulated data. Moreover, none of them deals with the problem of finding a *kernel* of (2.6) that could reproduce the cluster-size distributions.

As stated before, the most outstanding feature of the CSD of a BDLCA process with $x = 1/2$ is the monomer discrimination. According with the discussion in Sec. 5.3, the monomer discrimination is a consequence of the selective heteroaggregation: reactions between like monomers are forbidden and hence, the relative ability of monomers is smaller in BDLCA than in DLCA. This effect is less important for larger aggregates since it is more likely that a pair of oppositely charged particles touch in one of the successive collision of the cluster-cluster encounter. Hence, it is expected a crossover from BDLCA to DLCA for large cluster-sizes (López-López *et al.*, 2005). Therefore, the BDLCA *kernel* should have the following functional form:

$$k_{ij}^{\text{BDLCA}} = P_{ij} k_{ij}^{\text{Brown}} \quad (5.1)$$

In (5.1), k_{ij}^{Brown} is the Brownian *kernel*, and P_{ij} is a factor between 1/2 and 1. The lower limit is reached for the monomer-monomer aggregation rate, since only one half of the monomer encounters occurs between unlike particles. The upper limit is achieved in the encounter of two very of large clusters, since it is almost sure that one of the successive collisions would lead to a direct contact

between unlike particles. Hence, $P(i,j)$ satisfies the following conditions:

$$P_{11} = \frac{1}{2} \quad ; \quad \lim_{i,j \rightarrow \infty} P_{ij} = 1 \quad (5.2)$$

A somehow trivial functional form for P_{ij} that satisfies (5.2) is the following:

$$P_{11} = \frac{1}{2} \quad ; \quad P_{ij} = 1 \quad , \quad \forall i, j / i + j > 2 \quad (5.3)$$

It is similar to the addition-aggregation *kernel* (2.26), although it is multiplied by the Brownian *kernel*. Hence we propose the name “Brownian addition-aggregation *kernel*” for the *kernel* (5.1) with P_{ij} given by (5.3).

The coagulation equation (2.6), with the Brownian addition-aggregation *kernel*, is solved with the stochastic algorithm, and the solution is compared with: i) Brownian dynamics simulations of BDLCA processes (Fig. 5.14a), and ii) electrostatic heteroaggregation experiments at 10 mM KBr (Fig. 5.14b). In these figures, experimental and simulated data are normalised as described in Sec. 5.2.1. A qualitative good agreement is found in both cases. The monomer discrimination, especially, is correctly reproduced by this *kernel*. Nevertheless, important deviations are found in the long time behaviour of some clusters. Particularly, the dimer concentration is substantially underestimated by the Brownian addition-aggregation *kernel*.

The Brownian addition-aggregation *kernel* satisfies (5.2), although it is somehow a bit extreme. The monomer-dimer reaction rate constant, for instance, takes the same value than in the Brownian *kernel*. It means that *every time* a monomer and a dimer encounter each other, they react and form a trimer. Nevertheless, in a real BDLCA process, the probability of a monomer-dimer reaction during one encounter is, surely, smaller than 1. Therefore, we propose the following functional form for P_{ij} , that satisfies (5.2) but in a softly manner:

$$P_{ij} = 1 - \frac{1}{2^{i+1}} - \frac{1}{2^{j+1}} \quad (5.4)$$

This functional form is similar to the q -sum *kernel* (Eq. 2.27), with $q = 1/2$, although it is multiplied by the Brownian *kernel*. Hence we propose the name “Brownian q -sum *kernel*” for the *kernel* (5.1) with P_{ij} given by (5.4).

5. CLUSTER-SIZE DISTRIBUTIONS

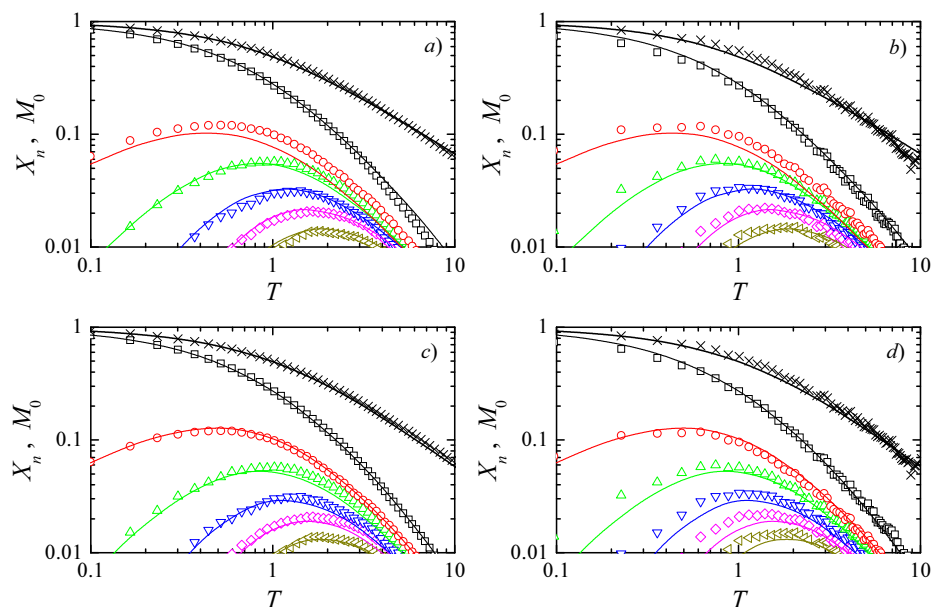


Figure 5.14.: Comparison between heteroaggregation experiments at 10 mM (“SCLS”, symbols), Brownian dynamics simulations of binary diffusion-limited cluster-cluster aggregation (“BDS”, symbols), Brownian addition-aggregation *kernel* solution (“add-aggr”, solid lines) and Brownian q -sum *kernel* with $q = 1/2$ (“ q -sum”, solid lines): (a) BDS / add-aggr, (b) SCLS / add-aggr, (c) BDS / q -sum and (d) SCLS / q -sum. In each graph are plotted the normalised concentration of n -mers up to hexamers, and the first moment of the CSD.

The coagulation equation (2.6), with the Brownian q -sum *kernel*, is solved with the stochastic algorithm, and the solution is compared with: i) Brownian dynamics simulations of BDLCA processes (Fig. 5.14c), and ii) electrostatic heteroaggregation experiments at 10 mM KBr (Fig. 5.14d). In these figures, experimental and simulated data are normalised as described in Sec. 5.2.1. As can be seen, the quantitative agreement improves substantially. Now, not only the concentration of monomers is correctly reproduced, but also the concentrations of dimers and larger clusters.

Attraction-driven aggregation

At lower electrolyte concentrations, attractive interactions between unlike particles become long-ranged. Therefore, they are supposed to drive the aggregation process. Accordingly, Puertas *et al.* (2001b) called this regime “attraction-driven cluster-cluster aggregation”. As stated in Sec. 5.3, one of the most important characteristics of this regime is the cluster-discrimination: clusters with an even number of particles disappear faster than those composed by an odd number of particles. Puertas *et al.* (2002) proposed the following aggregation scheme for this situation:

- Odd clusters can only be created by aggregation of another odd (charged) cluster and an even (neutral) one, and can die out by aggregation with neutral clusters, or with another odd one of opposite charge.
- Even clusters are formed by the reaction between two even clusters, or two odd ones (of opposite sign of charge), and disappear by aggregating with any other cluster.
- Aggregation between similarly charged clusters is forbidden, as no clusters with a net charge of two are found.

This aggregation scheme indeed induces odd-even cluster discrimination. At long times, when the death term prevails, even clusters can react with any other cluster, but odd clusters cannot form aggregates with oppositely charged odd clusters. Hence, the reactivities of even-sized clusters are higher than those of odd-sized ones.

5. CLUSTER-SIZE DISTRIBUTIONS

In a quite different context, (Leyvraz and Redner, 1986b) already proposed this aggregation scheme for two-component systems. They also suggested that the kinetics equations that rule such a system yield to the Smoluchowski equations when a parity dependent *kernel* is used. Nevertheless, this finally was pointed out to be an erratum (Leyvraz and Redner, 1986b). The problem arises from the existence of two different kinds of odd clusters of a given size. Only when both, concentration and reactivity, of the two types of odd-sized clusters are the same, the simplification is possible. In this case, the *kernel* has the following expression:

$$k_{ij} = \begin{cases} \frac{1}{2}k_{ij}^{(\pm)} & \text{for odd } i, j \\ k_{ij}^{(0)} & \text{any other case} \end{cases} \quad (5.5)$$

Where $k_{ij}^{(0)}$ is the aggregation rate constant for the reaction between two even (uncharged) clusters, or between an even-sized cluster and an odd-sized cluster; and k_{ij}^{\pm} is the aggregation rate constant for the reaction between two oppositely charged odd-sized clusters. Leyvraz and Redner (1986a) studied the double constant *kernel*, i.e., $k_{ij}^0 = L$ and $k_{ij}^{(\pm)} = M$. Please recall that this *kernel* is a particular case of the parity dependent *kernel* described in Sec. 2.1.4. The results reported by ? were, however, quantitatively incorrect because they did not take into account the $\frac{1}{2}$ factor that precedes the odd-odd reaction constants (Leyvraz and Redner, 1986b). Puertas *et al.* (2002) rederived the differential equations that govern the concentrations of neutral and charged clusters, and numerically solved them for two *kernels*¹⁷. They are the double constant *kernel* and a two-fold homogeneous *kernel* given by:

$$k_{ij} = \begin{cases} \frac{1}{2}k^{(\pm)} \left(\frac{i+j}{2}\right)^\lambda & \text{for odd } i, j \\ k^{(0)} \left(\frac{i+j}{2}\right)^\lambda & \text{any other case} \end{cases} \quad (5.6)$$

The solutions of the Smoluchoski equation with these two *kernels* are plotted in Fig. 5.15. According to the figure, they both exhibit an even-odd cluster discrimination. Other functional forms are of course possible. A “double Brownian *kernel*” is plotted in Fig. 5.15c. It corresponds to the general form (5.5) setting both $k_{ij}^{(0)}$ and $k_{ij}^{(\pm)}$ equal to the Brownian *kernel*. In this case, the odd-even

¹⁷These authors directly solved the correct kinetic equations and hence, did not discuss the possibility of using a parity dependent *kernel* for the classical Smoluchowski equations.

5.4. Electrostatic heteroaggregation regimes

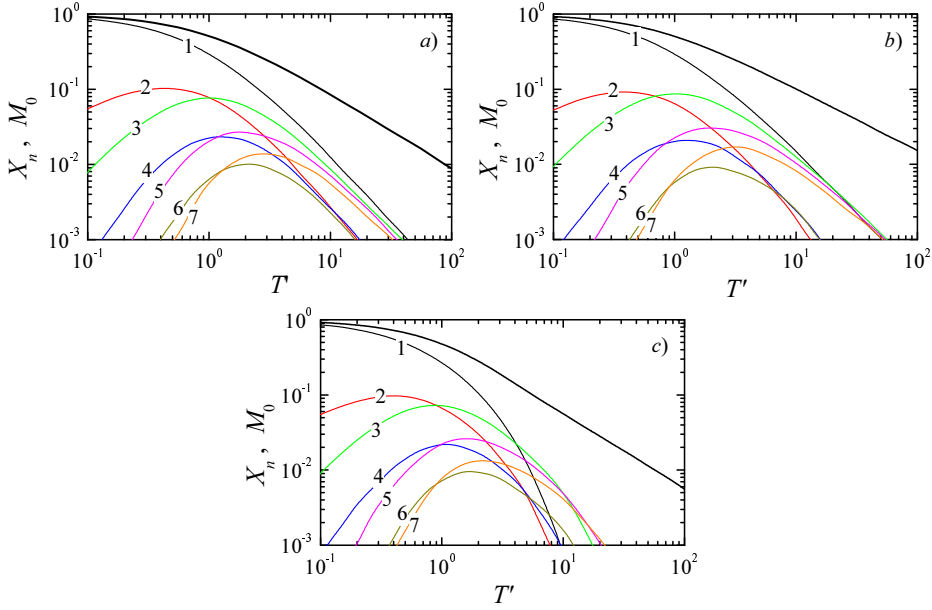


Figure 5.15.: Cluster-size distributions up to heptamers of some parity-dependent kernels: (a) double constant kernel with $k^{(\pm)} = k^{(0)}$, (b) two-fold homogeneous kernel with $k^{(\pm)} = 1.333k^{(0)}$ and $\lambda = -0.2$ and (c) double Brownian kernel with $k^{(\pm)} = k^{(0)}$ and $d_f = 1.3$.

cluster discrimination persists, although not so evident. Especially, monomers disappear faster since their reactivity with larger clusters increases strongly if compared with the constant kernel.

Nevertheless, the aggregation scheme described above reflects a quite idealised situation. The third condition is particularly strong. (Puertas *et al.*, 2002) reported that clusters with an absolute charge greater than one particle charge form even when extremely long-range interactions are imposed. The problem of finding a kernel that correctly describe the attraction-driven cluster-cluster aggregation regime is, therefore, still open.

5.4.2. Concluding remarks

In this section, we summarise the different heteroaggregation regimes found in 50/50 mixtures of oppositely charged colloids:

DLCA: At high electrolyte concentrations, above the CCC of the reactants, heteroaggregation behaves as a one-component colloidal system undergoing diffusion-limited colloidal aggregation. Effective dimer formation rate constant takes diffusive values. An excellent agreement between the experimental and the simulated cluster-size distributions is found. Additionally, this CSD is correctly described by the solution of the coagulation equation with the Brownian *kernel*.

BDLCA: At intermediate electrolyte concentrations, where selective heteroaggregation takes place, but the range of the particle-particle interactions is still negligible with respect to the particle radius, heteroaggregation follows a novel binary diffusion-limited colloidal aggregation regime. The effective dimer formation rate constant ranges between half the diffusion value and the diffusion value, approximately. The CSD is characterised by an excess of monomers, due to the selection rules that regulate monomer-monomer reactions. An excellent agreement between simulated and experimental BDLCA processes is found. Monomer discrimination is reproduced by some semiempirical *kernels*, in which the monomer-monomer reaction rate constant takes half the value than in DLCA. The best quantitative agreement is found for the Brownian q -sum *kernel*, with $q = 1/2$.

ADCA: At low and very low electrolyte concentrations, long-ranged particle-particle interactions take place. Then, the attractive interactions between unlike particles drive the aggregation processes (Puertas *et al.*, 2001*b*). Therefore, this regime is known as attraction-driven colloid aggregation. Effective and absolute heteroaggregation rate constants take values that clearly surpasses the diffusive one. Experimental CSD is characterised by a fast decrease of the dimer concentration. Brownian dynamics simulations with particle-particle interactions correctly reproduce this phenomenon. Moreover, they predict that at even lower electrolyte concentration, an even-odd cluster discrimination would take place, with a fast decaying

of even-sized clusters. According to Yoshioka *et al.* (2005), the cluster-discrimination is related to the tendency of small clusters to form chain-like structures, when long-ranged interactions take place. Fractal dimension measures (Puertas *et al.*, 2001*b*), as well as direct microscopy studies (Kim *et al.*, 2003) support this hypothesis.

ALCA: In the limit of infinitely long-ranged particle-particle interactions, where Brownian motion does not take place, selective heteroaggregation processes would follow an attraction-limited colloidal aggregation regime. This regime, however, has only been observed so far in macroscopical magnetic systems (Yoshioka *et al.*, 2005) and in electrorheological suspensions in a strong electric field (See and Doi, 1991).

6. ASYMMETRIC HETEROAGGREGATION: STABLE AGGREGATES

Previous chapters of the present study on electrostatic heteroaggregation have been focused only on *symmetric* systems, *i.e.*, those with the same particle concentration of both species. In this chapter, on the contrary, we focus on *asymmetric* systems, where the relative concentration of particles, x , is considerably different from $1/2$. Then, some interesting phenomena are found: clusters with a high kinetic stability (“stable aggregates”, reported by Meakin and Djordjević, 1986), reactions that rapidly stop after some initial aggregation (“stopped reactions”, reported by Puertas *et al.*, 2001a), and non bell-shaped $c_n(t)$ curves (“two hump effect”, López-López *et al.*, 2005).

First section focuses on binary diffusion-limited cluster-cluster aggregation processes (BDLCA), studied by means of off-lattice Brownian dynamic simulations. Both short and long time behaviours are described, with special emphasis on the formation and structure of stable aggregates. Furthermore, a simple scheme for the off-lattice BDLCA kinetics is proposed.

Second section deals with experimental results found in asymmetric electrostatic heteroaggregation at very low electrolyte concentrations. Since the anionic particles bear a higher electric charge than cationic colloids, different phenomena arise at $x \lesssim 0.2$ and $x \gtrsim 0.8$. In the former case, the process stopped rapidly after some initial aggregation. In the latter case, however, stable oligomers were found and bimodal $c_n(t)$ curves (“two-hump effect”) could be reported for the first time to the best of our knowledge. Both effects are qualitatively explained by analogy with the simulation results, and by using the model that will be described in

Sec. 6.1.4. Moreover, the discrepancies may be explained quantitatively when the particle-particle interactions are fully taken into account.

Finally, Sec. 6.3 summarises the conclusions, and discusses future work that could be performed in this direction.

6.1. Ideal BDLCA processes

In this section, we focus on the aggregation behaviour of one of the simplest examples of a multi-component system. Our system is formed by two types of equally sized colloidal particles. We assume the particles to diffuse freely and to react on contact, in such a way that only collisions between unlike particles lead to bond formation (see Sec. 3.4.1). This aggregation scheme is known as binary diffusion-limited cluster-cluster aggregation (BDLCA, see AlSunaidi *et al.*, 2000). Although it supposes a very ideal case of aggregation processes arising in multi-component systems, it will allow basic aspects of such processes to be studied and analysed. Moreover, it may even serve to model real systems such as electrostatic heteroaggregation of mixtures of positively and negatively charged particles when the electric interactions are sufficiently screened but not completely suppressed. In this case, only short-range repulsive and attractive interactions between like and unlike particles are present. Hence, the interactions control the stickiness of the particles but are not expected to alter their diffusivity.

Pioneering BDLCA simulations were carried out by Meakin and Djordjević (1986). They studied 10 000 monomers that occupy the cells of a cubic lattice at a volume fraction of $\phi = 4.8 \times 10^{-3}$. In their work, all clusters performed a random walk with a size-independent diffusivity. They found that only relatively small aggregates are formed when the initial relative concentration of the minority particles, x , falls below a critical value, x_c . In this case, all the minority particles achieve to be contained in small aggregates that are completely coated with majority particles. Evidently, these aggregates cannot react anymore with other majority particles and so, aggregation comes to an end.

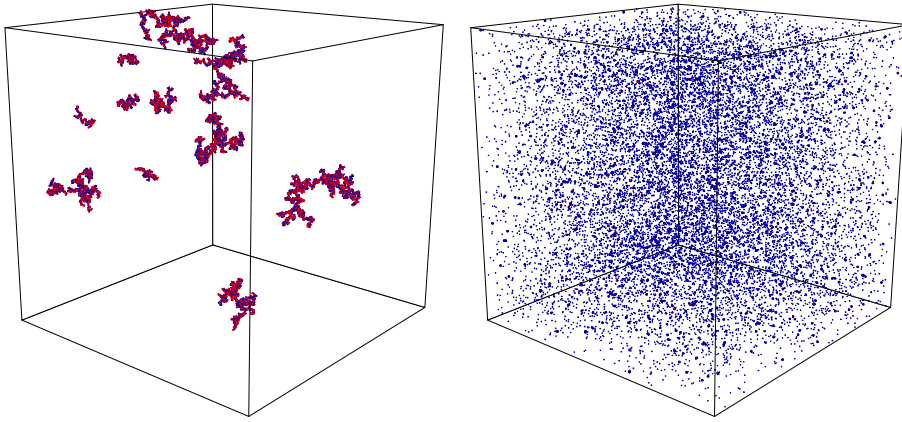


Figure 6.1.: Snapshots of simulated BDLCA processes, at a late stage of aggregation, for $x = 0.50$ (left) and $x = 0.05$ (right). Blue and red dots represent the majority and minority particles, respectively.

The two possible final states in BDLCA processes are shown in Fig. 6.1, where two snapshots of the aggregation state at very long times are plotted. The snapshot on the left side corresponds to a BDLCA process at a relative concentration of $x = 0.5$, which is clearly above the critical relative concentration x_c . In contrast, the plot on the right side corresponds to a BDLCA simulation which a relative concentration clearly below x_c . Differences between both late stages are evident. For $x > x_c$ only a small number of large aggregates remain in the system. For $x < x_c$, however, there is a large number of relatively small aggregates (mostly composed by only 10 to 20 particles).

BDLCA scheme has been studied in more detail by other authors apart from Meakin and Djordjević (1986). Stoll and Pefferkorn (1993), *e.g.*, performed more realistic simulations considering a size-dependent cluster diffusivity. They also noticed that for very asymmetric systems, the aggregation process stopped. Nevertheless, their BDLCA simulations were focused on studying dynamic quantities like the time evolution of the average number of particles. Moreover, the small number of particles used by these authors, probably does not allow them

6. ASYMMETRIC HETEROAGGREGATION

Table 6.1.: The table contains the main characteristics of some two-component simulations: initial number of monomers N_0 , volume fraction ϕ , diffusivity of an i -sized cluster D_i and on/off-lattice performance.

work	N_0	ϕ	D_i/D_1	lattice type
Meakin and Djordjević (1986)	10 000	0.0048	1	cubic
Stoll and Pefferkorn (1993)	1 000	0.0034	i^γ	cubic
AlSunaidi <i>et al.</i> (2000)	500 000	0.01	$a/R_g(i)$	cubic
Puertas <i>et al.</i> (2001c)	2 000	0.001	$a/R_g(i)$	off-lattice
López-López <i>et al.</i> (2005)	25 000	0.0001	$a/R_g(i)$	off-lattice

to extract reliable conclusions concerning these dynamical quantities. More recently, exhaustive on-lattice simulations reported by AlSunaidi *et al.* (2000) confirmed the existence of a critical relative concentration, x_c , separating two different aggregation regimes. For $x > x_c$, aggregation continues until a unique large cluster containing all the particles is formed. For $x < x_c$ more than one stable cluster remains in the system. They reported a value of x_c around 0.2. Nevertheless, on-lattice simulations limit bond formation to only a few sites on the particle surface. This quite unrealistic geometric constraints for the cluster structure implies that the size of the stable aggregates becomes restricted to 7, 12, 13, etc. if a cubic lattice is used. Meakin and Djordjević (1986) already mentioned the necessity of performing off-lattice simulations in order to avoid this unrealistic geometric constraint. The highly expensive computer-time, however, dissuaded them from performing off-lattice simulations.

Nowadays, the worthy improvement in computer technology made it possible to carry out off-lattice BDLCA simulations spending a reasonable time. Puertas *et al.* (2001c) performed such off-lattice simulations. They also included long-range attractive and repulsive particle-particle interactions (please see Sec. 3.4.2 for a description of their simulations). Nevertheless, these long-range interactions imply that their systems did not undergo binary diffusion-limited aggregation. In addition, as they focus mainly on the short time kinetics, stable aggregates were not reported. Table 6.1 summarises the main characteristics of the works reviewed here.

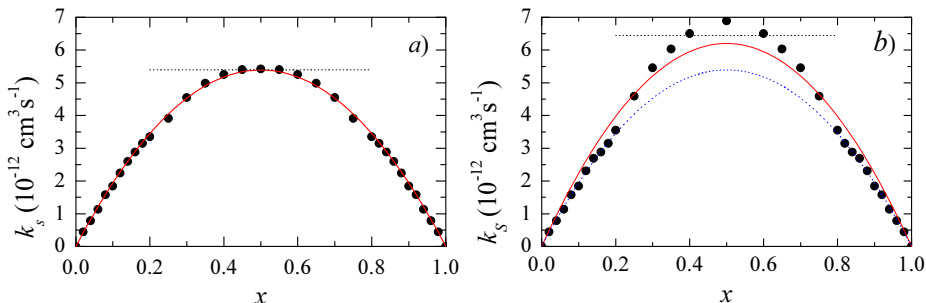


Figure 6.2.: Effective dimer formation rate, k_s , versus the relative concentration, x , obtained from BDLCA simulations (●) and the corresponding parabolic fit according to the HHF prediction (solid line). The particle volume fraction is: (a) $\phi = 10^{-4}$ and (b) $\phi = 10^{-3}$. The horizontal dotted lines indicate half the DLCA value in each case. The dotted parabola in (b) is the same fitting parabola plotted in (a).

The aim of this section is to study binary diffusion-limited cluster-cluster aggregation processes by means of off-lattice simulations. Both, short and long time kinetics will be investigated as a function of the initial relative concentration of the two species. We specially focus on the formation and growth of stable aggregates that are expected at low relative concentration. Kinetic and structural aspects will be discussed and contrasted with the results reported in the literature for on-lattice simulations.

6.1.1. Short time kinetics

BDLCA simulations were performed for a representative set of relative concentrations x . The particle volume fraction of $\phi = 0.0001$ was chosen to be as low as possible, in order to achieve the ideal dilute BDLCA regime. For further details about the BDLCA simulation, see Sec. 3.4.1. The effective dimer formation rate constant, k_s , was calculated according to the method described in Sec. 3.1.3. The results obtained are plotted in Fig. 6.2a. As predicted by the HHF approximation (2.34), the effective dimer formation rate constant reaches a maximum

6. ASYMMETRIC HETEROAGGREGATION

at $x = 0.5$ where $k_s \approx \frac{1}{2}k_{11}^{\text{Br}}$. This is clear from Fig. 6.2a since the theoretical predicted value is marked as a horizontal dotted line. Eq. (2.34) was used to fit the obtained k_s data. As can be appreciated in Fig. 6.2a, the corresponding parabolic fitting is excellent. Therefore, the HHF approximation is shown to be accurate for the early stages of BDLCA processes. The best fit was achieved for $k_{11}^{01} = (10.78 \pm 0.04) 10^{-18} \text{ m}^3 \text{ s}^{-1}$. As expected, this value is exactly the Brownian aggregation rate constant k_{11}^{Br} obtained in previous DLCA simulations.

The low particle volume fraction used here requires a long computing time. Nevertheless, it is necessary to work with very dilute systems if we want to correctly reproduce the ideal BDLCA regime. For example, if the particle volume fraction were ten times larger ($\phi = 10^{-3}$, a value still considered quite low), then the HHF prediction does not work so nicely anymore (Fig. 6.2b). At x values around 0.5, k_s takes larger values than it would be expected. Although the Brownian coagulation rate constant also takes larger values in the “concentrated” system than in the dilute one, $k_s > \frac{1}{2}k_{11}^{\text{Br}}$ for $x = 0.5$. The dotted parabolic line plotted in Fig. 6.2b is exactly the same function that correctly fits the data of the (a) figure. Note that the k_s points for relatively small x values follow quite nicely the parabola of the dilute system. Hence, we consider that, although the fitting for $\phi = 0.001$ is acceptable, it is preferable to use a more diluted system for studying the ideal BDLCA regime.¹

The fitting was restricted to a time interval of only 20 s in order to use only the most linear part of $g(t)$ (3.10). This interval is about one order of magnitude smaller than the Brownian aggregation time. Due to that short time interval, the procedure was so accurate that the relative deviation was always smaller than 1%. In Fig. 6.3, a representative set of $g(t)$ curves and the corresponding linear fit, is plotted. As can be seen, quite important deviations from the linear behaviour are found at long times, especially for small x values (Fig. 6.3k–l). Anyhow, these deviations occur at longer times than those used in the fitting procedure.

¹In the literature, $\phi = 10^{-3}$ is usually considered to be diluted enough for studying ideal aggregation regimes. Nevertheless, the behaviour at this particle concentration is not ideal, as can be seen comparing plots (a) and (b) of Fig. 6.2. The same concentration effect can explain some discrepancies found in the literature between the ideal parabolic curve and the x -dependence of k_s obtained by BDS. Please see, for example, Fig. 3 in Puertas *et al.* (2001c).

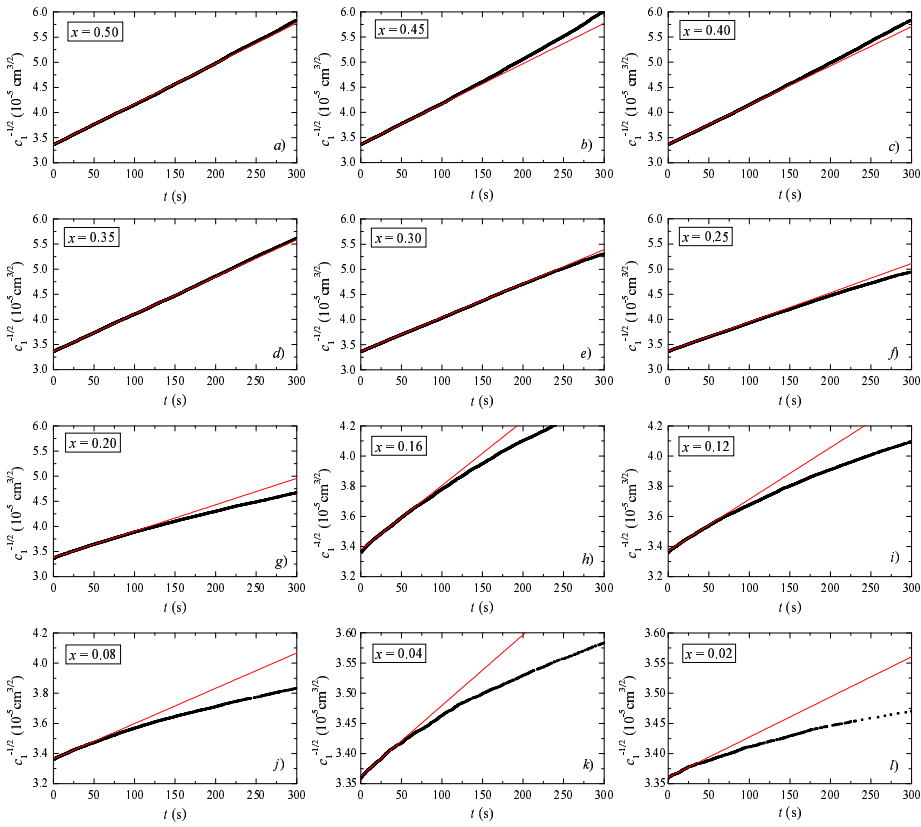


Figure 6.3.: Determination of k_S in BD/LCA simulations with different relative concentrations, x . Please note the changes in the vertical scale.

6. ASYMMETRIC HETEROAGGREGATION

This fact supports the suitability of the $g(t)$ function for obtaining an effective aggregation rate constant.

Even the non-linear behaviour of $g(t)$ may provide some valuable information. From the definition of k_S , it follows that the $g(t)$ derivative can be interpreted as a somehow-weighted average of the monomer-monomer aggregation rate, $k_{11}(t)$, and the monomer-cluster aggregation rate $k_{j1}(t)$.² At early stages of the aggregation process, the monomer-monomer reaction prevails and, hence, a linear behaviour is assured. The slope of the fitting straight line, consequently, is $k_S = k_{11}(t = 0)$. As time goes on, two effects may arise. On the one hand, both $k_{11}(t)$ and $k_{j1}(t)$ may change their values, due to a change in the population of the different cluster compositions. On the other hand, the relative importance of monomer-cluster reactions increases. Both effects, obviously, leads to a change in the slope of $g(t)$.

Taking into account the above discussion, now we try to interpret the $g(t)$ plots shown in Fig. 6.3:

- For $x < 0.35$,³ we obtain $g(t) \leq k_S t$ at any time. Moreover, the difference between both functions increases as x decreases. This slow down of the aggregation rate may be explained by considering that $k_{11}(t)$ is a decreasing function of time. When two monomers encounter each other, they form a bond with a probability $2x(1-x)$, *i.e.*, the same probability of they being of unlike species. In the derivation of the HHF approximation, we considered that x keeps its initial value $x_0 \equiv x(t = 0)$ for all times. But this is only true for $x_0 = \frac{1}{2}$. In any other case, the relative number of minority particles *decreases* in every monomer-monomer reaction. Consequently,

²The time dependence of the aggregation “constants” have to been introduced because we are not speaking about a homoaggregation process, and hence the aggregation abilities of clusters with the same number of particles, but different composition can be quite different. If the population of the different compositions changes, also the aggregation rate does. Please, also recall the discussion on page 23.

³It should be noted that simulations with a relative concentration x of particles of one type are, in turn, simulations with a relative concentration $(1-x)$ of particles of the other type. Hence, only simulations with $x \leq 0.5$ were actually performed. For the sake of simplicity, and considering this x -symmetry, the x -intervals indicated in this section refers only to $x \leq 0.5$. Accordingly, this paragraph actually refers to both $x < 0.35$ and $x > 0.65$.

the monomer-monomer reaction ability decreases with time. This effect is more important the larger the asymmetry of the system becomes. Hence, it is quite reasonable to state that the slow down of $g(t)$ for small x values is due to the relative rarefaction of the minority particles.

- For $x > 0.35$, on the contrary the $g(t)$ curve surpasses the fitting straight line. The minority particle rarefaction is also taking place here (except for $x = 0.5$) but it is not so dramatic since the asymmetry of the system is less important. In any case, this acts decreasing $g(t)$ as discussed above and, hence, cannot explain that $g(t) > k_S t$ at long times. This effect, however, may arise from an increasing importance of monomer-cluster reactions, if we assume that the monomer-cluster reaction capability is larger than the monomer-monomer reaction capability. It can be explained as follows: only a fraction $2x(1-x) \leq \frac{1}{2}$ of the monomer-monomer encounters corresponds to an encounter between unlike particles, which are the only encounters that lead to a bond formation. In contrast, in a monomer-cluster encounter, it is more feasible that the free monomer touches an unlike particle of the target cluster in anyone of the successive collisions of the encounter. Hence the probability of an effective encounter between a monomer and a j -mer increases as j does.

In summary, two competitive effects are concurring at the same time:

1. The intrinsic monomer- j -mer aggregation rate constant become the larger the larger j becomes, and the importance of these reactions increases as time goes on. This leads to an overall increase of the $g(t)$ slope.
2. The monomer-monomer aggregation rate decreases with time, due to a rarefication of minority particles. This leads to a decrease of the $g(t)$ slope. The importance of this effect increases for decreasing x values.

The former effect prevails for quasi-symmetric systems, while the latter prevails for highly asymmetric ones. They both are of similar importance at $x \approx 0.35$.

6.1.2. Long time behaviour

During the very early stages of BDLCA processes, only reactions between monomers take place. This allowed an effective initial dimer formation rate constant, k_s , to be determined. As time goes on, however, reactions between clusters of any size occur and so, the complete set of reaction rate constants has to be accounted for. Obtaining the complete aggregation kernel from experimental or simulated CSDs is a very challenging problem (Ramkrishna, 2000), that is far beyond the scope of this work. Nevertheless, valuable information about aggregation processes can be obtained directly from the cluster-size distributions without having to go through a detailed kinetic analysis.

Fig. 6.4 shows the time evolution of the CSD for BDLCA processes starting from different initial relative concentrations that range from the symmetric case ($x = 0.50$, Fig 6.4a) to a highly asymmetric one ($x = 0.05$, Fig 6.4f). The CSDs corresponding to some intermediate x values are also plotted in order to illustrate the transition between these two extreme regimes. As was done similar graphs along this thesis, the CSD plots show only the concentrations of the smaller clusters. However, it should be borne in mind that larger clusters are also present in the system. Their concentrations are not plotted for the sake of clearness. Instead, the total number of clusters, $M_0(t) = \sum_{i=0}^{\infty} n_i(t)$, is included. As can be observed, the overall behaviour of the CSD depends strongly on x . There are, however, some common features to all BDLCA simulations performed in this work, including those plotted in Fig. 6.4: (i) All of them start from monomeric initial conditions, $M_0(0) = n_1(0) = N_0$. (ii) The total number of aggregates decreases monotonically. That is to say, the average cluster size always grows. (iii) Whilst the number of monomers decreases monotonically, the number of larger aggregates reaches at least one maximum. (iv) The time at which these maxima are reached increases with the cluster size. The first three points are common to all systems that aggregate irreversibly starting from monomeric conditions.

In spite of these common features, there are substantial differences among these simulated BDLCA processes. One of the most outstanding points in this sense can be observed during the final stages of the aggregation processes. For relative

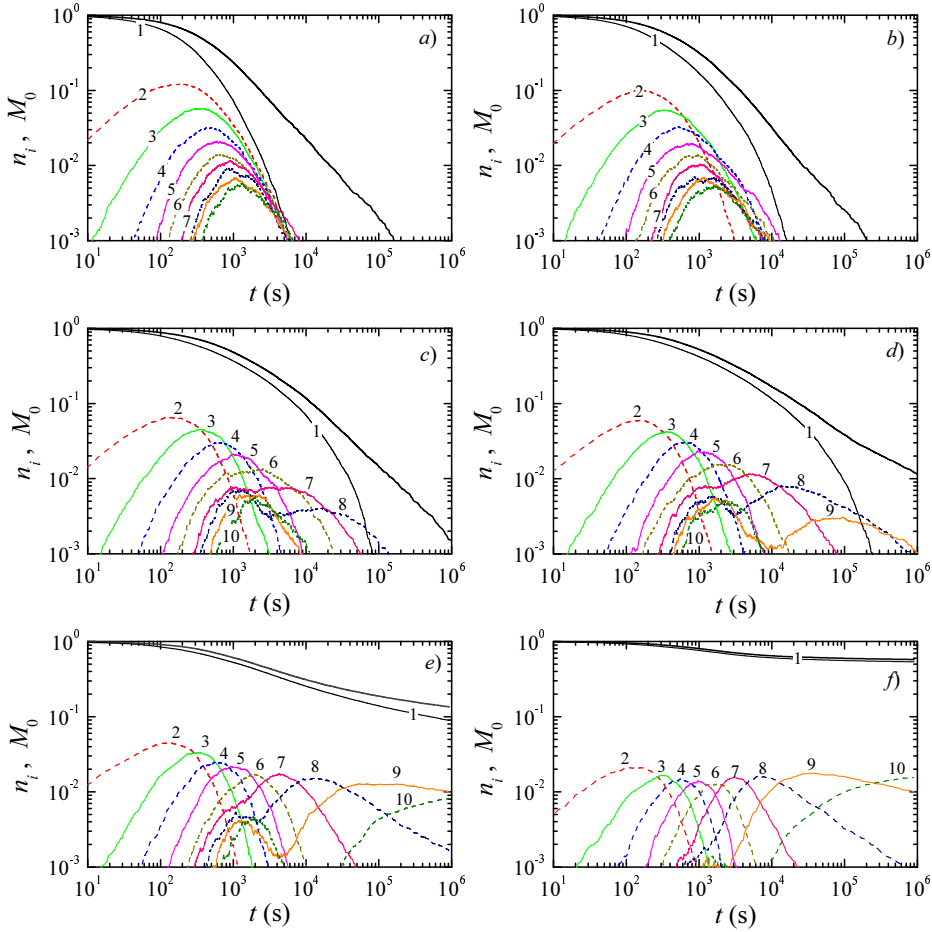


Figure 6.4.: Cluster-size distribution $n_i(t)$ up to 10-mers (thin lines, alternating between dashed and solid), and the overall number of aggregates $M_0(t)$ (thick solid line), for simulated BDLCA processes: (a) $x = 0.50$, (b) $x = 0.30$, (c) $x = 0.175$, (d) $x = 0.15$, (e) $x = 0.10$ and (f) $x = 0.05$. The numbers indicate the number of constituent particles of the clusters.

concentrations around 0.5, the system reacts until all the particles are contained in a single large cluster. When x takes low values, this unique large cluster is never formed and a large number of aggregates and monomers remain in the system (see also Fig. 6.1). Consequently, there must be a critical relative concentration x_c that divides both regions. Comparing Figs. 6.4c–e, it becomes clear that the critical relative concentration lies around $x = 0.15$. At this relative concentration, a unique large cluster could be formed, but only at extremely large aggregation times.

We start the analysis of the obtained results with a discussion of the CSDs that fall clearly in the single cluster forming region, well above x_c . At first sight, the time evolution of these CSDs seems to be very similar to the ones obtained for fast aggregating one-component systems (DLCA). There are, however, significant differences that deserve to be discussed in more detail (please see Fig. 5.6, where CSDs of ideal DLCA and BDLCA with $x = 0.5$ are plotted side-by-side). Evidently, BDLCA is always slower than DLCA since only a fraction of all cluster-cluster encounters leads to bond formation. This effect is more pronounced for the smallest clusters, especially for monomers. The latter finding may be understood as follows: at $x = 0.50$, e.g., one half of all monomer-monomer encounters occur between like particles and so, cannot give rise to dimer formation. Larger clusters, however, may collide several times during an encounter (Odrizola *et al.*, 2001b). Since they contain a similar number of particles of each type, it becomes quite likely that one of these consecutive contacts takes place between unlike particles. Consequently, two larger clusters will almost certainly aggregate once they encountered each other. This means that they behave like the sticky clusters in DLCA processes. Hence, BDLCA processes with a similar number of particles of each type are expected to cross over to DLCA after a certain time. As a consequence, there is a relative excess of monomers (*monomer discrimination*) that was already discussed in Sec. 5.3.

After having analysed the single cluster forming region, we focus our attention on the results obtained for relative concentrations well below x_c . Fig. 6.4f shows the CSD for $x = 0.05$. A very unusual aggregation behaviour is observed. For example, a large number of monomers remains in the system even at times as long as 10^6 s. These monomers are particles of the majority type that keep diffusing since they cannot find a free binding spot on a minority particle. Conse-

quently, all the minority particles must be contained inside a shell of majority particles such that any further reaction becomes practically impossible. Since these clusters cannot react any more, we refer to them as *stable aggregates*. As can be appreciate in Fig. 6.4e–f, the clusters composed by 9 and 10 particles have an extremely long lifetime and so, may be identified as such stable aggregates. These hardly reacting aggregates are analogous to the stable oligomers reported by Meakin and Djordjević (1986) for on-lattice BDLCA simulations. We postpone the discussion about the behaviour of these stable aggregates to next section.

The other plots on Fig. 6.4 show a continuous transition between the two aggregation regimes. As x decreases, the excess of monomers becomes larger and larger. In fact, for very asymmetric systems, some majority monomers remain in the system at any time (see Fig. 6.4e–f). The case with $x = 0.15$ deserves special attention because it is very close to the critical relative concentration. As can be seen comparing Fig. 6.4c and Fig. 6.4d, the total number of clusters decreases much more slowly for $x = 0.15$ than for $x = 0.175$, despite the relative small difference between their proportion of majority and minority particles. Moreover, an inflexion point is observed around $t = 10^5$ s for $x = 0.15$ which is not observed for $x = 0.175$. This means that the aggregation process slows down even further after this point. Nevertheless, it is not clear what the final stage will be. The system might react until a single large cluster is formed. However, if that happened, an extremely long time would be required. Hence, the considered aggregation process shows characteristics of both, the single and the stable cluster forming region. The inflexion point seems to be related with the point where all monomers have disappeared.

One of the most interesting features of the aggregation processes in the transition region (Fig. 6.4c–e) is observed for the 8-mers, 9-mers and 10-mers. The numbers of these oligomers go through two clearly distinguishable maxima just like the humps of a camel. This reveals that there should be two aggregation mechanisms that take place at different time scales. It should be mentioned that such a clear double peaking behaviour was not reported for on-lattice simulations. In fact, these two maxima correspond to two different oligomer compositions. As can be appreciated in the Fig. 6.5 for 8-mers, the short time maximum corresponds to clusters with two and three minority particles. The second maximum,

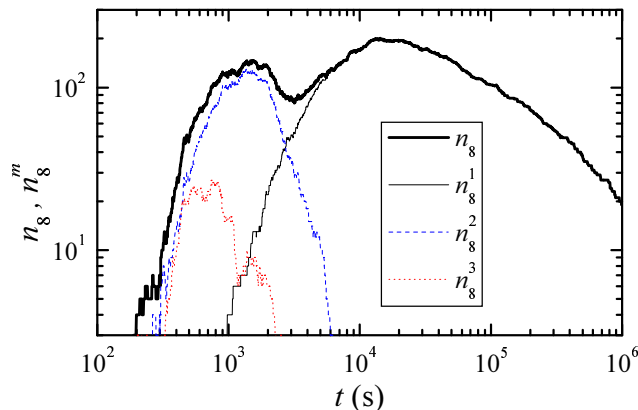


Figure 6.5.: Time evolution of the octamer-composition distribution, $n_8^l(t)$, at $x = 0.15$: $l = 1$ (thin solid line), $l = 2$ (dashed line) and $l = 3$ (dotted line). The total number of octamers, $n_8(t)$, is also plotted (thick solid line).

however, is only due to octamers containing one minority particle. A similar behaviour is found for 9-mers and 10-mers. The double peaks formation is strongly related to the formation and growth of the stable aggregates and will be discussed later.

In order to identify the critical relative concentration x_c , it is convenient to analyse the long time behaviour of the number of monomers $n_1(t)$ and the total number of aggregates $M_0(t)$. Both quantities are plotted in Fig. 6.6 for different values of x . Some free monomers are observed to remain in the system for $x \leq 0.10$. Obviously, a unique aggregate will never be achieved in this case and so, the critical relative concentration x_c must be larger than 0.10. This lower limit is quite reasonable since it falls clearly above the theoretical limit of $1/13 \approx 0.077$. The latter value is easily obtained if one takes into account that a minority particle can be covered by not more than 12 majority particles. Consequently, not all majority monomers can react if there are more than 12 majority particles per one minority particle.

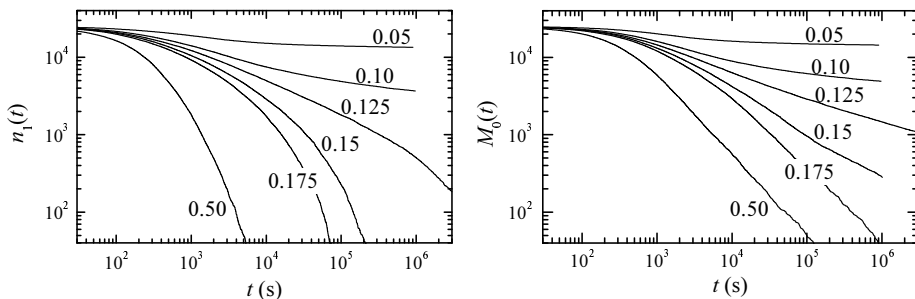


Figure 6.6.: Time evolution of the number of monomers (left) and the total number of aggregates (right) for different initial relative concentrations. The x values are indicated in the figures.

Fig. 6.6 also shows that monomers tend to disappear completely for all relative concentrations above $x \geq 0.125$. Nevertheless, this value should not be taken as an upper limit for the relative concentration x_c since all monomers could be arranged in stable aggregates that, however, will never form a unique cluster. This makes clear that the only way to determine the critical relative concentration x_c consists in analysing the time evolution of the total number of aggregates.

According to Fig. 6.6, the total number of aggregates tends towards a value above 1 for $x \leq 0.125$, while for $x \geq 0.175$, this quantity clearly tends towards 1. As was mentioned before, the results for $x = 0.15$ fall in a region where it is unclear what the final stage will be. Consequently, we can only ensure that the critical relative concentration x_c lies in the interval $]0.125, 0.175[$. It should be mentioned that AlSunaidi *et al.* (2000) obtained for the critical relative concentration an interval of $[0.190, 0.195]$ by means of on-lattice BDLCA simulations. Their interval, however, lies clearly above the interval determined in this work by means of off-lattice simulations. This implies that the minority particles are on average covered by more majority particles when the particle position is not constrained to a cubic lattice.

Special attention should be paid to the case $x = 0.125$, where all the monomers will have reacted and form part of a relatively large number of stable aggregates.

In other words, all the free majority particles will be bound in aggregates if minority particles are added to the system in a ratio of at least 15 : 100. Moreover, the production of those stable aggregates is most efficient in this case. Both findings might be useful for future industrial applications or serve as a starting point for further research (Manoharan *et al.*, 2003).

In the following section, we discuss the structure and growth of the stable aggregates that form at relative concentrations below x_c .

6.1.3. Stable aggregates

The stable clusters that remain in the system for relative concentrations below x_c are relatively small aggregates that are comprised by a few minority particles covered with a larger number of majority particles. In what follows, we will use the results for $x = 0.05$ as a representative example of the whole stable cluster forming region. Fig. 6.7 shows the cluster-size distribution profile at different times. As can be seen, the profile develops from its initial state towards a stable distribution characterised by several clearly distinguishable peaks. Each peak corresponds to aggregates with a fixed number of minority particles. We define the *order* of a cluster as its number of minority particles, *i.e.*, all clusters having the same l in the $\{n_l^i(t)\}$ set belong to the l -th order. According to the figure, the first order aggregates peak around size 9 (at $t_0 = 10^5$ s). The second and third order peaks are centred around sizes of 17 and 25, respectively. The small number of aggregates of fourth order does not allow to determine the peak position reliably. Nevertheless, they seem to peak at size 33. It is worth noting that the size differences between stable aggregates of consecutive orders are approximately equal in all cases. Here, this difference is eight particles.⁴ A schematic view of typical aggregates from first to fourth order is shown in Fig. 6.8.

In on-lattice BDLCA simulations, there are well-defined binding spots on the particle surface that are given by the structure of the employed lattice. Unreactive or stable aggregates definitely remain in the system as soon as the binding

⁴Since $33 - 25 = 25 - 17 = 17 - 9 = 8$. Furthermore, if we consider the free majority particles as “zeroth order” aggregates, what is consistent with the notation introduced here, we also have $9 - 1 = 8$.

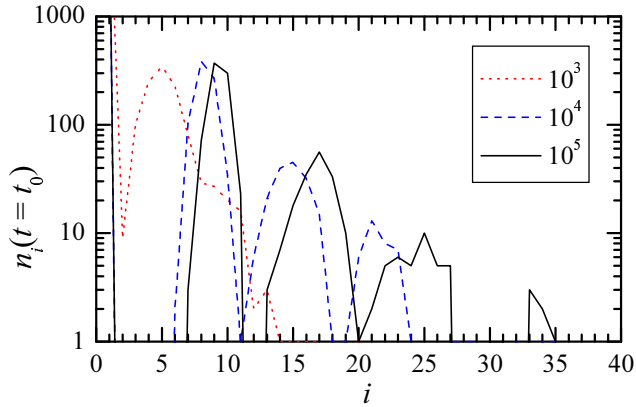


Figure 6.7.: CSD profile for simulated BDLCA with $x = 0.05$ at different times: 10^3 s (dotted line), 10^4 s (dashed line), and 10^5 s (solid line). Please note that the number of monomers falls outside the plotted range.

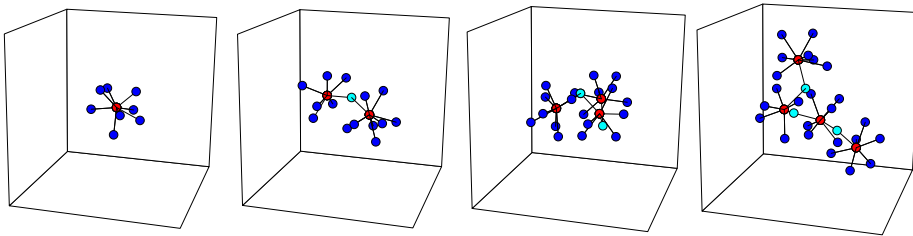


Figure 6.8.: Typical stable clusters obtained in off-lattice BDLCA simulations with $x < x_c$. Red circles represent minority particles, cyan circles represent majority particles that link two minority particles, and blue circles represent other majority particles.

sites on all minority particles are completely saturated by majority particles. At this final stage of BDLCA, the stable aggregates have a well-defined size and structure that depend on the type of the employed lattice. For a cubic lattice, *e.g.*, stable aggregates of first order are always of size 7. Second order aggregates may have two different sizes depending on the type of bond that they contain. If the two minority particles are joined through a single majority particle, then, the resulting cluster size is 13. If they contain a double bond, *i.e.*, the two minority particles bind simultaneously through two majority particles, the final cluster size is 12 (Meakin and Djordjević, 1986).

When no lattice is imposed, however, there are no well defined binding sites on the particle surface. Consequently, the structure and size of the stable aggregates is not predetermined. This implies that the stable aggregates that finally remain in the system have a wider size distribution. According to Fig. 6.7, the peaks for aggregates of first, second and third order comprise the intervals [7, 12], [13, 20] and [20, 27], respectively. The lower limit for the size of the first order aggregates can be understood if one takes into account that it is possible to saturate a minority particle with just 6 majority particles if they are located on the vertices of an octahedron centred in it. The upper limit is determined by the densest possible packing of spheres that restricts the maximum coverage of a minority particle to 12 majority particles. Nevertheless, both limiting configurations are extremely ordered and so, very unlikely to be observed in random processes such as off-lattice BDLCA. In fact, we obtained only one stable aggregate of size 7 and none of size 13 in a simulation with 25 000 particles.

Fig. 6.7 also shows that the peak structure of the CSD is well established at about $t = 10^4$ s. As time goes on, the peak positions shift slightly towards higher sizes. The peak height, however, remains approximately constant. In order to quantify this effect, we calculated the total number $N^l = \sum_{i=1}^{\infty} n_i^l$, and the average size $\langle n \rangle_l$ of all the aggregates of l -th order. The later quantity is given by

$$\langle n \rangle_l = \frac{\sum_{i=1}^{\infty} i n_i^l(t)}{N^l(t)}. \quad (6.1)$$

The obtained results are plotted in Fig. 6.9. At long times, N^l remains constant, although $\langle n \rangle_l$ slightly increases. The mean size of the aggregates of each order

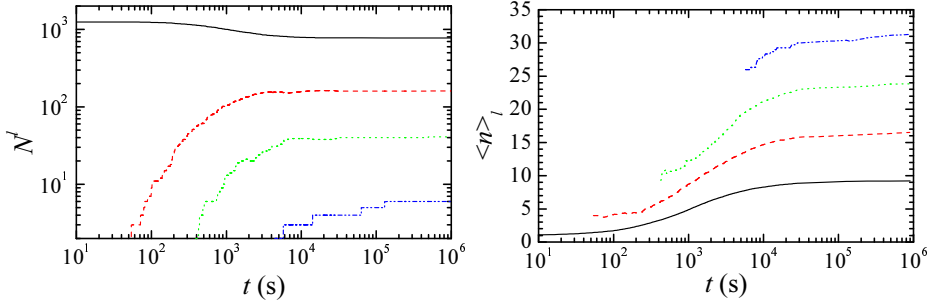


Figure 6.9.: Time evolution of the total number of aggregates of a given order (left) and their average size (right) obtained for $x = 0.05$, for different l values: $l = 1$ (solid line), $l = 2$ (dashed line), $l = 3$ (dotted line) and $l = 4$ (dash-dot-dot line).

correspond to the peak positions of the Fig. 6.7. Furthermore, the different cluster orders seem always to be approximately equally spaced, and this separation slightly increases in time. In the next subsection, we propose an aggregation model that tries to explain these findings.

6.1.4. Aggregation model for $x < x_c$

For a better understanding of the formation and growth of the stable aggregates at low x , it is convenient to study the time evolution of the total number of aggregates in the system and their average size. We exclude the monomers from these quantities in order to emphasise the behaviour of the relatively few aggregates that form. Hence, the total number of clusters excluding monomers is given by

$$M_0(t) - n_1(t) = \sum_{i=2}^{\infty} n_i(t), \quad (6.2)$$

and the corresponding average aggregate size by⁵

$$\langle n \rangle_{\text{aggr}} = \frac{N_0 - n_1(t)}{M_0(t) - n_1(t)}. \quad (6.3)$$

⁵Do not confuse this quantity with the average cluster-size, $\langle n \rangle_n$.

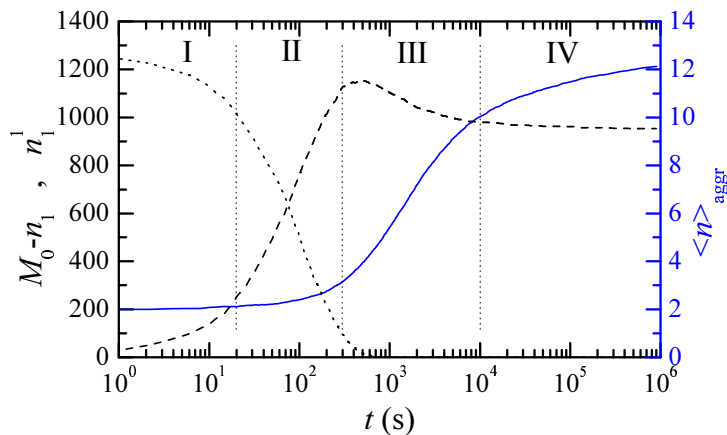


Figure 6.10.: Time evolution of the number of free minority particles $n_1^1(t)$ (dotted line, left scale), the total number of clusters composed by more than one particle (dashed line, left scale) and their average size (solid line, right scale) for BDLCA with $x = 0.05$. The vertical dotted lines approximately indicate the different aggregation stages.

These two quantities and the number of free minority particles are plotted in Fig. 6.10 for simulated BDLCA processes at $x = 0.05$. The curves allow us to distinguish several regions, labelled by roman numerals (López-López *et al.*, 2005).

During the early stages of the aggregation (stage I) the only possible reaction is dimer formation between minority and majority monomers. At very short times, $t \lesssim 20$ s, the number of minority monomers does not differ very much from its original value. This is the stage where the HHF approximation holds. Later (stage II), the total number of clusters increases quite fast while the average cluster size remains close to two. This process continues until the free minority monomers disappear at approximately $t = 3 \times 10^2$ s. At this time, the total number of aggregates reaches almost the number of minority particles. Consequently, all the minority particles have now reacted and are contained in small clusters. Only

a very small number of larger aggregates may have formed so far and most of them are of first order.

In the following region (stage III), the average cluster-size starts to increase quite rapidly, whilst the total number of aggregates decreases slightly. This means that the aggregates formed, which we call first order seeds, grow mainly due to addition of further majority particles. A few first order seeds, however, react among themselves forming aggregates that contain more than one minority particle. These higher order seeds will have a size of approximately a multiple of the average cluster size at that moment. This explains why aggregates of size 8 start to appear in the system when the predominant size of the first order seeds lies around 4 (see Figs. 6.4*f* and 6.9). Evidently, the octamers formed at that stage will be mostly second order seeds.

The next aggregation stage (IV) starts at approximately $t = 10^4$ s. At that time, the total number of clusters reaches a plateau while the average cluster size remains still somewhat increasing. This implies that the seeds do not react anymore among themselves but their size still increases due to the addition of free majority monomers. Consequently, some majority monomers still find some open spots on the surface of the seeds where they can attach to the core particles. At this stage, the above mentioned second order octamers will have grown up to fully developed second order aggregates with a size close to 17. At the same time, however, further octamers appear due to monomer addition to first order heptamers. This means that there are two octamer forming mechanisms that occur at very different time scales: a) relatively fast second order seed formation and b) quite slow first order seed completion. The combination of both mechanisms explains the camel-hump-like maxima mentioned in Sec. 6.1.2 (see Fig. 6.5). The first mechanism is of course the more pronounced the more minority particles are present in the system. The second mechanism occurs mainly when the number of first order seeds is much smaller than the number of majority particles. Close to the critical relative concentration x_c , the effect of both mechanisms is of the same order and this is why the camel-hump-like peaks in the CSD are observed best at $x = 0.15$.

Finally, aggregation stops once all the holes on the surface of the seeds have disappeared. Our simulations, however, can not unquestionably state this fi-

6. ASYMMETRIC HETEROAGGREGATION

nal point, but they give clear evidence. In summary, the proposed aggregation scheme for BDLCA processes for relative concentrations below x_c comprises the following five stages:

- I HHF stage: fast reactions between unlike monomers form dimers.
- II Seed formation stage: dimers keep being formed. They grow by adding further majority particles and become first order seeds. This stage ends when all free minority monomers have disappeared.
- III Seed aggregation stage: some first order seeds react among themselves forming higher order seeds. Simultaneously, all aggregates keep growing by adding majority monomers.
- IV Seed completion stage: the seeds are so highly covered that they cannot react any more among themselves. Nevertheless, they still can grow by adding majority monomers.
- V Stable aggregate stage: all the clusters are completely coated by majority particles. Aggregation comes to an end.

This aggregation scheme is representative for all the simulated BDLCA processes for relative concentrations clearly below x_c . However, the moments at which these stages start and end, depend on the initial relative concentrations.

6.2. Experimental evidences of stable aggregates

6.2.1. CSD in asymmetric two-component systems

In all the electrostatic heteroaggregation experiments discussed in Chap. 4 and Chap. 5, the systems were symmetric, *i.e.*, there was approximately the same concentration of positively and negatively charged particles. Nevertheless, the BDLCA simulations of Sec. 6.1 indicate that the formation of stable aggregates and related phenomena (such as the “two-hump effect”) takes place in asymmetric two-component systems. Consequently, some asymmetric heteroaggregation experiments were carried out. The single-cluster light-scattering technique was

used to measure the time evolution of the cluster-size distributions. Aggregation was started by mixing equal volumes of diluted dispersions of IDC and AS1 latexes (see Sec. 3.3). The particle concentration of the reactants was chosen to be different in order to obtain the desired x value and a final particle concentration about $8 \times 10^7 \text{ cm}^{-3}$. More details about the mixing process and the measuring protocol can be found in Sec. 3.1.3.

In Fig. 6.11, the experimental CSDs corresponding to four different relative concentrations of cationic particles are plotted. The dispersion medium of these experiments was ultrapurified water, with no added electrolyte. Hence, it is expected that long-range electrostatic particle-particle interactions are present. The dependence of the experimental CSDs on the relative concentration of particles, x , is quite important (please compare the plots in Fig. 6.11 among themselves and with those of Fig. 5.4). Clear differences are found in the monomer concentration curves. Since reactions between like particles are not allowed, there is an important excess of monomers with respect of the concentration of clusters. This excess is more important the more asymmetric the system becomes. Another quite noticeable difference is that the aggregation process stops completely for $x = 0.15$. This does not occur in the complementary case ($x = 0.85$), revealing that both types of particles are not equally charged. It is also quite noticeable the presence of stable aggregates in some experiments. This is the case for tetramers at $x = 0.75$ and pentamers and hexamers at $x = 0.85$. But probably the most striking finding is that some n -mer concentration curves are not bell-shaped (please see, especially, the pentamer curve at $x = 0.75$ and, in less extend, the hexamer curve at $x = 0.85$). In what follows, three of these features, namely, the monomer excess, the stopped reactions and the “two-hump effect”, are discussed. The experimental evidences of stable aggregates will be discussed in Sec. 6.2.2.

Monomer excess

In Sec. 6.1.2 we demonstrated that the sole presence of a “contact rule” which prevent the reaction between like particles is enough to provoke this monomer excess. The BDLCA simulations also reflect that the monomer excess is larger for very asymmetric systems. On the other hand, this kind of simulations are

6. ASYMMETRIC HETEROAGGREGATION

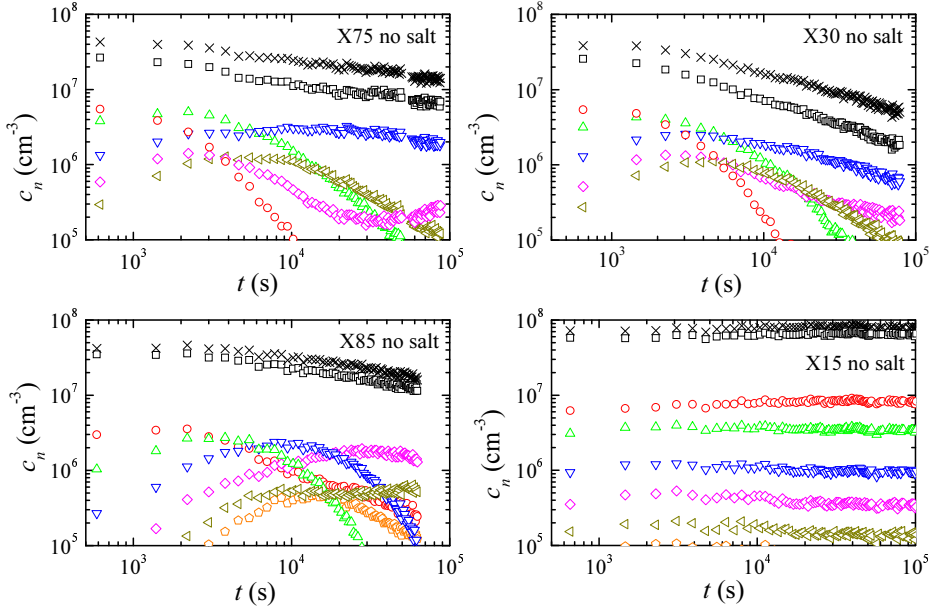


Figure 6.11.: Experimental CSDs for asymmetric mixtures of cationic and anionic colloids. In each plot, the concentration of j -mers ($j = 1$ □, $j = 2$ ○, $j = 3$ △, $j = 4$ ▽, $j = 5$ ◇, $j = 6$ ◁ and $j = 7$ ▷) and the overall concentration of clusters (×) are plotted.

strictly valid only in situations where the range of the particle-particle interactions is short if compared with the particle radius. This is not the case of the experiments, since no electrolyte was added and, so, the electrical double layers are expected to reach out substantially into the surrounding medium. Nevertheless, it is still true that reactions between like particles are not possible in the experiments. Hence, we claim the monomer excess found in asymmetric experiments to be due to this restriction in the possible monomer-monomer reactions. Please, note that a monomer excess—or *monomer discrimination*—was also found in electrostatic heteroaggregation experiments with *symmetric* systems at low and intermediate salt concentrations (López-López *et al.*, 2004b). The fact that the monomer discrimination becomes more relevant for more asymmetric

systems, is indeed supporting the hypothesis defended here.

Stopped reactions

The cluster-size distribution measured for a mixture of 15% cationic particles and 85% anionic particles, aggregating in a medium with no added salt, is quite interesting (Fig. 6.11*d*). Apparently, it reflects a slightly aggregated system, with a stationary cluster-size distribution. Accordingly to the figure, one could think that no aggregation had taken place at all. Nevertheless, SCLS measures of the initial aggregation state of both latexes before the mixing process demonstrate clearly that this is not the case. The dimer concentration after the mixing, for instance, rise to four times its initial value. For larger aggregates, the relative increment is even larger (eight times for trimers, five times for tetramers, and so on). And, obviously, the monomer concentration decreases accordingly. Hence, the actual description of the process comprises two steps: i) a very fast initial aggregation, and ii) a stationary cluster-size distribution.

Puertas *et al.* (2001*a*) found a similar behaviour —which they called “stopped reactions”— in asymmetric mixtures of oppositely charged colloids, when the majority particles bear a higher electrical charge than the minority ones. These authors used dynamic light-scattering to monitor the early stages of the aggregation process, and found that, after an initial aggregation, the process rapidly stopped. They proposed that the stationary state is composed by a large number of majority particles and some dimers with practically the same charge as the majority particles. The aggregation does not proceed because the resulting state is electrostatically stable.

The stabilisation mechanism proposed by Puertas *et al.* (2001*a*) can also explain our results. The low-angle light-scattering study of homoaggregation stability of both latexes versus the concentration of KBr (Tab. 3.1 and Fig. 3.11), established that the critical coagulation concentration is higher for the anionic latex (AS1) than for the cationic one (IDC). Therefore, and according to the DLVO theory, the anionic particles bear a higher electrical charge than the cationic ones. Effectively, the stopped reactions are found when the proportion of cationic particles is $x = 0.15$, but not in the complementary case, for $x = 1 - 0.15 = 0.85$.

Nevertheless, we found that the final state is composed not only by monomers and dimers, but also by larger clusters such as trimers and tetramers. This could be due to the fact that the difference between the CCCs of our systems is not as large as it was between the systems used by Puertas *et al.* (2001a) in their study.⁶ Hence, it is more likely that more than one majority particle attach to a single minority particle before the electrostatic stabilisation of the system. Additionally, the experimental technique used by Puertas *et al.* (2001a) only provides average information about the cluster-size distribution and, so, it is possible that also in their experiments some larger clusters were present in the system.

Two-hump effect

Non bell-shaped cluster-concentration curves have been measured in asymmetric systems where the concentration of cationic particles —the less charged ones— is larger than the concentration of anionic particles. Fine examples of this phenomenon are: the pentamer curves obtained for $x = 0.75$ (Fig. 6.11) and $x = 0.90$ (Fig. 6.12a), and the hexamer curve at $x = 0.90$ (Fig. 6.12b). In all these cases, the n -mer concentration grows initially until it reaches a maximum, then it decreases for some extend and, finally, it increases again. It is likely that at even longer times, $c_n(t)$ will decrease again. The limited duration of the experiments, however, does not allow us to confirm the presence of a second maximum in the n -mer concentration. Anyhow, the $c_n(t)$ listed above are, to the best of our knowledge, the first experimental confirmation of the two-hump effect discussed in Sec. 6.1.2 and Sec. 6.1.4.

The aggregation model proposed in Sec. 6.1.4 can explain this phenomenon. We think that the non bell-shaped n -mer concentration curves are due to a change in the composition of the n -mers. Let us focus, for example, in the $c_6(t)$ curve of one of the experiments at $x = 0.90$ (Fig 6.12b). The hexamers that are formed during the early stages contain mainly two anionic particles and four cationic ones while those formed at longer times are composed by only one anionic particle coated with five anionic colloids. Using the notation introduced in Sec. 6.1.4, the former

⁶The CCCs the cationic and anionic particles that we used in this work are 180 mM and 320 mM, respectively. The CCC of the particles used by Puertas *et al.* (2001a) —at pH=7, where they reported stopped reactions— were 200 mM and 700 mM for the positively and negatively charged particles, respectively.

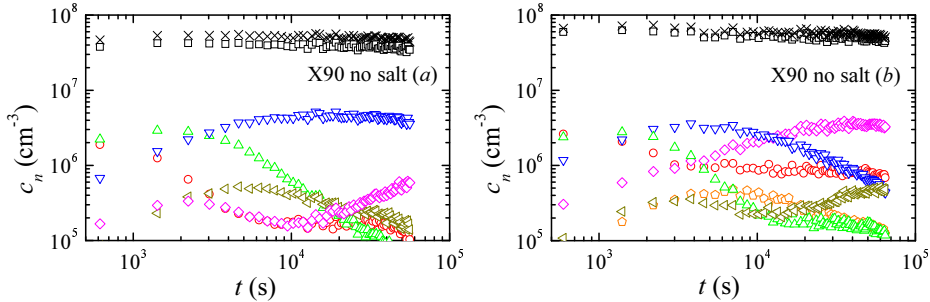


Figure 6.12.: Experimental CSDs for two highly asymmetric mixtures of cationic and anionic colloids, with $x = 0.90$. The meaning of the symbols is the same as in Fig. 6.11.

are second order seeds and the later are first order stable (or metastable) aggregates. Two mechanisms lead to the two different kinds of hexamers. On the one hand, $(4 + 2)$ -hexamers are formed by the reaction of two small aggregates, typically two trimers with one anionic and two cationic particles each one. On the other hand, $(5 + 1)$ -hexamers are typically formed by the addition of one cationic particle to a $(4 + 1)$ -pentamer. The second reaction is clearly more difficult, since the four cationic particles already present in the pentamer difficult the attachment of another cationic particle. This fact explains why $(5 + 1)$ -hexamers are formed at longer times. Additionally, these hexamers are quite stable because the addition of a sixth cationic particle to the aggregate is quite difficult. Unfortunately, the SCLS technique does not allow us to distinguish the composition of the clusters and, hence, we cannot undoubtedly state that a composition change is taking place. This could be done, for instance, using optical microscopy combined with fluorescent-marked microspheres, as reported Kim *et al.* (2003) in their very remarkable work about electrostatic heteroaggregation.

6.2.2. Stable aggregates in experiments

Aggregates with an important stability have been found in highly asymmetric systems where the concentration of cationic particles —the less charged ones—

6. ASYMMETRIC HETEROAGGREGATION

is larger than the concentration of anionic particles. Examples of aggregates of high stability are: tetramers for $x = 0.75$ (Fig. 6.11a) and $x = 0.90$ (Fig. 6.12a), and pentamers for $x = 0.85$ (Fig. 6.11c) and $x = 0.90$ (Fig. 6.12b). It should be noted that real stable aggregates can never be formed in real heteroaggregation processes, since even one-component systems slowly flocculate when they are not perturbed for several weeks.⁷ Hence, when we speak about “stable aggregates” in experiments, we refer to aggregates with a long lifetime.

The simulation study of the ideal BDLCA carried out in Sec. 6.1 has shown that the sizes of the stable aggregates are restricted to some regions, that correspond to aggregates of the same order, *i.e.*, aggregates having the same number of minority particles. This finding, however, is not appreciable in the CSD graphs shown in Fig. 6.11 and Fig. 6.12, because the $c_n(t)$ curves are plotted only up to $n = 7$.⁸ In order to check whether there is a second size range of stable clusters, we study directly the pulse area histograms obtained at different times. For further details about the meaning of the pulse area histograms, please see Sec. 3.1.2).

Fig. 6.13 shows three pulse area histograms corresponding to a heteroaggregation experiment. In this experiment, the relative concentration of cationic particles was $x = 0.90$ and no electrolyte was added.⁹ In order to improve data statistics, each one of the histograms was obtained as an average of three consecutive SCLS measurements.¹⁰ In the histogram for short times the cluster-size profile is almost monotonous, although it is already appreciable that the concentration of trimers and tetramers surpasses the concentration of dimers slightly. At intermediate times, most clusters are concentrated around two different size

⁷Nevertheless, this slow flocculation is reversible, as stated in Sec. 3.3.1.

⁸In fact, in Fig. 6.11a–b and Fig. 6.12a, CSDs are plotted only up to $n = 6$, because the non-linear light-pulse classifying method (see Sec. 3.1.2) was not implemented yet.

⁹It is indeed the same experiment whose cluster-size distribution was plotted in Fig. 6.12b. Please notice that only the concentrations of clusters composed by up to seven particles were displayed in that figure. Nevertheless, the pulse area histograms clearly show that clusters composed by 8, 9 and 10 particles were also distinguishable in the measurements.

¹⁰The pulse area histogram corresponding to $t \approx 1.5 \times 10^4$ s, for instance, was calculated as the average of the measured histograms obtained at times 14 245 s, 15 048 s and 15 851 s. Furthermore, each measurement collects data during 512 s. Hence, the histograms shown in Fig. 6.13 have to be understood as time averages of the actual pulse intensity histograms.

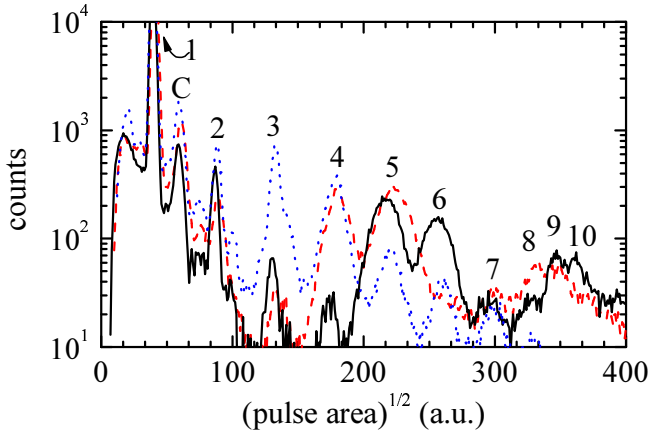


Figure 6.13.: Pulse area histogram for an asymmetric system ($x = 0.90$) with no added salt at times $t \approx 10^3$ s (dotted line), $t \approx 1.5 \times 10^4$ s (dashed line), and $t \approx 10^5$ s (solid line). Each histogram is the average of three consecutive measurements. The numbers on top of the peaks indicate the corresponding cluster size. The ‘C’ peak is caused by monomer coincidences. Please note that the monomer peak falls outside the plotted range.

intervals: 4–5 and 8–9. Clusters with an intermediate size, *i.e.*, 6-mers and 7-mers, practically do not exist. Comparing this experimental histogram with the cluster-size profiles obtained in simulations of BDLCA processes (Fig. 6.7), a qualitative agreement is found. Hence, it is reasonable to assume that the first stability region (4-mers and 5-mers) corresponds to clusters of first order, while the second stability region (8-mers and 9-mers) corresponds to clusters of second order. It is worth noting that the size difference between the monomers and the stable aggregates of first order is the same that the size difference between the first second order clusters. This results is also in qualitative agreement with our BDLCA simulations, and can be explained in terms of the model described in Sec. 6.1.4.

At longer times, the size of the clusters with a large kinetic stability increases and the first stability region —presumably, first order aggregates— shifted to

5-mers and 6-mers, and the second region —second order aggregates— to 9-mers and 10-mers. Please recall that also in ideal BDLCA processes, the size of the clusters with high stability slightly increases before it reaches its final value (Sec. 6.1.3 and Fig. 6.9*b*). The qualitative agreement between simulations and experiments allows us to conclude that the experimentally observed size shift of the stable clusters is due to a slow attachment of majority monomers. A quantitative agreement is, however, not expected to be achieved, since the clusters with large stability found in the experiments are composed by a smaller number of particles than those formed in BDLCA simulations.

6.2.3. Influence of the electrolyte concentration

According to Vincent *et al.* (Vincent *et al.*, 1980; Luckham *et al.*, 1983), there are two sets of interactions which must be considered in heterocoagulation. These are the initial interactions expected between the approaching oppositely charged particles; and the increasing lateral interactions which occur between the adsorbed particle layer. Lateral interactions will affect the extent of coverage, because of the repulsion of identical double layers. Hansen and Matijević (1980) studied the extent of the adsorbed layer and calculated the number of small particles that adsorb onto a larger particle. An increase of the electrolyte concentration give rise to a larger maximum coverage (Hansen and Matijević, 1980; Vincent *et al.*, 1980), due to decreasing lateral repulsion forces. These authors studied two-component systems with high size-asymmetry in which the small particles adsorb onto the surface of the larger ones. Nevertheless, their theory should also be applicable to the case of equally sized particles.

The ideal BDLCA regime simulated in Sec. 6.1, where the range of the lateral repulsion is negligible if compared with the particle radius, is somehow an ideal situation. In real experiments, homo- and hetero-aggregation take place simultaneously when the electric double layers are compressed. Hence, some lateral repulsion between like particles must exist that prevents homoaggregation. In summary, the stable aggregates formed in real life binary colloidal dispersions are expected to be smaller than those formed in ideal BDLCA processes. More-

over, the sizes of the stable aggregates will most likely decrease as the particle-particle interaction range increases.

The discussion given above explains the quantitative discrepancy between the size of the stable clusters formed in electrostatic heteroaggregation experiments (5-mers and 6-mers) and the corresponding aggregates obtained in ideal BDLCA processes (9-mers and 10-mers). It also may explain the relatively large differences between two runs of the same experiment, namely, those plotted in Fig. 6.13. According to Fig. 6.13*a*, the tetramers are quite stable while the pentamer concentration presents a two-hump like curve. In contrast, the stable aggregates in Fig. 6.13*b* are the pentamers, and the two-hump effect is observed for the hexamer concentration. This implies most likely that the particle-particle interaction range was longer in case (*a*) than in case (*b*). Both experiments were performed in absence of any added electrolyte and, hence, even very little impurities could change the electric double layer thickness quite dramatically.

In order to check this explanation, Brownian dynamics simulations with interactions have been performed (details about these simulations were given in Sec. 3.4.2, please see also Puertas *et al.*, 1999*a*). The cluster-size distributions obtained from two of these simulation runs are plotted in Fig. 6.14. The relative concentration of particles is $x = 0.10$, the dimensionless Debye screening parameter was set to $\kappa a = 1.0$ (figure *a*) and $\kappa a = 2.0$ (figure *b*). For the remaining parameters, the values indicated in Sec. 3.4.2 were used.

The similarities between the CSDs plotted in Fig. 6.14 and those plotted in Fig. 6.12 are quite surprising. Nevertheless, no attempt of parameter fitting has been carried out. On the one hand, the simulated CSD for $\kappa a = 1.0$ exhibits high stability for tetramers and a two-hump effect for pentamers. Both features were also found in the experiment shown in Fig. 6.12*a*.¹¹ On the other hand, the pentamers of the simulation for $\kappa a = 2.0$ (Fig. 6.14*b*) exhibit a high stability, as they did in the experiment plotted in Fig. 6.12*b*. This qualitative —and even quantitative— agreement between simulations and experiments strongly supports our conclusion regarding the influence of lateral forces on the size of the stable aggregate.

¹¹The heptamers of this simulation also exhibit a high degree of stability. Unfortunately, this feature can not be compared with the experimental CSD shown in Fig. 6.12*a*. In early SCLS measurements, heptamers still felt outside the detection range of the instrument.

6. ASYMMETRIC HETEROAGGREGATION

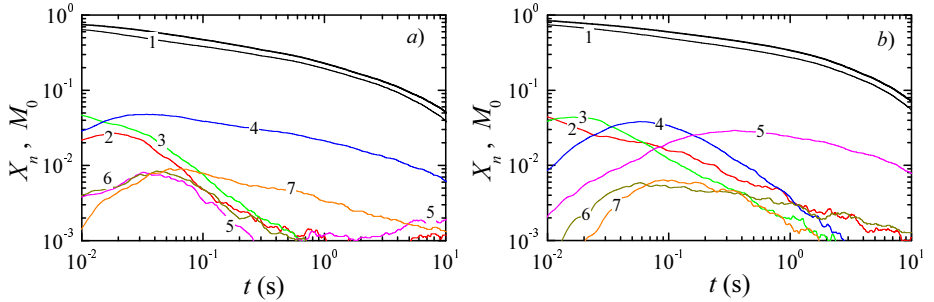


Figure 6.14.: Simulated cluster-size distributions, up to heptamers, obtained by Brownian dynamics simulations with interactions. The relative concentration of particles is $x = 0.10$ and the dimensionless Debye screening parameter is: (a) $\kappa a = 1.0$ and (b) $\kappa a = 2.0$. In each plot, thin lines are $X_n = N_n/N_0$ (n is indicated by a number) and the thick line is the overall concentration of clusters, M_0 .

6.3. Concluding remarks

Ideal binary diffusion-limited cluster-cluster aggregation processes were studied by means of off-lattice simulations. The fundamental role played by the relative concentration, x , was investigated for both, short and long aggregation times. At short aggregation times, the predominant reaction is dimer formation due to bond formation between two unlike particles. In this region, the effective dimer formation rate constant, $k_s(x)$, follows the parabolic behaviour predicted by the HHF approximation.

At long aggregation times, the aggregation behaviour is highly dependent on x . For $x > x_c \approx 0.15$, aggregation continues until a single cluster is formed. In this region, the time evolution of the CSD is somewhat similar to the well-known DLCA processes. The main difference was found to be an excess of monomers that is observed even for $x = 1/2$. This monomer excess seems to be identical to the monomer discrimination recently found in electrostatic heteroaggregation arising in oppositely charged colloids at low electrolyte concentrations (please see Chap. 5.3 and López-López *et al.*, 2004b). In other words, our BDLCA

simulations show that monomer discrimination may occur even in absence of any particle-particle interaction.

At x values close to x_c , an atypical time evolution was found for oligomers composed by 8 to 10 particles. Their number reached two maxima at different time scales. These maxima were shown to correspond to clusters with two different compositions. At short times, these clusters contains several minority particles. At long times, however, they are composed of only one minority particle covered by several majority particles. Such as behaviour was not reported for on-lattice BDLCA simulations.

At relative concentrations below x_c , stable aggregates remain diffusing in the system and a single cluster is never formed. In on-lattice simulations, the size and structure of these stable aggregates is restricted to a few fixed values that are determined by the geometry of the lattice imposed. In off-lattice simulations, however, the stable aggregates group in wider bell-shaped distributions that correspond to clusters with a given number of minority particles. Furthermore, the minority particles are on average covered by more majority particles. Consequently, the critical relative concentration x_c was found to be far lower than in on-lattice simulations. Additionally, we developed a five stage model for a suitable description of the formation and growth of stable aggregates in the low x region. Our model also explains the “two hump effect” for the oligomers.

SCLS experiments have been carried out in asymmetric mixtures of cationic and anionic particles with no added electrolyte. The time evolution of the corresponding cluster-size distributions was found to depend quite strongly on the relative particle concentration, x . The most interesting results are found in highly asymmetric systems: for $x \lesssim 0.2$ and $x \gtrsim 0.8$.

At $x = 0.15$, when the number of the highly charged anionic particles exceeds the number of the cationic particles, a stopped reaction is found. In this case, the process stopped almost immediately after some initial aggregation. n -mers with $n \leq 7$ are rapidly formed at the very early stages of the aggregation and then, a stationary cluster-size distribution is achieved. The presence of stopped reactions can be explained in terms of the charge stabilisation mechanism proposed by Puertas *et al.* (2001a).

6. ASYMMETRIC HETEROAGGREGATION

When the number of cationic particles prevails, however, we found the same interesting phenomena observed in BLCA simulations at $x \lesssim x_c$, *i.e.*, two hump effect and aggregates with high kinetic stability. According to the simulation results, we claim the two hump effect to be due to a change in the composition of clusters of a given size during the aggregation process. It should be noted that, to the best of our knowledge, this is the first time that a non bell-shaped n -mer concentration curve is reported.

Highly stable aggregates are found in at least two precise size-ranges that are approximately equally spaced. The average size of the clusters of these stability size-intervals slightly increases with time. Both effects can be qualitatively explained with the stable-aggregate formation model developed for simulated BDLCA processes. Nevertheless, the quantitative comparison fails and the size of stable aggregates found in the experiments were systematically smaller than the size of the stable aggregates formed by simulated BDLCA processes. The critical relative concentration x_c could not be determined from our SCLS experiments because a large number of long-time measurements would be required. Nevertheless, it could be as large as 0.25, since the stability of tetramers found in experiment with 25% of anionic particles seems to be large enough for considering these tetramers as stable aggregates. Hence, also here we find a quantitative discrepancy between experiments and simulations.

We suggest the quantitative discrepancies to be due to lateral repulsions between like particles which prevents the attachment of other particles of the same species (Vincent *et al.*, 1980). This means that i) stable aggregates are composed by a smaller number of particles and ii) a larger number of unbound majority particles remain in the system. The second point explains why the critical relative concentration x_c is larger in experiments than in ideal BDLCA processes. In any case, our simulations of ideal BDLCA processes give a clear idea about what one expects in the limit of pure contact forces, *i.e.*, extremely short range interactions.

Finally, Brownian dynamics simulations with particle-particle interactions have been performed for highly asymmetric systems. It could be shown that the long-range interactions decrease the size of the stable aggregates. This effect becomes

more significant as the interaction range increases. Moreover, a good qualitative agreement between these simulations and the corresponding experimental cluster-size distributions was found. This explains the discrepancies between experiments and ideal BDLCA processes. Therefore, we expect that the size of the stable aggregates formed in electrostatic heteroaggregation experiments increases as the electrolyte concentration does. This could, however, only be observed if the electrolyte concentration is low enough to prevent homoaggregation. Future work on that direction is planned to be done.

7. SUMMARY AND CONCLUSIONS

This PhD thesis is devoted to the study of the heteroaggregation between equally sized but oppositely charged colloidal particles. Both, aggregation rates and kinetic behaviour are studied as a function of the range of the electrostatic interactions and of the relative concentration of both species x . Two complementary approaches have been followed. On the one hand, heteroaggregation processes arising in mixtures of polymeric colloidal dispersions have been monitored by means of single-cluster light scattering (SCLS). On the other hand, Brownian dynamics simulations (BDS) have been performed. The following paragraphs briefly summarise the main points of is work.

Characterisation of the systems and improvements of the single-cluster light scattering set-up

- ✓ The data acquisition software of our SCLS instrument has been rewritten. A non-linear pulse-classifying algorithm has been developed that increases the maximum resolvable cluster-size from 6–7 to 9–11. Other improvements comprise a real time representation of the aggregation state, and a cluster break-up detection algorithm.
- ✓ SCLS has shown to be suitable for monitoring real heteroaggregation processes. A measuring protocol for performing reproducible measurements of the cluster-size distribution (CSD) has been established.
- ✓ Two model colloidal dispersions of equally sized but oppositely charged particles, have been selected. Transmission electron microscopy, low-angle static light-scattering and electrophoretic mobility measurements

7. SUMMARY AND CONCLUSIONS

have been carried out in order to characterise them completely. The critical coagulation concentration (CCC) of the cationic latex was found to be smaller than the CCC of the anionic sample.

- ✓ The homoaggregation behaviour of both, anionic and cationic particle dispersions, has been studied by means of SCLS. It has been shown that both samples behaves regularly —according to the DLVO theory predictions— when KBr is added. Nevertheless, non-standard behaviours (and even reversible aggregation) have been found when different electrolytes have been added.

Heteroaggregation rate of symmetric two-component colloidal dispersions

- ✓ The effective heteroaggregation rate constant k_S has been measured for electrolyte concentrations ranging over six orders of magnitude. The absolute heteroaggregation rate constant k_{AB} has been obtained from k_S by applying the HHF approximation. k_{AB} was found to decrease continuously for increasing electrolyte concentrations. k_S , however, was found to exhibit a minimum at intermediate electrolyte concentrations.
- ✓ At high electrolyte concentrations, well above the CCCs of the reactants, both k_S and k_{AB} approach the Brownian aggregation rate k_{11}^{Brw} . This indicates that the particle-particle interactions of electrostatic origin are completely screened. This finding is in good agreement with the DLVO-HHF theory predictions.
- ✓ At intermediate electrolyte concentrations, k_S takes values below the Brownian aggregation rate. On the contrary, k_{AB} still remains of the same order than k_{11}^{Brw} . Hence, the decrease of k_S has to be due to a decreasing homoaggregation rate. The DLVO theory predicts an energy barrier between like particles below the CCC that is responsible for this effect.
- ✓ At low electrolyte concentrations, a plateau is found where k_S approaches again k_{11}^{Brw} . We claim that selective heteroaggregation is taking place in this region, although the particle-particle interactions are still short-ranged.

The existence of such a plateau is predicted by the DLVO-HHF theory for relatively large colloids, as those used in this study.

- ✓ At very low electrolyte concentrations ($\lesssim 1$ mM), k_S is found to increase extraordinarily. In fact, when no electrolyte was added, k_{AB} was found to be $(35 \pm 7) \times 10^{-12} \text{ cm}^3 \text{ s}^{-1}$. This is the largest value ever measured. Hence, long-range attractive interactions have to be acting. This is indeed predicted by the DLVO-HHF theory. It is worth noting that a good quantitative agreement was found between the measured and theoretical k_S values, despite the fact that no parameter fitting procedure was carried out.
- ✓ BDS have been performed in order to complement the SCLS experiments. A general qualitative agreement was found, although some significant differences were found. Especially the plateau region at low electrolyte concentrations could not be reproduced by the simulations. This could be a size effect, although further work is needed to clarify this point.

Electrostatic heteroaggregation regimes for symmetric two-component colloidal dispersions

- ✓ The time evolution of the CSD of electrostatic heteroaggregation processes has been monitored by means of SCLS. The shape of the CSD was found to depend strongly on the electrolyte concentration. Experimental CSDs were compared with BDS and with solutions of the coagulation equation for several semiempirical *kernels*. From this study, at least three clearly different aggregation regimes could be observed.
- ✓ At high electrolyte concentrations, well above the CCC of the reactants, heteroaggregation behaves as if it were a one-component colloidal system undergoing diffusion-limited colloidal aggregation (DLCA). An excellent agreement between the experimental and simulated CSDs was found. As expected, both are perfectly described by the solution of the coagulation equation with the Brownian *kernel*.

7. SUMMARY AND CONCLUSIONS

- ✓ At intermediate electrolyte concentrations selective heteroaggregation takes place, although the range of the particle-particle interactions is still negligible with respect to the particle radius. Then, heteroaggregation follows a novel binary diffusion-limited colloidal aggregation (BDLCA) regime. The CSD is characterised by an excess of monomers (“monomer discrimination”) that is mainly due to the selection rules that govern the monomer-monomer reactions. An excellent agreement between simulated and experimental BDLCA processes was found. Monomer discrimination could be reproduced by some semiempirical *kernels*, in which the monomer-monomer reaction rate constant takes half the DLCA value. The best quantitative agreement was found for the Brownian q -sum *kernel* with $q = 1/2$.
- ✓ At low electrolyte concentrations, long-range particle-particle interactions are present and the corresponding colloidal aggregation regime is said to be attraction-driven (ADCA). At very low electrolyte concentrations, dimers are found to disappear faster than other clusters (“dimer discrimination”). BDS of ADCA processes predict an even-odd cluster discrimination in such a way that clusters composed by an even number of particles disappear faster. We could confirm this experimentally for monomers and dimers.

Electrostatic heteroaggregation processes arising in asymmetric two-component colloidal dispersions

- ✓ The influence of x on ideal BDLCA processes has been investigated by means of off-lattice BDS. At short aggregation times, $k_S(x)$ follows the parabolic behaviour predicted by the HHF approximation. At long aggregation times, a critical relative concentration x_c exists such that aggregation continues until a single cluster is formed for $x > x_c$. For $x < x_c$, however, some stable aggregates remain diffusing in the system. We estimated x_c to be approximately 0.15. This value is far lower than the value predicted by on-lattice BDS simulations. Such a discrepancy reveals a larger extent of particle coating when no lattice is imposed.
- ✓ At x values close to x_c , an atypical time evolution of oligomers composed by 8 to 10 particles was observed. The number of these aggregates reached

two maxima at different time scales (“two-hump effect”). We could prove that these maxima correspond to two different aggregate compositions: several minority particles per cluster at short times and just one minority particle per cluster at long times. This behaviour was not reported for on-lattice BDLCA simulations.

- ✓ SCLS experiments have been carried out in asymmetric mixtures of cationic and anionic particles with no added electrolyte. Since the anionic particles bear a higher electric charge than cationic colloids, different phenomena arise at $x \lesssim 0.2$ and $x \gtrsim 0.8$. In the former case, the process stopped rapidly after some initial aggregation. In the latter case, however, stable oligomers were found and bimodal $c_n(t)$ curves (“two-hump effect”) could be reported for the first time to the best of our knowledge.
- ✓ Both, in simulations and in experiments, clusters of high stability were found in at least two precise size-ranges that are approximately equally spaced. We developed a five stage model for a suitable description of the formation and growth of these stable aggregates. It also explains the “two hump effect” for the oligomers.
- ✓ A quantitative comparison between simulated BDLCA processes and experiments fails because in the latter case: i) the stable clusters are smaller and ii) x_c seems to be larger. We suggest these discrepancies to be due to lateral repulsion between like particles which impedes the attachment of other particles of the same species. When long-range interactions are included in the BDS, the size of the stable aggregates is in fact found to decrease. Therefore, also in experiments of selective heteroaggregation processes, the size of stable aggregates is expected to increase with the electrolyte concentration. Future work in this direction is planned.

A. RESUMEN Y CONCLUSIONES

Esta tesis doctoral trata acerca de los procesos de heteroagregación electrostática que se dan en dispersiones coloidales bicomponentes, formadas por partículas de igual tamaño pero carga eléctrica de signo opuesto. Se han estudiado tanto las tasas de agregación como el comportamiento cinético general, en función de dos variables: la concentración de electrolito del medio y la fracción de partículas de cada especie. El trabajo tiene dos vertientes complementarias: una experimental y otra de simulación.

El estudio experimental se basa principalmente en el uso de la técnica de dispersión de luz por agregados individuales (SCLS¹).² Esta técnica nos permite determinar la distribución de tamaños de agregado (CSD³) sin necesidad de recurrir a un modelo para la estructura de los mismos (Fernández-Barbero *et al.*, 1996). Otras técnicas experimentales se han utilizado en menor medida (nefelometría, medidas de movilidad electroforética. . .).

Por otra parte, se han utilizado simulaciones de dinámica Browniana (BDS⁴) para complementar e interpretar los resultados experimentales. Se han utilizado dos tipos de BDS: i) BDS donde las interacciones entre partículas se sustituyen por reglas que determinan si se produce o no agregación en el contacto,⁵ y ii)

¹*single-cluster light scattering*

²El instrumento de SCLS utilizado fue construido por el Dr. Miguel Cabrerizo Vílchez (Universidad de Granada), como parte de la tesis doctoral del Dr. Antonio Fernández Barbero (actualmente en la Universidad de Almería). Posteriormente, el Dr. Artur Schmitt (Universidad de Granada) y el Dr. Gerardo Odriozola (Instituto Mexicano del Petróleo) introdujeron importantes mejoras en el funcionamiento del dispositivo.

³*cluster-size distribution*

⁴*Brownian dynamics simulations*

⁵*BDS with contact rules*, implementadas por el Dr. Arturo Moncho Jordá (Universidad de Granada).

BDS con un modelo de interacción entre partículas.⁶ Las primeras son adecuadas para estudiar procesos en los que las interacciones entre partículas sean de corto alcance (Meakin, 1983; Moncho-Jordá *et al.*, 2001), mientras que las segundas pueden utilizarse aunque éstas sean de un alcance comparable al radio de las partículas (Puertas *et al.*, 1999c).

Finalmente, este trabajo se ha completado mediante métodos numéricos, destacando el algoritmo estocástico para resolver la ecuación maestra de coagulación⁷ (Odriozola *et al.*, 2003).

Los puntos principales de este estudio son:

Selección y caracterización de los sistemas experimentales y adaptación del dispositivo de SCLS

- ✓ Se ha reescrito completamente el *software* de adquisición y tratamiento de datos del instrumento de SCLS. Esto ha permitido introducir algunas mejoras, como son:
 - Un nuevo algoritmo de clasificación de pulsos, que mejora la capacidad del dispositivo para discernir agregados según su tamaño (López-López *et al.*, 2004c). Así, ahora es posible discriminar agregados compuestos por hasta 11 partículas, mientras que con el anterior algoritmo difícilmente se llegaba a agregados de 7 partículas.
 - Posibilidad de seguir la evolución del histograma de frecuencia de pulsos en tiempo real. Esto facilita en gran medida el proceso de calibrado del instrumento.
 - Implementación de un criterio estadístico para determinar si se produce ruptura de agregados durante el proceso de medida. Hay que

⁶*BDS with DLVO-HHF particle-particle interactions*, implementadas por el Dr. Antonio Puertas (Universidad de Almería).

⁷*Stochastic algorithm to solve the coagulation master equation*, implementado por el Dr. Gerardo Odriozola Prego (Instituto Mexicano del Petróleo).

decir que, en las pruebas realizadas, el resultado de este test siempre ha sido negativo (no se produce ruptura).

- ✓ Se ha comprobado que la técnica SCLS es adecuada para estudiar procesos de heteroagregación coloidal. Con anterioridad a este trabajo, esta técnica sólo se había aplicado al estudio de la homoagregación (Broide and Cohen, 1990; Pelssers *et al.*, 1990a; Schmitt *et al.*, 2000b). Además, se ha establecido un protocolo de medida que permite realizarlas de manera reproducible.
- ✓ Se han seleccionado dos dispersiones coloidales modelo, cuyas partículas tienen el mismo tamaño, pero carga eléctrica de signo opuesto. Además, se ha realizado una completa caracterización de estos látex que incluye:
 - Determinación del tamaño de partícula e índice de polidispersidad (PDI⁸) mediante microscopía electrónica de transmisión (TEM⁹).
 - Estudio de la estabilidad cinética y determinación de la concentración crítica de coagulación (CCC¹⁰), mediante nefelometría¹¹. Se debe señalar que la CCC del látex catiónico es algo menor que la del aniónico, lo cual indica que las partículas positivas están menos cargadas.
 - Estudio de la movilidad electrofóretica¹² frente al pH y frente a la concentración de KBr.
- ✓ Se han estudiado los procesos de homoagregación de los dos sistemas frente a la concentración de varias sales. Cuando se utilizó KBr, ambos respondieron acorde a la teoría clásica de los coloides liofóbicos, la teoría DLVO (Derjaguin and Landau, 1941; Verwey and Overbeek, 1948): agregación limitada por difusión (DLCA¹³) para concentraciones de KBr por encima

⁸*polydispersity index*

⁹*transmission electron microscopy*

¹⁰*critical coagulation concentration*

¹¹*nephelometry, low-angle static light-scattering*

¹²*electrophoretic mobility*

¹³*diffusion-limited colloid aggregation*

de la CCC, y agregación limitada por reacción (RLCA¹⁴) muy por debajo de esta concentración de KBr. Hay que resaltar que cuando se utilizaron otras sales se encontraron comportamientos que no pueden explicarse con esta teoría. Especialmente notable es el caso del sulfocianuro potásico. A la concentración de 600 mM de NaSCN, se encontró que el látex catiónico agregaba mediante un mecanismo reversible (Lopez-León *et al.*, 2006).

Estudio de la velocidad de agregación en dispersiones coloidales binarias simétricas

- ✓ Se ha medido la constante aparente de formación de dímeros¹⁵, k_S , en dispersiones coloidales binarias simétricas siguiendo el método de Drake (1972). La concentración de KBr en el estudio ha variado seis órdenes de magnitud: desde 1 M KBr hasta una concentración total de electrolito de aproximadamente $3 \mu\text{M}$ ¹⁶. Utilizando la aproximación HHF (Hogg, Healy and Fuerstenau, 1966), y conocidas las constantes de homoagregación por experimentos independientes, fue posible determinar también la constante intrínseca de formación de dímeros mixtos¹⁷, k_{AB} . Se encontró un aumento continuo de k_{AB} conforme se reducía la concentración de electrolito.
- ✓ A altas concentraciones de electrolito —por encima de las CCCs de los sistemas monocomponentes— se encontró que tanto k_S como k_{AB} tomaban valores considerados típicos para la agregación limitada por difusión (alrededor de $4 \times 10^{-12} \text{ cm}^3\text{s}^{-1}$). Esto nos indica que todas las partículas reaccionan de la misma manera, independientemente de sus propiedades eléctricas. Este resultado está en buen acuerdo con la teoría DLVO-HHF, que predice que, por encima de la CCC, las interacciones de origen electrostático están completamente apantalladas.

¹⁴*reaction-limited colloid aggregation*

¹⁵*effective dimer formation rate constant*

¹⁶Este caso corresponde a experimentos donde no se añadió nada de sal. Fue posible alcanzar concentraciones de electrolito tan bajas porque no se utilizó ningún tampón de pH.

¹⁷*absolute heteroaggregation dimer formation rate constant*

-
- ✓ A concentraciones de electrolito intermedias —de 50 mM a 200 mM, es decir por debajo de la CCC, pero del mismo orden de magnitud que ésta— se encontró que k_S tomaba valores inferiores al difusivo. Sin embargo, k_{AB} , lejos de disminuir, incluso aumentaba levemente. Esto lo explica perfectamente la teoría DLVO, que predice la aparición de una barrera de energía potencial que dificulta la agregación de partículas iguales, para concentraciones de electrolito inferiores a la CCC.
 - ✓ A bajas concentraciones de electrolito —aproximadamente entre 1 mM y 10 mM— se encontró una zona de *plateau* en la que k_S tomaba de nuevo un valor típicamente difusivo. Sin embargo, medidas independientes de homoagregación demuestran que a esas concentraciones de sal los dos sistemas son completamente estables. Se trata, por tanto, de procesos de heteroagregación selectiva¹⁸, en los que las interacciones entre partículas aún tienen un alcance relativamente corto. La teoría DLVO-HHF predice la existencia de una región así para partículas relativamente grandes, como son las utilizadas en este estudio.
 - ✓ A concentraciones de electrolito aún más bajas —por debajo de 1 mM—, se encuentra un incremento extraordinario en el valor de k_S . Por tanto, necesariamente tiene que haber interacciones atractivas de largo alcance entre las partículas. Hasta tal punto ocurre esto que, cuando no se añade electrolito, se midió un valor para k_{AB} tan grande como $(35 \pm 7) \times 10^{-12} \text{ cm}^3 \text{ s}^{-1}$. Hasta donde nosotros sabemos, se trata de la constante cinética de agregación más alta medida en un sistema coloidal diluido. La teoría DLVO-HHF predice este incremento en la tasa de agregación de partículas de distinto tipo a muy bajas concentraciones de electrolito. Debemos resaltar que, a pesar de no haber hecho ningún tipo de proceso de ajuste de parámetros, el acuerdo entre los valores de k_{AB} predichos por esta teoría y los medidos en el laboratorio es satisfactorio, incluso a nivel cuantitativo.
 - ✓ Para completar el estudio de las constantes cinéticas de agregación, se han realizado simulaciones de dinámica Browniana de mezclas simétricas de partículas de carga opuesta. Las interacciones entre partículas contempladas por estas BDS son las proporcionadas por la teoría DLVO-HHF. Se

¹⁸*selective heteroaggregation*

ha encontrado un acuerdo razonable entre simulaciones y experimentos: agregación rápida para interacciones de muy corto alcance, un mínimo en k_S para valores intermedios, y un fuerte aumento cuando el alcance de las interacciones se hace comparable al radio de las partículas. Falla, sin embargo, el acuerdo cuantitativo. Además, en las BDS no se encuentra la región de *plateau* que sí estaba presente en los experimentos. Es posible que esto se deba a un efecto del tamaño de partícula, aunque será necesario más trabajo para clarificar esta cuestión.

Regímenes de heteroagregación en dispersiones coloidales bicomponentes simétricas

- ✓ La distribución de tamaños $c_n(t)$ en procesos de heteroagregación electrostática en dispersiones coloidales bicomponentes simétricas se ha medido mediante SCLS. Se ha encontrado una fuerte dependencia de la cinética de la CSD con la concentración de electrolito. Además, las CSDs experimentales se han comparado con las obtenidas mediante BDS y con soluciones de la ecuación de coagulación para varios *kernels* semiempíricos. De todo esto, se ha podido establecer la existencia de, al menos, tres regímenes de agregación diferentes según la concentración de electrolito.
- ✓ A altas concentraciones de electrolito, la heteroagregación transcurre como si se tratara de homoagregación a esa misma concentración de electrolito. Es decir, sigue el régimen DLCA. Se ha encontrado un acuerdo excelente entre la CSD experimental y la correspondiente a una simulación de un proceso ideal de agregación limitada por difusión. Más aún, se ha comprobado que la CSD experimental se reproduce perfectamente cuando se resuelve la ecuación de agregación con el *kernel* Browniano. Debemos destacar que, aunque ya se sabía que el *kernel* Browniano reproduce correctamente la homoagregación en el régimen DLCA (ver, por ejemplo, Schmitt *et al.*, 2000b), esta es la primera vez que se comprueba que también lo hace para la heteroagregación en ese régimen.
- ✓ A concentraciones de electrolito intermedias, donde la heteroagregación es selectiva, pero el alcance de las interacciones entre partículas es aún

corto, se encuentra un régimen de agregación nuevo: agregación coloidal binaria limitada por difusión (BDLCA¹⁹). La principal característica de la CSD de este régimen es el exceso relativo de monómeros a tiempos largos o “discriminación de monómeros”²⁰ (López-López *et al.*, 2004b). Este régimen queda perfectamente descrito por dos reglas (Meakin and Djordjević, 1986): i) todos los contactos entre partículas de distinto tipo forman un enlace y ii) los enlaces entre partículas iguales están prohibidos. Se realizaron BDS con estas reglas de contacto y se encontró un acuerdo excelente con los experimentos (López-López *et al.*, 2005). La discriminación de monómeros también se encontró al resolver la ecuación de coagulación con *kernels* en los que la constante cinética de formación de dímeros vale la mitad que en el *kernel* Browniano. El mejor acuerdo cuantitativo se obtuvo con una variación del *kernel* q -suma de Calogero and Leyvraz (1999), con $q = 1/2$. Debemos resaltar que ésta es la primera vez, hasta donde nosotros sabemos, que este *kernel* ha sido utilizado para describir procesos reales de agregación coloidal.

- ✓ A baja concentración de electrolito, el alcance de las interacciones entre partículas ya no es despreciable. Las CSDs experimentales se caracterizan por un fuerte incremento de la tasa global de agregación y por la rápida desaparición de los dímeros, o “discriminación de dímeros”²¹ (López-López *et al.*, 2004b). Este régimen se conoce como de agregación dirigida por atracción (ADCA²²) (Puertas *et al.*, 2001b). Las simulaciones de dinámica Browniana con interacciones describen correctamente este fenómeno y predicen que la discriminación entre agregados pares e impares se extiende a tamaños de agregado mayores cuando el alcance de las interacciones se incrementa más aún (Puertas *et al.*, 2002). En este trabajo hemos confirmado la discriminación de monómeros y dímeros, pero no ha sido posible comprobar la validez de esta hipótesis para agregados mayores.

¹⁹*binary diffusion-limited colloid aggregation*

²⁰*monomer discrimination*

²¹*dimer discrimination*

²²*attraction-driven colloid aggregation*

Estudio de la heteroagregación electrostática de sistemas coloidales bicomponentes asimétricos

- ✓ La influencia de x , la proporción de partículas de cada tipo, en los procesos ideales de BDLCA se ha estudiado mediante simulaciones de dinámica Browniana fuera de red²³. A tiempos cortos se ha demostrado la validez de la aproximación HHF (Hogg *et al.*, 1966). A tiempos largos se ha encontrado que existe una proporción crítica x_c tal que, para $x > x_c$ la agregación continúa hasta que se forma un único agregado, mientras que para $x < x_c$ algunos agregados permanecen estables. El valor encontrado para x_c , alrededor de 0.15, es claramente inferior al determinado por AlSunaidi *et al.* (2000) para procesos BDLCA en un red cúbica²⁴. Esta discrepancia se debe al mayor grado de recubrimiento que es posible cuando las partículas no están obligadas a ocupar las posiciones de una red cúbica simple (López-López *et al.*, 2005).
- ✓ Para valores de x cercanos a x_c se encuentra un comportamiento muy atípico en la concentración de ciertos n -méros, especialmente las correspondientes a $8 \leq n \leq 10$: su concentración alcanza dos máximos a diferentes escalas temporales, de tal manera que la curva $c_n(t)$ recuerda al perfil de la espalda de un camello (“efecto de las dos jorobas”²⁵). Se encuentra que estos dos máximos corresponden a dos composiciones distintas: agregados con varias partículas minoritarias, para tiempos cortos; y agregados con tan sólo una partícula minoritaria para tiempos largos (López-López *et al.*, 2005). Debemos resaltar que este comportamiento no se encuentra en simulaciones BDLCA en red.
- ✓ Se han realizado experimentos de SCLS con dispersiones coloidales binarias asimétricas, sin electrolito añadido. Debido a la diferencia de carga efectiva entre los dos tipos de partículas utilizados, se han encontrado fenómenos distintos para $x \lesssim 0,2$ que para $x \gtrsim 0,8$. En el primer

²³*off-lattice Brownian dynamics simulations*

²⁴*on-lattice BDLCA*

²⁵“two-hump effect”

caso la agregación se detiene rápidamente, alcanzándose una CSD estacionaria. Se trata de un ejemplo de las reacciones detenidas²⁶ de Puertas *et al.* (2001a). En el segundo caso, se encuentran agregados metaestables y ejemplos de curvas $c_n(t)$ bimodales (“efecto de las dos jorobas”). Hasta donde nosotros sabemos, estas son las primeras curvas de concentración con esta característica encontradas en sistemas reales.

- ✓ Tanto en simulaciones como en experimentos, el tamaño de los agregados estables se encuentra comprendido dentro de intervalos discretos precisos. Hemos desarrollado un modelo en cinco etapas para la formación de los agregados estables que da cuenta de este fenómeno. Además, nuestro modelo explica la presencia del “efecto de las dos jorobas” en ciertos oligómeros.
- ✓ La comparación cuantitativa entre experimentos y simulaciones falla en dos puntos: i) los agregados (meta) estables encontrados en los experimentos son de menor tamaño y ii) en los experimentos $x_c \approx 0,25$, valor mucho mayor que el obtenido en simulaciones. Creemos que estas discrepancias se deben a la repulsión lateral que sufren las partículas del mismo tipo dentro de la capa de recubrimiento de una partícula de signo opuesto. Esta interacción dificulta la adición de más partículas a esa capa, reduciendo el grado medio de recubrimiento. De hecho, cuando se incluyen interacciones de largo alcance en las BDS, se encuentra que el tamaño de los agregados estables decrece. Por tanto, se espera que en experimentos de heteroagregación selectiva, el tamaño de los agregados estables aumente al aumentar la concentración iónica. Pretendemos continuar este trabajo en esa dirección.

²⁶*stopped reactions*

Bibliography

- Abend, S., Bonnke, N., Gutschner, U. and Lagaly, G. (1998), 'Stabilization of emulsions by heterocoagulation of clay minerals and layered double hydroxides', *Colloids Polym. Sci.* **276**(8), 730–737.
- Allain, C., Cloitre, M. and Wafra, M. (1995), 'Aggregation and sedimentation in colloidal suspensions', *Phys. Rev. Lett.* **74**(8), 1478–1481.
- AlSunaidi, A., Lach-Hab, M., González, A. E. and Blaisten-Barojas, E. (2000), 'Cluster-cluster aggregation in binary mixtures', *Phys. Rev. E.* **61**, 550–556.
- Adler, P. M. (1981), 'Interaction of unequal spheres I. Hydrodynamic interaction: Colloidal forces', *J. Colloid Interface Sci.* **84**(2), 461–473.
- Aubert, C. and Cannell, D. S. (1986), 'Restructuring of colloidal silica aggregates', *Phys. Rev. Lett.* **56**(7), 738–741.
- Bandini, P., Prestidge, C. A. and Ralston, J. (2001), 'Colloidal iron oxide slime coatings and galena particle flotation', *Minerals Eng.* **14**(5), 487–497.
- Barany, S., Cohen Stuart, M. A. and Fleer, G. J. (1996), 'Coagulation rate of silica dispersions investigated by single-particle optical sizing', *Colloids Surf. A* **106**, 213–221.
- Bastos-González, D. (1992), *Coloides modelo de poliestireno sulfonados: Preparación, propiedades electrocinéticas y estabilidad coloidal*, Master's thesis, Universidad de Granada, Spain.
- Broide, M. L. (1988), 'Experimental study of aggregation kinetics: dynamic scaling of measured cluster-size distributions', PhD thesis, Massachusetts Institute of Technology, USA.
- Broide, M. L. and Cohen, R. J. (1990), 'Experimental evidence of dynamic scaling in colloidal aggregation', *Phys. Rev. Lett.* **64**(17), 2026–2029.
- Buffle, J., Wilkinson, K. J., Stoll, S., Filella, M. and Zhang, J. (1998), 'A generalized description of aquatic colloidal interactions: The three-colloidal component approach', *Environ. Sci. Technol.* **32**(19), 2887–2899.
- Caballero, J. B., Puertas, A. M., Fernández-Barbero, A. and de las Nieves, J. (2005), 'Oppositely charged colloidal binary mixtures: A colloidal analog of the restricted

Bibliography

- primitive model', *J. Chem. Phys.* **121**(5), 2428–2435.
- Caballero, J. B., Puertas, A. M., Fernández-Barbero, A. and de las Nieves, J. (2005), 'Formation of clusters in a mixture of spherical colloidal particles oppositely charged', *Colloid Surf. A* **270**, 285–290.
- Cacace, M. G., Landau, E. M. and Ramsden, J. J. (1997), 'The Hofmeister series: salt and solvent effects on interfacial phenomena', *Q. Rev. Biophys.* **30**, 241–277.
- Calogero, F. and Leyvraz, F. (1999), 'A new solvable model of aggregation kinetics', *J. Phys. A: Math. Gen.* **32**, 7697–7717.
- Calogero, F. and Leyvraz, F. (2000), 'New results on a parity-dependent model of aggregation', *J. Phys. A: Math. Gen.* **33**, 5619–5629.
- Chandrasekhar, S. (1943), 'Stochastic problems in physics and astronomy', *Rev. Mod. Phys.* **15**(1), 1–89.
- Chung, H. S. and Hogg, R. (1985), 'Stability criteria for fine-particle dispersions', *Colloids Surf.* **15**, 119–135.
- Cölfen, H., Völkel, A., Eda, S., Kobold, U., Kaufmann, J., Puhmann, A., Göltner, C. and Wachernig, H. (2002), 'Mechanism of nanoparticle-enhanced turbidimetric assays applying nanoparticles of different size and immunoreactivity', *Langmuir* **18**(20), 7623–7628.
- Collins, K. D. and Washabough, M. W. (1985), 'The Hofmeister effect and the behaviour of water at interfaces', *Q. Rev. Biophys.* **18**(4), 323–422.
- Costa, A. L., Bezzi, G., la Torreta, T. M. G. and Verna, S. (2002), 'New process for the preparation of pigment-coated phosphors on the base of electroacoustic characterization', *J. Eur. Ceramic Soc.* **22**, 1667–1672.
- Deng, H. and Lu, Z. (1998), 'Heteroaggregation and photoelectric conversion of porphyrins on a nanostructured TiO₂ electrode', *Supramolecular Sci.* **5**(5–6), 669–674.
- Derjaguin, B. V. and Landau, L. (1941), 'Theory of the strongly charged lyophobic sols and of the adhesion of strongly charged particles in solutions of electrolytes', *Acta Physiochim. USSR* **14**, 633–662.
- Deshiikan, S. R. and Papadopoulos, K. D. (1997), 'Visual microscopic studies on heteroaggregation and selective aggregation', *Colloids Polym. Sci.* **275**(5), 440–448.
- di Feo, A. and Finch, J. A. (2002), 'Sphalerite/Silica interactions: Model predictions', *Int. J. Miner. process.* **64**(4), 219–227.
- di Feo, A., Finch, J. A. and Xu, Z. (2001), 'Sphalerite-silica interactions: Effect of pH and calcium ions', *Int. J. Miner. Process.* **61**(1), 57–71.

- Drake, R. L. (1972), 'A general mathematical survey of the coagulation equation', in G. M. Hidy and J. R. Brock, eds, 'Topics in Current Aerosol Research', Pergamon Press, New York.
- Einstein, A. (1905), 'Über die von der molekularkinetischen Theorie der Wärme geforderte Bewegung von in ruhenden Flüssigkeiten suspendierten Teilchen', *Annalen der Physik* **17**, 549–560. Note: republished in *Annalen der Physik* **14** (2005), 182–193.
- Family, F., Meakin, P. and Vicsek, T. (1985), 'Cluster size distribution in chemically controlled cluster-cluster aggregation', *J. Chem. Phys.* **83**(8), 4144–4150.
- Fernández-Barbero, A. (1994), 'Estudio de Agregación en Fluidos Complejos: Escalado Espacial y Temporal', PhD thesis, Universidad de Granada, Spain.
- Fernández-Barbero, A., Martín-Rodríguez, A., Callejas-Fernández, J. and Hidalgo-Álvarez, R. (1994), 'On the calculation of electrokinetic potential and Hamaker constant of model colloids', *J. Colloid Interface Sci.* **162**(1), 257–260.
- Fernández-Barbero, A., Schmitt, A., Cabrerizo-Vílchez, M. and Martínez-García, R. (1996), 'Cluster-size distribution in colloidal aggregation monitored by single-cluster light scattering', *Physica A* **230**(1–2), 53–74.
- Fernández-Barbero, A. and Vincent, B. (2001), 'Charge heteroaggregation between hard and soft particles', *Phys. Rev. E.* **63**, 011509–7.
- Findlay, A. D., Thompson, D. W. and Tipping, E. (1996), 'The aggregation of silica and haematite particles dispersed in natural water samples', *Colloids Surf. A* **118**(1–2), 97–105.
- Fuchs, N. (1934), 'Über die Stabilität und Aufladung der Aerosole', *Z. Phys.* **89**, 736–743.
- Furusawa, K., Matsumura, H. and Majima, T. (2003), 'Characterization of silica-coated hematite and application to the formation of composite particles including egg yolk PC liposomes', *J. Colloid Interface Sci.* **264**, 95–100.
- Galindo-González, C., de Vicente, J., Ramos-Tejada, M. M., López-López, M. T., González-Caballero, F. and García-Durán, J. D. (2005), 'Preparation and sedimentation behavior in magnetic fields of magnetite-covered clay particles', *Langmuir* **21**(10), 4410–4419.
- Galleto, P., Lin, W., Mishchenko, M. and Borkovec, M. (2005a), 'Light-scattering form factors of asymmetric particle dimers from heteroaggregation experiments', *J. Phys. Chem. B* **123**, 064709–8.
- Galleto, P., Lin, W. and Borkovec, M. (2005b), 'Measurement of heteroaggregation rate

Bibliography

- constants by simultaneous static and dynamic light scattering', *Phys. Chem. Chem. Phys.* **7**, 1464–1471.
- Garcia-Perez, P., Pagnoux, C., Rossignol, F. and Baumard, J.-F. (2006), 'Heterocoagulation between SiO₂ nanoparticles and Al₂O₃ submicronparticles; influence of the background electrolyte', *Colloids Surf. A* **281**, 58–66.
- Gillespie, D. T. (1977), 'Exact stochastic simulation of coupled chemical reactions', *J. Phys. Chem.* **81**(25), 2340–2361.
- González, A. E. (1993), 'Universality of colloid aggregation in the reaction limit: the computer simulations', *Phys. Rev. Lett.* **71**(14), 2248–2251.
- Goodwin, J. W., Hearn, J., Ho, C. C. and Ottewill, R. H. (1974), 'Studies on the preparation and characterisation of monodisperse polystyrene latices: III. Preparation without added surface active agents', *Colloids Polym. Sci.* **252**(6), 464–471.
- Hall, R. J., Pinkrah, V. T., Chowdhry, B. Z. and Snowden, M. J. (2004), 'Heteroaggregation studies of mixed cationic co-polymer/anionic homopolymer microgel dispersions', *Colloids Surf. A* **233**, 25–38.
- Hamaker, H. C. (1937), 'The London-van der Waals attraction between spherical particles', *Physica (Utrecht)* **4**(10), 1058–1072.
- Hansen, F. K. and Matijević (1980), 'Heterocoagulation. Part 5.— Adsorption of a carboxylated polymer latex on monodispersed hydrated metal oxides', *J. Chem. Soc., Faraday Trans. 1* **76**, 1240–1262.
- Harley, S., Thompson, D. W. and Vincent, B. (1992), 'The adsorption of small particles onto larger particles of opposite charge, direct electron microscope studies', *Colloids Surf.* **62**(1–2), 153–162.
- Hayashi, H., Nihei, T., Ono, M., Tsuneda, S., Hirata, A. and Sasaki, H. (2001), 'Rapid recovery of bacterial cells from a stable dispersion by heterocoagulation to a fibrous collector', *J. Colloid Interface Sci.* **243**, 109–115.
- Hendriks, E. M. and Ernst, M. H. (1984), 'Exactly soluble addition and condensation models in coagulation kinetics', *J. Colloid Interface Sci.* **97**(1), 176–194.
- Hidalgo-Álvarez, R., de las Nieves, F. J., Van der Linde, A. J. and Bijsterbosch, B. H. (1989), 'Conformational changes of polyglutamic acid adsorbed on cationic polystyrene as characterized by microelectrophoresis technique', *Colloid Polymer Sci.* **267**, 853–856.
- Hidalgo-Álvarez, R., Martín, A., Fernández, A., Bastos, D., Martínez, F. and de las Nieves, F. J. (1996), 'Electrokinetic properties, colloidal stability and aggregation kinetics of polymer colloids', *Adv. Colloid Interface Sci.* **67**, 1–118.

- Hogg, R., Healy, T. W. and Fuerstenau, D. W. (1966), 'Mutual coagulation of colloidal dispersions', *Trans. Faraday Soc.* **62**, 1638–1651.
- Holthoff, H., Schmitt, A., Fernández-Barbero, A., Borkovec, M., Cabrerizo-Vílchez, M. Á., Schurtenberger, P. and Hidalgo-Álvarez, R. (1997), 'Measurement of absolute coagulation rate constants for colloidal particles —comparison of single and multiparticle light scattering techniques', *J. Colloid Interface Sci.* **192**(2), 463–470.
- Honig, E. P., Roeberson, G. J. and Wiersema, P. H. (1971), 'Effect of hydrodynamic interaction on the coagulation rate of hydrophobic colloids', *J. Colloid Interface Sci.* **36**, 97–109.
- Hunter, R. J. (1987), *Foundations of Colloid Science*, Clarendon Press, United Kingdom.
- Ion, R.-M., Yilmaz, I. and Bekaroglu, O. (1999), 'Supramolecular assemblies of pyridyl porphyrin and diazadithia phthalocyanine', *J. Serb. Chem. Soc.* **64**(7–8), 453–462.
- Islam, A. M., Chowdhry, B. Z. and Snowden, M. J. (1995), 'Heteroaggregation in colloidal dispersions', *Adv. Colloid Interface Sci.* **62**, 109–136.
- Ito, H., Hayashi, H. and Sasaki, H. (2002), 'Rapid separation of oil particles from low-concentrated O/W emulsions in the presence of anionic surfactants using fibrous slag', *J. Colloid Interface Sci.* **252**, 214–221.
- Jadhav, S., Bochner, B. S. and Konstantopoulos, K. (2001), 'Hydrodynamic shear regulates the kinetics and receptor specificity of polymorphonuclear leukocyte-colon carcinoma cell adhesive interactions', *J. Immunol.* **167**(10), 5986–5993.
- James, R. O., Homola, A. and Healy, T. W. (1977), 'Heterocoagulation of amphoteric latex colloids', *J. Chem. Soc. Faraday Trans.* **73**, 1436–1445.
- Kerker, M. (1969), *The Scattering of Light and other Electromagnetic Radiation*, Academic Press, Inc., London.
- Kihira, H., Ryde, N. and Matijević, E. (1992), 'Kinetics of heterocoagulation. Part 2—The effect of the discreteness of surface charge', *J. Chem. Soc. Faraday Trans.* **88**(16), 2379–2386.
- Kim, A. Y. and Berg, J. C. (2000), 'Fractal heteroaggregation of oppositely charged colloids', *J. Colloid Interface Sci.* **229**, 607–614.
- Kim, A. Y., Hauch, K. D., Berg, J. C., Martin, J. E. and Anderson, R. A. (2003), 'Linear chains and chain-like fractals from electrostatic heteroaggregation', *J. Colloid Interface Sci.* **260**, 149–159.
- Kolb, M. (1984), 'Unified description of static and dynamic scaling for kinetic cluster formation', *Phys. Rev. Lett.* **17**, 1653–1656.
- Lagaly, G., Mecking, O. and Penner, D. (2001), 'Colloidal magnesium aluminum hy-

- droxide and heterocoagulation with a clay mineral. II. Heterocoagulation with sodium montmorillonite', *Colloid Polym. Sci.* **279**, 1097–1103.
- Langevin, P. (1908), 'Sur la théorie du mouvement brownien', *Comptes rendus* **146**, 530–533.
- Lattuada, M., Sandkühler, P., Wu, H., Sefcick, J. and Morbidelli, M. (2003), 'Aggregation kinetics of polymer colloids in reaction limited regime: experiments and simulations', *Adv. Colloid Interface Sci.* **103**, 33–56.
- Leyvraz, F. and Tschudi, H. R. (1981), 'Singularities in the kinetics of coagulation processes', *J. Phys. A: Math. Gen.* **14**(12), 3389–3405.
- Leyvraz, F. and Redner, S. (1986a), 'Nonuniversality and breakdown of scaling in a two-component coagulation model', *Phys. Rev. Lett.* **57**(2), 163–166.
- Leyvraz, F. and Redner, S. (1986b), "Erratum in 'Nonuniversality and breakdown of scaling in a two-component coagulation model' ", *Phys. Rev. Lett.* **57**(24), 3123.
- Leyvraz, F. and Redner, S. (1987), 'Non-universality and breakdown of scaling in two-species aggregation', *Phys. Rev. A* **36**(8), 4033–4049.
- Leyvraz, F. (2003), 'Scaling theory and exactly solved models in the kinetics of irreversible aggregation', *Phys. Reports* **383**, 95–212.
- Lyklema, J. (1991), *Fundamentals of Interface and Colloid Science. I. Fundamentals*, Academic Press, London.
- Lin, M. Y., Lindsay, H. M., Weitz, D. A., Klein, R., Ball, R. C. and Meakin, P. (1990a), 'Universal diffusion-limited colloid aggregation', *J. Phys.: Condens. Matter* **2**, 3093–3113.
- Lin, M. Y., Lindsay, H. M., Weitz, D. A., Ball, R. C., Klein, R. and Meakin, P. (1990b), 'Universal reaction-limited colloid aggregation', *Phys. Rev. A* **41**(4), 2005–2020.
- Lin, W., Kobayashi, M., Skarba, M., Mu, C., Galletto, P. and Borkovec, M. (2006), 'Heteroaggregation in binary mixtures of oppositely charged colloidal particles', *Langmuir* **22**, 1038–1047.
- Lips, A., Smart, C. and Willis, E. J. (1971), 'Light scattering on a coagulating polystyrene latex', *J. Chem. Soc. Faraday Trans.* **67**, 2979.
- Lipskier, J. F. and Tran-Thi, T. H. (1993), 'Supramolecular assemblies of porphyrins and phthalocyanines bearing oppositely charged substituents. First evidence of heterotrimer formation', *Inorg. Chem.* **32**(5), 722–731.
- López-García, J. J., Horno, J. and Grosse, C. (2002), 'Numerical solution of the Poisson-Boltzmann equation for a spherical cavity', *J. Colloid Interface Sci.* **251**, 85–93.
- López-León, T., Bastos-González, D., López-López, J. M., Schmitt, A., Odriozola, G.

- and Ortega-Vinuesa, J. L. (2006), ‘Hofmeister effects in colloidal suspensions: experimental evidences in aggregation kinetics’, sent to *Phys. Rev. E*.
- López-López, J. M., Schmitt, A., Callejas-Fernández, J. and Hidalgo-Álvarez, R. (2003), ‘Estudio experimental de la cinética de la heteroagregación gobernada por carga eléctrica superficial’, in L. Liz-Marzán, P. Hervés, J. C. Mejuto and C. Tojo, eds, ‘Coloides e Interfases’, Servicio de Publicacións da Universidade de Vigo, Spain, pp. 105–110.
- López-López, J. M., Schmitt, A., Callejas-Fernández, J. and Hidalgo-Álvarez, R. (2004a), Time-resolved measurements of the cluster-size distributions arising in charge-heteroaggregation processes, in V. Cabuil, P. Levitz and C. Treiner, eds, ‘Trends in Colloid and Interface Science XVII’, Vol. 126 of *Progr. Colloid Polym. Sci.*, Springer-Verlag, Germany, pp. 151–154.
- López-López, J. M., Schmitt, A., Callejas-Fernández, J. and Hidalgo-Álvarez, R. (2004b), ‘Cluster discrimination in electrostatic heteroaggregation’, *Phys. Rev. E* **69**(1), 011404–7.
- López-López, J. M., Odriozola, G., Schmitt, A., Callejas-Fernández, J. and Hidalgo-Álvarez, R. (2004c), ‘Improved sample handling and data acquisition for single cluster light scattering’, in I. Nopens, K. Malisse, C. A. Biggs and J. J. Ducoste, eds, ‘Advances in Population Balance Modelling’, EUROSIS Publications, Belgium, pp. 231–234.
- López-López, J. M., Moncho-Jordá, A., Schmitt, A. and Hidalgo-Álvarez, R. (2005), ‘Formation and structure of stable aggregates in binary diffusion-limited cluster-cluster aggregation processes’, *Phys. Rev. E* **72**, 031401–9.
- López-López, J. M., Schmitt, A., Moncho-Jordá, A. and Hidalgo-Álvarez, R. (2006), ‘Colloidal stability of binary colloids: Kinetics and structural aspects of heteroaggregation processes’, accepted for publication at *Soft Matter*.
- Luckham, P. F., Vincent, B. and Tadros, T. F. (1983), ‘The controlled flocculation of particulate dispersions using small particles of opposite charge. III. Investigation of floc structure using rheological techniques’, *Colloids Surf.* **6**(2), 101–118.
- Luna-Xavier, J. L., Guyot, A. and Bourgeat-Lami, E. (2002), ‘Synthesis and characterization of silica/poly(methyl methacrylate) nanocomposite latex particles through emulsion polymerization using a cationic Azo initiator’, *J. Colloid Interface Sci.* **250**, 82–92.
- Manoharan, V. N., Elsesser, M. T. and Pine, D. J. (2003), ‘Dense packing and symmetry in small clusters of microspheres’, *Science* **301**(5632), 483–487.
- Maroto, J. A. and de las Nieves, F. J. (1998), ‘Influence of multiple light scattering on the

Bibliography

- estimation of homocoagulation and heterocoagulation rate constants by turbidity measurements', *Colloids Surf. A* **132**, 153–158.
- Maruyama, K., Kawaguchi, M. and Kato, T. (2001), 'Heterocoagulation behavior of poly(styrene-co-butadiene) and poly(butyl acrylate) at high particle concentrations', *Colloids Surf. A* **189**, 211–223.
- McCarty, O. J. T., Jadhav, S., Burdick, M. M., Bell, W. R. and Konstantopoulos, K. (2002), 'Fluid shear regulates the kinetics and molecular mechanisms of activation-dependent platelet binding to colon carcinoma cells', *Biophys. J.* **83**(2), 836–848.
- McCormack, D., Carnie, S. L. and Chan, D. Y. C. (1995), 'Calculations of electric double-layer force and interaction free energy between dissimilar surfaces', *J. Colloid Interface Sci.* **169**, 177–196.
- McLeod, J. B. (1962), 'On an infinite set of non-linear differential equations', *Q. J. Math. Oxford* **13**, 119.
- Meakin, P. (1983), 'Formation of fractal clusters and networks by irreversible diffusion-limited aggregation', *Phys. Rev. Lett.* **51**, 1119–1122.
- Meakin, P., Vicsek, T. and Family, F. (1985a), 'Dynamic cluster-size distribution in cluster-cluster aggregation: Effects of cluster diffusivity', *Phys. Rev. B.* **31**, 564–569.
- Meakin, P., Chen, Z. and Deutch, J. M. (1985b), 'The translational friction coefficient and time dependent cluster size distribution of three dimensional cluster-cluster aggregation', *J. Chem. Phys.* **82**(8), 3785–3789.
- Meakin, P. and Djordjević, Z. B. (1986), 'Cluster-cluster aggregation in two-monomer systems', *J. Phys. A: Math. Gen.* **19**, 2137–2153.
- Melzak, Z. A. (1953), 'The effects of coalescence in certain collision processes', *Q. J. Appl. Math.* **11**, 231.
- Miao, X. and Marquis, P. M. (1992), 'Vitreous sintering of heterocoagulated alumina silica sols', *Nanostructured Mater.* **1**(1), 31–36.
- Mobilia, M., Krapivsky, P. L. and Redner, S. (2003), 'Kinetic anomalies in addition-aggregation processes', *J. Phys. A: Math. Gen.* **36**, 4533–4542.
- Molina Bolívar, J. A. (1999), 'Mecanismos de Estabilidad Coloidal: Teoría y Aplicación a Inmunoensayos', PhD thesis, Universidad de Granada, Spain.
- Moncho-Jordá, A., Odriozola, G., Martínez-López, F., Schmitt, A. and Hidalgo-Álvarez, R. (2001), 'The DLCA-RLCA transition arising in 2D-aggregation: simulations and mean field theory', *EuroPhys. J. E.* **5**, 471–480.
- Moncho-Jordá, A., Odriozola, G., Tirado-Miranda, M., Schmitt, A. and Hidalgo-

- Álvarez, R. (2003), 'Modeling the aggregation of partially covered particles: Theory and simulation', *Phys. Rev. E* **68**, 011404–12.
- Morris, G. E., Skinner, W. A., Self, P. G. and Smart, R. S. C. (1999), 'Surface chemistry and rheological behaviour of titania pigment suspensions', *Colloids Surf. A* **155**(1), 27–41.
- Mukherjee, S., Basak, S. and Khowala, S. (2002), 'Regulation (alteration) of activity and conformation of sucrase by coaggregation with cellobiase in culture medium of *Termitomyces clypeatus*', *Biotechnol. Prog.* **18**(2), 404–408.
- Ninham, B. W. and Yaminsky, V. (1997), 'Ion binding and ion specificity: the Hofmeister effect and Onsager and Lifshitz theories', *Langmuir* **13**(7), 2097–2108.
- Odriozola, G., Schmitt, A., Callejas-Fernández, J., Martínez-García, R. and Hidalgo-Álvarez, R. (1999), 'Dynamic scaling concepts applied to numerical solutions of Smoluchowski's rate equation', *J. Chem. Phys.* **111**(16), 7657–7667.
- Odriozola, G. (2001), 'Agregación reversible de sistemas coloidales en medios binarios', PhD thesis, Universidad de Granada, Spain.
- Odriozola, G., Tirado-Miranda, M., Schmitt, A., Martínez-López, F., Callejas-Fernández, J., Martínez-García, R. and Hidalgo-Álvarez, R. (2001a), 'A light scattering study of the transition region between diffusion- and reaction-limited cluster aggregation', *J. Colloid Interface Sci.* **240**(1), 90–96.
- Odriozola, G., Moncho-Jordá, A., Schmitt, A., Callejas-Fernández, J., Martínez-García, R. and Hidalgo-Álvarez, R. (2001b), 'A probabilistic aggregation kernel for the computer-simulated transition from DLCA to RLCA', *Europhys. Lett. E* **53**(6), 797–803.
- Odriozola, G., Schmitt, A., Moncho-Jordá, A., Callejas-Fernández, J., Martínez-García, R., Leone, R. and Hidalgo-Álvarez, R. (2002), 'Constant bond breakup probability model for reversible aggregation processes', *Phys. Rev. E* **65**, 031405–8.
- Odriozola, G., Schmitt, A., Callejas-Fernández, J., Martínez-García, R., Leone, R. and Hidalgo-Álvarez, R. (2003), 'Simulated reversible aggregation processes for different interparticle potentials: the cluster aging phenomenon', *J. Phys. Chem. B* **107**(10), 2180–2188, 14145.
- Odriozola, G., Leone, R., Schmitt, A., Callejas-Fernández, J., Martínez-García, R. and Hidalgo-Álvarez, R. (2004), 'Irreversible versus reversible aggregation: Mean field theory and experiments', *J. Chem. Phys.* **121**(11), 5468–5481.
- Ottewill, R. H., Schofield, A. B., Waters, J. A. and Williams, N. S. J. (1997), 'Preparation of core-shell polymer colloid particles by encapsulation', *Colloids Polym. Sci.* **275**(3), 274–283.

Bibliography

- Ouali, L., Pefferkorn, E., Elaissari, A., Pichot, C. and Mandrand, B. (1994), 'Heterocoagulation of sensitized latexes in the presence of HCG protein: the pregnancy test', *J. Colloid Interface Sci.* **171**, 276–282.
- Overbeek, J. Th. G. (1977), 'Recent developments in the understanding of colloid stability', *J. Colloid Interface Sci.* **58**(2), 408–422.
- Overbeek, J. Th. G. (1990), 'The role of energy and entropy in the electrical double layer', *Colloids Surfaces* **51**, 61–75.
- Padding, J. T. and Louis, A. A. (2006), 'Hydrodynamic interactions and Brownian forces in colloidal suspensions: Coarse-graining over time and length-scales', *Phys. Rev. E*, to appear.
- Pelssers, E. G. M., Cohen Stuart, M. A. and Fler, G. J. (1990a), 'Single particle optical sizing (SPOS); I. Design of an improved SPOS instrument and application to stable dispersions', *J. Colloid Interface Sci.* **137**(2), 350–361.
- Pelssers, E. G. M., Cohen Stuart, M. A. and Fler, G. J. (1990b), 'Single particle optical sizing (SPOS); II. Hydrodynamic forces and applications to aggregating dispersions', *J. Colloid Interface Sci.* **137**(2), 362–372.
- Plunkett, K. N., Mohraz, A., Haasch, R. T., Lewis, J. A. and Moore, J. S. (2005), 'Light-regulated electrostatic interactions in colloidal suspensions', *J. Am. Chem. Soc.* **127**(42), 14574–14575.
- Puertas, A. M., Fernández-Barbero, A. and de las Nieves, F. J. (1999a), 'Brownian dynamics simulation of diffusive mesoscopic particle aggregation', *Comput. Phys. Commun.* **121–122**, 353–357.
- Puertas, A. M., Maroto, J. A., Fernández-Barbero, A. and de las Nieves, F. J. (1999b), 'On the kinetics of heteroaggregation versus electrolyte concentration: Comparison between simulation and experiment', *Colloids Surf. A* **151**, 473–481.
- Puertas, A. M., Maroto, A. J., Fernández-Barbero, A. and de las Nieves, F. J. (1999c), 'Particle interactions in colloidal aggregation by Brownian dynamics simulation', *Phys. Rev. E* **59**(2), 1943–1947.
- Puertas, A. M., Maroto, A. J., Fernández-Barbero, A. and de las Nieves, F. J. (2000), 'Aggregation between oppositely charged colloidal particles', in V. Buckin, ed., 'Trends in Colloid and Interface Science XIV', Vol. 115 of *Progr. Colloid Polym. Sci.*, Springer-Verlag, Germany, pp. 55–58.
- Puertas, A. M., Fernández-Barbero, A. and de las Nieves, F. J. (2001a), 'Charged colloidal heteroaggregation kinetics', *J. Chem. Phys.* **114**(1), 591–595.
- Puertas, A. M., Fernández-Barbero, A. and de las Nieves, F. J. (2001b), 'Colloidal ag-

- gregation induced by attractive interactions', *J. Chem. Phys.* **115**(12), 5662–5668.
- Puertas, A. M., Fernández-Barbero, A. and de las Nieves, F. J. (2001c), 'Kinetics of charge heteroaggregation by Brownian dynamics simulation: Role of the interaction potential profile', *Colloids Surf. A* **195**, 189–195.
- Puertas, A. M., Fernández-Barbero, A. and de las Nieves, F. J. (2002), 'Kinetics of colloidal heteroaggregation', *Physica A* **304**, 340–352.
- Puertas, A. M., Fernández-Barbero, A. and de las Nieves, F. J. (2003), 'Induced asymmetries in the heteroaggregation of oppositely charged colloidal particles', *J. Colloid Interface Sci.* **265**, 36–43.
- Puertas, A. M., Fernández-Barbero, A. and de las Nieves, F. J. (2004), 'Internal structure of clusters from charge heteroaggregation', *J. Colloid Interface Sci.* **274**, 346–348.
- Puertas, A. M., Fernández-Barbero, A., de las Nieves, F. J. and Rull, L. F. (2004), 'Colloidal aggregation induced by long range attractions', *Langmuir* **20**, 9861–9867.
- Puertas, A. M., Fernández-Barbero, A. and de las Nieves, F. J. (2005), 'Structure factor scaling in colloidal charge heteroaggregation', *Europhys. J. E.* **18**, 335–341.
- Ramkrishna, D. (2000), *Population Balances: Theory and Applications to Particulate Systems in Engineering*, Academic Press, San Diego (USA).
- Reiner, E. S. and Radke, C. J. (1993), 'Double layer interactions between charge-regulated colloidal surfaces: pair potentials for spherical particles bearing ionogenic surface groups', *Adv. Colloid Interface Sci.* **47**, 59–147.
- Rim, Y. H., Cawley, J. D., Ansari, R. R. and Meyer, W. V. (1992), 'In-situ light scattering study of aggregation', in M. J. Cima, ed., 'Forming Science and Technology for Ceramics', Vol. 26 of *Cerm. Trans.*, American Ceramic Society, Ohio, pp. 54–65.
- Routh, A. F. and Vincent, B. (2004), 'Some anomalous effects of sodium ions on the electrophoretic mobility and heteroaggregation of microgel particles', *J. Colloid Interface Sci.* **273**, 435–441.
- Rubio, J., Souza, M. L. and Smith, R. W. (2002), 'Overview of flotation as a wastewater treatment technique', *Minerals Eng.* **15**, 139–155.
- Ryan, J. N. and Elimelech, M. (1996), 'Colloid mobilization and transport in groundwater', *Colloids Surf. A* **107**, 1–56.
- Ryde, N. and Matijević, E. (1994), 'Kinetics of heterocoagulation. Part 4. Evaluation of absolute coagulation rate constants using a classical light-scattering technique', *J. Chem. Soc. Faraday Trans.* **90**(1), 167–172.
- Schmitt, A. (2000), 'Escalado Temporal en Procesos de Agregación en Biocoloides', PhD thesis, Universidad de Granada, Spain.

Bibliography

- Schmitt, A., Fernández-Barbero, A., Cabrerizo-Vílchez, M. A. and Hidalgo-Álvarez, R. (2000a), 'Dynamic scaling in surface-controlled colloidal aggregation', *J. Phys.: Condens. Matter* **12**, A281–A286.
- Schmitt, A., Odriozola, G., Moncho-Jordá, A., Callejas-Fernández, J., Martínez-García, R. and Hidalgo-Álvarez, R. (2000b), 'Multiple contact kernel for diffusionlike aggregation', *Phys. Rev. E* **62**(6), 8335–8343.
- Schmitt, A., Moncho-Jordá, A., Odriozola, G., López-López, J. M., Callejas-Fernández, J. and Hidalgo-Álvarez, R. (2005), 'Agregación coloidal: aspectos cinéticos', in 'Coloides e interfases', Ed. Universidad de Salamanca, Spain, pp. 211–216.
- See, H. and Doi, M. (1991), 'Aggregation kinetics in electro-rheological fluids', *J. Phys. Soc. Jpn.* **60**(8), 2778–2782.
- Škvarla, J. (1993), 'On the decay of polar surface forces between hydrophobic surfaces and colloids', *J. Colloid Interface Sci.* **155**(2), 506–508.
- Snoswell, D. R. E., Rogers, T. J., Howe, A. M. and Vincent, B. (2005), 'Controlling porosity within colloidal heteroaggregates', *Langmuir* **21**(24), 11439–11445.
- Sonntag, H. and Strenge, K. (1987), *Coagulation Kinetics and Structure Formation*, Plenum Press, New York.
- Spielman, L. A. (1970), 'Viscous interaction in Brownian coagulation', *J. Colloid Interface Sci.* **33**, 562–571.
- Stoll, S. and Pefferkorn, E. (1992a), 'Modes of spontaneous and provoked cluster fragmentation. I. During diffusion-limited aggregation', *J. Colloid Interface Sci.* **152**(1), 247–256.
- Stoll, S. and Pefferkorn, E. (1992b), 'Modes of spontaneous and provoked cluster fragmentation. II. During reaction-limited aggregation', *J. Colloid Interface Sci.* **152**(1), 257–264.
- Stoll, S. and Pefferkorn, E. (1993), 'Kinetics of heterocoagulation', *J. Colloid Interface Sci.* **160**, 149–157.
- Stoll, S. and Pefferkorn, E. (1996), 'Monte Carlo simulation of controlled colloid growth by homo- and heterocoagulation in two dimensions', *J. Colloid Interface Sci.* **177**, 192–197.
- Strutt, J. W. (Lord Rayleigh) (1899), 'On the transmission of light through an atmosphere containing small particles in suspension, and on the origin of the blue of the sky', *L. Philos. Mag.* **47**, 375.
- Sunagawa, Y., Yamamoto, K. and Muramatsu, A. (2006), 'Improvement in SOFC anode performance by finely-structured Ni/YSZ Cermet prepared via heterocoagulation',

J. Phys. Chem. B, In press.

- Sunkel, J. M. and Berg, J. C. (1996), 'The stability behavior of sol-emulsion systems', *J. Colloid Interface Sci.* **179**, 618–624.
- Takayashu, M. M. and Galembeck, F. (1993), 'Polystyrene latex coagulation: A study using centrifugation in density gradients', *J. Colloid Interface Sci.* **155**, 16–22.
- Tangboriboonrat, P. and Buranabunya, U. (2001), 'Composite natural rubber-polychloroprene latex particles produced by the heterocoagulation technique', *Colloids Polym. Sci.* **279**(6), 615–620.
- Taylor, M. L., Morris, G. E. and Smart, R. S. C. (2003), 'Influence of aluminum doping on titania pigment structural and dispersion properties', *J. Colloid Interface Sci.* **262**(1), 81–88.
- Thorn, M. and Seesselberg, M. (1994), 'Dynamic scaling in colloidal aggregation: Comparison of experimental data with results of a stochastic simulation', *Phys. Rev. Lett.* **72**(22), 3622–3625.
- van Dongen, P. G. J. and Ernst, M. H. (1985a), 'Cluster size distribution in irreversible aggregation at large times', *J. Phys. A* **18**, 2779.
- van Dongen, P. G. J. and Ernst, M. H. (1985b), 'Dynamic scaling in the kinetics of clustering', *Phys. Rev. Lett.* **54**(13), 1396–1399.
- Vanni, M. (2000), 'Approximate population balance equations for aggregation-breakage processes', *J. Colloid Interface Sci.* **221**, 143–160.
- Verwey, E. J. W. and Overbeek, J. T. G. (1948), *Theory of the Stability of Lyophobic Colloids*, Elsevier Publishing Company, Inc., Amsterdam.
- Vincent, B., Bijsterbosch, B. H. and Lyklema, J. (1970), 'Competitive adsorption of ions and neutral molecules in the Stern layer on silver iodide and its effect on colloid stability', *J. Colloid Interface Sci.* **37**(1), 171–178.
- Vincent, B., Edwards, J., Emmett, S. and Jones, A. (1986), 'Depletion flocculation in dispersions of sterically-stabilised particles ("soft spheres")', *Colloids Surf.* **18**(2–4), 261–281.
- Vincent, B., Young, C. A. and Tadros, Th. F. (1980), 'Adsorption of small, positive particles onto large, negative particles in the presence of polymer. Part 1.— Adsorption isotherms', *J. Chem. Soc., Faraday Trans. 1* **76**, 665–673.
- von Smoluchowski, M. (1906), 'Zur kinetischen Theorie der Brownschen Molekularbewegung und der Suspensionen', *Annalen der Physik* **21**, 756–780.
- von Smoluchowski, M. (1914), 'Studien ber Molekularstatistik von Emulsionen und deren Zusammenhang mit der brownschen Bewegung', *Sitzungsberichte. Wien*

Bibliography

- 123, 2381–2405.
- von Smoluchowski, M. (1916), ‘Drei vorträge über Diffusion, brownsche Molekularbewegung und Koagulation von Kolloidteilchen’, *Physik. Z.* **17**, 557–571, 585–599.
- von Smoluchowski, M. (1917), ‘Versuch einer mathematischen Theorie der koagulationskinetik kolloider Lösungen’, *Z. Phys. Chem.* **92**, 129–168.
- Wang, Q. J. (1992), ‘A study on shear coagulation and heterocoagulation’, *J. Colloid Interface Sci.* **150**(2), 418–427.
- Weitz, D. A. and Oliveria, M. (1984), ‘Fractal structures formed by kinetic aggregation of aqueous gold colloids’, *Phys. Rev. Lett.* **52**(16), 1433–1436.
- Yang, B., Matsumura, H., Katoh, K., Kise, H. and Furusawa, K. (2001), ‘Formation of multilayer composite particles comprised of silica/vesicle/silica particles by heterocoagulation’, *Langmuir* **17**(8), 2283–2286.
- Ying, Q., Zhang, J., Liang, D., Nakanishi, W., Isobe, H., Nakamura, E. and Chu, B. (2005), ‘Fractal behavior of functionalized fullerene aggregates. I. Aggregation of two-handed tetraaminofullerene with DNA’, *Langmuir* **21**(22), 9824–9831.
- Yoshioka, N., Varga, I., Kun, F., Yukawa, S. and Ito, N. (2005), ‘Attraction-limited cluster-cluster aggregation of Ising dipolar particles’, *Phys. Rev. E* **72**, 061403–6.
- Yu, W. L. and Borkovec, M. (2002), ‘Distinguishing heteroaggregation from homoaggregation in mixed binary particle suspensions by multiangle static and dynamic light scattering’, *J. Phys. Chem. B* **106**(51), 13106–13110.
- Yu, W. L., Matijević, E. and Borkovec, M. (2002), ‘Absolute heteroaggregation rate constants by multiangle static and dynamic light scattering’, *Langmuir* **18**(21), 7853–7860.
- Ziff, R. M. and Stell, G. (1980), ‘Kinetics of polymer gelation’, *J. Chem. Phys.* **73**, 3492.

Nomenclature

a	particle radius
A, A_{132}	Hamaker constant
a_{ij}	i -mer- j -mer reaction probability density, see equation (3.23)
AS1	arbitrary name of the anionic latex used in this work
$c^\gamma(t)$	concentration of clusters of the γ type
c_0	initial particle concentration
c_j^m	concentration of j -mers with m particles of type A
$c_n(t)$	concentration of clusters composed by n particles, CSD
δ_i^j	Kronecker's symbol
D	diffusivity used in simulations
D_0	self-diffusion coefficient, see equation (2.35)
ϵ_0	dielectric permittivity of the vacuum
ϵ_m	relative dielectric permittivity of the dispersion medium
η	medium viscosity
\vec{E}	electrical field intensity
ϕ	volume fraction of particles
f_{flow}	pump flow factor, page 52
γ	friction coefficient
$g(t)$	Drake's function, see equation (3.10)

Nomenclature

$\langle I(\vec{q}, t) \rangle$	average light intensity in a LS experiment
$I(t)$	light intensity in a LS experiment
IDC	arbitrary name of the cationic latex used in this work
κ	Debye-Hückel parameter, see equation (2.56)
$k^{\text{Brw}}, k_{11}^{\text{Br}}$	monomer-monomer reaction rate constant for ideal DLCA processes
$k^{\alpha, \beta}$	aggregation rate constant between clusters of the species α and β
k_B	Boltzmann's constant
k_S	effective aggregation rate constant, see equation (3.11)
k_{11}^{HHF}	HHF approximation for the dimer formation rate constant, see equation (2.34)
k_{AA}, k_{BB}	absolute homoaggregation dimer formation rate constants
k_{AB}	absolute heteroaggregation dimer formation rate constant
K_{ij}	dimensionless aggregation <i>kernel</i>
k_{ij}	aggregation rate constant between clusters of masses i and j
λ_0	light wavelength
L	side length of the simulation box
μ_e	electrophoretic mobility, see equation (3.15)
M_0	(normalised) overall concentration of clusters, see equation (2.14)
M_n	n -th moment of the CSD, see equation (2.11)
$\vec{N}(t)$	vector state in the stochastic description
$N^\gamma(t)$	number of aggregates of the γ type
N^l	total number of aggregates with l minority particles
N_0	total number of particles in simulations
$N_i(t)$	number of i -mers

- $\langle n \rangle_l$ average size of aggregates with l minority particles, see equation (6.1)
- n_m medium refraction index
- $\langle n \rangle_n$ number-average cluster size, page 112
- ψ^* effective surface potential in the Stern layer, page 37
- $P_R(\tau, i, j)$ reaction probability density function
- P_s sticking probability, page 78
- \vec{q} scattering vector, see equation (3.1)
- R_g radius of gyration, see equation (2.37)
- R_{sc} radius of the scattering centre
- T dimensionless time
- T temperature
- t_{aggr} aggregation time, see equation (2.10)
- t'_{aggr} alternative aggregation time, see equation (2.15)
- \vec{v}_e electrophoretic drift velocity
- V system volume
- V_{inj} sample volume injected in a SCLS measurement
- V_{sc} scattering-centre volume
- W Fuchs stability ratio, see equation (3.14)
- x relative particle concentration, number fraction
- x_c critical relative concentration in BDLCA processes
- X_n dimensionless cluster-size distribution
- X50,X70... arbitrary names used for mixtures with 50%, 70%... of cationic particles.